POWER CONDITIONING UNIT FOR SMALL SCALE HYBRID PV-WIND GENERATION SYSTEM

ASHRAF AHMED-MAHMOUD

AHMED-MAHMOUD, ASHRAF (2011) POWER CONDITIONING UNIT FOR SMALL SCALE HYBRID PV-WIND GENERATION SYSTEM. Doctoral thesis, Durham University.

POWER CONDITIONING UNIT FOR SMALL SCALE HYBRID PV-WIND GENERATION SYSTEM

By
ASHRAF ABDEL HAFEEZ AHMED MAHMOUD

A Thesis presented for the degree of
Doctor of Philosophy

New and Renewable Energy Group
School of Engineering and Computing Sciences
Durham University
UK

2010

POWER CONDITIONING UNIT FOR SMALL SCALE HYBRID PV-WIND GENERATION SYSTEM

Submitted for the degree of Doctor of Philosophy

ABSTRACT

Small-scale renewable energy systems are becoming increasingly popular due to soaring fuel prices and due to technological advancements which reduce the cost of manufacturing. Solar and wind energies, among other renewable energy sources, are the most available ones globally. The hybrid photovoltaic (PV) and wind power system has a higher capability to deliver continuous power with reduced energy storage requirements and therefore results in better utilization of power conversion and control equipment than either of the individual sources. Power conditioning units (p.c.u.) for such small-scale hybrid PV-wind generation systems have been proposed in this study. The system was connected to the grid, but it could also operate in standalone mode if the grid was unavailable. The system contains a local controller for every energy source and the grid inverter. Besides, it contains the supervisory controller.

For the wind generator side, small-scale vertical axis wind turbines (VAWTs) are attractive due to their ability to capture wind from different directions without using a yaw. One difficulty with VAWTs is to prevent over-speeding and component over-loading at excessive wind velocities. The proposed local controller for the wind generator is based on the current and voltage measured on the dc side of the rectifier connected to the permanent magnet synchronous generator (PMSG). Maximum power point tracking (MPPT) control is provided in normal operation under the rated speed using a dc/dc boost converter. For high wind velocities, the suggested local controller controls the electric power in order to operate the turbine in the stall region. This high wind velocity control strategy attenuates the stress in the system while it smoothes the power generated. It is shown that the controller is able to stabilize the nonlinear system using an adaptive current feedback loop. Simulation and experimental results are presented.

The PV generator side controller is designed to work in systems with multiple energy sources, such as those studied in this thesis. One of the most widely used methods to maximize the output PV power is the hill climbing technique. This study gives guidelines for designing both the perturbation magnitude and the time interval between consecutive perturbations for such a technique. These guidelines would improve the maximum power point tracking efficiency. According to these guidelines, a variable step MPPT algorithm with reduced power mode is designed and applied to the system. The algorithm is validated by simulation and experimental results.

A single phase H-bridge inverter is proposed to supply the load and to connect the grid. Generally, a current controller injects active power with a controlled power factor and constant dc link voltage in the grid connected mode. However, in the standalone mode, it injects active power with constant ac output voltage and a power factor which depends on the load. The current controller for both modes is based on a newly developed peak current control (p.c.c.) with selective harmonic elimination. A design procedure has been proposed for the controller. Then, the method was demonstrated by simulation. The problem of the dc current injection to the grid has been investigated for such inverters. The causes of dc current injection are analyzed, and a measurement circuit is then proposed to control the inverter for dc current injection elimination. Characteristics of the proposed method are demonstrated, using simulation and experimental results.

At the final stage of the study, a supervisory controller is demonstrated, which manages the different operating states of the system during starting, grid-connected and standalone modes. The operating states, designed for every mode, have been defined in such a hybrid model to allow stability and smooth transition between these states. The supervisory controller switches the system between the different modes and states according to the availability of the utility grid, renewable energy generators, the state of charge (SOC) of energy storage batteries, and the load. The p.c.u. including the supervisory controller has been verified in the different modes and states by simulation.

Dedicated to my Father (Shikh Abdel hafeez Alsony) who passed away during the course of this work
May Allah rest his gentle soul in eternal peace
Aamen

Declaration

The work in this thesis is based on research carried out within the New and Renewable Energy Group, School of Engineering and Computing Sciences, Durham University, United Kingdom. No part of this thesis has been submitted elsewhere for any other degree or qualification and it all my own work unless referenced to the contrary in the text.

Acknowledgements

First, I would like to thank Allah, for His mercy on me during all my life, and praise the prophet Mohamad (peace be upon him!). I dedicate this work to my father (Shikh Abdel hafeez Alsony-May ALLH give mercy to his soul), my mother, my brothers (Arfat-Soliman-Ahmed), my sisters and my wife. Furthermore, I greatly appreciate the support which I received from my supervisors, Dr. Li Ran and Dr. Jim Bumby. Finally, I want to declare that this work was supported and funded by the Government of Egypt (Desert Research Centre (DRC) – Cairo).

List of publications

[1] Ahmed, L. Ran, and J. R. Bumby, "New Constant Electrical Power Soft-Stalling Control for Small-Scale VAWTs," *IEEE Transactions on Energy Conversion*, vol. 25, no. 4, pp. 1125-1161, 2010.

[2] A. Ahmed, L. Ran, and J. R. Bumby, "Stalling Region Instability Compensation for Constant Power Soft Stalling Control," 5th IET International Conference on Power Electronics, Machines and Drives (PEMD), Brighton, UK, 2010.

[3] A. Ahmed, L. Ran, and J. R. Bumby, "Sizing and Best Management of Stand Alone Hybrid PV-Wind System using logistical model," IFAC conference on control methodologies and technology for energy efficiency, Vilamoura, Portugal (CMTEE), 2010.

[4] A. Ahmed, L. Ran, and J. R. Bumby, "Sizing and Best Management of Stand Alone Hybrid PV-Wind System using logistical model," The First International Conference on Sustainable Power Generation and Supply (SUPERGEN), Nanjing, China, 2009.

[5] A. Ahmed, L. Ran, and J. R. Bumby, "Simulation and control of a hybrid PV-wind system," 4th IET International Conference on Power Electronics, Machines and Drives (PEMD), York, UK, 2008.

[6] A. Ahmed, L. Ran, and J. R. Bumby, "PV Generator Control in Multi Source Renewable Energy Systems," to be submitted soon for Journal publication.

CONTENTS

LIST OF FIGURES

LIST OF TABLES

NOMENCLATURE

e_w	Generator emf (V) (refers to dc side of generator rectifier)
v_w	Generator rectifier dc side voltage (V)
i_w	Generator rectifier dc side current (A)
K_w	Generator emf constant (V.s/rad)
C_p	Wind turbine power coefficient
R_w	Twice of PMSG per phase resistance (Ω)
ω_m	Rotor speed (rad/s)
J	Moment of inertia (kg.m^2)
ρ	Air density (kg/m^3)
λ	Tip speed ratio of wind turbine
v_s	Wind velocity (m/s)
R	Equivalent radius of turbine (m)
T_m	Turbine mechanical torque (N.m)
T_e	Generator electrical torque (N.m)
T_c	Time constant of soft stalling compensator (s)
v_L	Dc side voltage to grid inverter (V)
A	Swept area of wind turbine (m^2)
d	Duty ratio of dc link boost converter
a_1, a_2, a_3	Quadratic curve fitting coefficients of Cp-λ relationship
m_1, m_2, m^3	Quadratic curve fitting coefficients of the V_w-I_w lookup table where V_w and I_w are the mean values of the generator rectifier dc side voltage and current
K	The Boltzmann constant
T	The temperature in Kelvin
q	The charge of electron
R_s	The series resistance (Ω)
I_0	The diode reverse saturation current (A)
R_{sh}	The shunt resistance (Ω)
m	The ideality factor of the diode
μ_{Isc}	The short current temperature coefficient (A/K)
T_c	The cell temperature
ε	The semiconductor energy band gap in electron volt (eV)
μ_{Voc}	The temperature coefficient of the of the open circuit voltage (V/K)
δd_p	The duty ratio perturbation value for direct MPPT algorithm
δT_p	The time interval between every perturbation for the MPPT algorithm
R_{pv}	the instantaneous resistance (V_{pv}/I_{pv})
R_{pvss}	the incremental resistance (dV_{pv}/dI_{pv})
d_{inc}	The incremental conductance factor
P.c.c	Peak current control
p.u.	Per unit

CHAPTER (1)

INTRODUCTION

This chapter is an introduction to the research described in this thesis. It aims to provide an overview of small scale PV and wind generation systems in the market today and discuss the advantage of using hybrid PV-Wind generation systems. The proposed system and research objectives are presented, and the thesis structure is outlined at the end of the chapter.

1.1. SMALL SCALE HYBRID PV-WIND SYSTEMS

The consumption of energy continues to grow as both the world population and the living standard increase [1]. The demand increases even though energy efficiency has largely been improved; the biggest demand today and in the future is for electrical power generation [2]. This will increase fuel prices causing that the world is looking for alternative sources of energy [3, 4]. Wind and PV are the most promising renewable sources, in addition to hydroelectric power sources which have been traditionally exploited [5].

Small-scale systems represent one type of the key renewable energy applications. To the end-users of electricity, small-scale wind or PV units are becoming attractive due to soaring fuel prices and technological advancements which reduce their manufacturing cost. There is a scarcity of studies concerning hybrid PV-Wind systems, as most research considers each source individually. This study is concerned with a sub-set of small-scale systems – that of residential applications with a *1-10 kW* power range. These kinds of small-scale systems are mostly grid-connected. Below *1 kW*, systems are mainly standalone, while those with larger power outputs (from *11 kW* to *100 kW*) are primarily commercial [6].

The PV market for small-scale systems is very promising and is larger than the small-scale wind market. Units of less than *20 kW* account for more than *60%* of the total PV market. In this year (2010), residential applications of PV account for *17 GW* whilst the world's total PV capacity is *27 GW*. At the end of the next decade, the installed PV systems are estimated to reach *210 GW*, of which *181 GW* is generated by systems producing less than *20 kW* each [7].

For small-scale wind systems, the USA and the UK are the largest markets. An AWEA (American Wind Energy Association) report indicates that small-scale wind turbines contributed *100 MW* of power generation in the world in 2009. The year 2008 witnessed a *78%* growth over the previous year (2007), while the world-wide growth rate was comparable at *53%*. This growth was *15%* higher in 2009 and *40%* of the added capacity are in 2009 are residential wind turbines. The majority of those turbines are grid-connected. In the UK, *7.24 MW* worth of small-scale turbines were installed in 2008. This increased to *8.64 MW* in 2009, which brought the total installed capacity to *28.7 MW*. The installed capacity is expected to be more than *40 MW* in (2010) and more than *80 MW* in the following year. In 2005, only *8%* of such UK turbines were grid-connected. This increased to *56%* in 2008 due to the introduction of grid codes or guidelines to permit and regulate the connection. The majority of the installed units generate less than *10 kW*. Globally, *42 MW* were installed in 2009, an increase of *10%* compared to 2008 [8]. These market numbers show a rapid development in small-scale wind turbine installation.

Multi-source hybrid renewable energy sources to some extent overcome the intermittency, uncertainty, and low availability of single-source renewable energy systems, which has made the power supply more reliable. PV and wind power are complementary because sunny days generally have very low wind while cloudy days and nighttimes are more likely to have strong wind. Therefore, hybrid PV-Wind systems have higher availability and reliability than systems based on individual PV or wind sources [1, 9, 10]. Therefore, this study is orientated towards small-scale residential grid-connected PV-Wind systems.

Hybrid PV-Wind versus single source systems

A study has been carried out to compare the use of hybrid PV-Wind generation systems and single-sourced systems (see reference [11]). Sizing software of PV-Wind energy systems with battery storage is proposed, based on a logistical model. The software has been used to size different profiles for two different regions in Egypt. One region contains high solar energy but wind energy is low, and the other region contains both high solar and wind energy. It is concluded that hybrid PV-Wind systems are more economical and reduce the need for high battery storage capacities.

1.2. STUDY SYSTEM AND RESEARCH OBJECTIVES

Figure (1.1) shows the hybrid PV-Wind energy conversion system (with battery storage) proposed in this thesis as a small-scale grid-connected system. The main energy sources for the system are wind and PV generators, while the battery bank works as an energy storage backup source. The utility grid works as a secondary backup supply in this system. The system is intended to be for residential applications, which may be building demand or a water pumping system with domestic demand.

The research proposes a power conditioning unit (p.c.u.) which controls such a small-scale system. The small-scale system requires simple controllers and circuits that are easy to implement, and this is the core objective of this study. The present study always considers this to reduce the cost and size of the controllers and the system.

The system components could be connected in several ways, depending on the proposed power electronics topology. One option is to connect the sources with the load and the grid via an ac bus bar, using an inverter for every source. This will increase the redundancy of the system, as every source can work independently from the other sources. However, this will increase the overall system cost. Another option, which is proposed in this study, is to connect the sources to a dc bus bar. Subsequently, an inverter will be used to supply the load and connect to the grid. This method is less costly and easier to control for the standalone mode of operation [12]. The sub-system components, power electronics, and control units are outlined in the following sub-sections.

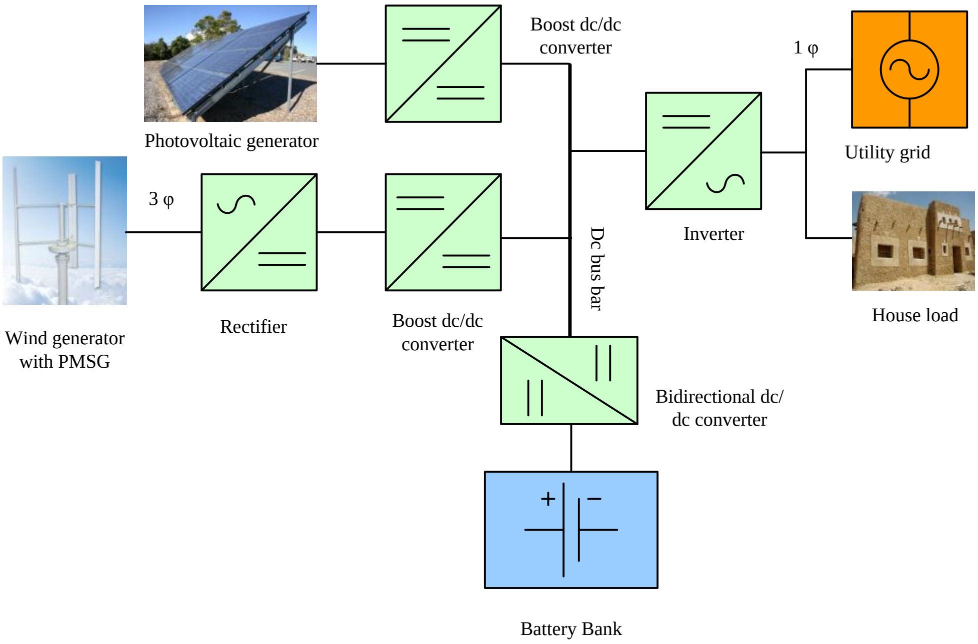

Figure (1.1) A schematic for the system

1.2.1. WIND GENERATOR SIDE

Vertical axis wind turbines (VAWTs) are attractive as applications in the built environment due to their ability to capture wind from different directions without using a yaw mechanism; this avoids the associated cost of the yaw system [13]. The electrical components that require maintenance are normally positioned on the supporting platform, and a VAWT is also regarded as being quiet. The VAWT is developing, and it has recently begun to take share in the market [8]. Permanent magnet synchronous generators (PMSG) are favoured to be coupled with VAWTs due to their light weight, high power density, and high efficiency. The PMSG is often directly coupled with the turbine, eliminating the need for a gearbox and its associated cost and maintenance issues, whilst increasing the system reliability [14, 15]. A boost-rectifier converter is the power electronics employed to control the wind generator side. This combination is likely to be used in residential applications as it offers lower cost and is simpler to implement and easier to control [16].

Problem definition and proposed solution on the wind generator side:

A problem which makes a VAWT less advantageous is that it is ***difficult to be controlled at high wind velocities***. A horizontal axis wind turbine (HAWT) is easier to be aerodynamically stalled, compared to a VAWT. At high wind velocity, the power, rotor speed, and voltage are increased above the rated values. This will cause damage to the mechanical and electrical system components. In this study, the problem of VAWTs' high wind velocity control will be investigated, and an ***electrical stalling control method*** will be proposed. This method will reduce the cost of the turbine, as complex and unreliable aerodynamic control will be eliminated. Maximum power point tracking will be retained at low and moderate wind velocities.

1.2.2. PV GENERATOR

The PV generator is controlled by a boost dc/dc converter to maximize the power output under normal operating conditions of the system (see Figure 1.1).

Problem definition and proposed solution on the PV generator side:

There are a large number of publications regarding the maximum power point tracking (MPPT) of the PV generator. However, ***a proper design for the MPPT controller parameters*** has rarely been discussed in the literature. In this study, the design of the MPPT parameters will be proposed, and according to that an ***efficient, fast, practical, and easy to implement MPPT controller*** will be developed to fit this task. There are other system conditions requiring the generated output power to be reduced. The PV generator is easier to control, to work in ***reduced power mode*** as compared to the wind generator. The conditions and methods to control the PV generator to perform in this mode with power curtailment will be investigated.

1.2.3. INVERTER SIDE

Power electronics have seen rapid developments in the last few years due to the development of faster and higher-rated semiconductor switches. Furthermore, fast progress in digital signal processing and microcontrollers helped with advanced controller implementation [14, 17]. ***Single phase dc/ac inverters*** are one of the main applications of power electronics technology and control. In this research, a single phase inverter is used to offer ***grid synchronization with standalone capability*****.** Dc/ac inverters can basically be divided into 2-level and multi-level inverters. The multi-level topology has many advantages, but it has a main disadvantage in that there may be voltage unbalance between the capacitors [14]. This topology becomes more and more economical as the rating of the system increases. As the work proposed in this research is concerned with a small-scale renewable energy system (less than *10 kW*), the basic 2-level inverter is taken into account. There are many topologies of single phase inverters. One of the topologies is a half bridge inverter which has the advantage of no dc current injection problem. It was used with many industrial inverters [18]. One of the main drawbacks of the half bridge inverter is the need for larger dc capacitors because the full current at fundamental frequency will pass through the capacitors. Another drawback is the need for doubling the dc voltage of full bridge inverters. Furthermore, it needs higher switching frequency and bigger output filters. This will increase the overall losses, cost, and size of the inverter. There are many modifications proposed on the half bridge inverter topology to reduce these disadvantages [14, 18]. Another approach is to use the H-bridge inverter but remove the dc component in the output current [19-22]. This study will focus on the primary form of the H-bridge inverter.

Problem definition and proposed solution on the inverter side:

The research in this part of the thesis will concentrate on the following points:

- Developing an efficient with low THD, fast tracking and stable ***current controller*** for single phase inverters is not an easy task. However, a few methods have been proposed in the literature (see Chapter 2). A new current controller will be developed in this study, which will satisfy the international standards on power quality.
- According to this current control method, a ***grid connection controller*** will be developed. This controller will inject active and reactive power with high power quality into the load and the grid.
- A ***standalone mode controller*** will also be taken into account, which will supply high quality power to the load.
- At the final part of the study, the ***dc current injection problem*** will be addressed. A dc injection detection circuit, based on resonant circuit theory, will be developed, and a controller will be designed to eliminate this dc component.

1.2.4. SUPERVISORY CONTROLLER

In the final part of the study, a supervisory controller proposed to will be proposed to supervise the local controllers and manage the power in the system. It will work based on the battery state of charge in conjunction with the conditions of the utility grid, PV generator, and wind generator.

1.3. THESIS OUTLINE

The thesis is outlined Figure 1.2. The next chapter (Chapter 2) provides a review of relevant research literature.

Chapter 3 is concerned with the ***wind generation aspect*** of the system. Modelling and analysis of the power circuit of the system will be proposed. Based on that, a control algorithm will be developed and implemented. The transient response and stability analysis of the control method will also be analyzed. At the end, dynamic simulation and experimental verification results will be presented.

Chapter 4 is concerned with the ***PV generation aspect*** of the system. Modelling and transient analysis of the PV generator and power circuit will be developed. According to this, a direct switching duty control using a variable step incremental conductance algorithm will be proposed with guidelines to optimize the controller parameters. These guidelines will improve the controller tracking efficiency and speed. The proposed controller may have to work in a reduced power mode according to the supervisory controller signal. The controller will also be verified by dynamic simulation and experimental results.

Chapter 5 addresses the ***inverter side*** of the system. It will start by developing a current controller based on the peak current control method which is usually used with dc choppers. The control will be based on a unipolar PWM method to provide ac current and voltage waveforms with improved quality. An instability slope compensation for the controller will be designed. To improve the quality further, an L-C-L output filter will be designed for the inverter, followed by application of selective harmonic elimination which allows the switching frequency to be reduced. Then, the inverter will be simulated and the resultant current and voltage waveforms will be analysed by FFT and evaluated interms of THD. In the section that follow, the control of active and reactive powers will be developed and verified by dynamic simulation. The standalone control will also be proposed using the same peak current control method, with simulation verification. At the end of the chapter, a new dc injection elimination strategy will be proposed, and verified by dynamical simulation and by laboratory experiment.

The ***supervisory controller*** will be developed in Chapter 6. A preview of the local controllers, load demand, and the overall system configuration will be provided. The supervisory controller will be discussed regarding the different modes of operation (including the operating states of each mode). In addition, the ways in which the system would transfer between the different modes will be discussed. This will be followed by the control algorithm development and discussion. Dynamical simulation results are presented.

The last chapter draws a conclusion on the work described in this thesis.

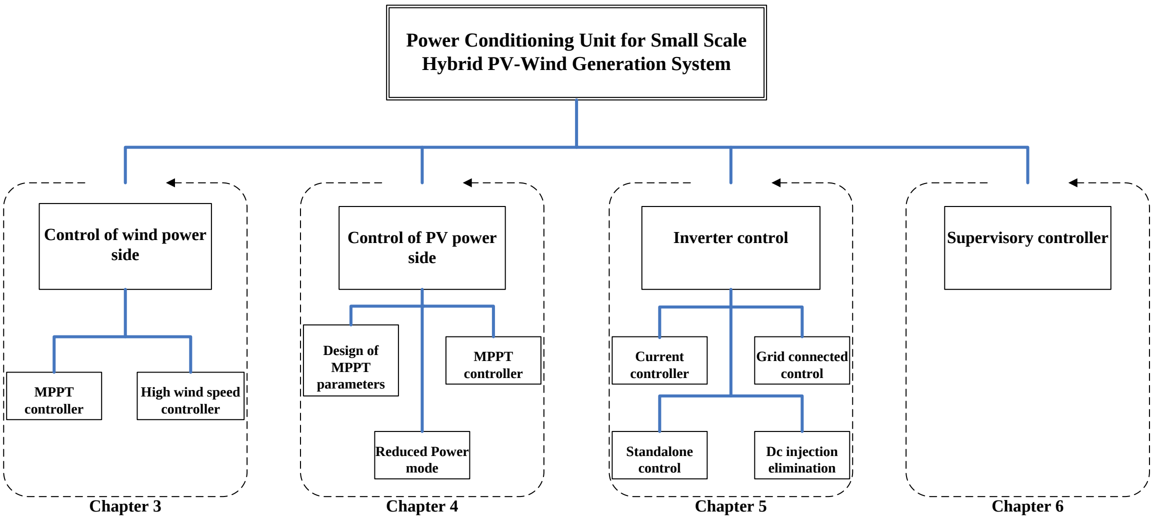

Figure 1.2 Diagram describes the proposed research in the thesis

CHAPTER (2)

REVIEW OF PREVIOUS WORK

This chapter provides an overview of the literature pertaining to the proposed research project. The review will discuss the research proposed according to the thesis outline (see Figure (1.2)). In the first section, the wind generation control methods will be reviewed, while the present study’s newly developed control method will be proposed in Chapter 3. The second section focuses on a review of the literature concerning the PV generator controller; the controller itself will be proposed in Chapter 4. This is followed by number of surveys discussing the single phase inverter control. The single phase inverter control itself will be developed in Chapter 5. The last section will provide a review of the literature concerning supervisory controllers for Hybrid PV-Wind generation systems.

2.1. WIND GENERATOR CONTROL

Power generation from wind energy can be divided into constant speed operation and variable speed operation. Variable speed generation can be applied by aerodynamic control, power electronics control, or a combination of the two. The combination control is advantageous as it can provide maximum power point tracking at operating wind velocities. Although all older versions of commercial wind turbines are operated at constant speed, the interest nowadays lies in variable speed turbines. The advantages of variable speed wind turbines are increased energy capture and improved power quality with attenuated grid impact from wind fluctuations. The focus of this study lies on implementing a control strategy based on power electronics [23, 24]. Reviews of controlling the wind generator in MPPT mode (Section 2.1.1) and high wind limiting mode (Section 2.1.2) are discussed in this section.

2.1.1. MPPT ALGORITHMS

A wind turbine has a maximum level of power which can be extracted from the wind, which is related to the Betz limit (*59%* efficiency). The power coefficient (C_p) is the percentage of power in the wind extracted by the wind turbine. The power coefficient value depends on the specific wind turbine shape, the wind velocity, the turbine rotor speed, and the turbine's blade pitch. The curve depicting this coefficient (C_p) with rotor speed has only one maximum point. Therefore, the main objective of the MPPT process is to adjust the wind turbine to work at the maximum point of that curve. The operating strategy of MPPT in wind power systems is to match the generator loading with the wind turbine characteristics. Consequently, the rotor operates continuously at speeds as close as possible to the maximum power points (MPPs) [23, 24].

The turbine power can be calculated from Equation (2.1) as a function of wind velocity and the efficiency coefficient (C_p) which is a function of the tip speed ratio (TSR) and pitch angle θ. TSR is calculated from Equation (2.2) [25]:

$$P_w = 0.5\rho A R v_s^3 C_p(\lambda, \theta) \tag{2.1}$$

$$\lambda = \frac{R\omega_m}{v_s} \tag{2.2}$$

Due to the nonlinear characteristics of the wind generator and the continuous rapid change in wind velocity (wind gusts), MPPT is a challenging issue for wind power generators. The MPPT for wind generator can be divided into aerodynamic control and power electronics control.

Aerodynamic control is either based on the pitch method or the stall method. The purpose of pitch or stall control methods is to track the MPPs of wind turbines with changing blades pitch angle or the attack angle of wind on the blades respectively [26-30]. However, as the size of the turbine increases, the aerodynamic control becomes more and more complex and costly. Other drawbacks are the increased cost and the maintenance cost of the turbine. Furthermore, this kind of control will reduce the reliability and life span of the unit.

The usage of power electronic converters allows for variable speed operation of the wind turbine and for enhanced maximum power extraction, supplying the load with improved quality of power. The work proposed is concerned with the power electronics control. There are many power electronic converter schemes used to control the wind generator’s power output [16, 31]. The applied power electronic scheme depends on the electrical generator type, the load supplied by the wind generator, and the control topologies used in the system.

Sensor control

Sensor control is to use, as control parameters for the control circuits, a wind velocity sensor or rotor speed sensor to measure wind velocity or rotational speed respectively. The simplest method is to measure the wind velocity, and then the power against wind velocity is fitted to the curve. The result of the curve fitting is used to adjust the operating points of the system [32-35]. The wind speed is measured and the reference MPP is determined accordingly. Then, the controller adjusts the system to this operating point. Wind velocity is not a satisfactory control parameter because of the following:

1. The erratic nature of wind velocity.
2. The difficulty of measuring wind velocity close to the turbine.
3. The time delay associated with the measurement of wind velocity.

One of the methods to avoid the delay of measurement results is to use neural networks to predict the wind velocity. After that, the MPP can be established from the relation between wind velocity and output power. This method is closely connected to the reduction of power fluctuation produced by pitch control [36]. The drawback of this method is the need to track wind velocity via a database for a long time before the implementation of the system. Another disadvantage is the high prediction accuracy that is required. Furthermore, the wind speed sensor is still needed. This method is not applicable to small scale generators as the site of installation is not known when the turbines are mass produced; on-site tuning of the neural network is not justifiable economically for small scale turbines.

Using a rotational speed sensor (shaft encoder) is another method proposed in the past. This method ensures maximum wind power capture by controlling the rotor speed to send the wind turbine to the maximum power point. The rotor speed is controlled by means of the electrical power from the generator which is driven by the wind turbine, and this is achieved through the power electronics interface. As an example, for a PMSG (permanent magnet synchronous generator), the generator torque is proportional to the machine’s current (Equation 2.3, assuming unity power factor) which can be set, while the rotational shaft speed of the generator determines the target torque (Equation (2.4)). Consequently, if the wind generator’s output current is controlled to change the torque, the rotor speed will be changed to maximize the power output of the wind turbine.

$$T_g = KI_g \tag{2.3}$$

$$T_g = K_\omega \omega_r^2 \tag{2.4}$$

where T_g is the generator torque, I_g is the generator’s output current, and K, K_w are proportional constants which depend on generator and turbine designs respectively [37-41].

A fuzzy controller could be used to achieve MPPT. It was used to control the modulation index or the PWM inverter. The fuzzy controller uses two signals, i.e. the difference between the rotor speed signal and the delayed speed signal, and the output power or the difference between the measured power and the delayed value. This method is considered as a searching algorithm for the maximum power point [42-44].

Other artificial intelligence techniques could be used to approximate the nonlinear characteristics of the wind turbine generator system. Achieving maximum power tracking by using a neural network controller for a wind energy conversion system could be very promising. This is due to the high ability of neural networks to achieve an approximation of the nonlinear function. The training process for the neural networks is normally accomplished offline, using data which are produced by accurate simulation or site tests. A proposed method is to teach neural networks to estimate the wind velocity according to the measured output power, rotational speed and pitch angle. Then the estimated wind speed is used to find the optimum rotational speed [45-47].

Sensorless Control

In this category, MPPT is achieved without either wind velocity sensors or rotor speed sensors. Depending on such sensors increases the cost of the controller and reduces the robustness of the overall system. Consequently, the objective of the method is to perform MPPT by measuring other parameters such as output voltages and currents. There are several sensorless control algorithms that have been used in practice.

Voltage and current curve fitting are normally used with wind turbines driving PMSGs. This is due to the direct proportionality of the rotational speed and the rectified value of dc output voltage. Therefore, the dc output voltage is used as the control variable to maximize the output power [48-50]. A curve fitting of the maximum power or the dc current at maximum power versus the dc voltage is used to determine the operating points of the wind turbine generator.

The Frequency – Voltage method is a sensorless method which normally controls the direct connection between wind turbine and PMSG without a gearbox. It is based on assuming that the maximum power coefficient value is constant for a specific turbine. Then, a curve fitting could be performed for the relationship between the PMSG ac output frequency and the rectifier output dc voltage, at optimum power values [51, 52].

An estimation of the rotor speed or position method is developed by measuring the generator ac output currents and voltages, and then estimating the generator rotor speed or position accordingly. One advantage of this method is to improve the efficiency of the generator [53-57].

The hill climbing method is an algorithm, performed by climbing the power curve to determine or stay near the maximum power point. The advantage is to achieve MPPT without having knowledge of the turbine characteristics. The generator output power is calculated by measuring the dc link current and voltage. Then the operating point is perturbed by increasing/decreasing the magnitude of the reference current. The new value of output power is then compared with the previous value and depending on the difference the magnitude of the reference current is further increased or decreased [58-65]. A fuzzy logic controller can also be used to provide hill climbing [66]. The main drawback of this method is that the method will fail to track the MPPs accurately during times when the wind velocity changes very quickly.

2.1.2. HIGH WIND VELOCITY CONTROL

Control at high wind velocities can also be divided into aerodynamic and power electronics-based or simply electrically-based methods.

A. AERODYNAMIC HIGH WIND VELOCITY CONTROL

In a large horizontal axis wind turbine (HAWT), electrical control is usually used for maximum power point tracking (MPPT) and aerodynamic control is used at high wind velocities to limit the turbine power and rotational speed.

Pitching the turbine blades changes the power coefficient (C_p) and constrains the generator current, voltage, and speed [31, 67-69]. Pitch control increases the system cost and is justifiable for large turbines. A solution for smaller wind turbines is to embed in the blade design a passive stall mechanism which is activated by high wind velocities. This can reduce the efficiency, increase the turbine’s fatigue loading, and reduce the power quality performance; more importantly, it will add great complexity to a vertical axis wind turbine [70].

B. ELECTRICALLY BASED HIGH WIND VELOCITY CONTROL

Constant speed soft stalling has been proposed for vertical axis turbines to regulate the rotor speed or the output dc side voltage of the generator rectifier [33, 48, 71-74]. This control stalls the turbine and reduces the power captured. Figure (2.1) plots the output power against the rotor speed in such a scheme; MPPT is normally applied at low wind velocities, while at high wind velocities the rotor speed is kept constant. A problem with this is that the power output is still greater than the rated power, although it is lower than it would have been if MPPT control had continued to be used at the increased wind velocity. The generator and power electronics must be rated accordingly.

Another scheme for electrical control is to connect a mechanically-switched 3-phase resistor bank to the generator terminal [49, 75]. This induces cost and can reduce generator lifetime as uncontrolled current pulses are drawn.

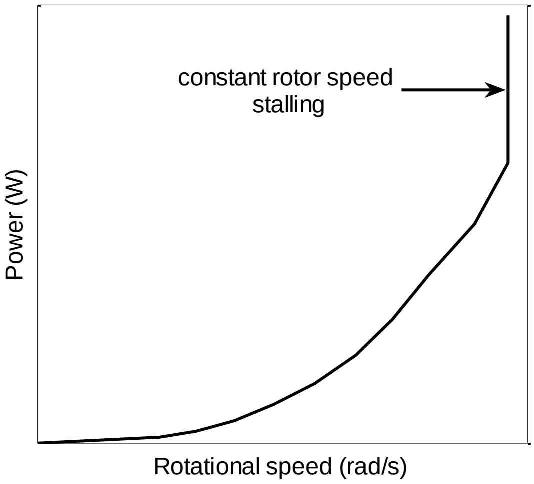

Figure (2.1) Power-rotor speed curve in constant speed soft stalling

2.1.3. SUMMARY AND GUIDELINES

From the discussion of the different MPPT methods and algorithms (summarized in Figure (2.2)), the following points can be taken into account when applying MPPT to a small-scale wind generator:

1. Avoiding the use of rotational speed or wind velocity sensors that make the controller costly and reduce the overall system’s robustness.
2. Avoiding the use of aerodynamic control, which increases the complexity, capital cost, and maintenance cost of the wind turbine generator.
3. Avoiding the use of complex control methods such as artificial intelligence-based methods which require on-site tuning.
4. It is better and more reliable to use voltage and current-based methods, as the controller would also be more compact. This method is usually referred to as sensorless control.
5. Avoiding searching methods during periods of rapid change in wind velocity as this would result in hunting.
6. The proposed controller should be easy to implement in the microcontroller.

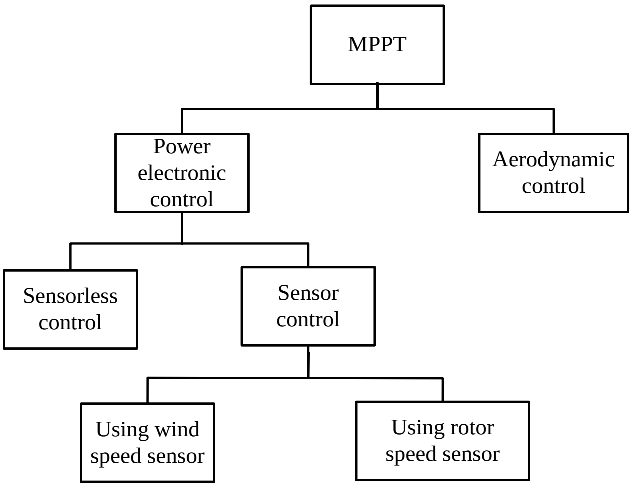

Figure (2.2) Categorization of wind turbine generator MPPT control algorithms

It is found that the dc current-dc voltage control scheme is the simplest and most efficient method. This method is also easy to implement and very suitable to the proposed power electronics configuration [13]. Therefore it is very suitable to small-scale wind turbine generators which are the topic of our study.

2.2. PV CONTROL REVIEW

In applications where photovoltaic arrays are used to provide energy, maximum power point trackers are used to match the variations in the current-voltage (I-V) characteristics of the solar cells. In the typical silicon cell I-V curve, as the output voltage of the PV rises, the PV will produce significantly less current. The current-voltage curve will change depending upon temperature, solar radiation, load, and consistency of cell quality in the PV array [76]. For the array to be able to produce the maximum possible amount of power, either the operating voltage or current needs to be carefully controlled. Hence, a device is needed which finds the MPP and converts the PV panel voltage to the system voltage. Such devices are known as maximum power point trackers or trackers [77, 78]. In general, there are two forms of MPPT: one is matching dc-load characteristics to the MPPs of the PV source, and the other is using a matching circuit [77-79].

In the first form, the PV source is connected directly to the load without the need of matching circuit. The load characteristics are designed to operate at or close to the PV generator's MPPs. This method is mainly used with dc motor loads, where the dc motor field winding control is designed in such a way that the dc motor characteristics match the PV source's MPPs as much as possible [79-82]. One of the drawbacks of this method is the nonlinearity of the PV system; it is very difficult to make a perfect matching without considering the system's temperature, which has a very significant effect on the PV characteristics. Another drawback is that the tracking efficiency is reduced when compared with using matching circuits. Also, the method is only applicable to special loads such as dc motors and batteries.

Many algorithms use a matching circuit for MPPT. These algorithms can be classified as either direct or indirect methods, depending on the control method employed [83]. Direct methods include algorithms that use measuring currents, voltages, power, temperature or solar radiation of the solar array. Indirect methods are those which use an outside signal to estimate the MPP. Such outside signals may be given by measuring the short circuit current or the open circuit voltage of a reference solar cell (monitoring cell). A set of physical parameters has to be given, and the maximum power set point is derived from the monitoring signals. In the following sections, the direct and indirect methods will be proposed.

2.2.1. DIRECT MPPT METHODS

The direct methods mentioned above are simpler and have a lower cost than the indirect methods. This is because we will not need to use separate devices as the monitoring cell. The various direct algorithms will be divided according to the control variables chosen to achieve the maximum power point tracking control.

A. DATABASE METHOD

In the lookup table method, MPPT is performed by registering the MPPs in an extensive database of MPP voltages at all light radiation levels. This control algorithm has several disadvantages but mainly it is only valid with regard to particular PV panels and the database must be changed as the PV panel degrades. A large memory lookup table size is needed for a wide range of solar radiation and temperature levels [84].

B. OPEN CIRCUIT VOLTAGE CONTROL

The solar array terminal voltage is used as the control variable for the system. The reference control voltage signal is set with respect to the array open circuit voltage to determine the maximum power points. The basic function is used to assign the reference control voltage shown in Equation (2.5) [85]. This method assumes that the proportionality of voltage-factor (K_v) is fixed for a given PV generator regardless of temperature, solar radiation, and panel configuration but depends on cell material and make [86, 87]. This property is used to achieve temperature and solar radiation-independent MPPT for PV generators with a simple technique. The open circuit voltage is continuously measured by a microcontroller and is used to estimate the operating maximum power point of the system. Moreover, this method can be implemented using an analogue circuit [85].

$$V_{mpp} = K_v V_{oc} \tag{2.5}$$

where K_V is the voltage proportional constant, V_{mpp} the MPP voltage and V_{oc} the open circuit voltage. Obviously, the drawbacks of the voltage control method are

1. The wasted available energy when the load is disconnected from the PV array to measure the open circuit voltage.
2. It is proposed that the proportional constant of the open circuit voltage (K_v) is constant with solar radiation and temperature. However, in the reality, the K_v values vary in the range from *73* to *80%* according to solar radiation and temperature.
3. The degradation in PV array characteristics also affects (K_v) value.

C. SHORT-CIRCUIT CURRENT CONTROL

The short-circuit current is used as the reference parameter in this method. The reference current is adjusted according to the short-circuit current. This method is based on the fact that the MPP current is a constant percentage of the short-circuit current. To implement this algorithm, a switch is placed across the input terminals of the converter and switched on momentarily. The short-circuit current is measured and the MPP current calculated from the Equation (2.6):

$$I_{mpp} = K_i I_{sc} \tag{2.6}$$

where, K_i is the current proportional constant, the PV array output current is then adjusted by the MPPT until the calculated MPP current is reached [88]. In a more complicated method, a PV scanning is performed every few minutes in order to calculate K_i . This scan is performed to overcome the online change of K_i with solar radiation and temperature, and the PV array degradation effect. After K_i is obtained, the system remains with the approximation until the next calculation of K_i is carried out [89].

The drawbacks of the current control method are

1. The available energy is wasted when short-circuiting the PV source.
2. The added complexity in the power electronics to short-circuit the PV source.
3. With the complexity of this method, the method is not acceptable for large power applications.

D. POWER CONTROL

The system power is used as the control variable, where the power is measured and adjusted according to the change in the atmospheric conditions. Most of the Power control algorithms use the hill-climbing method; this method is to climb the power curve to reach the MPPs. In the following sections several MPPT search algorithms will be discussed, which make use of different characteristics of solar panels and the location of the MPPs.

Perturb and observe method (P&O) is the most commonly used MPPT algorithm, due to its ease of implementation in its basic form [90-94]. Knowledge of the PV generator characteristics is not required. This method has many modifications: one of them is to directly use the dc/dc converter duty cycle (D) as a control parameter and force the derivative dP/dD to be zero, where (P) is the PV array output power [95]. Another modification is to perturb the current instead of the voltage [96]. However, this method also has some drawbacks such as the continuous oscillations around the MPP. Also, as the amount of sunlight decreases, the P–V curve flattens out which makes it difficult for the MPPT to track the location of the MPP, and it fails under rapidly changing atmospheric conditions.

The incremental conductance (I.C.) is another searching method which tracks the MPP accurately by comparing the I.C. and instantaneous conductance of a PV array [12, 97-100]. This method is based on the principle that at the MPPs:

$$\frac{dP}{dV} = 0 \tag{2.7}$$

Because P=VI, the following equation can be derived:

$$\frac{dV}{dI} = -\frac{V}{I} \tag{2.8}$$

This is the basic rule for the I.C. method where P, V, I are the PV array output power, voltage and current, respectively. The direction, in which a perturbation must occur to move the operating point toward the MPPs, is determined as follows:

$$if\ \frac{dV}{dI} > -\frac{V}{I}\ then\ \frac{dP}{dV} < 0, and\ if\ \frac{dV}{dI} < -\frac{V}{I}\ then\ \frac{dP}{dV} > 0. \tag{2.9}$$

There are many variations of this method. One of them is to reduce calculations and make the algorithm more applicable to the microprocessor [100]. Another modification is to propose another algorithm which depends on the relationship between the load line and the tangent line angles of the I-V characteristic curve [101].

The incremental conductance method is faster than the P&O method and it operates successfully even in cases of rapidly changing atmospheric conditions where the P&O method fails. This is because it actually calculates the direction in which to perturb the array’s operating point to reach the MPP, and it can determine when it has actually reached the MPP. Thus, under rapidly changing conditions, it does not track in the wrong direction, as the P&O method does. Nor does it oscillate around the MPP once it reaches it.

There are other power control algorithms which use hill-climbing, but these are different from the P&O and the I.C.. One proposed algorithm is applying a hybrid MPPT algorithm of the I.C. and P&O methods [99]. Another method is to use neural networks to compute the maximum power point [102-104]. Using fuzzy logic controllers has the advantage of working with imprecise inputs, not needing an accurate mathematical model, and being capable of handling nonlinearity [105-108]. An algorithm in reference [109] is based on the analysis of the current and voltage low-frequency oscillations.

2.2.2. INDIRECT METHOD

The indirect MPPT method proposes that the constant voltage or current method is to be used, but the open-circuit voltage or short-circuit current measurements are made on a small solar cell called a pilot cell. This cell has the same characteristics as the cells in the larger solar array and is subject to the same atmospheric condition. The pilot cell measurements can be used by the MPPT to operate the main solar array at its MPP, eliminating the loss of PV power during the V_{OC} or I_{SC} measurement. Reference [110] introduced this algorithm. The disadvantages of this method are as follows: there will be unavoidable errors due to the mismatch between the characteristics of the pilot cell and the PV array; the shadow effect is unavoidable; each pilot cell-solar array pair must be calibrated, increasing the effort required to build the system.

2.2.3 SUMMARY AND GUIDELINES

From the study of the different MPPT algorithms (summarized in Figure (2.3)), a new MPPT control algorithm will be proposed. It will take into account the drawbacks of existing algorithms and will have the following advantages:

1. The method is easy to implement in microcontrollers.
2. No extra power electronics are added to the system, which decreases circuit complexity.
3. There is no energy waste as the load disconnection case from the PV array with open circuit voltage control or short circuit current control.
4. The controller is generic and can be used with many PV generators without any changes required to adapt to different PV sizes.
5. Avoiding the usage of costly and bulky solar radiation and temperature sensors.

6. Avoiding the usage of a pilot cell which needs to be calibrated against the main PV array.

The proposed algorithm is one in the I.C. category but with a variable step size. Further more the proposed algorithm is based on direct duty cycle control without the need of PI or other kind of regulators as proposed before [95]. This algorithm can be easily implemented in a microcontroller, and it will reduce the overall cost of the controller.

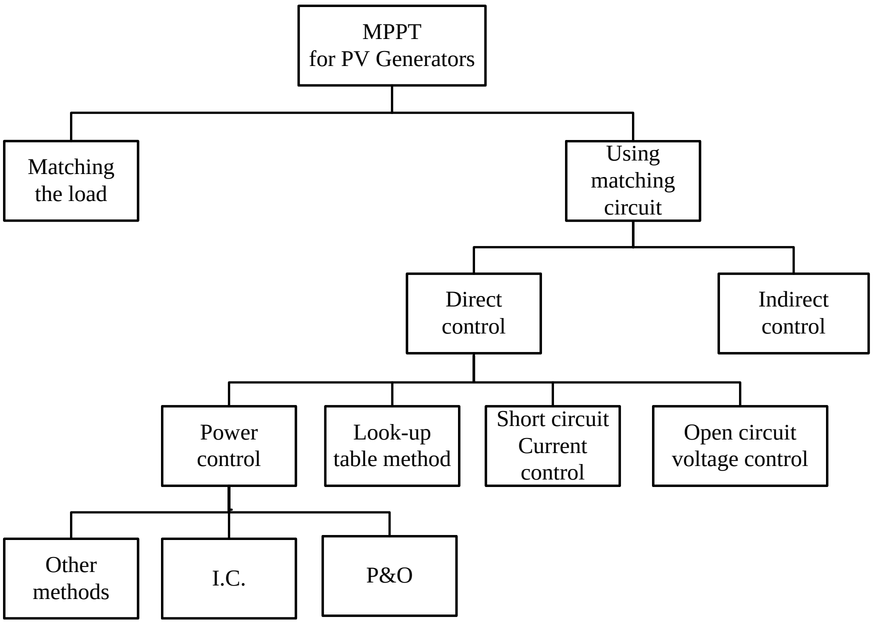

Figure (2.3) A chart shows the different PV MPPT algorithms

2.3. INVERTER SIDE CONTROL

The study will focus on control of a H-bridge single phase inverter. Furthermore, we will investigate four different subjects in the single phase inverter. The first is the current control in single phase inverters, which will be reviewed in Section 2.3.1. This will be followed by surveys for grid connected controllers (Section 2.3.2.) and standalone controllers (Section 2.3.3). In Section 2.3.4., a literature review will be proposed for dc current injection elimination methods.

2.3.1. CURRENT CONTROL METHODS

Generally, one of the main functions of the current controller is that the output current should track the applied reference signal with as little error as possible. Furthermore, the output signal should have acceptable transients without undesirable over- and undershoots or low dynamic speed response. On the other hand, the total harmonic distortions should be as low as possible and below the standard threshold values. These objectives of the current control should be delivered with competitive cost and size of the converter. With respect to dc/ac converters, the problem is not as direct as in dc/dc converters. This is because the tracking of a sine wave signal is not as easy or direct as the tracking of a dc signal. The current control methods of single phase inverters will be reviewed in the following subsections.

A. LINEAR REGULATOR BASED METHOD

In this method, the output current is controlled by linear regulators associated with a carrier-based PWM, and it is also called carrier-based method in many studies. There are many PWM switching strategies proposed to reduce the THD of the output current. Among these, the sinusoidal PWM methods (unipolar and bipolar) are commonly used with the H-bridge [111, 112]. Other methods such as centroid based switching [113], hybrid PWM [114] and random hybrid PWM [115] have also been proposed to improve the quality of the current wave.

One advantage of the carrier-based control method associated with linear regulators is the constant switching frequency operation. A simplified diagram describing this method is shown in Figure (2.4).

Applying PI controller is very common with small-scale inverters [115], but this kind of controller has relatively poor performance. One reason is the common steady state error produced by the inability to track the sinusoidal reference. Furthermore, this controller is unable to reject the noise in the current signal [116].

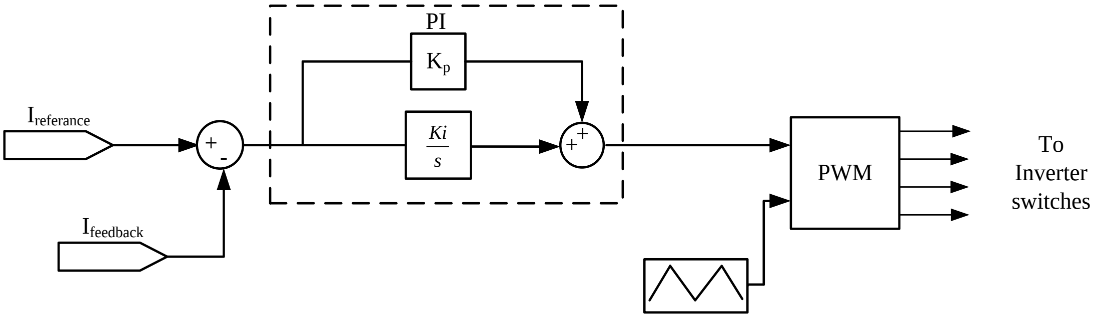

Figure (2.4) Carrier-based method with PI regulator

Another carrier-based method, described in references [116] and [117], proposes that the current control transfer function is a P or PI controller with a sine transfer function (PIS compensator). The resonant frequency of this transfer function is equivalent to the utility frequency. As a result, the gain of the proposed current controller is infinite at the line fundamental frequency. This controller is shown in Figure (2.5).

One of the drawbacks is that the compensator is very sensitive to variation in the mains frequency and that it has a low response speed. Furthermore, a large phase margin around the mains frequency was found, which may cause stability problem in the system.

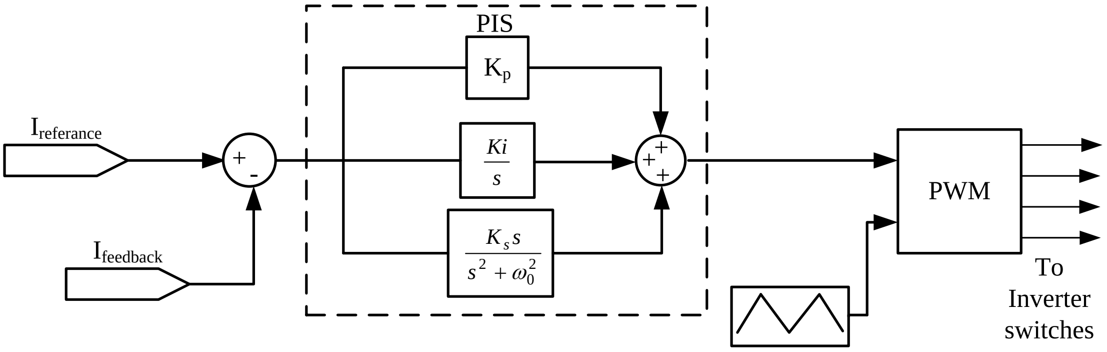

Figure (2.5) Carrier-based control with PIS regulator

The general drawback of the carrier-based method is the delay in the linear regulators, which causes low response compared to other direct current control methods such as hysteresis-based controllers.

B. HYSTERESIS CONTROL METHOD

This method is considered as direct control since the current is controlled in a hysterias loop. The hysteresis current control method is simple, robust, fast-responding, and easy to implement (see Figure (2.6) for a simplified block diagram). It also guarantees a peak current limiting capability. The method is based on the switch status, i.e. whether it is on or off when the current error touches its low or high boundary respectively. To reduce the THD in the output current, the hysteresis band has to be reduced, but this would increase the switching losses. Otherwise, a wider hysteresis band would increase the THD. Therefore, the hysteresis band is chosen to compromise between the low THD and the low losses. The simple hysteresis controller has a variable switching frequency and therefore a relatively high THD. The frequency band width in the current waveform depends on the system parameters, the switching mode, the load and the dc voltage. More advanced types of the controller were developed to limit the bandwidth of the switching frequency.

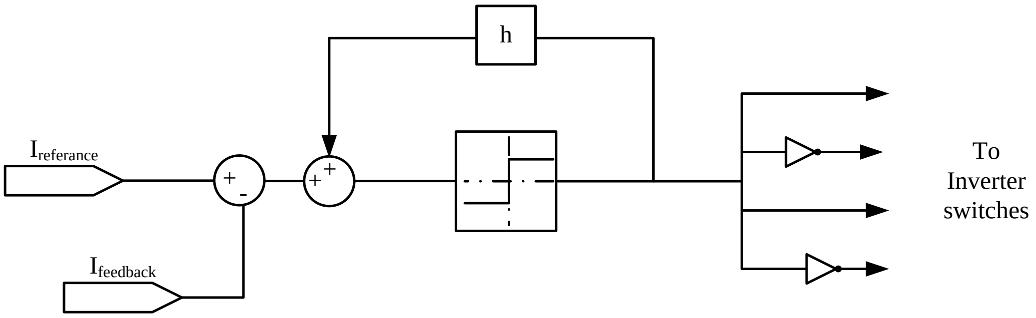

Figure (2.6) Hysteresis-based current controller

The hysteresis band was modulated online according to the system parameters to keep the switching frequency almost constant in [118] and [119]. It was calculated as a function of dc link voltage, the slope of the reference current, the system circuit parameters, and the load. It is clear that a number of signals need to be measured online which would increase the number of sensors with wide bandwidth.

An adaptive hysteresis band was proposed for current error comparison in [120]. A proper time was chosen to add the zero dc voltage mode control according to an adaptive inner band. The inner adaptive band is designed off-line according to the system voltages, currents and filter inductances. Fewer sensors and less online calculation are needed, compared to the on-line adaptive hysteresis method. However, the switching frequency change will be higher.

A three-level hysteresis current control strategy for a single phase voltage source inverter has been proposed in [121]. To achieve this, two hysteresis comparators with a small offset are used.

The random hysteresis method is one of the most common methods in this field [122]. The method is based on a random number provided to define the upper and the lower bands of the hysteresis controller. The random signal is distributed to provide an output current with narrow distributed frequency spectrum contents. Furthermore, the average frequency can be kept at a low value to reduce the switching losses. Describing in detail the different algorithms of the random hysteresis method is out of the scope of this review.

The methods proposed to solve the variable frequency problem of the hysteresis method could not make the frequency entirely constant. Furthermore, the tolerance and the variations in the system parameters may disturb the controller. Mainly, these methods need powerful DSP to perform the calculation.

C. PREDICTIVE CONTROL

The controller predicts the output of the inverter based on the system model. Subsequently, a suitable sequence of control signals is then applied to grant an acceptable tracking error. A cost function is minimized to design the predicted control sequence for the following sampling interval [123-125]. This method was also applied to parallel connected inverters in this reference [126]. The predictive control method is entirely based on an effective system model, and a fast high-performance DSP is essential to perform the calculations every sampling period [127].

2.3.2. GRID-CONNECTED CONTROL

There are many methods to determine the injected active and reactive power to the grid, depending on the converter topologies, the PWM methods, and the control techniques. These methods might also be used with active power filters which compensate for reactive power and distorted currents.

In single-source systems, the inverter could directly maximize the power from the source and provide power factor control [94,128 and 129]. The inverter works in this case as a current controller and the dc input voltage would be variable to provide MPPT. This method is not suitable for multi-source inverters such as those proposed in this study where the dc link is shared.

Another method controls the power output of the inverter by controlling the phase shift between the inverter output (V_{inv}) and the grid (V_g) voltages (the power angle). The reactive power is controlled in this method using the modulation index. This method uses a lookup table to find the required phase shift according to the active and reactive power demands [130]. The reactive power is very sensitive to the power angle and accurate design of the controllers is needed. Furthermore, using lookup tables is not favourable because it causes the controller to be largely affected by the system parameters as the line inductances.

The p-q method is originally used with three phase systems and was extended to a single phase case [131-133]. The method is based on separation of instantaneous active and reactive power in two coordinates, and then the reference current is calculated [14]. The method was also used with a single-phase inverter supplied by a PV generator [135]. This method is normally used with PI regulators, which are slow in response compared to direct regulators.

2.3.3. STANDALONE MODE CONTROL

In the inverter’s standalone mode of operation, the objective is to maintain the ac output voltage waveform in specified reference over all loading conditions. An easy method normally used in early uninterruptible power system (UPS) inverters is based on forward open loop control. The grid voltage magnitude was controlled using an r.m.s. feedback loop to control the magnitude. This method has a slow response and no-disturbance reduction to the ac wave [136].

The hysteresis control mentioned before in Section (2.3.1) was used in UPS applications which have the disadvantages discussed in the same section [137, 138]. Another proposed method is based on estimating the output filter values [139]. The tolerance, which reaches *20%* in practical inductors and capacitors, will affect the controller operation for this method. Analogue methods were proposed based on capacitor current feedback control [140] or inductor current feedback control [141] as normally the LC-filter is used in UPS applications.

2.3.4. DC -ELIMINATION METHOD REVIEW

The inclusion of a low frequency (50 or 60 Hz) isolation transformer at the output of the inverter eliminates the injection of dc on the grid side. Drawbacks of using this type of transformer are the cost, weight, and size added to the inverter system, as well as the reduced overall efficiency. A low frequency transformer is more bulky than a high frequency isolation transformer which however cannot prevent dc injection into the grid [22, 142].

For a transformerless topology, the research to overcome the dc injection problem could be basically classified into three categories as follow:

B. USING ALTERNATIVE INVERTER TOPOLOGIES

A half bridge inverter has been proposed to remove the dc injection to the grid, but there are many problems, such as using double dc link voltage, increased losses, and the large size of the dc link capacitors. This also increases the overall cost and size of the inverter. Using such a kind of inverter will also increase the ripple and reduce the total harmonic distortion [14, 18].

Using neutral point diode clamped multilevel is proposed in reference [143]; this has better efficiency compared to the basic half bridge inverter. However, it still needs twice of the dc voltage value of the H-bridge, and larger capacitors.

C. MODIFYING THE H-BRIDGE TOPOLOGY

The basic idea is to modify the H-bridge inverter to eliminate the dc component of the current. One of the topologies is to add switches on the dc side to clamp the voltage during the zero voltage periods [103]. This idea could also be applied by clamping on the ac side [20]. Both methods could not guarantee elimination of the dc component as the unbalance due to forward IGBTs voltages and PWM control would not be removed.

D. DC ELIMINATION BY CONTROL

A solution to the dc injection problem is to use a feedback control loop to eliminate the dc offset in the inverter output voltage, and such an approach is adopted in this study. Although this was also adopted in previous studies [22, 144-146], a challenge remaining to be addressed further is the accurate measurement of the usually very small dc component mixed with a large fundamental ac current component.

Reference [22] proposes a method of auto-calibrating the current sensing device to remove its error. The dc component on the ac output side of the inverter is deduced from the reading of the calibrated current sensor on the dc side, assuming the knowledge of the inverter switching pattern. This method can reduce the dc injection but will not eliminate it because it only intends to compensate the dc injection due to inaccuracy in the PWM process, while the dc component caused by unequal on-state voltage of the semiconductor devices in the inverter cannot be compensated. Furthermore, the method is subject to the influence of noises and achieves its objective at the cost of increased inductance between the dc link capacitor bank and the inverter bridge which should ideally be kept as low as possible to constrain switching transient and avoid EMC problems.

2.4. SUPERVISORY CONTROL METHODS REVIEW

Hybrid renewable energy systems can be classified into two main types: grid-connected and standalone. The renewable energy sources can be PV or wind generators (or both), according to the availability of solar radiation or wind velocity (or both) at the system site. Batteries are often used as a backup source to supply the system when the renewable energy source is unavailable. Other backup sources can be used with or without batteries such as fuel cells (e.g. electrolysers, supercapacitors and flywheel energy storage). Diesel generators could be used as secondary sources of renewable energy. The standalone system might provide dc power, ac power, or both dc and ac power [147-149].

The grid-connected systems can work on standalone mode when the utility grid is unavailable. In grid-connected systems, the utility grid is a secondary source. For the most part, fuel cells and diesel generators are not used with such grid-connected systems. The supervisory controllers manage the power according to the type and different components of the system. In this section, a survey of the supervisory controllers adapted to the different renewable energy systems will be discussed. The supervisory controllers could be divided generally to two kinds; conventional-based and artificial intelligence-based methods.

2.4.1. CONVENTIONALLY-BASED METHODS

A small-scale hybrid PV-Wind generation system with batteries works only in standalone mode as proposed in [63]. The power conditioning unit is limited to maximize the output power from both the wind and the PV generators to the batteries. The charging and discharging methods of batteries, over power ratings and load management, are not taken into account in this system.

A design of a supervisory controller based on a sliding mode control is presented in reference [150]. The system is a standalone hybrid PV-Wind generation system. For the design of such a supervisory controller, the wind generator plays the role of the main generator while the solar generator is a secondary power source. The system has three modes of operation: in the first mode, the wind generator is regulated to supply the system while the PV generator is OFF. In the second mode, the wind power is maximized and the PV power is regulated. Both PV and wind are maximized in the last mode. In the proposed control strategy, the battery state of charge is not taken into account. Furthermore, the wind power regulation strategy is not explained.

A wind generation system with storage batteries is controlled to work in both grid and standalone operation modes discussed in this chapter [147]. The supervisory controller in this system is designed to provide smooth transitions between the modes. Furthermore, it controls the inverter, providing fault ride through to limit the output current during utility grid side faults. This fault ride through strategy is explained in reference [151].

The supervisory controller of a standalone hybrid Wind-PV-fuel cell (FC) energy system is proposed in [152-154]. Every source is connected to the ac bus bar via an inverter to supply the load. The FC–electrolyzer combination is used as a backup and long-term storage system. The battery bank is used in the system as a short-time backup to supply the transient power. At any given time, the supervisory controller controls any excess wind-PV-generated power to be supplied to the electrolyser. The hydrogen, which is delivered to the hydrogen storage tanks by a gas compressor, is consequently generated. If the generated power is less than the load demand, the FC stack begins to produce energy for the load using hydrogen from the storage tanks. A steady state model was used in the papers with no dynamical results.

This study demonstrates that the low voltage distribution network is supervised to optimize energy flow and control power quality [155]. This kind of system is supplied by renewable energy sources, diesel generators, and energy storage backups. The system is controlled, according to international power quality standards. The algorithm is universal and adapts its control variables. This controller is concerned with the utility grid not with controlling the local generators.

A power mangement program is proposed in refrence [156] for a grid-connected wind-generated system with energy storage. The energy storage is controlled to smooth the power output of the energy generation system to the grid. The average wind velocity is forecast for the next hour and then the energy storage output is mananged according to the forecast value.

A new scheme of a standalone hybrid PV-Wind system with batteries is proposed in [157]. The PV is directly connected in parallel with the batteries to supply the ac load through a three phase inverter which is connected from the other side to a wind generator. The power management strategy is simplified in this configuration as the batteries act as a constant voltage load line which charges both ways by the PV and the wind generators. A dump load can be switched on with batteries fully charged but the batteries are later disconnected to prevent overcharging. One of the drawbacks is that there is no ability in this scheme to provide PV or wind generators control. Furthermore, the batteries’ charging and discharging is not fully controlled.

2.4.2. ARTIFICIAL INTELLIGENCE-BASED METHODS

A standalone system with hybrid PV-diesel power generators and flywheel backup energy storage system is proposed in [158]. A pump is used as an auxilary load to absorb the extra power from the system. A fuzzy logic supervisory controller is proposed to manange the power from the generators to the load. According to the generated PV power and the rotor speed of the flywheel, the fuzzy controller adjusts the refrences for the diesel generator output power and the pump demand.

A fuzzy logic supervisor is proposed also in reference [159] for a grid-connected wind generated system. The supervisory controller regulates the power of the wind generator according to the change in the grid frequency. The pitch angle is controlled to match the reference power generated by the supervisory controller.

The same system used in the last reference is used in this reference [160] with the exception that there is a flywheel controlled by a fuzzy supervisor to smooth the output power of the wind generator. A storage capacitor could be used also in the same manner [161].

In a microgrid system [162], the PV generators could be used to remove frequency deviations using fuzzy supervisory controller. This controller increases or decreases the PV output power to match a high frequency or a low frequency respectively.

In reference [163], the fuzzy supervisor controls the pitch angle of a fixed speed wind generator and the reactive power output of the static VAR compensator to smooth the wind generator output power and regulate the grid voltage respectively.

A neural networks-based supervisory controller manages the power in a PV standalone system with batteries. Two neural networks are used: one neural network for direct control and the second to adapt the first one to optimize the system’s operation [164].

2.4.3. SUMMARY AND GUIDELINES

The proposed control methods diverge according to the system components, the system operational modes, and the adopted algorithms. The following points could be concluded:

1. Using artificial intelligence is not advantageous for such small-scale systems, as the conventional algorithms are easier to be programmed. Artificial intelligence might be taken into account if the control process is complicated or needs online optimization.

2. Many research papers model only the steady state operation of the system and do not take transient dynamics into account. This does not give the right indication about the system’s capability to work in the different modes of operation. Nevertheless, it will demonstrate the stable transitions between those modes.
3. Load management is a very important issue in this field of study, as the system works in standalone mode.
4. Storage means are a vital component in the PV-Wind renewable energy system. That is due to the disability of such systems to provide 100% availability, and to improve the quality of the output power.

CHAPTER (3)

CONTROL ON WIND POWER SIDE

3.1. INTRODUCTION

This chapter focuses on the wind turbine generator side of the system. The advantages of using a VAWT which directly drives a PMSG have already been discussed in Chapter (1). In this chapter, the control of this configuration will be proposed. The control of the wind turbine generator aims to deals with two different wind velocity scenarios:

- MPPT control in low and moderate wind velocities when the maximum power produced and rotor speed is less than the rated value.
- High wind velocity control when the output power and rotor speed of the generator could exceed rated values.

The study in this chapter intends to develop a controller which maximizes the power of the wind generator at low and moderate wind velocities. As the wind velocity goes beyond the rated value, the controller limits the output power and rotor speed. The high wind velocity control is found to be a general problem in VAWTs. It is not easy to be mechanically stalled because adding mechanical control to the turbine will significantly complicate the turbine and reduce its reliability. Furthermore, it will increase cost and size of the turbine. A literature review was presented in Chapter 2, discussing the different control methods for MPPT and high wind speed control.

The configuration of the proposed wind generation side is shown in Figure (3.1). It consists of a VAWT driving a PMSG. The main control action for the wind generator is provided by a boost dc-dc converter, which supplies the power to the inverter.

Section (3.2) will introduce the proposed control method. This is followed by a section outlining the general concept of the proposed control scheme which is then designed in Section (3.4). Part of Section (3.4) is dedicated to the stability of the controller in the stall mode. Simulation results are presented in Section (3.5), followed by a comparison of the proposed concept versus the speed stalling concept (Section 3.6). Experimental validation is provided in Section (3.7).

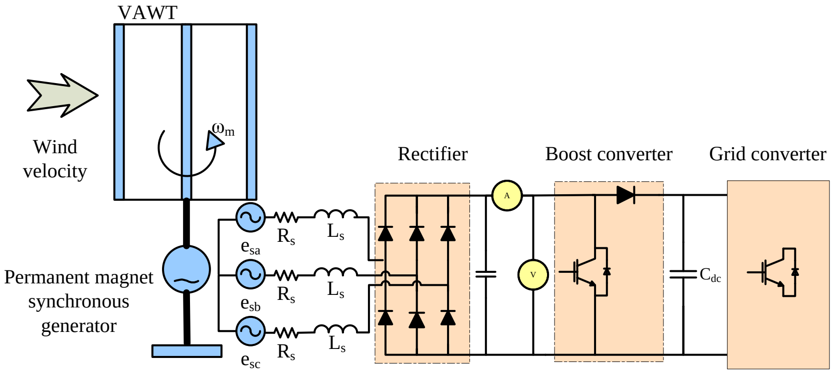

Figure (3.1) Block diagram - wind turbine with PMSG and grid connection

3.2. THE PROPOSED CONTROL METHOD

The main enhancement proposed in this study aims to stall the turbine at high wind velocities by keeping the power at the rated value while reducing the speed. This can reduce the cost and improve the quality of the power generated. This requires identifying the target operating point, which changes with wind velocity, and to stabilize the system at that point.

The intended contribution here is to demonstrate that the difficulty of identifying the target operating point can be resolved by reversing the normal power tracking control algorithm. An encoderless scheme is developed in which the rotor speed is measured via the dc side voltage of the generator rectifier, while the power is measured via the dc side current. The proposed control scheme is set to regulate the speed according to the measured current. For reasons that will become clear, this will naturally drive the turbine into the stall mode as soon as the wind velocity exceeds the range for maximum power tracking. The total power is kept at the rated value with the increased current drawn from the machine but at reduced voltage and speed. The stability issue is addressed in the study for a typical vertical axis turbine.

Operation in the MPPT region can be shown to be inherently stable, while operation in the stall region needs to be stabilized using additional control terms as will be shown later. The resultant dynamic system is nonlinear and many methods could be employed to deal with the control problem, including sliding mode [165, 166], adaptive [167, 168], and predictive control [169], or their combinations. Such methods may not be easy to implement using a simple micro-controller and may be difficult to tune. The method proposed is based on designing a PI controller to regulate the rectifier dc side voltage via generator speed at low wind velocities where the control objective is MPPT. At high wind velocities, the controller aims to stall the turbine at rated power and further compensates for stability because normal control will be unstable in this region. An advantage of the method is the ease of implementation. Furthermore, the controller tuning process to produce stable soft stalling is easier and more straightforward.

3.3. CONSTANT POWER SOFT STALLING CONCEPT

The system configuration is shown in Figure (3.1) where the permanent magnet synchronous generator is represented as a 3-phase Thévenin equivalent feeding into a diode bridge rectifier. The dc-dc converter controls the power extracted from the generator, while the grid inverter maintains the power balance to keep the voltage across the capacitor C_{dc} constant.

A fixed pitch turbine with a C_p-λ curve, as shown in Figure (3.2) [170], should normally operate near the maximum efficiency point (C_{pmax}) by adjusting the speed to maintain the tip speed ratio at its optimum value, defined here as λ_{max}. If this control is continued at excessive wind velocities, the electrical power, speed, and voltage will exceed the rating of the generator and converter. The control method proposed is to limit the output power and rotor speed by forcing the turbine into the low speed stall region. To do this the generator output is temporarily increased by the dc-dc converter to force the turbine to stall. Note that the power coefficient is a function of the tip speed ratio, which subsequently depends on the rotor speed.

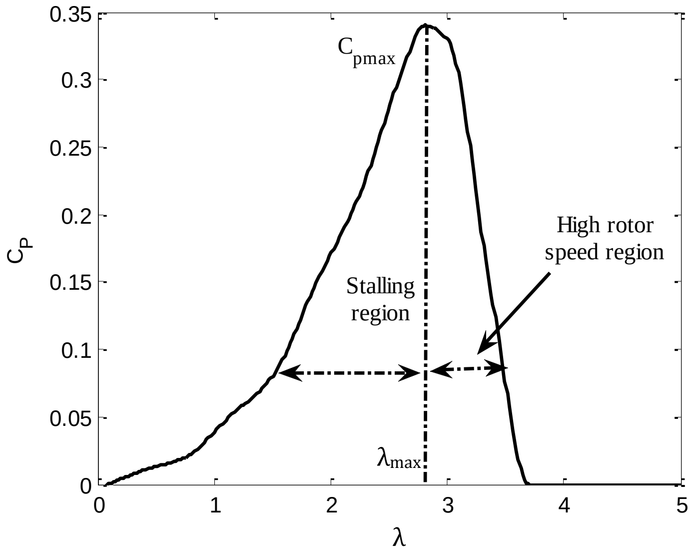

Figure (3.2) Typical Cp-λ Curve for VAWT

A wind turbine can either increase or decrease its speed to reduce the power capture by adopting a lowered C_p value. Figure (3.3) shows the rotor peed versus power and torque of the wind generator. The proposed control decreases the speed which further prevents the over voltage problem. As the wind velocity increases from the cut-in value, the rotor speed initially increases for maximum power tracking. Beyond this region, say >12 m/s wind velocity, power will be kept constant at the rated value. The intended operating points are A, B and C for wind velocities 15 m/s, 20 m/s and 25 m/s respectively. If the wind velocity later reduces to the region for maximum power tracking, the controller should detect that and return to the MPPT mode.

The operating points A, B or C are not explicitly obtainable if the wind velocity is unknown. With a PMSG, the dc side voltage of the machine rectifier is proportional to the rotor speed. Given the dc side voltage, power is proportional to the current on the dc side of the rectifier. Based on this, the proposed control is to first establish a lookup table where the rectifier dc side current is measured to determine the target dc side voltage (hence speed) as shown in Figure (3.4).

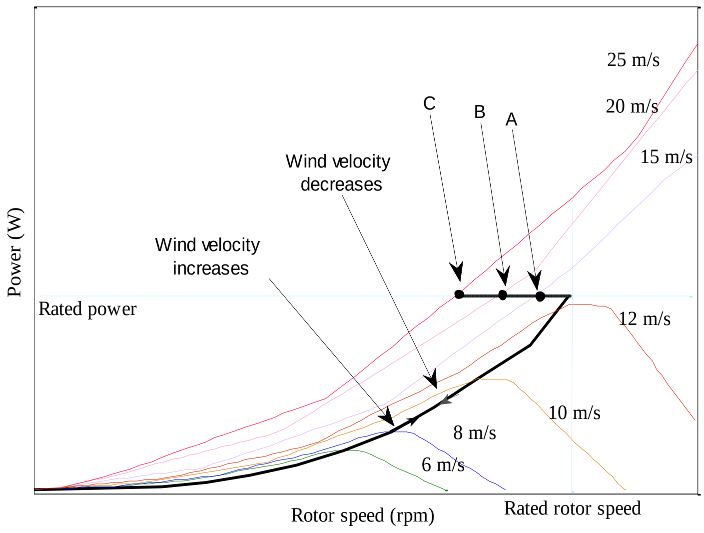

(a)

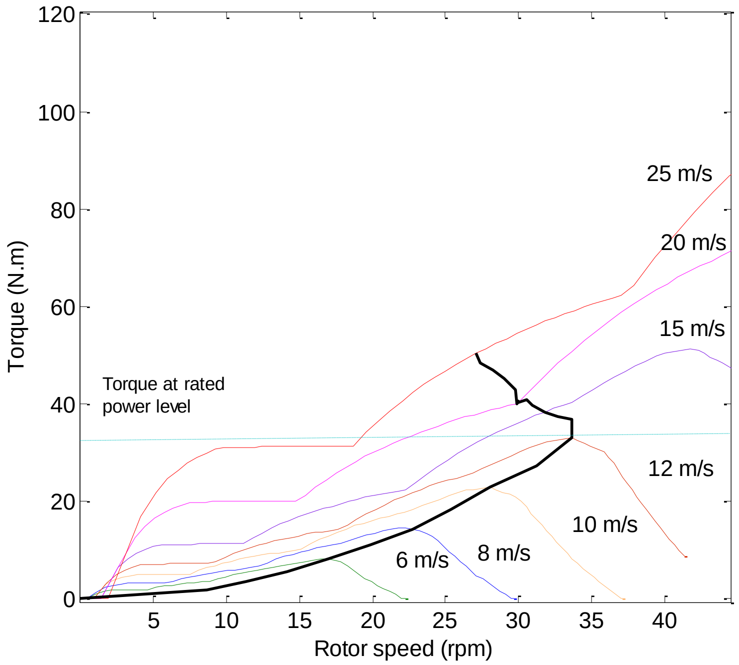

(b)

Figure (3.3) Concept of constant power soft stalling control (a)Power- rotor speed characteristics (b) Torque- rotor speed characteristics

The power tracking control and stalling control then are both reduced to dc side voltage or speed control, where the control demand is set according to the measured dc side current. As the wind velocity increases, the power initially increases and so does the current. For instance at point ‘a’, the controller will measure the dc side current i_a and adjust the generator speed so that the dc side voltage reaches v_a for optimum power extraction. As the wind velocity continues to increase, the dc side voltage and current increase to the values corresponding to point ‘b’ where the rated condition is reached. Any further increase of the measured dc side current will require stalling to enforce a reduced turbine speed and hence dc side voltage. If the controller continued to work with MPPT, the generator would follow curve (b-c"), which is a continuation of ‘o-a-b’, while with constant speed control the system will follow curve (b-c’). Using constant power stalling, the system is forced into curve (b-c) where the turbine speed can be decreased by temporarily increasing the electrical power extracted from the generator. The control strategy outlined here for stalling the turbine is indeed the reverse of what is normally used for MPPT. It is clear that by reversing the dc side voltage and current as in the conventional power tracking control, there is no need to explicitly find the operating point of constant power stalling, which changes with the wind velocity. The stability and dynamic performance rely on the controller design which is described in the next section.

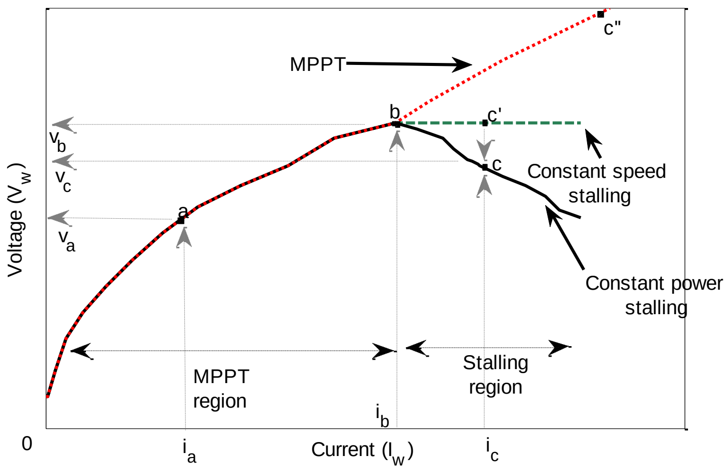

Figure (3.4) Dc side voltage-current relationship

3.4. SYSTEM MODELING AND CONTROL DESIGN

Referring to Figure (3.3), the generator is controlled in the MPPT mode when the wind velocity is low, i.e. below 12 m/s. As the wind velocity is increased, the power extracted from the turbine is maintained at the rated value. The control is based on a lookup table where the rectifier dc side current is measured to determine the target dc link voltage as shown in Figure (3.4).

3.4.1. SYSTEM MODELING

The electrical circuit dynamics of the generator have little effect on the overall mechanical dynamics and can be ignored in the control design. The equivalent circuit of a permanent magnet generator and the diode rectifier can be simplified as shown in Figure (3.5) viewed from the dc side of the rectifier. The Thévenin series resistance R_w has a value of twice the per phase resistance of the generator, neglecting the commutation overlap in the rectifier as the PM generator used has low inductance. The source emf (e_w), is proportional to the generator speed (ω_m).

$$e_w = K_w \omega_m \tag{3.1}$$

where K_w is a constant depending on the machine design.

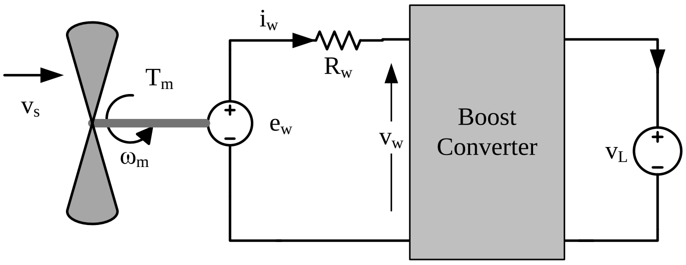

Figure (3.5) A simplified wind generator system

The Thévenin equivalent of the generator and diode bridge rectifier feeds a boost type dc-dc converter which supplies the dc link of the grid inverter represented as a voltage source v_L. The power drawn by the inverter from the dc link maintains the voltage constant; with a passive diode rectifier the power level is to be set by the duty cycle control of the dc-dc converter. The turbine torque is represented by the following equation.

$$T_m = \frac{1}{2} \rho A R v_s^2 C_p(\lambda)/\lambda \tag{3.2}$$

taking into account that (λ) was proposed before in Equation (2.2) (see Chapter (2)). With a fixed pitch angle, the whole operating region of C_p can be approximated in the following quadratic form as a function of λ.

$$C_p = a_1\lambda^2 + a_2\lambda + a_3 \tag{3.3}$$

The coefficients of this equation can be obtained using curve fitting techniques. Values of the coefficients for the turbine used here, with the power characteristic shown in Figure (3.2), are given in Table (3.1), together with other parameters of the system.

Neglecting damping and friction, the mechanical dynamics can be reduced to:

$$J\frac{d\omega_m}{dt} = T_m - T_e \tag{3.4}$$

$$T_e = \frac{P_e}{\omega_m} = \frac{e_w i_w}{\omega_m} = K_w i_w \tag{3.5}$$

From Equations (3.1), (3.4) and (3.5),

$$\frac{de_w}{dt} = -\frac{K_w}{J} i_w + b_1 v_s e_w + b_2 v_s^2 + b_3 \frac{v_s^3}{e_w} \tag{3.6}$$

where $b_1 = K_t R a_1 / J$

$$b_2 = K_t K_w a_2 / J$$

$$b_3 = K_t K_w^2 a_3 /(JR)$$

$$K_t = 0.5\rho A R$$

On the electrical side, the relationship between the dc side voltage of the rectifier and the voltage as the input to the grid side inverter can be simplified as

$$v_w = (1-d)v_L \tag{3.7}$$

The average dc side current can be calculated as follows.

$$i_w = \frac{1}{R_w}[e_w - (1-d)v_L] \tag{3.8}$$

Linearization and combination of Equations (3.6), (3.7) and (3.8) gives the following equation which represents the total system dynamics.

$$\frac{de_w}{dt} = A_1 e_w + B_1 d + B_2 v_L + B_3 v_s \tag{3.9}$$

where $A_1 = -K_w^2/(JR_w) + b_1V_{s0} - b_3V_{s0}^3/E_{w0}^2$

$B_1 = -K_w^2V_{L0}/(JR_w)$

$B_2 = K_w^2(1 - D_0)/(JR_w)$

$B_3 = b_1E_{w0} + 2b_2V_{s0} + 3b_3V_{s0}^2/E_{w0}$

Table (3.1) PMSG and wind turbine parameters

Parameters	**values**
Wind turbine rated wind velocity	12 m/s
System output power, rated	1 kW
value	3.4 A
Generator rated current	1 m
Turbine radius	240 V
Generator rated voltage	1.7 mH
Generator inductance	2.1 Ω
Generator resistance	10.48
Generator emf constant	V/(rad/s)
a_1	.037
a_2	.011
a_3	-.0035
V_{L0}	400 V
Moment of inertia	5 kg.m^2

Based on the dynamic model, a controller, as shown in Figure (3.6), can be designed. The control objective is to force the turbine to a specific speed according to the measured dc side current by means of power control, as implied by Figure (3.4).

The encoderless speed control is implemented by controlling the average dc side voltage at the rectifier output. $v_w = f(i_w)$ is a lookup table relating the dc side current and the reference dc side voltage. The transfer function of the PI controller in the speed loop is defined as

$$C(s) = \frac{K_p s + K_i}{s} \tag{3.10}$$

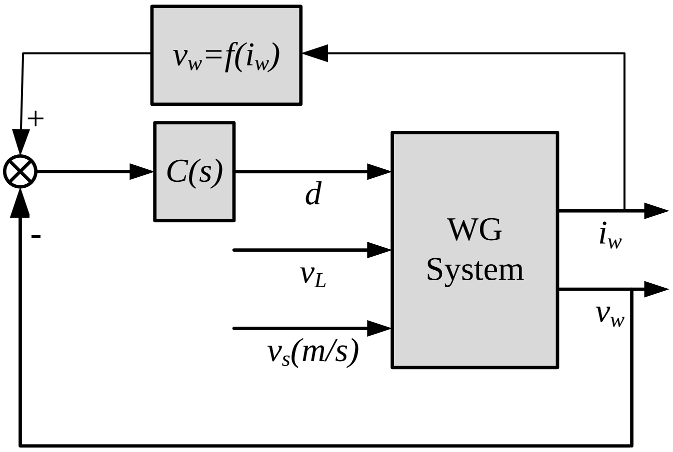

Figure (3.6) PI control algorithm

where gains K_p and K_i are determined based on the linearized system model at the rated wind velocity. The Ziegler-Nichols tuning algorithm, built in the Matlab Control System Toolbox, was used to determine the values for the test system: K_p=*-0.38* and K_i= *-0.11*. Empirically this would give a satisfactory step response of the model.

Figure (3.7) shows how the real part of the poles of the closed-loop system changes as the wind velocity increases. The poles are obtained using the closed-loop transfer function which can be derived from the above relationships. Below *12* m/s, the real part is negative. It becomes positive and the system is unstable when the wind velocity is above *12* m/s. This is true for all values of K_p and K_i due to the operation in the stall region.

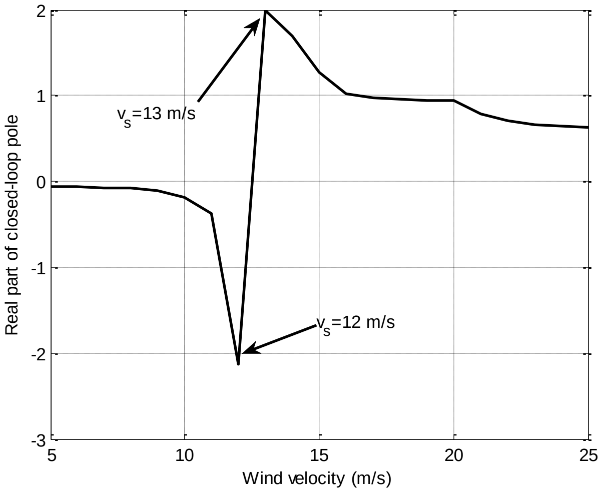

Figure (3.7) Stability analysis of original control algorithm

3.4.2. HIGH WIND VELOCITY STABILITY COMPENSATION

To compensate for stability in the stall region, a pole is added in the dc side current feedback loop as shown in Figure (3.8) where

$$K_c(s) = \frac{1}{T_c s + 1} \tag{3.11}$$

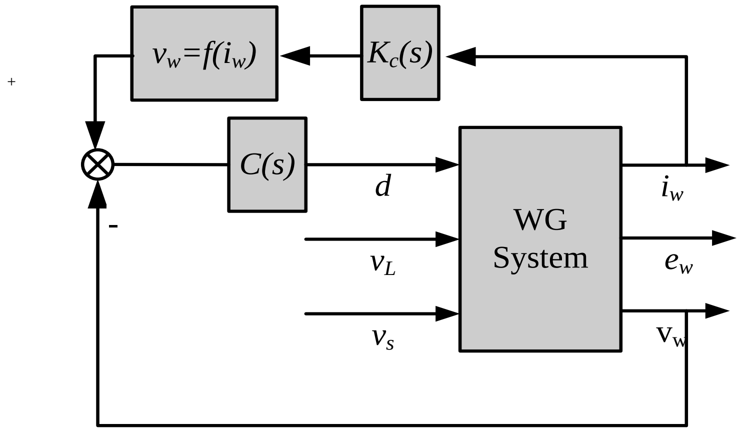

Figure (3.8) Control algorithm with stability compensation

This 1st order lag will not change the steady-state condition but will make the desired speed change more slowly. It tends to stabilize the equilibrium point in the stall region because the effect of variation in i_w is attenuated, giving the PI controller time to keep the turbine/generator speed constant until the disturbance is over. The value of T_c is thus chosen according to the moment of inertia (J). To demonstrate that, the transfer function from the wind velocity (V_s) to the produced emf (E_w), which is directly proportional to the rotor speed, is derived from Equations (3.9), (3.10), and (3.11) as

$$E_w = \frac{B_3(s^2 + d_1 s + d_2)}{s^3 + n_1 s^2 + n_2 s + n_3} V_s \tag{3.12}$$

where $d_1 = \dfrac{1 - K_p V_{L0} - T_c K_i V_{L0} - K_{VI} K_p V_{L0} / R_w}{T_c (1 - K_p V_{L0})}$

$$d_2 = \frac{-K_i V_{L0} - K_{VI} K_i V_{L0} / R_w}{T_c (1 - K_p V_{L0})}$$

$$n_1 = d_1 - A_1$$

$$n_2 = d_2 - \frac{B_1 K_{VI} K_p}{R_w T_c (1 - V_{L0} K_p)} - d_1 A_1$$

$$n_3 = - \frac{B_1 K_{VI} K_i}{R_w T_c (1 - V_{L0} K_p)} - d_2 A_1$$

$$K_{VI} = 2 m_1 I_{w0} + m_2$$

where m_1 and m_2 are the coefficients of a quadratic curve-fitting function for the entire V-I characteristics shown in Figure (3.4), which are used in the control design. It is noted that the designed controller can be further tuned on a computer model using a more accurate representation (e.g. a lookup table) of the desired V-I relationship.

$$V_w = m_1 I_w^2 + m_2 I_w + m_3 \tag{3.13}$$

Figure (3.9) shows the loci of the dominant roots of the closed-loop system against the time constant T_c. Without the 1st order lag, the system is unstable as soon as the increased wind velocity activates the stalling operating mode. As T_c increases, the real part of the roots moves towards the left-hand side of the complex plane and the system is stabilized. Targeting a maximum wind velocity of *25* m/s, it is found that for the test system the minimum value of T_c (in seconds) is about the same as the moment of inertia J (in kg.m^2). This is incidental and depends on the maximum wind velocity chosen.

For more clarification, the two dominant real parts of the real pole are plotted versus the wind velocity and T_c. That is shown in Figures (3.10 and 3.11), which are plotted for inertia of *8* kg.m^2. It is clear that the poles are stable as the wind velocity is less than *12* m/s for all the values of T_c. At high wind velocities, as T_c increases, the poles are closer to the stable region. According to that, the instability in the system can be compensated by adding such a pole in the average dc current (i_w) feedback loop.

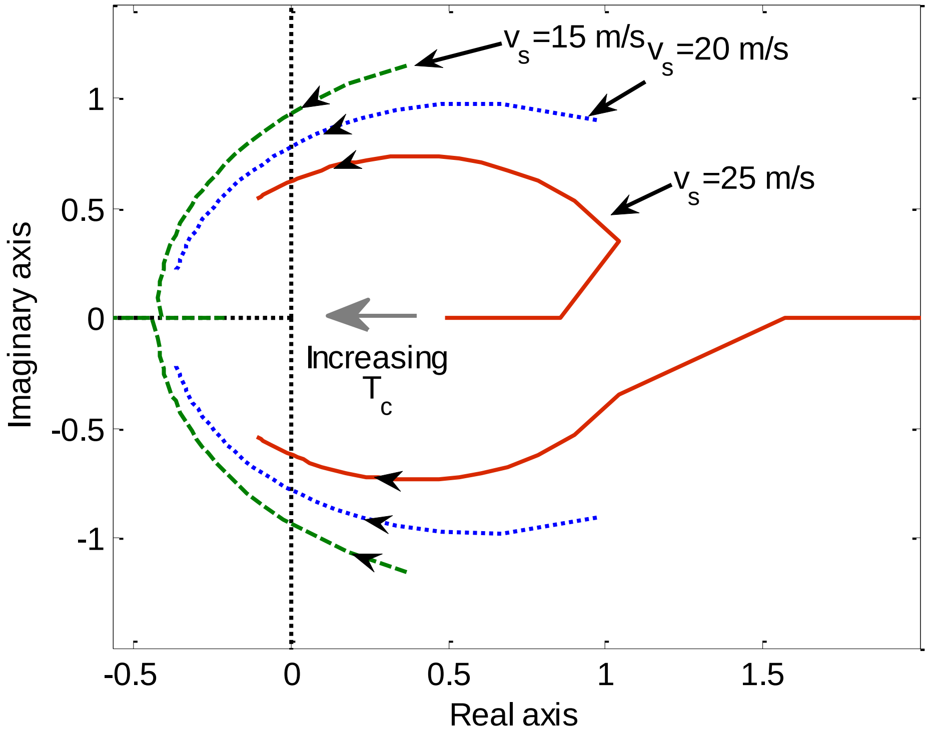

Figure (3.9) Root locus of closed-loop system

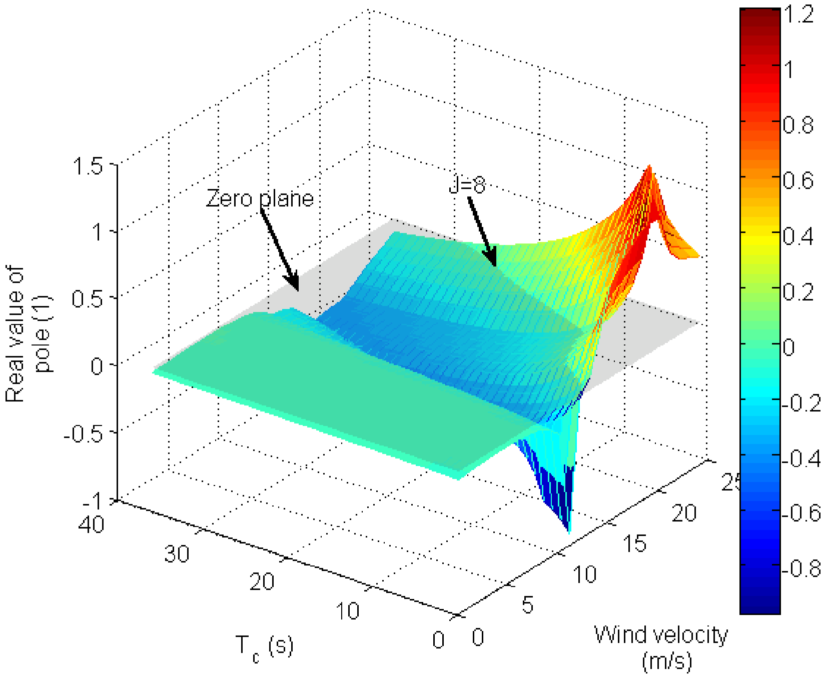

Figure (3.10) First pole with inertia=8

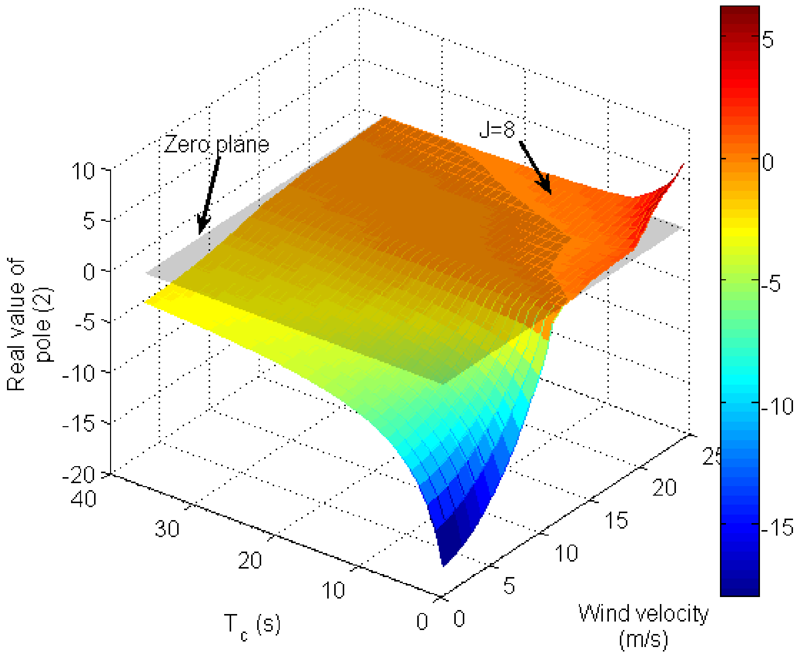

Figure (3.11) Second pole with inertia=8

The effect of moment of inertia (J) on the stabilizing T_c value is shown in Figure (3.12). The figure plots the change of the real part of the dominant pole with wind velocity and T_c for two different values of (J). The plotted wind velocity range is in the stalling region, which is from *12* m/s to *25* m/s. The figure demonstrates that, as the inertia increases, the system will be stable at a higher value of T_c. It is found that choosing T_c slightly greater than the value of the inertia (J) is sufficient to stabilize the system with an acceptable margin.

The aerodynamic characteristic of a VAWT relies on many factors including the solidity. Higher solidity means that the C_p-λ curve will have a narrower range of λ, and the maximum C_p will occur at a lower λ [170].

The turbine in this study has a medium solidity, self-starting torque, and rigid design; the tip speed ratio values seen in Figure (3.2) are on the low side compared to some other turbines. The solidity will also affect the moment of inertia which has been shown to be important in the controller design. It is noted that the thrust force on the rotor generally reduces as the turbine is sent into the stall region [25]. While it is expected that the concept of constant power soft stalling can be applied to many different types of vertical axis wind turbines, a customized design of the controller will be necessary to recognize the characteristics of individual turbine series. It is hoped that this study provides a useful guideline for such an exercise.

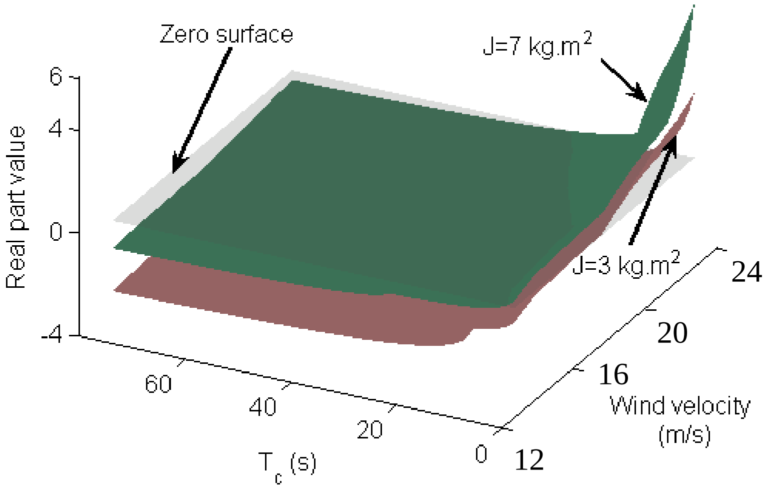

Figure (3.12) Effect of inertia on the value of T_c to stabilize the system

3.4.3. ADAPTIVE SOFT STALLING CONTROL LOOP

A method has been proposed to compensate for the stability of the system operating in the stall mode by adding a pole (1st order lag) in the current feedback loop as shown in Figure (3.8). This is only needed at overrating wind velocities. At low wind velocities, the system is inherently stable and using it will result in sluggish response reducing the MPPT efficiency. To delay feedback at high wind velocities and to avoid MPPT efficiency reduction, an adaptive time constant (T_c) is proposed. The time constant value needs to be high at high wind velocities and zero at low wind velocities; therefore, T_c is calculated online as a function of the average dc side current of the diode rectifier.

$$K_c(s) = \frac{1}{T_c(i_w)s+1} \qquad (3.14)$$

The effect of using such an adaptive feedback is demonstrated by simulation in Figure (3.13) for the test system where a step change of wind velocity (from *0* m/s to *12* m/s) is applied at t=*15* s. The output power response shows faster tracking capability using the adaptive delay control loop ($T_c=0$) as compared to a fixed time constant ($T_c=J$) needed to stabilize the system at the highest wind velocity. A block diagram for the proposed controller is shown in Figure (3.14).

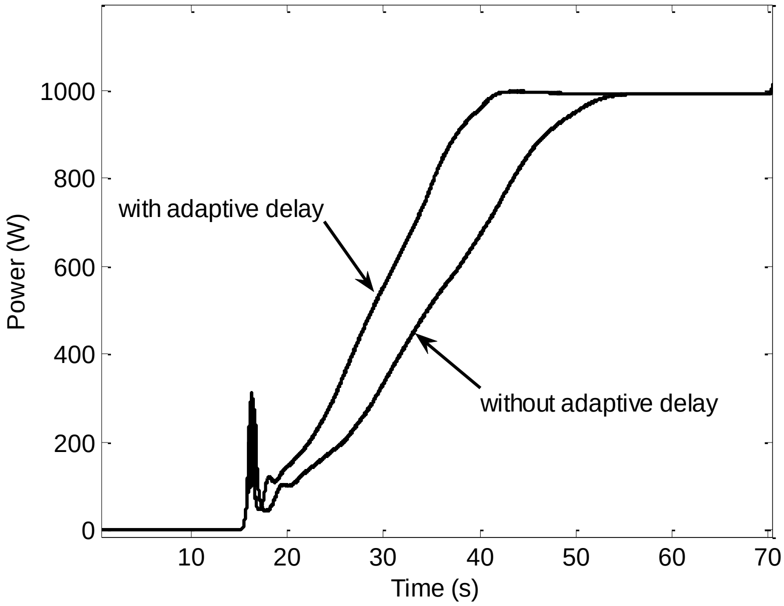

Figure (3.13) Adaptive control loop effect

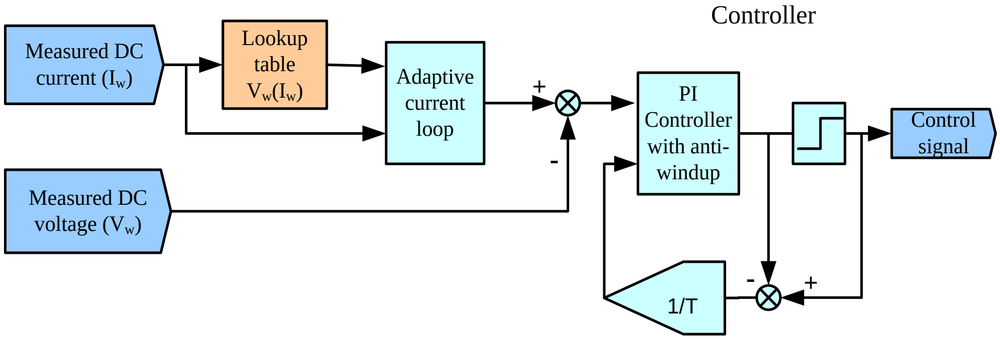

Figure (3.14) The proposed controller

3.5. SIMULATION RESULTS

The system simulated is grid-connected as shown in Figure (3.1), and has an *S1210 H-type* Darrieus VAWT driving a PMSG [170]. The PMSG supplies power to the grid through the power electronics interface stage as described here. The boost converter acts as the wind generator controller. The C_p-λ curve of the turbine is the same as shown previously in Figure (3.2).

A set of simulation results are presented in Figure (3.15) and Figure (3.16), showing the wind velocity, diode rectifier dc side voltage, dc side current, and the output power. The target power is also shown for the wind turbine generator in the grey line according to the same wind profile. In Figure (3.15), the wind velocity changes between *3* m/s and *12* m/s while in Figure (3.16) it changes between *6* m/s and *24* m/s.

Figure (3.15) shows the results for the system working in the MPPT mode of operation, as the wind velocities were under the rated value (*12* m/s). The figure shows that the target maximum power curve is tracked accurately by the proposed controller. The wind velocity increases to slightly less than the rated value at t=*100* s in the time scale. According to this, the power output reaches near to the rated value (*1000* W). The figure also shows that, even with highly turbulent wind velocity data, the MPPT process is performed without any problem.

For Figure (3.16), focus first on the period between t=*120* s and t=*160* s. The controller works in the MPPT mode because the wind velocity is below *12* m/s and the output power is correspondingly less than the rated value (*1000* W). Then consider the period from t=*200* s to t=*400* s, when the wind velocity is consistently above *12* m/s. The dc side voltage of the diode rectifier is minimum at t=*240* s, and this occurs when the wind velocity is at the maximum of about *24* m/s. The power during this period is controlled almost constantly at the rated value, showing that the system is indeed operating in the soft stall mode. The output power from the generator tracks the target power in all the regions.

The largest power increase occurs around t=*460* s, caused by a fast increase of wind velocity from *13* m/s to *18.5* m/s in less than *1* s (see also Figure (3.16)). The turbulence is faster than the wind generator system's rotor dynamics. Figure (3.16) shows the fast increase in wind speed between t=*458* and t=*459*. This caused the mechanical (T_m) and the electrical (T_e) torques to increase as the rotor speed could not be decreased instantly by the controller. The reason for this is the inertia of the rotor and the small delay in the electrical system. As a result, the control response is delayed and the power temporarily exceeds the nominal *1000* W, which should be taken into account in semiconductor device rating but has little effect on the cooling design. As is to be confirmed later by the test results, such power spikes are inevitable when the wind velocity during a gust quickly increases beyond its rated value. However the amplitude of the resulting power "spike" is significantly lower than the power level that would result if the proposed control method were not used. This is illustrated next.

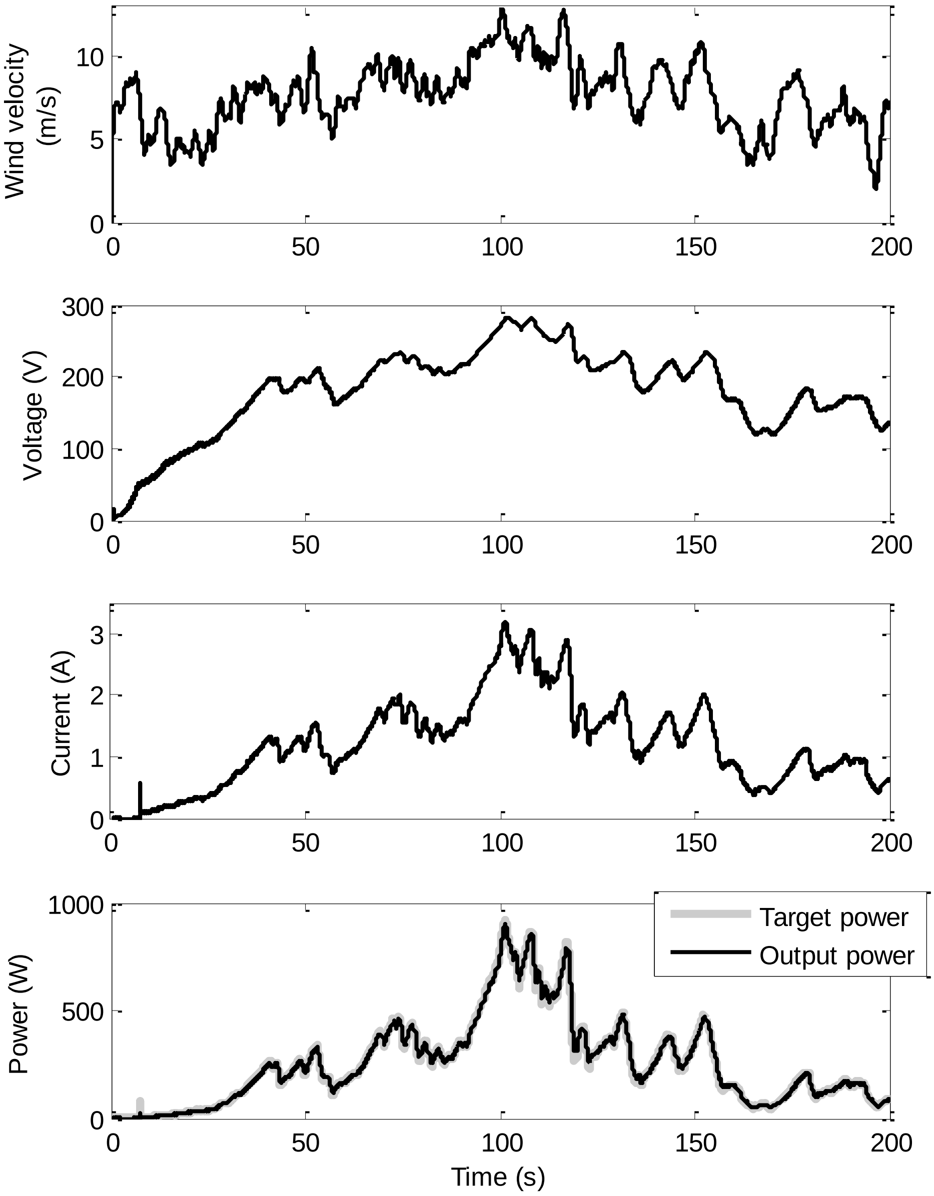

Figure (3.15) Simulation results with wind velocities lower than the rated values

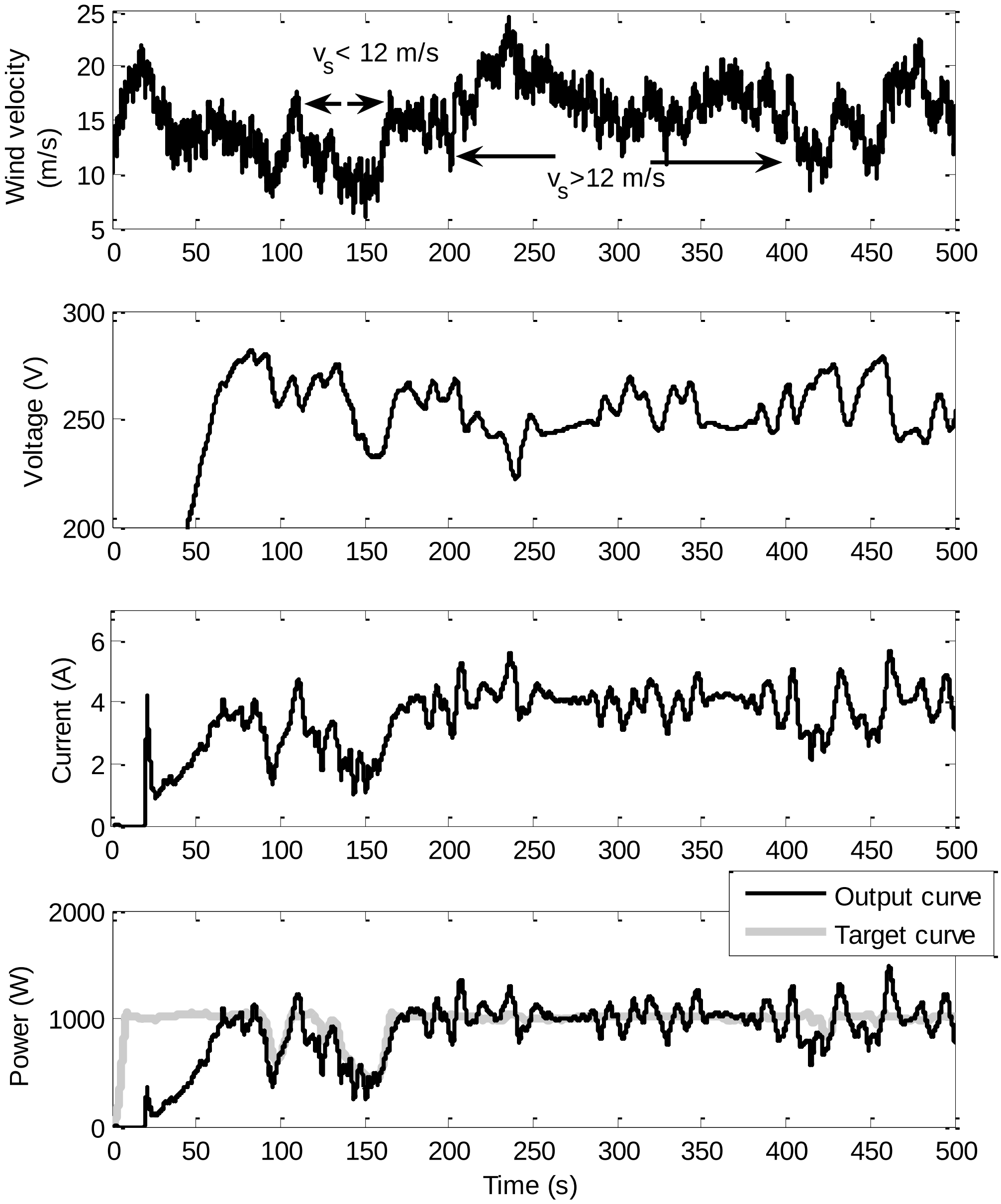

Figure (3.16) Simulation results with wind velocities higher than the rated values

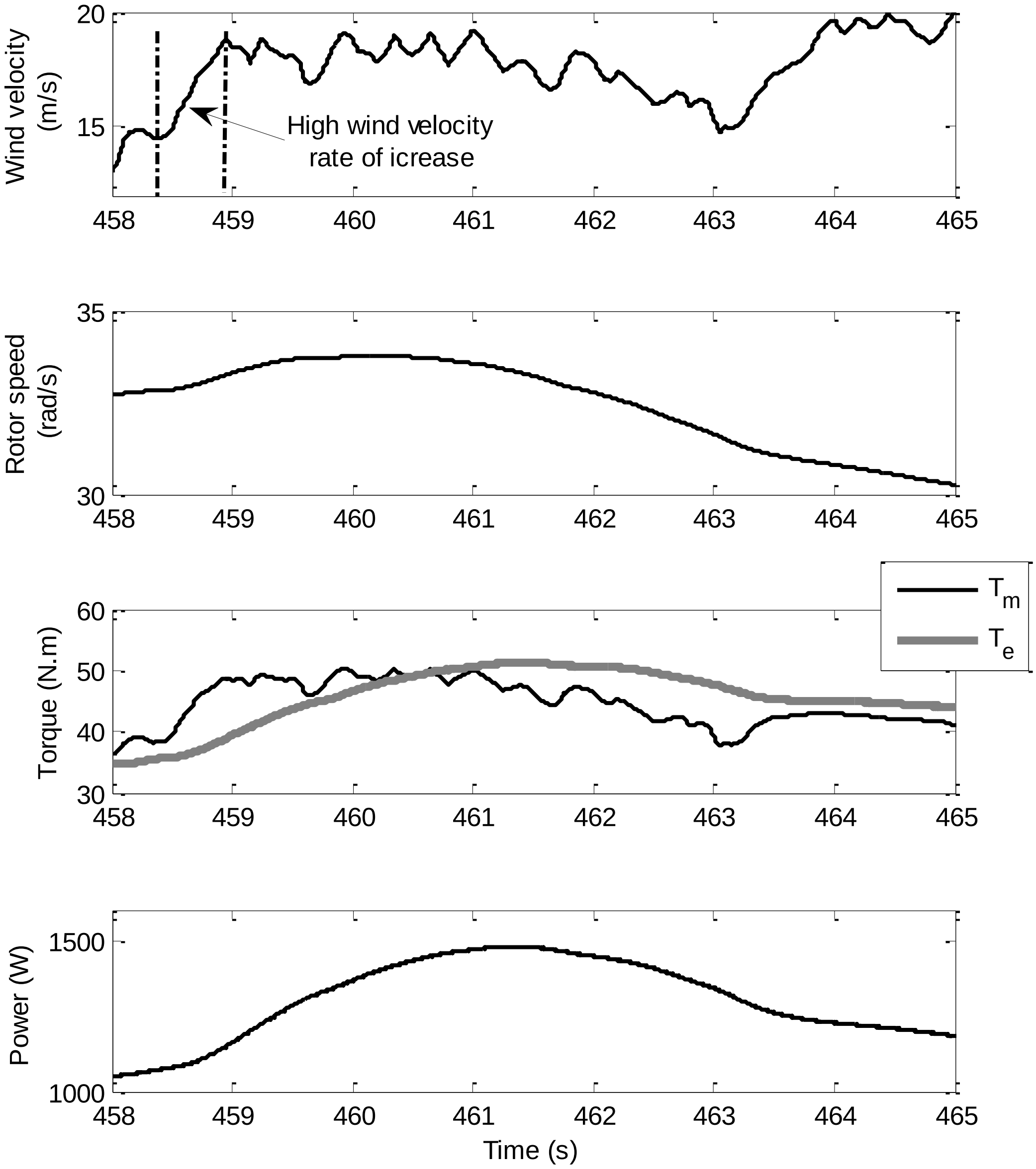

Figure (3.17) Fluctuations due to rapid wind velocity change

3.6. CONSTANT SPEED VERSUS CONSTANT POWER STALLING

To compare constant power stalling with constant speed soft stalling, both strategies are applied to the same system, with the same wind velocity data. The dc output power, current, and voltage responses are contrasted in Figure (3.18). The output power and current voltage in constant power soft stalling are lower than that in constant speed stalling at wind velocities above rated. The figure also shows that constant power stalling does not affect MPPT because with wind velocity below *12* m/s the power is the same in both cases, except in the initialization stage of the simulation.

In the high wind velocity range, the response in constant speed stalling reaches *2000* W, while in constant power stalling it just fluctuates around the rated power and only temporarily reaches *1200* W. Therefore, the electrical system needs to be over rated for constant speed stalling to withstand the large power at high wind velocities. This will increase the size and cost of the system, including the cooling design for the power semiconductor devices, which have relatively short thermal time constants. The problem is largely attenuated in constant power stalling.

A dynamic thermal model was built in the Matlab/Simulink with Plecs software for the PMSG, using parameters of the simulated generator [171]. The PMSG temperature according to both control methods is shown in Figure (3.19). The figure clearly shows the advantage of the proposed method with respect to the constant speed stalling method. Hence, the temperature rise in the proposed method is always reduced.

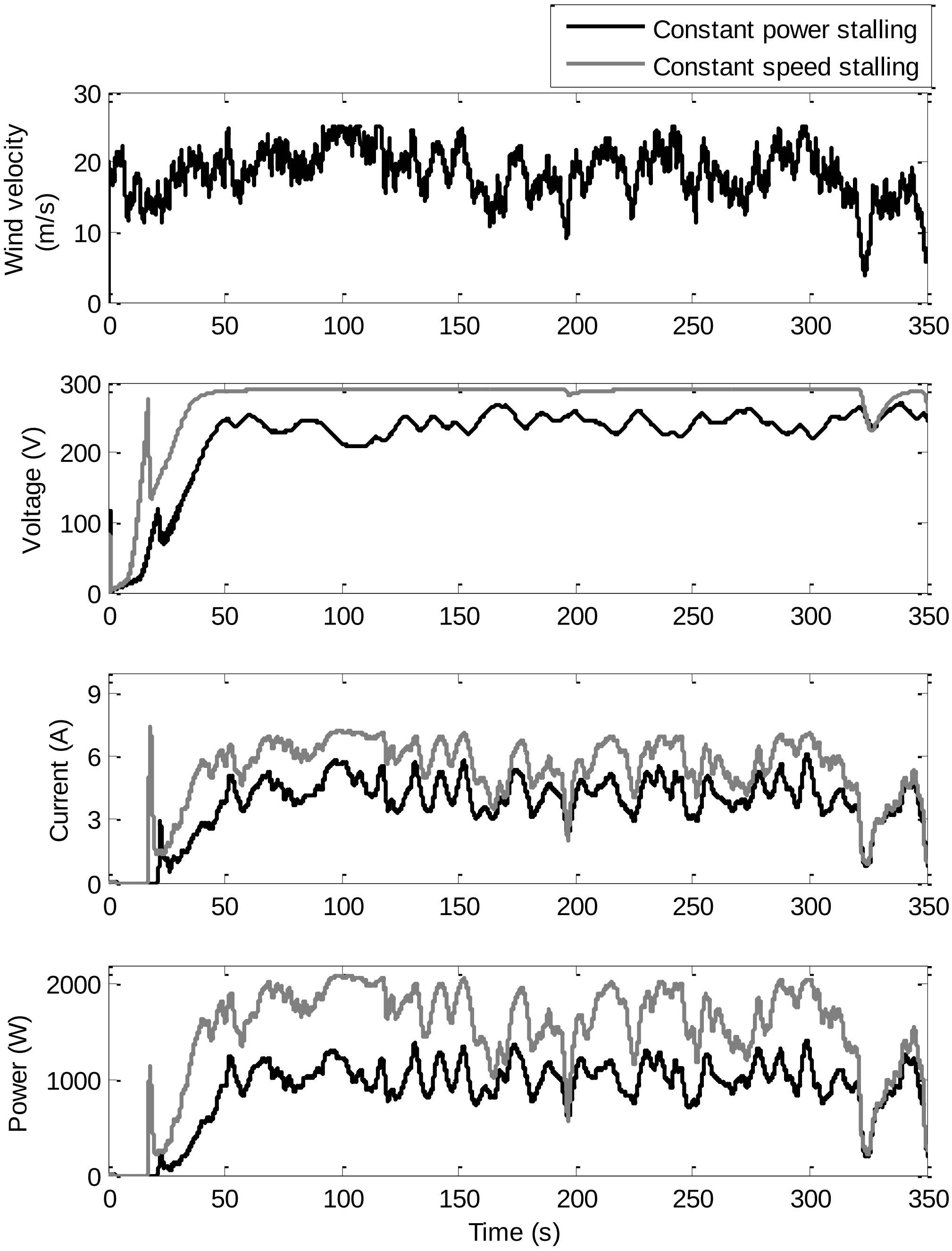

Figure (3.18) Power output: constant power stalling vs constant speed stalling

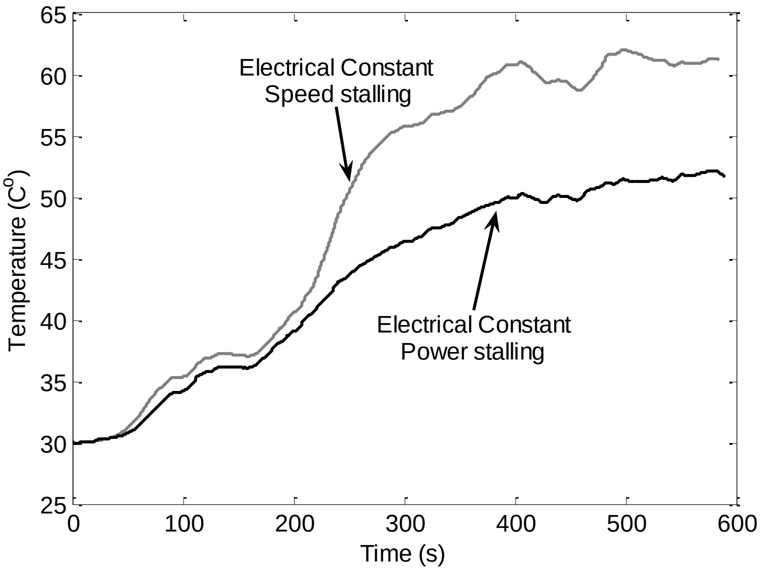

Figure (3.19) PMSG Temperature rise with constant speed stalling and constant power stalling methods

3.7. EXPERIMENTAL VERIFICATION

The active soft stalling concept at excessive wind velocities, as developed in this study, can prevent complex aerodynamic control and also smooth the power supplied to the grid. To verify the control method, a laboratory test is carried out and Figure (3.20) shows a picture of the test rig setup. A simplified block diagram, Figure (3.21), outlines the hardware arrangement.

The vertical axis wind turbine itself is emulated by an induction motor (IM) driving a PMSG through a step-down gear box. The IM is driven by an inverter working in the torque control mode where the torque demand is set according to the measured rotational speed and the given wind velocity. The same turbine characteristic of the *1000* W system as shown previously in Figure (3.1) are implemented using a desktop computer hosting a dSPACE real time control system which can be programmed in the Matlab/Simulink environment [172]. The system parameters and the control gains are the same as those used in simulation. The generated power is returned to the grid through a commercially available WindyBoy inverter (‘Load’ in Figure (3.21) set to regulate its dc link voltage.

A simple block diagram reveals the wind turbine model shown in Figure (3.22), as the inputs of the model are the rotor speed measured signal and the wind velocity data.

The output of this model is the torque reference signal. The losses in the IM driver must be taken into account in the torque signal applied to the driver.

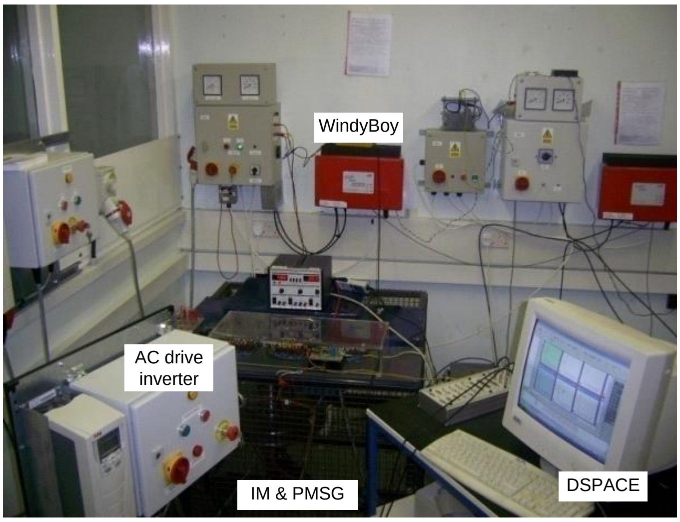

Figure (3.20) Laboratory test rig

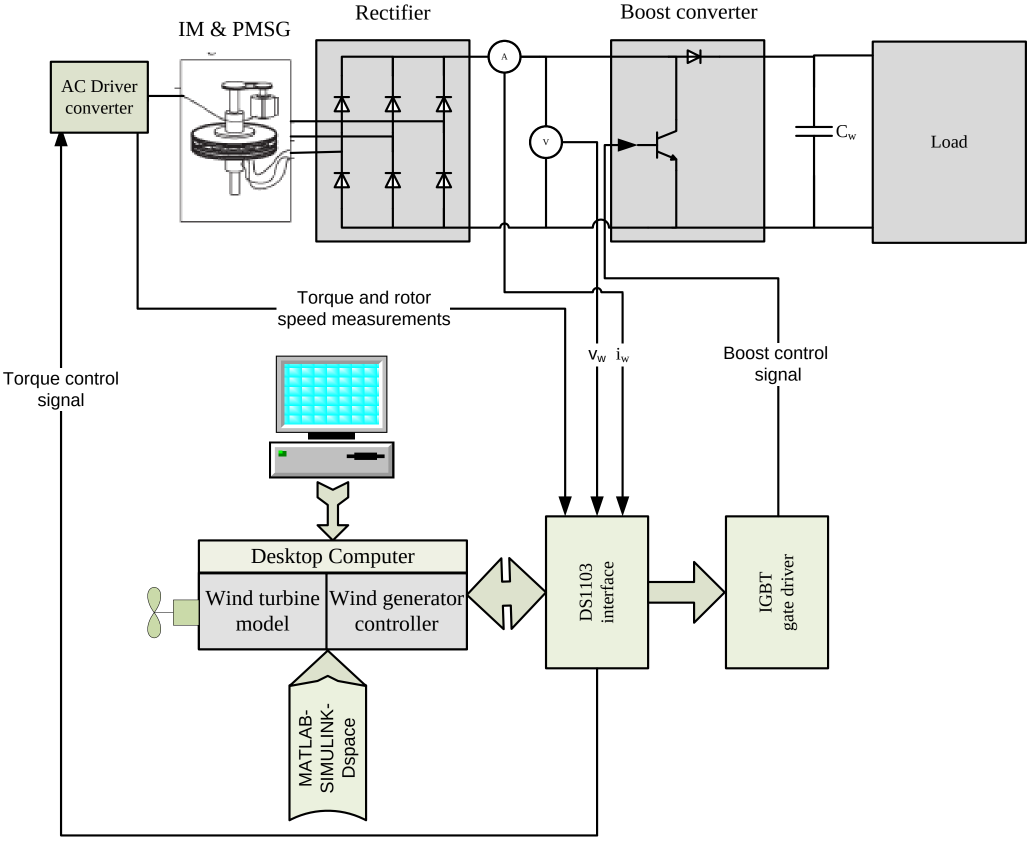

Figure (3.21) Arrangement of laboratory system

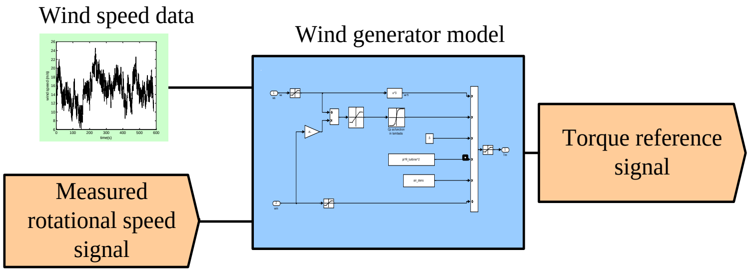

Figure (3.22) Block diagram for the wind turbine model

To demonstrate the stalling control algorithm and verify the controller design, step changes of wind velocity are applied to the wind turbine system, as shown in Figure (3.23).

In the stall region, the wind velocity is increased up to *25* m/s. The controller stalls the generator by reducing the rectifier dc side voltage, which is achieved by reducing the rotational speed. The power extracted from the generator is quickly regulated to be constant as the dc side current and torque (not directly measured) increase. The results show that the power indeed stays roughly constant, whatever the change of wind velocity is, as long as it is higher than the preset *12* m/s. As the wind velocity reduces to below *12* m/s, i.e. in the MPPT region, the controller tracks the maximum power points and the power output is less than the rated *1000* W. The power increases temporarily when activating the constant power stalling mode, depending on the difference between the initial and final values of the wind velocity.

The results show that the biggest power spike happens when the maximum step change in wind velocity occurs from *12* m/s to *25* m/s. Further examination of the results showed that the power spike at each step is less than what was predicted by simulation (not shown). This is due to the actual moment of inertia of the generator system being slightly less than the theoretical value and that there is a delay when a torque change is applied to the PMSG, which is attributed to the damper on the shaft connecting the drive to the generator.

A time-series of dynamic wind velocity similar to that used in the simulation (Figure (3.17) is used in the experiment to further demonstrate the effectiveness of the proposed control method.

The experimental results are shown in Figure (3.24). At t=*30* s, the wind velocity increases above *12* m/s. Therefore, the controller reduces the rectifier dc side voltage by driving the system into the stall region. The dc side current increases and the power is almost constant around *1000* W even with wind velocity being over 20 m/s. As the wind velocity returns to below *12* m/s at around t=*280* s, the system resumes the MPPT control mode and the generated power is less than *1000* W.

The power response contains spikes with the largest occurring at about t=*320* s; this is because at that time the wind velocity increases at a high rate. Another observation is that the power spike at t=*320* s with wind velocity of 17 m/s is higher than that at t=*410* s with wind velocity of *23* m/s, implying that the power spike depends on the rate of change of the wind velocity.

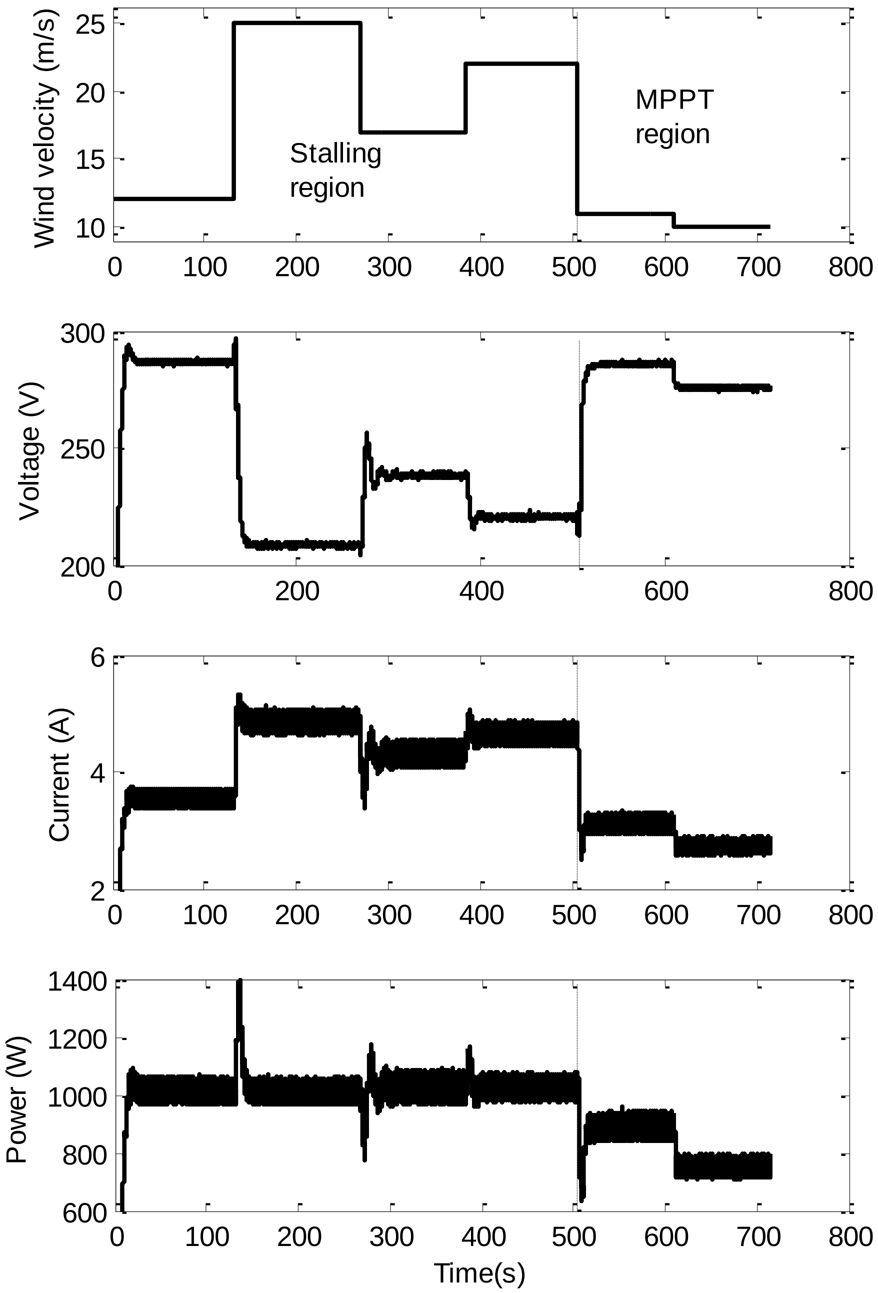

Figure (3.23) Experimental results with step changes in wind velocity

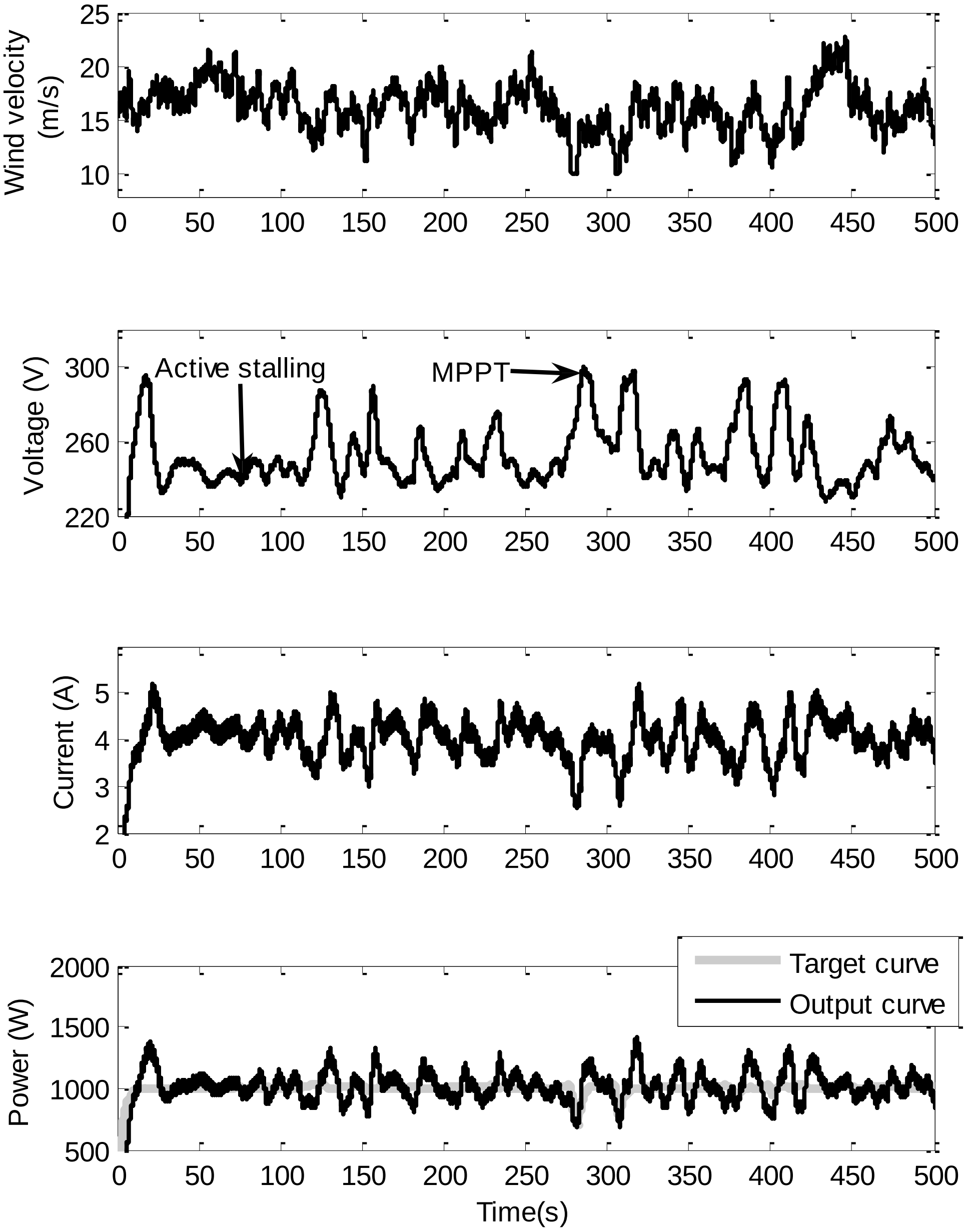

Figure (3.24) Experimental results with a dynamic wind velocity time-series

CHAPTER (4)

CONTROL ON PV POWER SIDE

4.1. INTRODUCTION

This chapter discusses the control of the PV generator in a small scale hybrid PV-Wind generation system, which could be applied generally in multi-source renewable energy systems. The PV generator is controlled to provide maximum power point tracking (MPPT) control or reduced power control according to a signal from the supervisory controller. Many methods have been applied to achieve maximum power point tracking (MPPT) control in photovoltaic (PV) power generation systems, as discussed before in Chapter (2). These methods, with a wide variety of algorithms for implementation, include open circuit voltage control, short circuit current control, hill climbing, pilot cells and artificial intelligence techniques. Hill climbing, which is widely used, can be divided mainly into perturb and observe (P&O) and incremental conductance (I.C.) algorithms. The hill climbing approach has the advantages of low cost, generality and ease of implementation. Hill climbing can directly set the duty cycle of the dc/dc converter to control the PV generating system [195, 173]. Direct duty cycle control can be easily implemented without the need for a PI controller, and it will also increase the generality of the method.

As this study is a part of a multi-source small-scale renewable energy system connected to the grid, the research will provide reduced power mode. The reasons of the need for such mode of operation will be discussed in details in Subsection (4.4.2).

The objectives of the study in this chapter are as follows:

1. Developing a version of the direct hill climbing algorithm which is more suitable to hybrid PV-Wind systems.

2. Dealing with the over rating power problem by developing a reduced power control mode.
3. Analyzing the dynamic behavior of the system.
4. The direct MPPT control parameters, which are duty perturbation value (δd_p) and the required time between consecutive perturbations (δT_p), will be designed. Furthermore, general guidelines for the design will be provided.
5. Providing simulation and experimental results for verification.

The PV generating system proposed in this study is connected to a grid inverter through a boost stage, which is commonly used in a multi-source renewable energy system. A block diagram of the system is shown in Figure (4.1). First, the PV generator model will be developed in Section (4.2). Then, A design of the perturbation parameters is developed based on transient analysis of the circuit shown in Figure (4.1). The proposed control method, based on a variable step incremental conductance with reduced power mode, is presented at the end of the chapter.

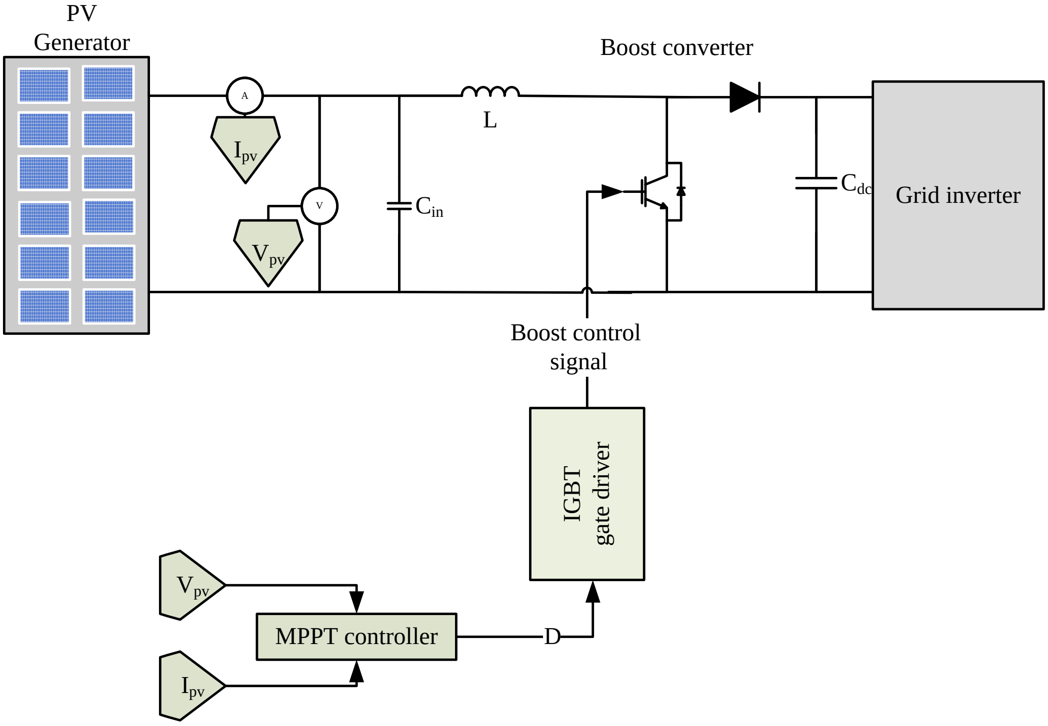

Figure (4.1) A block diagram of the proposed system

4.2. PV GENERATOR MODEL

The PV generator is an array of PV modules connected in series and parallel; a PV module is an array of solar cells. A detailed PV solar cell electrical model is used in this study based on the Shockley diode equation. The same model for the solar cell is used for the module taking into account the number of cells in the module [174-177].

The PV generator output power is a nonlinear function of the solar radiation, cell temperature, and load condition. Many models which are derived from physics, using curve fitting or artificial intelligence, have been proposed [77]. In this work, a previously proposed model [177] is adopted because the emphasis here is control. This model is based on the single diode assumption, while the parameters can be extracted from the PV module datasheet. In the single diode assumption, the solar cell, PV module or PV array can be simplified to an equivalent circuit of a diode and a current source connected in parallel. The current source represents the generated photocurrent when the sunlight hits the solar panel, and the diode represents the P-N transition area of the solar cell. The series and parallel resistances represent the losses due to the body of the semiconductor and the contacts. The equivalent circuit of the solar cell is shown in Figure (4.2).

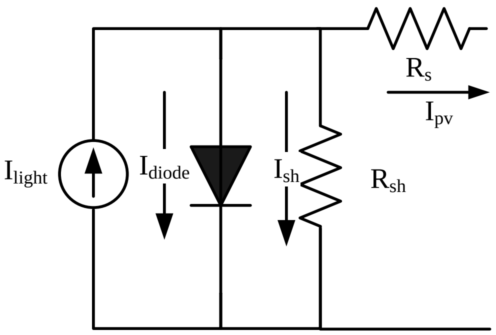

Figure (4.2) the solar cell model

The current relationship of the simplified solar cell can be derived from Kirchhoff's current law:

$$I_{pv} = I_{light} - I_{diode} - I_{sh} \tag{4.1}$$

where I_{pv} is the output current, I_{light} the light generated current, I_{diode} the diode current and I_{sh} the shunt resistance current. Subsequently, the output current (I_{pv}) can be calculated as in Equation (4.2). In this equation, the last term can be neglected by assuming that the shunt resistance (R_{sh}) is very large. Equation (4.2) is the solar cell model which can be used as the model of a module by considering that the whole module is working as a large- area solar cell.

$$I_{pv} = I_{light} - I_0 (e^{\frac{V_{pv} + I_{pv} R_s}{A}} - 1) - \frac{V + I_{pv} R_s}{R_{sh}} \tag{4.2}$$

The equations to calculate the parameters R_s, R_{sh}, A, I_0, are provided in (137). I_{light} can be calculated from Equation (4.3).

$$I_{light} \cong I_{sc} = \frac{S}{S_r} \left(I_{scr} + \mu_{sc} (T_c - T_{cr}) \right) \tag{4.3}$$

where

$$A = \frac{mKT}{q} \tag{4.4}$$

where m depends on the recombination of the carriers in the junction. For a non-ideal junction, in which some carriers do recombine in the junction, (m) has a value between 1, 2.

The light-generated current (I_{light}) is nearly equal to the short circuit current (I_{sc}), and is directly proportional to the solar radiation and cell temperature. From the reference conditions (S_{ref}, T_{c_ref}), the light-generated current can be calculated from the following equation as a function of solar radiation (S) and cell temperature (T_c):

$$I_{light} \cong I_{sc} = \frac{S}{S_{ref}} (I_{sc\_ref} + \mu_{Isc} (T_c - T_{c\_ref})) \tag{4.5}$$

At a fixed radiation level, increasing temperature leads to decreased open circuit voltage and slightly increased short circuit current. The increase in the short circuit current is due to the increase of the minority carriers' diffusion lengths and the small reduction of the band gap. In order for this model to reproduce these effects, it is necessary to know how the model parameters I_0, I_L, and A vary with temperature. From Equation (4.4), A is almost directly proportional to the temperature:

$$A = A_{ref} \left(\frac{T_c}{T_{c\_ref}}\right) \tag{4.6}$$

where the subscript ref refers to the reference conditions of temperature and solar radiation. The reverse saturation current (I_o) may be written in terms of material characteristics and the cell temperature, as shown in Equation (4.7):

$$I_0 = I_{0\_ref} \left(\frac{T_c}{T_{c\_ref}}\right)^3 e^{\frac{\varepsilon(1-(T_{c\_ref}/T_c))}{A_{ref}}} \tag{4.7}$$

From Equations (4.6 and 4.7), the reference parameters (I_{0_ref}, A_{ref}) can be calculated from the reference conditions of solar radiation and temperature. The reference saturation current (I_{0_ref}) at open circuit conditions could be found from Equation (4.2) considering the output current zero. Furthermore, the light generated current is the short circuit current, and the exponential term is larger than one. Then I_{0_ref} can be found as follows:

$$I_{0\_ref} = I_{sc\_ref}\, e^{\frac{-V_{oc\_ref}}{A_{ref}}} \tag{4.8}$$

R_s and A_{ref} can be found by solving Equation (4.2) considering the conditions of short circuit, open circuit, and maximum power.

$$R_s = \frac{A_{ref}\left(\ln\left(1-\frac{I_{mp\_ref}}{I_{sc\_ref}}\right)\right) - V_{mp\_ref} + V_{oc\_ref}}{I_{mp\_ref}} \tag{4.9}$$

$$A_{ref} = \frac{\mu_{Voc} T_{c\_ref} - V_{oc\_ref} + \varepsilon}{\frac{\mu_{Isc} T_{cref}}{I_{sc\_ref}} - 3} \tag{4.10}$$

In order to predict properly the performance of the photovoltaic module, it is necessary to determine the operating cell temperature. For the purpose of simplicity, the temperature of the solar cell is assumed uniform on the surface of the photovoltaic module. The cell temperature can be calculated from the equation of the energy balance around the PV cell. By a conventional analysis for the energy out and into the solar cell, the following steady state equation for cell temperature can be deduced;

$$T_c = T_a + \frac{S}{S_{ref}}(T_{c\_ref} - T_{a\_ref})(1 - \frac{\eta_{PV}}{0.9}) \qquad (4.11)$$

In this study, a *0.975* kW system is simulated with the datasheet parameters provided in Table (4.1) under the reference solar radiation (*1000* W/m^2) and cell temperature (*25*^{o}C) condition. The change of the steady-state characteristics with the solar radiation and cell temperature are shown Figure (4.4).

Table (4.1) PV generator datasheet parameters

Module (BP 365) Characteristics	Values
Maximum power	65 (W)
Voltage at maximum power	17.6 (V)
Current at maximum power	3.69 (A)
Short circuit current (I_{scr})	3.99 (A)
Open circuit voltage (V_{ocr})	22.1 (V)
Temperature coefficient of I_{sc} (μ_{sc})	(0.065±0.015)%/°C
Temperature coefficient of V_{oc} (μ_{sc})	-(80±10)mV/°C
Number of modules	15

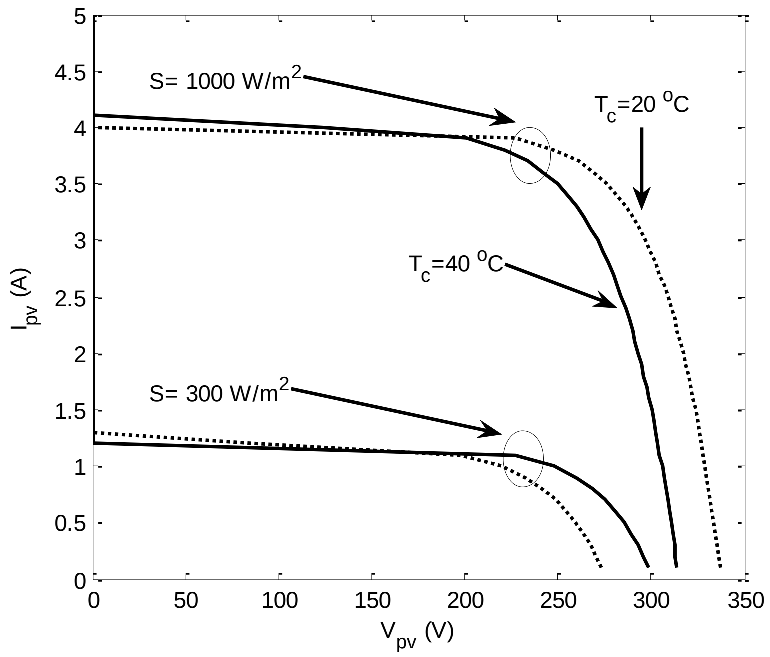

(a)

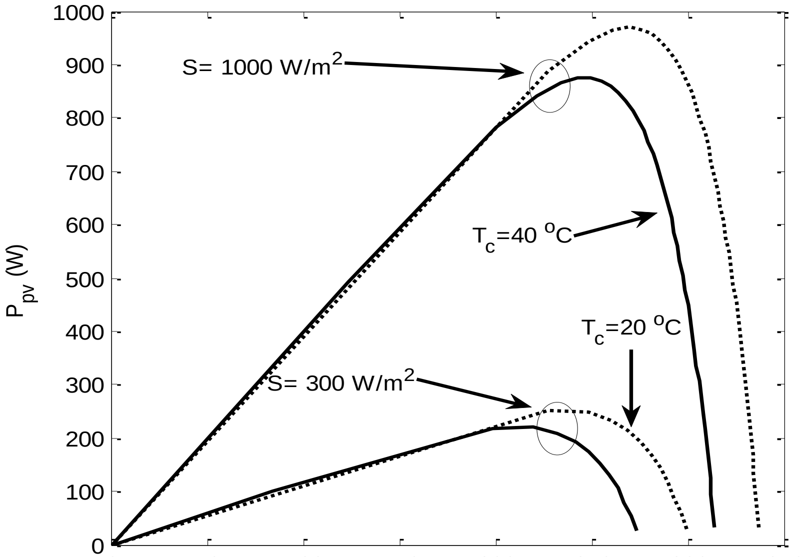

(b)

Figure (4.3) PV generator characteristics for solar radiation 1000 W/m^2 and 300 W/m^2, temperature 20^{o}C and 40^{o}C: (a) current (I_{pv}) vs. voltage (V_{pv}) and (b) power (P_{pv}) vs. voltage (V_{pv}).

4.3. PERTURBATION PARAMETERS DESIGN

Although a wide range of research results have been published using this method, an analysis of the transient behaviour of the system has rarely been carried out. Moreover, there are no guidelines to design the duty ratio perturbation value (δd_p) and the required time interval between consecutive perturbations (δT_p). This section gives a set of guidelines for designing both the perturbation magnitude and the time interval between consecutive perturbations. These guidelines would improve the maximum power point tracking efficiency. This part of the work is a step forward towards designing a simple and fast-acting MPPT unit for a small scale hybrid PV-Wind generation system connected to the grid. One of the objectives of the work in this section is to analyze the dynamic behaviour of the system. Another is to provide design guidelines for the choice of the duty perturbation value and the required time between consecutive perturbations. The proposed design is demonstrated at the end of the section by simulation.

4.3.1. TRANSIENT ANALYSIS

A small signal transient analysis model for the hill climbing MPPT technique has been developed to investigate the effects of perturbation factor (δd_p) and the perturbation time (δT_p, the time interval between two consecutive perturbations) on the system dynamics. A simplified circuit for the system is shown in Figure (4.3), where the PV generator is linked to a grid inverter via a dc/dc boost converter. For this analysis, the equivalent series resistances of the inductor (L) and the capacitor (C_{in}) have been neglected. Moreover, the equivalent shunt resistance (R_{sh}) of the solar array is also neglected. The inverter d.c. link voltage is considered as a voltage source (e). The inputs of the system are the solar radiation (S), the cell temperature (T_c), the inverter equivalent voltage (e), and the dc/dc converter duty ratio (d). The outputs are the PV generator output voltage (v_{pv}) and current (i_{pv}). The temperature dynamic effect can usually be ignored due to small thermal inertia and small perturbations in power [178]. By analyzing the system, the following circuit equations can be obtained:

$$\dot{i}_L = \frac{1}{L}\left(v_{pv} - e(1 - d)\right) \tag{4.12}$$

$$\dot{v}_{pv} = \frac{1}{C_{in}}(i_{pv} - i_L) \qquad (4.13)$$

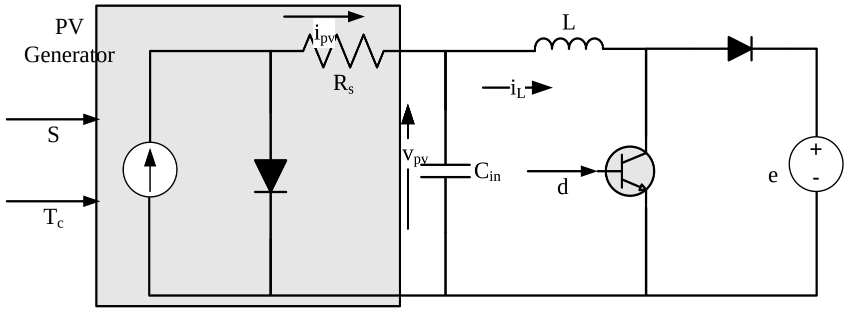

Figure (4.4) Simplified circuit for the system model

Furthermore by linearizing Equations (4.12 and 4.13):

$$\frac{\partial i_{pv}}{\partial V_{pv}} = K_{pv} = \frac{-I_o}{Ae^{-(-\frac{V_{pv0+R_S I_{pv0}}}{A})} + I_0 R_S} \qquad (4.14)$$

$$\frac{\partial i_{pv}}{\partial S} = K_s = \frac{1}{S_r}(I_{scr} + \mu_{sc}(T_{c0} - T_{cr})) \qquad (4.15)$$

Using small signal analysis, the state space representation of the system can be provided in the form of Equations (4.16 and 4.17) which are expanded in Equations (4.18 and 4.19). Prefix (δ) distinguishes small signals (increment) from ac signals. (*0*) in the subscript corresponds to the zero initial condition at t=*0*.

$$\dot{x} = Ax + Bu \qquad (4.16)$$

$$y = Cx + Eu \qquad (4.17)$$

$$\begin{bmatrix} \delta\dot{i}_L \\ \delta\dot{v}_{pv} \end{bmatrix} = \begin{bmatrix} -\frac{R_L}{L} & \frac{1}{L} \\ -\frac{1}{C_{in}} & \frac{K_{pv}}{C_{in}} \end{bmatrix} \begin{bmatrix} \delta i_L \\ \delta v_{pv} \end{bmatrix} + \begin{bmatrix} \frac{E_o}{L} & 0 & -\frac{(1-D_0)}{L} \\ 0 & \frac{K_s}{C_{in}} & 0 \end{bmatrix} \begin{bmatrix} \delta d \\ \delta s \\ \delta e \end{bmatrix} \qquad (4.18)$$

$$\begin{bmatrix} \delta i_{pv} \\ \delta v_{pv} \end{bmatrix} = \begin{bmatrix} 0 & K_{pv} \\ 0 & 1 \end{bmatrix} \begin{bmatrix} \delta i_L \\ \delta v_{pv} \end{bmatrix} + \begin{bmatrix} 0 & K_s & 0 \\ 0 & 0 & 0 \end{bmatrix} \begin{bmatrix} \delta d \\ \delta s \\ \delta e \end{bmatrix} \qquad (4.19)$$

The transfer function G_{vpv} between $\delta V_{pv}(s)$ and $\delta d_p(s)$ can be obtained, taking into account that the solar radiation and temperature are not changing. This transfer function is given in Equation (4.20). The steady state temperature value affects K_{pv} (see Equation (4.14)), and as a result it affects the dynamic characteristics. Another interesting notice is that the solar radiation has a very small effect on K_{pv} and G_{vpv}, and it does not directly affect the system dynamics. These simplifications, which have been applied in this study, are only applicable to values of V_{pv} around and less than that at the (MPP). The operating point of the PV generator remains in that region.

$$G_{Vpv}(s) = \frac{-E_0}{LC_{in}s^2 - LK_{pv}s + 1} \qquad (4.20)$$

The time domain response for the second order system can be worked out as follows:

$$\delta v_{pv}(t) = -E_0\left(1 - \frac{e^{-\zeta\omega_n t}}{\sqrt{1-\zeta^2}}\sin(\omega_d t + \theta)\right)\delta d \qquad (4.21)$$

where

$$\zeta \approx -\frac{K_{pv}}{2}\sqrt{\frac{L}{C_{in}}}$$

$$\omega_n \approx 1/\sqrt{LC_{in}}$$

$$\omega_d = \omega_n\sqrt{1-\zeta^2}$$

The time domain equation for the produced perturbation in power will be:

$$\delta p_{pv}(t) = K_{pv}\delta v_{pv}^2(t)$$

$$\delta p_{pv}(t)=K_{pv}E_0^2\left(1-\frac{e^{-\zeta\omega_n t}}{\sqrt{1-\zeta^2}}\sin(\omega_d t+\theta)+\frac{e^{-2\zeta\omega_n t}}{1-\zeta^2}\sin^2(\omega_d t+\theta)\right)\delta d_p{}^2 \qquad (4.22)$$

The high order term in the last equation can be neglected.

4.3.2. DESIGN OF PERTURBATION PARAMETERS

The minimum time interval (δT_p) required between every perturbation in the duty cycle can be worked out from Equation (4.22). δT_p could be considered equivalent to the 2% settling time (T_{sttl}) for the power transient signal. The reason is that the signal would nearly settle down to the steady state within this time. As a result, misguided controller hunting, which is caused by oscillations is prevented. δT_p, is provided in Equation (4.23), which shows the capacitor effect in the dynamic behavior of the system.

$$\delta T_p \approx T_{sttl} = 4/\zeta\omega_n \approx -\frac{8C_{in}}{K_{pv}} \tag{4.23}$$

From Equation (4.22), the minimum perturbation value in the duty cycle can be calculated, considering that the perturbation in power will be unity. Additionally, K_{pv} is calculated with respect to the maximum power point:

$$\delta d_p \approx \frac{1}{\sqrt{(-K_{pv}E_0{}^2)}} \tag{4.24}$$

The first order system – when no capacitor (C_{in}) is connected – is a special case of Equation (4.22), considering $C_{in}=0$. In this case, δd_p is the same as in Equation (4.24), while δT_p can be calculated from the following equations:

$$\delta T_p = 4LK_{pv} = 4L/R_{pv} \tag{4.25}$$

The V_{pv}-I_{pv} curve shape has the main effect on the system's dynamic behavior. Figure (4.5) shows that curve where there are points (a) with a voltage value less than the MPP value, (b) with a voltage value very close to the MPP value and (c) with a voltage value higher than the MPP value. The root locus according to the V_{pv}-I_{pv} curve is shown in Figure (4.6). The figure shows that the system is oscillatory at low voltage and, as the voltage increases, the system is more damped until it is over-damped at voltages near the open circuit voltage value. Points a, b, and c have also been marked in the root locus curve, where (a', b' and c') is the conjugate pole of every point respectively in the (s) plane. The system is simulated with an inductance value L=3 mH, and a capacitance value C_{in}=*100* µF.

The V_{pv}-I_{pv} curve shape effect comes from the fact that: $R_{pv} = {}^{1}/_{K_{pv}}$. As the voltage increases, the absolute value of (R_{pv}) decreases and this causes the system to be more damped (see Equation (4.21)). The significant reduction in the absolute value of (R_{pv}) as (V_{pv}) increases is shown in Figure (4.7).

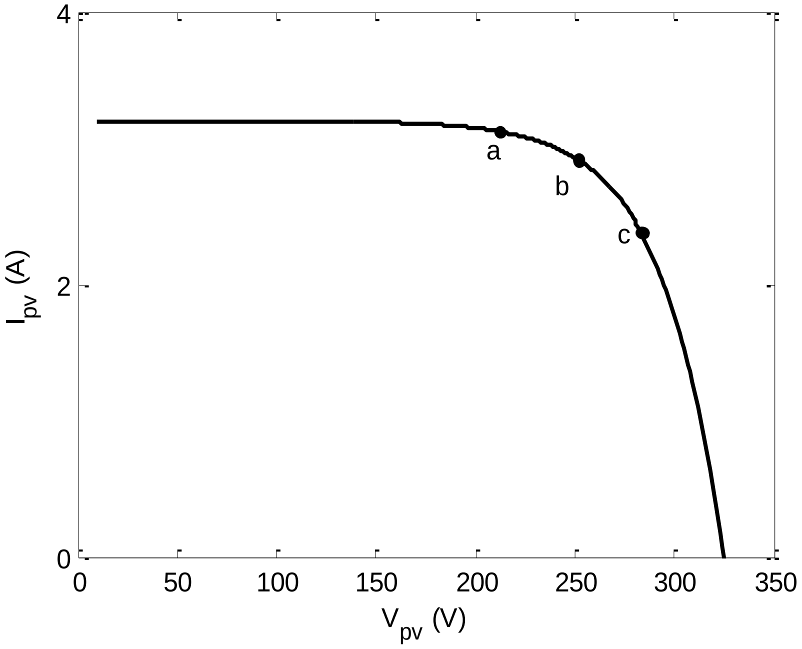

Figure (4.5) I_{pv}-V_{pv} curve are T_c=20^{o}C, S=800 W/m^2

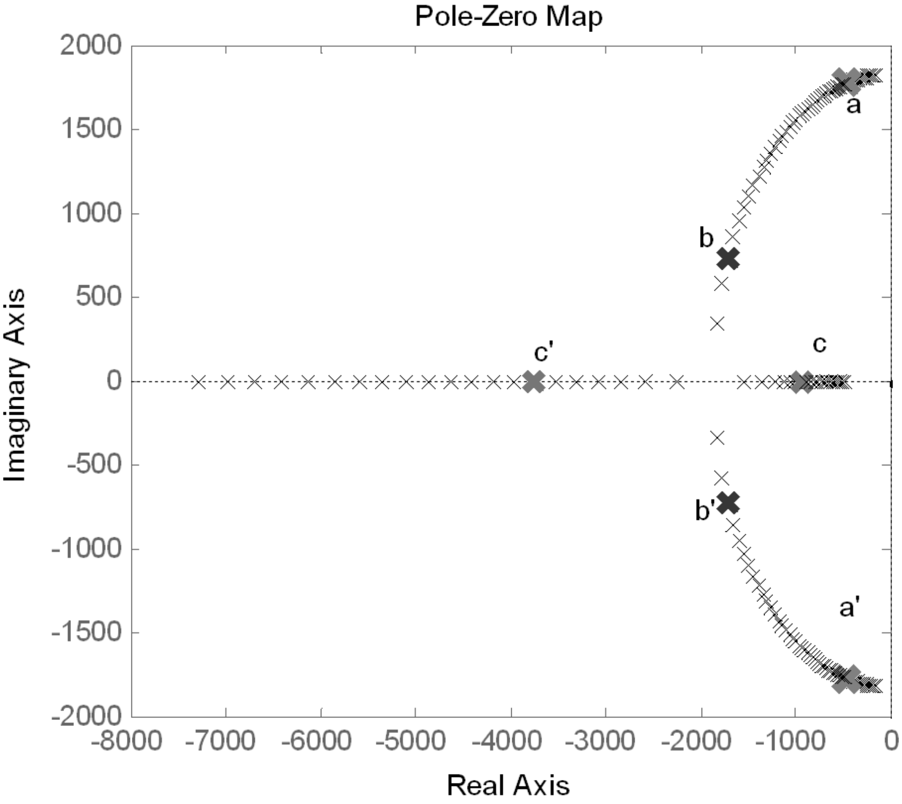

Figure (4.6) Root locus for the PV system according to I_{pv}-V_{pv} curve shown in Figure (4.5)

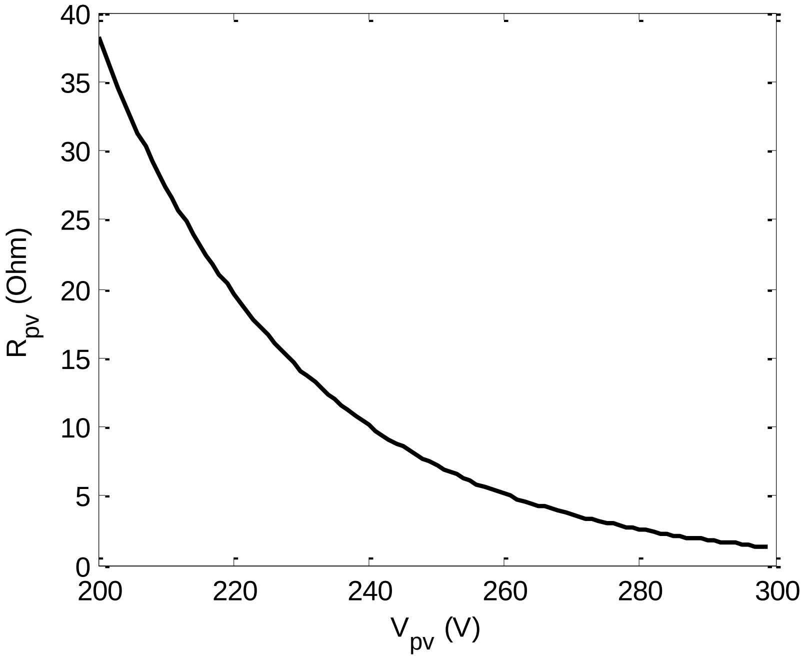

Figure (4.7) Absolute value of R_{pv} plotted against V_{pv}

The small signal step response in power (δP_{pv}) due to the step change in (δd_p), which is applied to the operating points (a, b and c), is shown in Figures (4.8-a, 4.8-b, and 4.8-c), respectively. The figures show that the system is oscillatory at point (a), the oscillations decrease at point (b), and the system is over-damped at point (c). Therefore, the lowest voltage operating point has to be considered in the design of δT_p as it is the worst case. The figures show that δT_p decreases as V_{pv} increases due to the reduction in oscillation as V_{pv} increases from point (a) to point (b). However, at point (c) δT_p increases again as the system is over damped. The oscillation in low voltage can greatly mislead the MPPT controller and has to be taken into account in the design of the perturbation parameters.

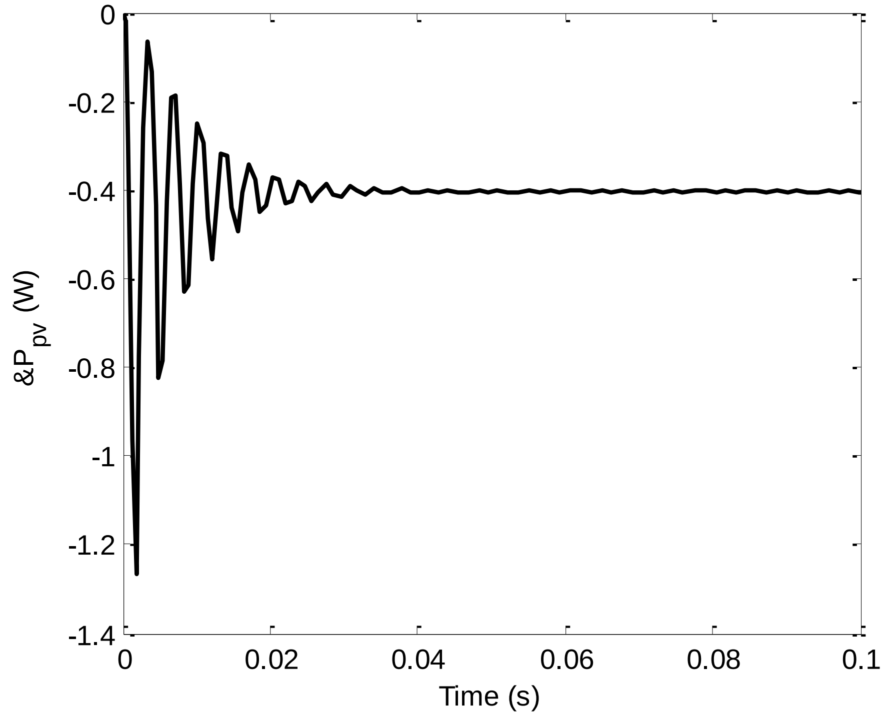
0
-0.2
-0.4
-0.6
-0.8
-1
-1.2
-1.4
&P_{pv} (W)
0
0.02
0.04
0.06
0.08
0.1
Time (s)

(a)

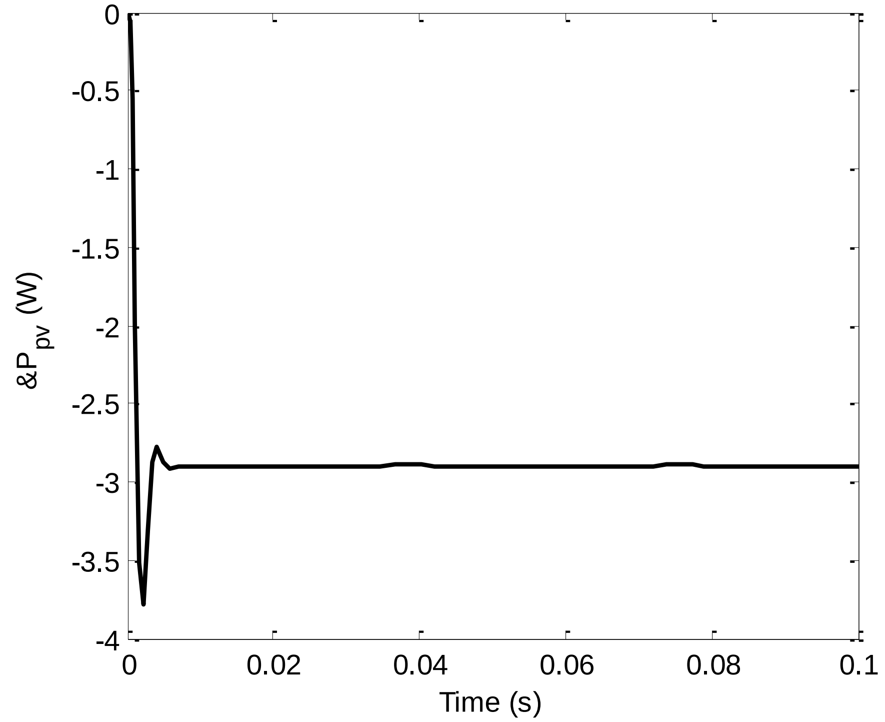
0
-0.5
-1
-1.5
-2
-2.5
-3
-3.5
-4
&P_{pv} (W)
0
0.02
0.04
0.06
0.08
0.1
Time (s)

(b)

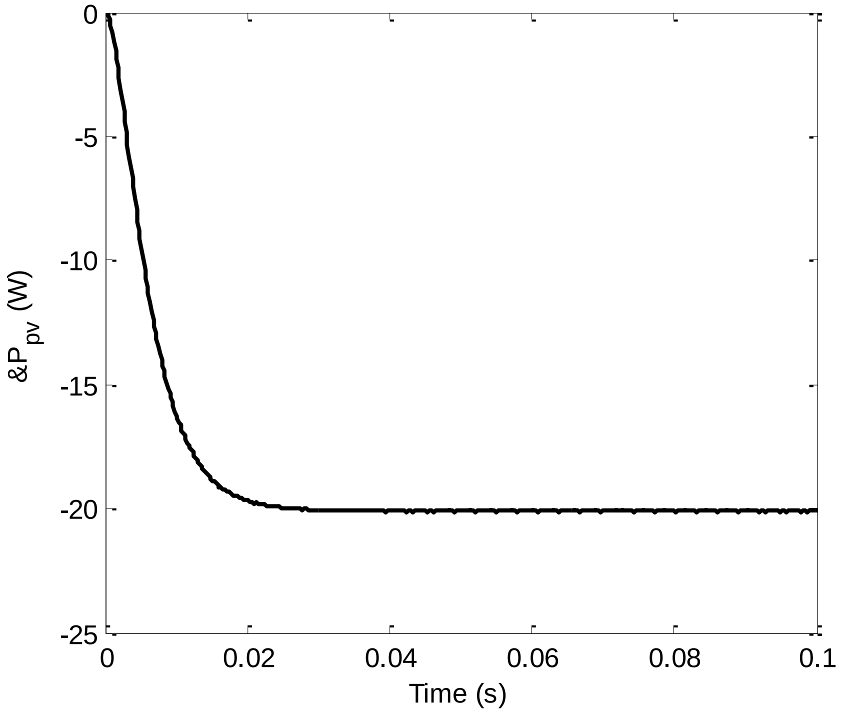

(c)

Figure (4.8) Step response in δP_{pv} according to: (a) operating point a, (b) operating point b, and (c) operating point c as shown in Figure (4.8)

4.3.3. DESIGN VERIFICATION

A schematic circuit diagram of the *0.975* kW PV-generating system was shown in Figure (4.1), which has been simulated using the Matlab/Simulink package with PLECS software. To demonstrate the proposed design results, the P&O algorithm as shown in Figure (4.9) has been developed to control the system. The MPPT controller was implemented with different perturbation parameters which are presented in Table (4.2). A solar radiation step change was applied to the system from *0.4* kW/m^2 to *0.8* kW/m^2 and back again to the initial value.

The MPPT controller was first applied using δT_p smaller than the optimum design value, while δd_p was equivalent to the optimum. Then, the controller was applied with a δd_p smaller than the optimum design value, while δT_p was equivalent to its optimum. Finally, both δd_p and δT_p were set equivalent to their respective optimum design values. If δT_p is larger than the optimum value, the system's response will be slower and the efficiency will be reduced. Besides, if δd_p is larger than the optimum value, the system's response will be more oscillatory and the efficiency will also be reduced. Therefore, these two cases are not adopted in the evaluation.

Table (4.2) Perturbation parameters

Cases	δd_p	δT_p
smaller δT_p	0.02	0.01
smaller δd_p	0.0005	0.03
optimum values	0.002	0.03

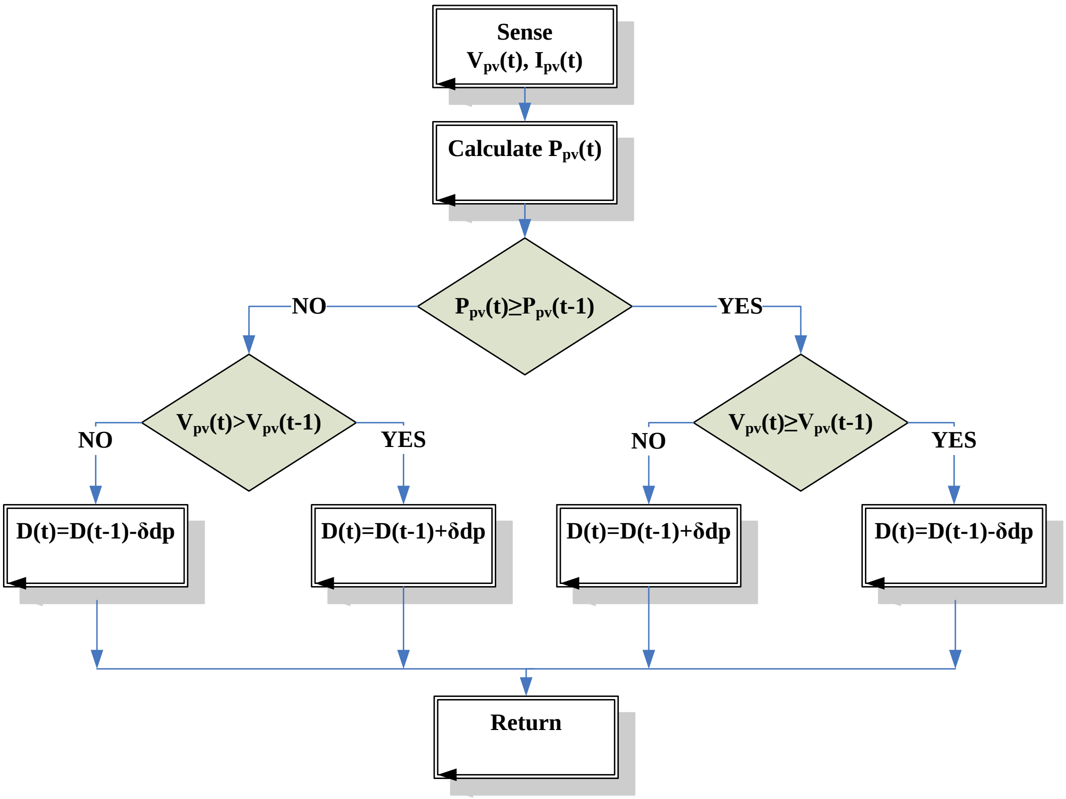

Figure (4.9) Perturb and observe algorithm

The resultant output power is shown in Figure (4. 10); in the optimum design case, the system tracks the maximum power faster and the produced power is higher. Therefore, the efficiency of the MPPT controller is improved. The figure also shows that less oscillation around the maximum power point is achieved with the optimum design case; this is due to lower tracking errors happening in the MPPT controller. There is always a steady state error between the optimum power level and the power output, even with the optimum design of δd_p. This is predictable due to the oscillations around the maximum power point. The proposed algorithm can attenuate this problem by using a modified variable step I.C. method.

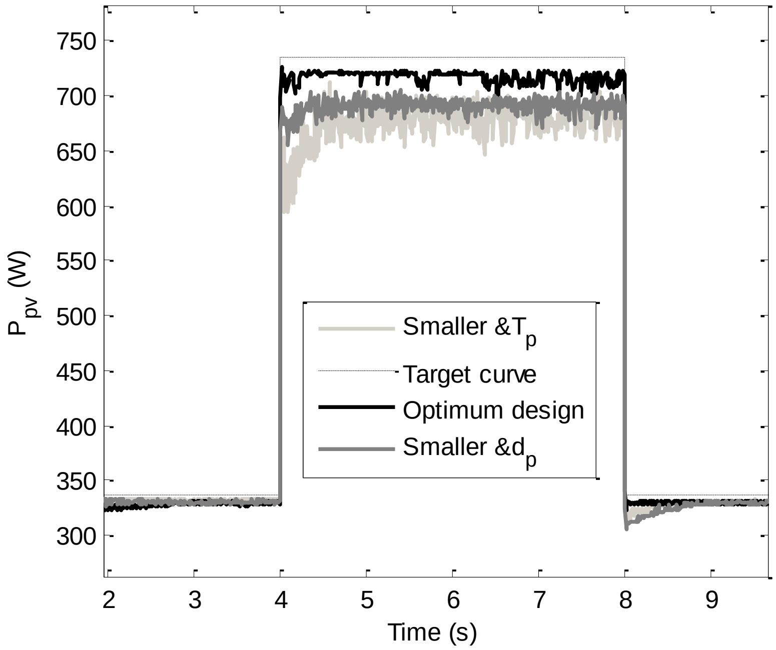

Figure (4.10) P_{pv} output with different design perturbation parameters

In Figure (4.11), the solar radiation was almost constant at the first *20* s of the simulation time. For both smaller duty and smaller time perturbation, the controller oscillates more around the maximum power point compared to the optimal design case. This is very clear in voltage (V_{pv}) and power (P_{pv}) waveforms. To make it clearer, the duty ratio waveforms for the three cases were zoomed between t=5 and t=10, as shown in Figure (4.12). It is clear in the figure that, in the optimum design case, the perturbations around the maximum power point are more educated as compared to the other two cases. This will improve the MPPT efficiency and reduce fluctuation in power supplied to the inverter. Due to the fast change in solar radiation around t=50 s, the change in duty ratio, at smaller duty ratio case, is very high compared to the designed case. However, the smaller time perturbation has better tracking in this special case.

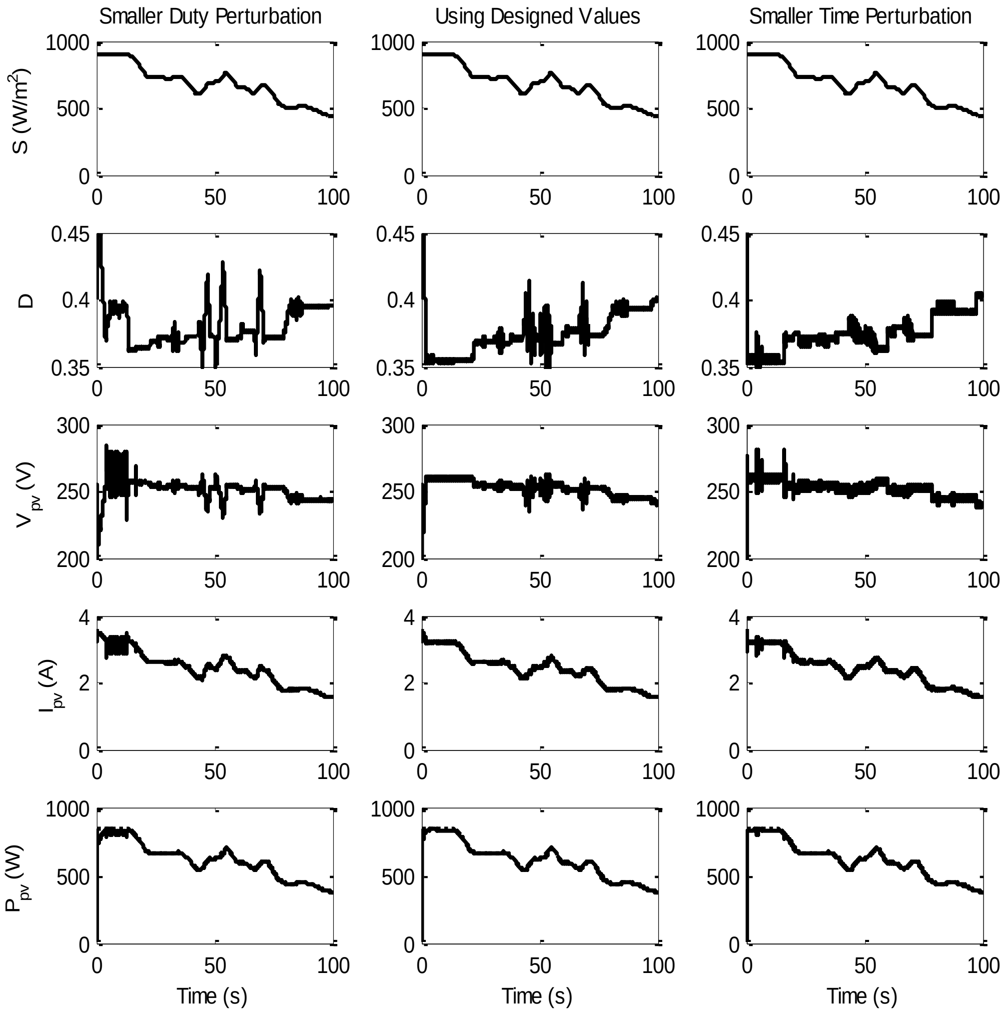

Figure (4.11) The measured solar radiation (S), the Duty ratio (D), the dc output voltage (V_{pv}), the dc output current (I_{pv}) and the dc output power (P_{pv}) for the three simulation cases

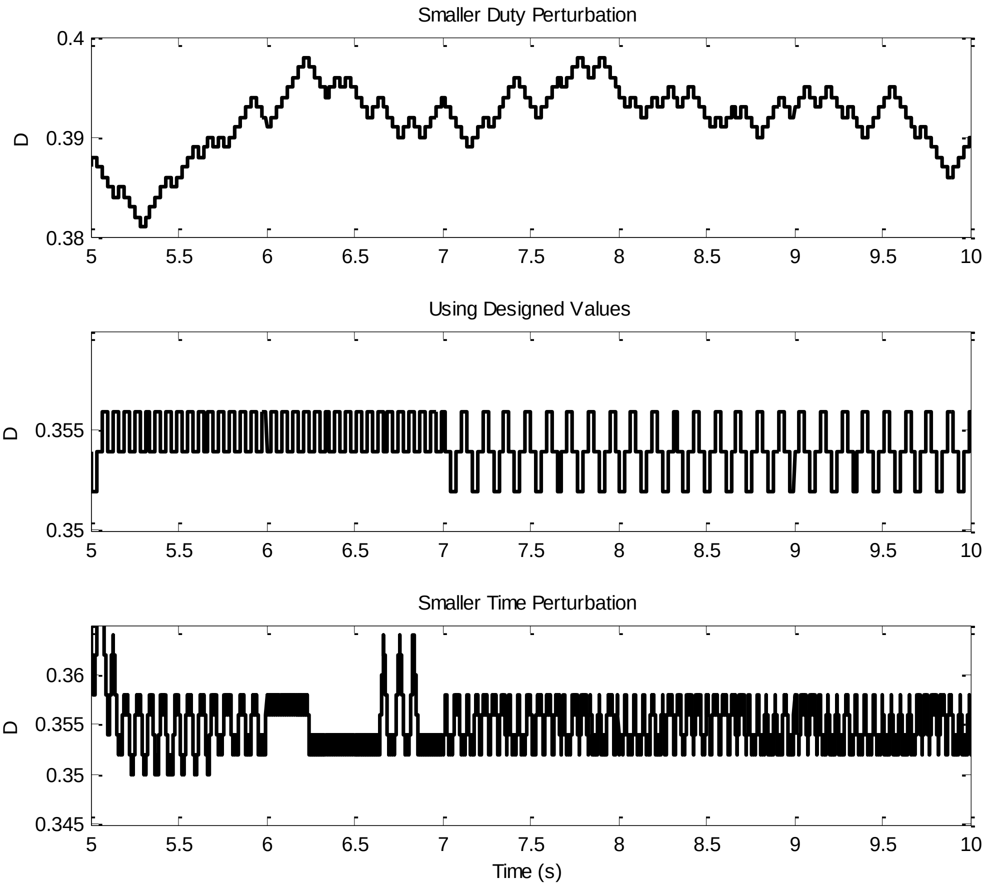

Figure (4.12) Duty waveforms zoom between t=5 and t=10 in Figure (4.11)

4.3.4. SUMMARIZING THE RESULTS

Design Guidelines for a hill climbing algorithm perturbation parameters have been proposed. These guidelines, which are based on dynamic analysis of a PV generator controlled by a boost converter, can be summarized as follows:

1. Calculation of perturbation value (δd_p): Firstly, the value of K_{pv} is calculated according to Equation (4.14), and by using the maximum value of the voltage and current at the reference condition provided by the data sheet. Then, the optimum perturbation value is calculated from Equation (4.24).
2. Calculation of perturbation time step (δT_p): the value of K_{pv} is calculated according to Equation (4.14). The minimum operating voltage value is used as the design point as it is the worst case as mentioned before. Consequently,

Equation (4.23 or 4.25) is used to calculate the minimum perturbation time, according to the availability of C_{in} in the circuit.

The V-I curves in the data sheet can be used to calculate (K_{pv}), which is used to calculate the design parameters δd_p and δT_p. Figure (4.13) shows a V-I curve similar to the data sheet curves. Point (a) is the design point for the parameter δT_p. K_{pv}, which can be found for this point by taking V_{PVa1}, V_{PVa2} around (a), which refers to points I_{PVa1}, I_{PVa2}, respectively, in the V-I curve. K_{pv} could be calculated from

$$K_{pv} = \frac{I_{PVa1} - I_{PVa2}}{V_{PVa1} - V_{PVa2}}$$

The same equation can be used with point (b) (V_{PVb1}, V_{PVb2}, I_{PVb1} and I_{PVb2}) to find K_{pv} which is used in δd_p design.

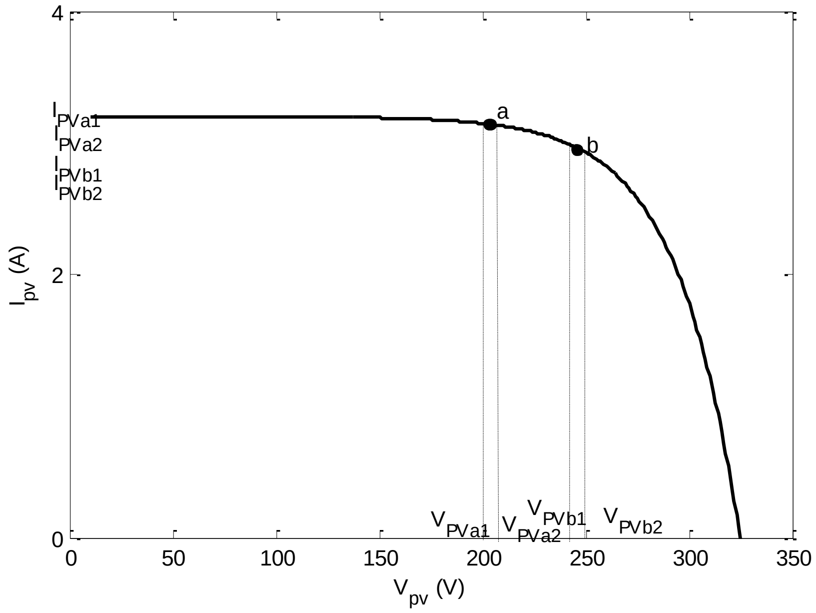

Figure (4.13) data sheet design of the perturbation parameters

4.4. PV CONTROL ALGORITHM WITH REDUCED POWER MODE

Direct duty ratio MPPT algorithms, as mentioned before in the literature are mainly based on P&O methods. In this work, an MPPT controller was developed which is based on variable step I.C. MPPT method. The algorithm has the following advantages:

1. It is based on the I.C. MPPT method, which is faster in tracking the maximum power than P&O and has a better dynamic performance under fast-changing atmospheric conditions. Furthermore, I.C. MPPT causes less oscillation around the maximum power point in the steady state, as it detects the maximum power according to the incremental conductance sign.
2. Variable step size will produce faster MPPT at rapidly changing conditions. The reason is that the duty ratio step size determines how fast the MPP is tracked. Fast tracking can be achieved with bigger step size, but the system will not operate at the MPP and will continuously oscillate around it. By contrast, when using a small step size, the system will be slow. In both cases, the tracking efficiency will be reduced. The variable step size method will make a tradeoff between the two sides, where the step size will be large when it is far away from the MPP, but will be small around the MPP, and approaches zero on the MPP. Therefore, the system will rapidly track the MPP and will not oscillate around it.
3. The proposed algorithm will also have the ability to work in a reduced power mode. In this mode, the supervisory controller determines the power output produced by the PV generator.
4. The proposed method is also very easy to be implemented in DSP.

In the following, the algorithm will be described and proved mathematically. Then, a verification of the method by simulation will be proposed. A reduced power mode will be added and simulation results will be presented.

4.4.1. VARIABLE STEP SIZE I.C. (V.S.I.C) METHOD

The incremental conductance method, one of the most widely used methods in the field of MPPT control, is based on the fact that the slope of the PV array power with respect to voltage is zero at the maximum power point, positive on the left of it, and negative on the right (see Equation (4.26)).

$$\frac{\mathrm{dP_{pv}}}{\mathrm{dV_{pv}}}\begin{cases} < 0 \text{ at the left of the MPP} \\ = 0 \text{ at the MPP} \\ > 0 \text{ at the right of the MPP} \end{cases} \qquad (4.26)$$

$$As\ P_{pv} = V_{pv} I_{pv}$$

$$then\ \frac{\mathrm{V_{pv}}}{\mathrm{I_{pv}}}\begin{cases} < \left|\frac{\mathrm{dV_{pv}}}{\mathrm{dI_{pv}}}\right| \text{at the left of the MPP} \\ = \left|\frac{\mathrm{dV_{pv}}}{\mathrm{dI_{pv}}}\right| \text{at the MPP} \\ > \left|\frac{\mathrm{dV_{pv}}}{\mathrm{dI_{pv}}}\right| \text{at the right of the MPP} \end{cases} \qquad (4.27)$$

where V_{pv}/I_{pv} is the instantaneous resistance (R_{pvss}), and dV_{pv}/dI_{pv} is the incremental resistance (R_{pv}) in the V_{pv}-I_{pv} curve. The absolute values of the instantaneous resistance (R_{pvss}) and the incremental resistance (R_{pv}) plotted against the steady state voltage (V_{pv}) are shown in Figure (4.14). The difference between R_{pv} and R_{pvss} (d_{inc}), which is the incremental conductance factor, against V_{pv} as described by Equation (4.31) is also shown in the same figure. R_{pvss}, R_{pv} and d_{inc} are in per unit (p.u.) values while V_{pv} is in (V).

$$d_{inc} = |R_{pv}| - |R_{pvss}| \qquad (4.28)$$

Figure (4.17) shows that as V_{pv} increases the absolute value of R_{pv} decreases while the absolute value of R_{pvss} increases. At the MPP, R_{pv} is equivalent to R_{pvss}. Therefore, d_{inc} is positive at V_{pv} less than the MPP, zero at the MPP and negative at V_{pv} more than the MPP. This is used to track the MPP in the regular fixed step size incremental conductance algorithm. In the proposed algorithm, this will also be used to change the step size of the duty ratio.

The incremental conductance factor (d_{inc}) is engaged to directly control the converter duty ratio, which will keep the controller simple and easier to implement in a DSP. The new duty ratio is calculated from Equation (4.29). The duty ratio perturbation (δd_p) is changed from zero to maximum according to d_{inc}. Figure (4.15) shows δd_p versus d_{inc}. As d_{inc} is higher than the maximum allowed perturbation, which is assumed to be *5* times the optimum perturbation (*.002* in this case), the perturbation will be limited to this value (*.01* in this case). However, if d_{inc} is less than the optimum perturbation (*.002*) the duty perturbation will not be considered. This means that the system has reached a maximum power point.

According to the discussion above, coefficient K_d could be calculated from Equation (4.30) as a function of the optimum perturbation parameter (δd_p=*.002* in this case).

$$D(t) = D(t - \delta Tp) - K_d d_{inc} \tag{4.29}$$

$$K_d = \frac{5 \times \delta dp}{V_{PVa1}/I_{PVa1}} \tag{4.30}$$

where V_{pva1} and I_{pva1} is the voltage and current respectively in point (a), which was shown in Figure (4.13).

Choosing the value of the maximum and minimum duty cycle perturbation is very important in order to have a stable and smooth tracking. The step time between every perturbation is constant at the optimum designed value (δT_p), which can be calculated from Equation (4.23). The designed value for this PV generator is *.03* s. The control algorithm is shown in Figure (4.16).

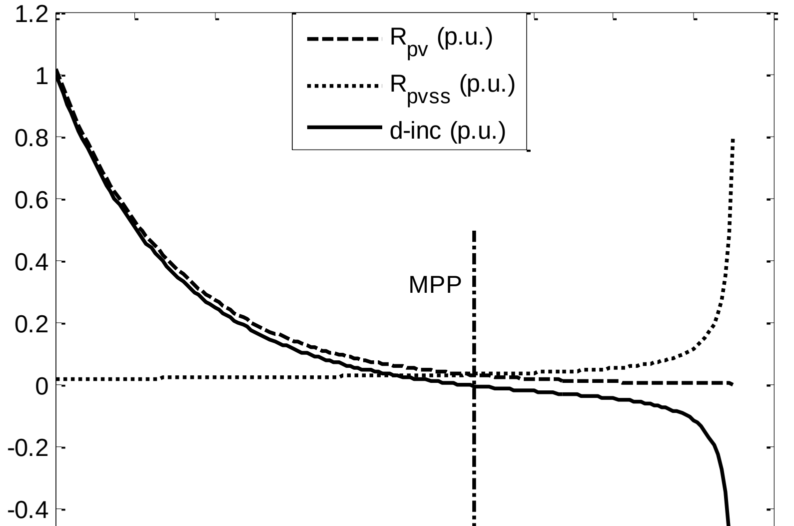

Figure (4.14) The basic idea for the V.S.I.S. method

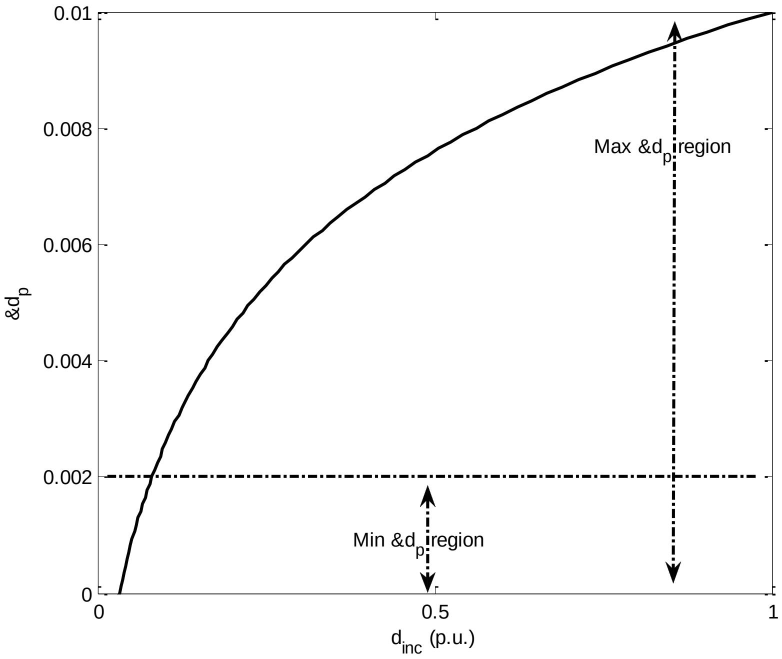

Figure (4.15) δd_p versus d_{inc}

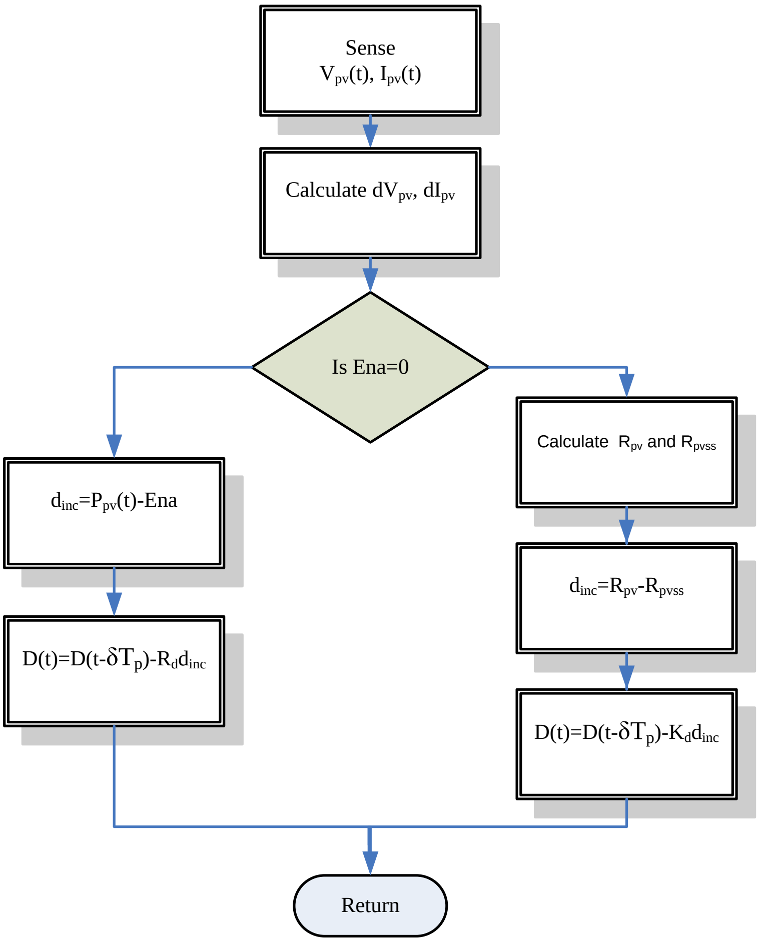

Figure (4.16) The proposed algorithm for V.S.I.C method

4.4.2. THE REDUCED POWER MODE

There is a supervisory controller which states the operational modes of the system and controls the power flow. Due to the following reasons, the supervisory controller may need to reduce the output power from the PV generator. These reasons can be summarized as follows:

1. The PV generator, due to high solar radiation or low temperature, can produce more power than the system rated value [179]. The power electronics have a rated value of power, but it is mainly slightly over rated. In spite of this, it will not be enough if the solar radiation is increased to high values or the temperature reduced to near zero ^{o}C. In winter both of these two conditions can happen. These conditions can last for seconds, minutes and even hours. This can be demonstrated by Figure (4.17), where the system has a rated power of (*950* W) in solar radiation (*1000* W/m2) and cell temperature of (*25* ^{o}C). The figure shows that when T_c is reduced to (*0* ^{o}C) the power is increased by (*13.68* %) of the rated value, but when S is increased to (*1200* W/m^2), the power is increased by (*22 %*). Furthermore, the power is increased by (*39 %)* when S is increased to *1200* W/m2 and T_c is reduced to *0* ^{o}C. Consequently, due to these conditions, the power has to be reduced around the rated values.
2. The wind generator output power can fluctuate more than the rated value due to the high wind speed stalling control. If the inertia is high, the fluctuation will be with a large time constant and it may also cause problems in the power electronics.
3. In the standalone mode, the power demand by the load might be less than the power produced by the generator, and the batteries are fully charged. The supervisory controller can shut down the generator and use the battery energy so the average power captured by the system will be reduced. Another solution is to use dump load to absorb the extra power from the system. The best solution is to reduce the output power from the PV generator, saving the battery energy, and eliminating the need for dump resistance.

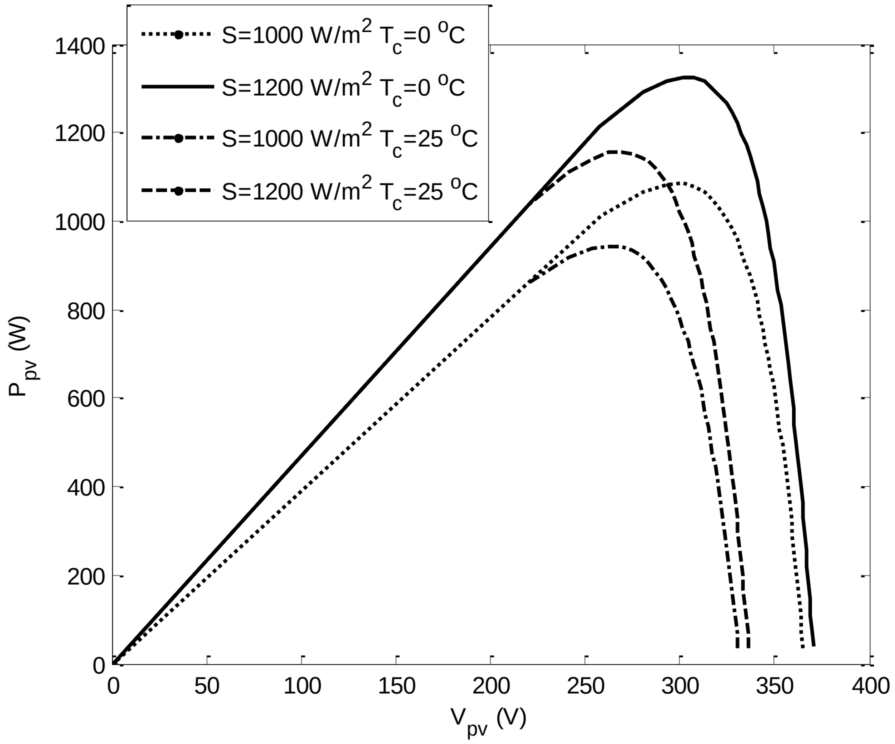

Figure (4.17) Overrating levels of the PV output pwer with decreasing in temperature and increasing in solar radiation.

The proposed reduced power mode is shown in Figure (4.16). The algorithm will choose this mode according to signal (Ena) in the figure. If a non-zero signal (Ena) is supplied from the supervisory controller the algorithm will drive the PV generator to the reduced power mode. The perturbation value and direction is calculated in this mode according to d_{inc} as the MPPT mode. Equation (4.31) shows how d_{inc} is calculated.

$$d_{inc} = P_{pv}(t) - Ena \qquad (4.31)$$

As P_{pv} (t) is the measured power and Ena is the target power reference supplied by the supervisory controller. The duty ratio can be calculated from Equation (4.32) where R_d is a scaling factor that can be calculated from Equation (4.33). Quantity maximum (d_{inc}) is the maximum expected reduction in power, which can be considered the rated value of the PV generator.

$$\mathrm{D(t)} = \mathrm{D(t - \delta Tp)} - R_{\mathrm{d}}\mathrm{d_{inc}} \qquad (4.35)$$

$$\mathrm{R_d} = \frac{5\times\delta\mathrm{dp}}{\mathrm{maximum}\ (\mathrm{d_{inc}})} \qquad (4.33)$$

4.4.3. THE PROPOSED V.S.I.C. METHOD VS THE P&O ALGORITHM

The P&O MPPT algorithm described before in Figure (4.9) is used to be compared with the proposed V.S.I.C. MPPT algorithm. The V.SI.C. algorithm has the advantage of not oscillating around the steady state as shown in Figure (4.18). This figure is based on simulating the PV system described by Figure (4.1). This advantage of non-oscillatory steady state also increases the MPPT tracking efficiency.

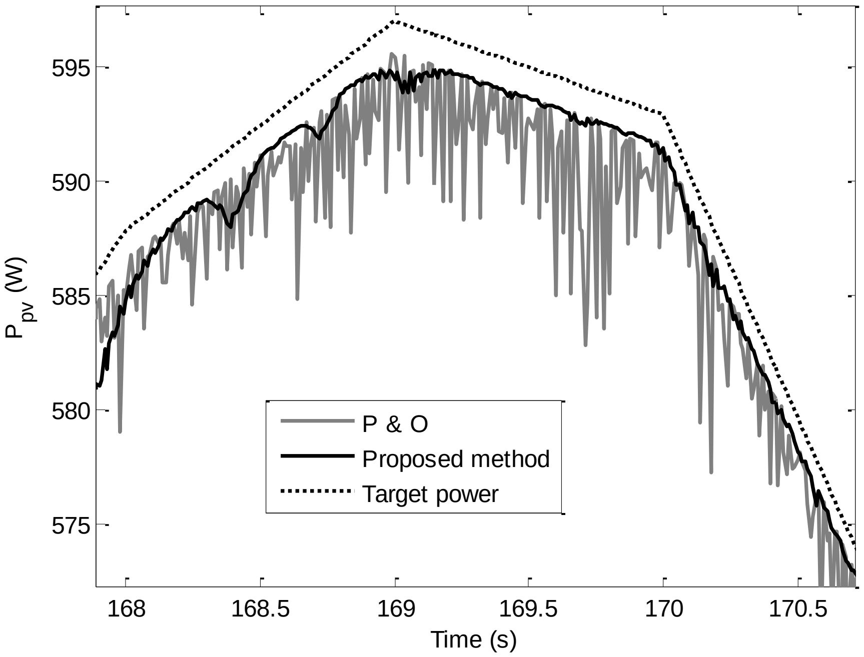

Figure (4.18) The PV output power produced by the proposed V.S.I.C algorithm compared to The P&O algorithm

To demonstrate the advantage of fast tracking with variable step with respect to fixed step algorithms, the P&O, I.C. and V.S.I.C. algorithms were applied to the system shown in Figure (4.1). A step change was applied to the PV generator to reveal fast-changing atmospheric conditions. The step was made very big to make the change in power as clear as possible. The change in the duty ratio applied by the three control algorithms and the produced output power are shown in Figure (4.19). It is clear how fast the V.S.I.C. is, with respect to the other fixed speed algorithms.

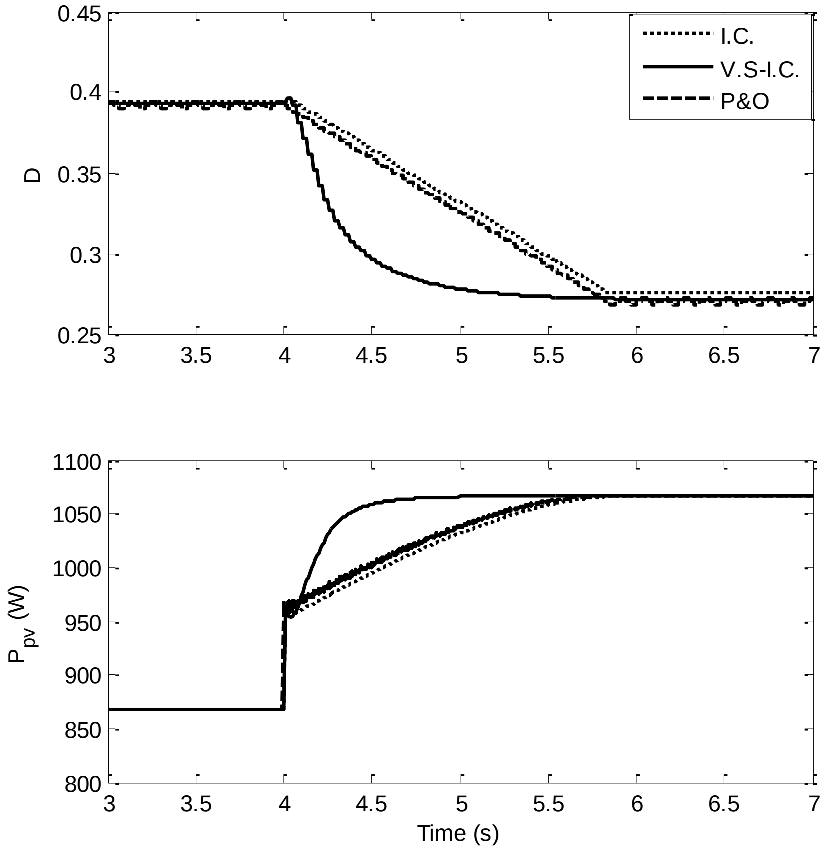

Figure (4.19) The proposed V.S.I.C tracking speed compared to I.C. and P&O

4.4.4. DYNAMIC SIMULATION RESULTS

The simulation verification through real solar radiation (S) data is shown in Figure (4.20). The data were collected at Durham University in rapidly changing weather conditions to verify the ability of the MPPT algorithm in these conditions. The ambient temperature is considered constant at *25* ^{o}C. The system shown in Figure (4.1) was simulated using Matlab/Simulink with PLECS software. The PV generator parameters are as proposed in Table (4.1).

The solar radiation is changing between *400* W/m^2 and *900* W/m^2 in a time period of *215* s. The target power against the simulation output is shown in the Figure (4.20), which shows that the target power is accurately tracked with a very small error. The voltage (V_{pv}) in the output of the PV generator has some large changes as the solar radiation changes rapidly, as shown between *40* s and *60* s in the time scale. This happens because the algorithm provides the maximum duty ratio perturbation as the operating point is rapidly moving away from the maximum power point. However, from *0* s to *30* s and *70* s to *100 s*, the changes in the solar radiation are slow, and so the variation in V_{pv} is very small. In these cases, the slow change in solar radiation makes a slow movement of the maximum power point and small duty ratio perturbations (d_{inc}). In many parts of the simulation, the variations are almost terminated when the solar radiation is almost constant. This can be seen between *10* s and *18* s in the time scale. The MPPT efficiency according to the rapidly changing input simulation weather data is more than *99%*.

The same system and part of the data used before (the first *100* seconds) is used to verify the reduced power mode. As shown in Figure (4.21), between *20* s and *70* s, the reduced (curtailed) power mode was applied. The controller drives the system accurately into and out from the reduced power mode. Furthermore, whatever the changes in solar radiation the power was kept constant at the target value.

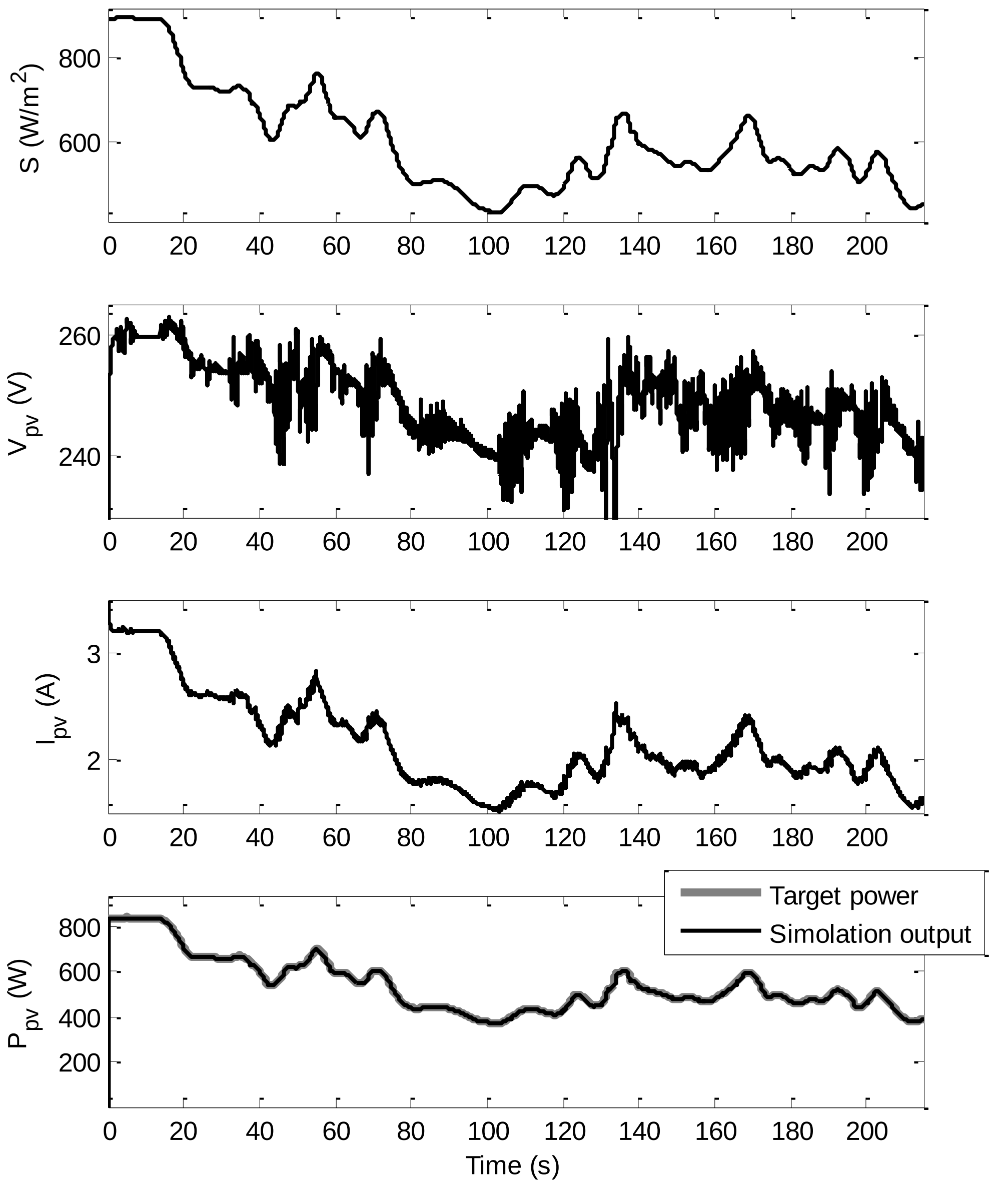

Figure (4.20) Dynamic simulation results verifyng the accuracy of the proposed V.S.I.C.method in the MPPT mode of operation

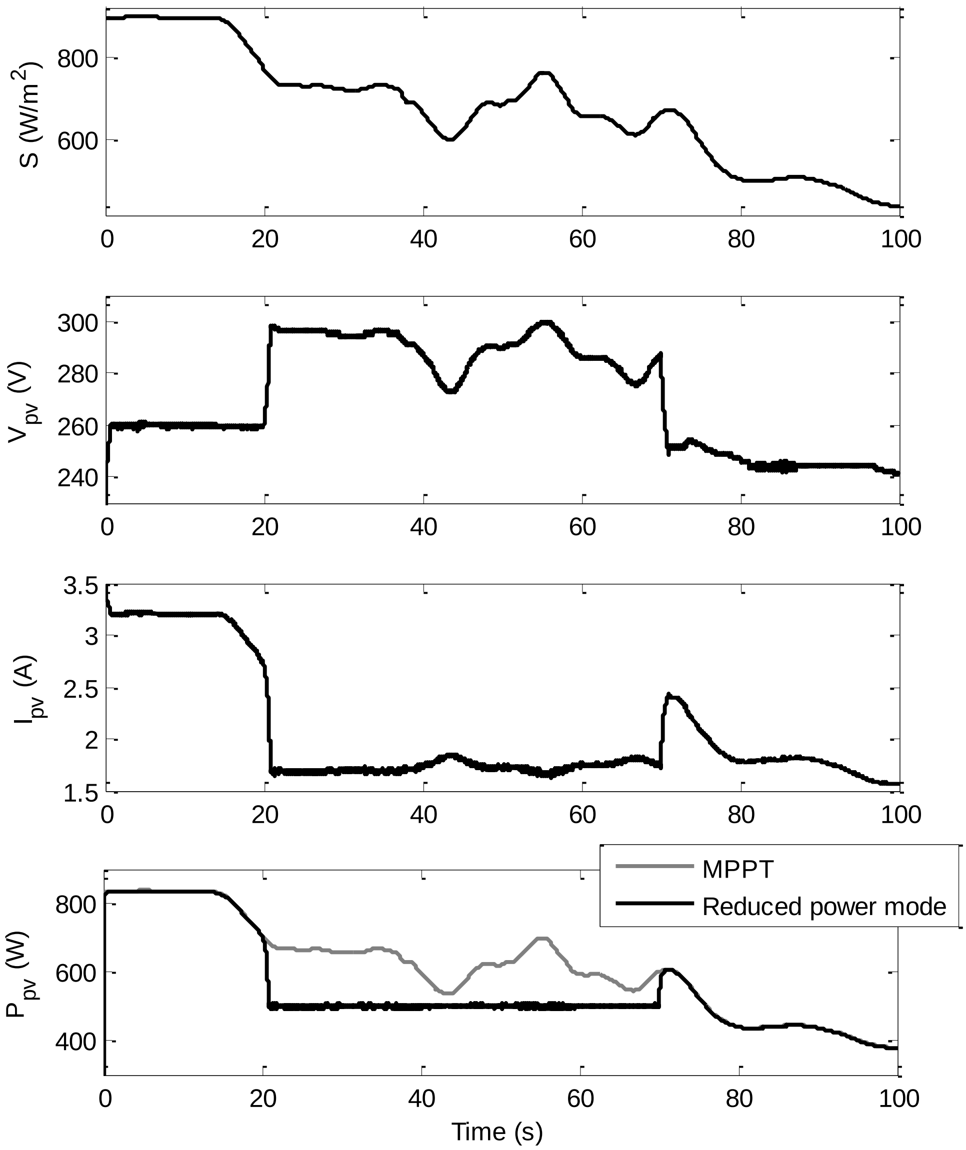

Figure (4.21) Dynamic simulation results verifyng the accuracy of the proposed V.S.I.C. method in the reduced power mode of operation

4.5. EXPERIMENTAL VERIFICATION

The PV controller proposed in this study is simple and easy to implement. Furthermore, it deals with two operational modes: MPPT and reduced power modes. The two algorithms are based on variable step perturbations of the duty ratio, which increases the tracking speed and efficiency. To verify the control algorithm, a laboratory test is carried out and Figure (4.22) shows a picture of the test rig setup. A simplified block diagram, Figure (4.23), outlines the hardware arrangement.

An Agielnt-E4350B solar simulator is used to emulate the PV generator. A single module described in Table (4.1) is simulated by the solar simulator to illustrate the control method. The solar simulator was remotely controlled from a laptop computer as shown in Figure (4.22). The control and data acquisition are implemented using a desktop computer hosting a dSPACE real time control system which can be programmed in the Matlab/Simulink environment [172]. The system and the control parameters are the same as those used in simulation.

Figure (4.24) shows the experimental results as the characteristics of the PV simulator were changed from (solar radiation=*500* W/m^2, *40* ^{o}C) at (time=*41* s) to (solar radiation=*1000* W/m^2, *25* ^{o}C), and then the characteristics were changed back again to the last values at (time=*91* s). The output results demonstrated that the proposed control algorithm tracks the maximum power points with accurate and fast response. In the figure, the measured power tracks the target power which is the maximum power according to the solar radiation and temperature conditions.

To verify the V.S.I.C method speed, it was compared to the fixed regular I.C. as illustrated in Figure (4.25). As shown in the figure, the duty ratio reaches a point around the optimum value very fast in the proposed method in comparison with the ordinary method.

The experimental verification of the reduced power mode is shown in Figure (4.26). First, the controller was in MPPT mode under (solar radiation=*1000* W/m^2 and *25* ^{o}C temperature). Then, the reduced power mode was applied at (time=*41* s) with a constant target power (P_{pv}=*50* W). At (time= *83* s), the MPPT mode was applied to the system. The results show that: the proposed controller accurately works in the reduced power mode as the output power was kept in the target value.

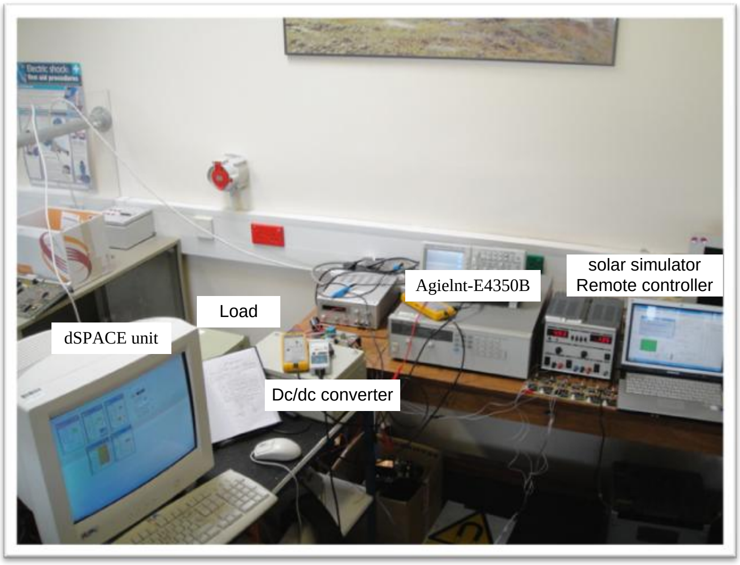

Figure (4.22) Laboratory test rig

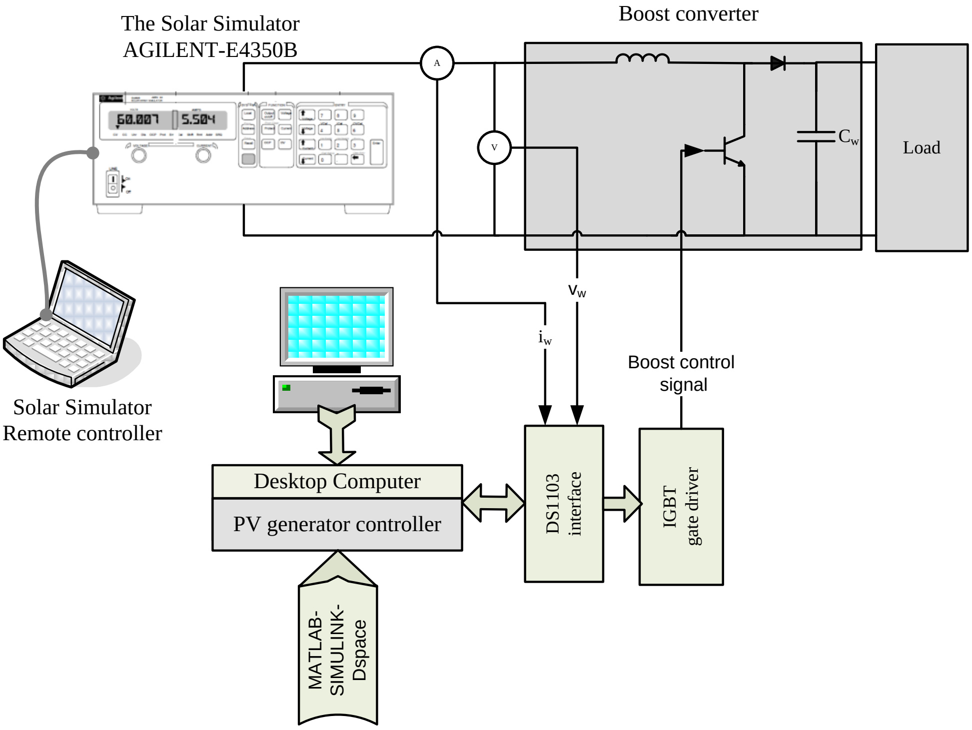

Figure (4.23) Arrangement of laboratory system

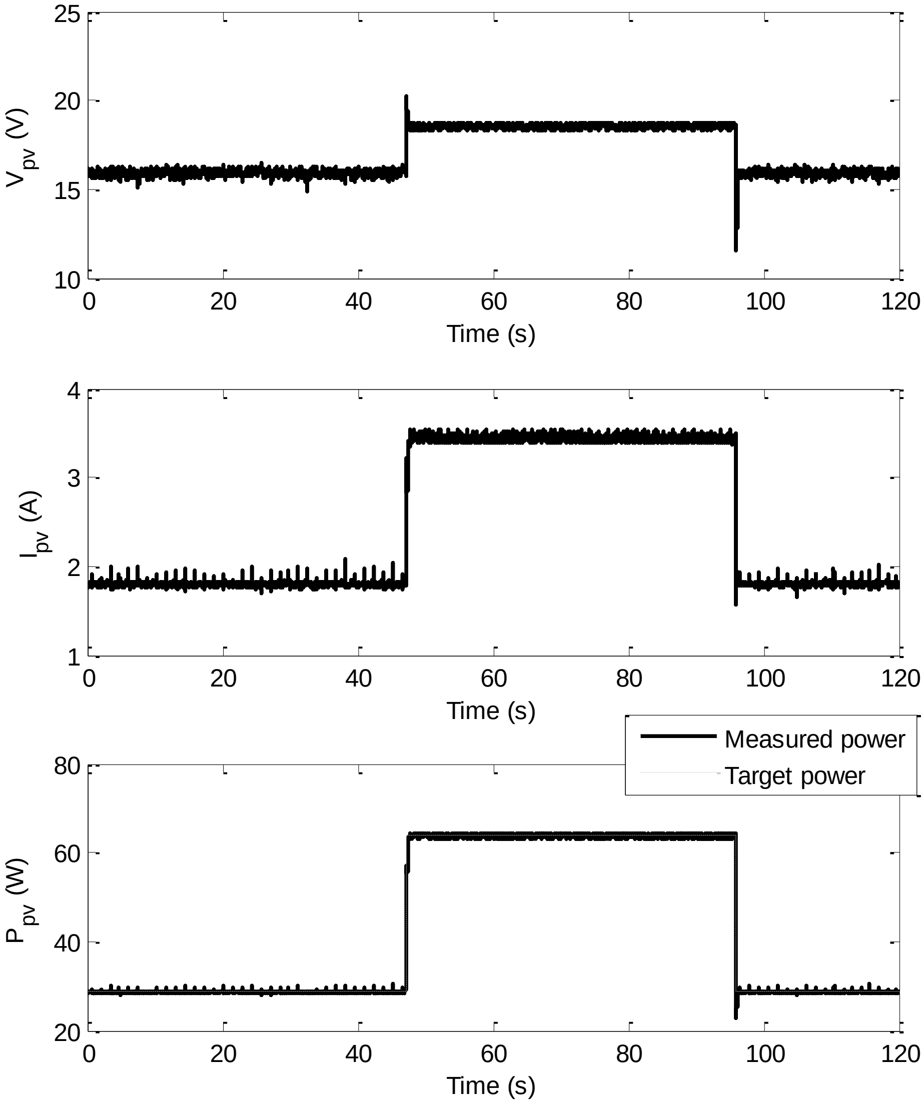

Figure (4.24) Experimental results for MPPT mode of operation as the solar radiation and temperature change from (*1000* W/m^2 and *25* ^{o}C) to (*500* W/m^2 and *40* ^{o}C) respectively

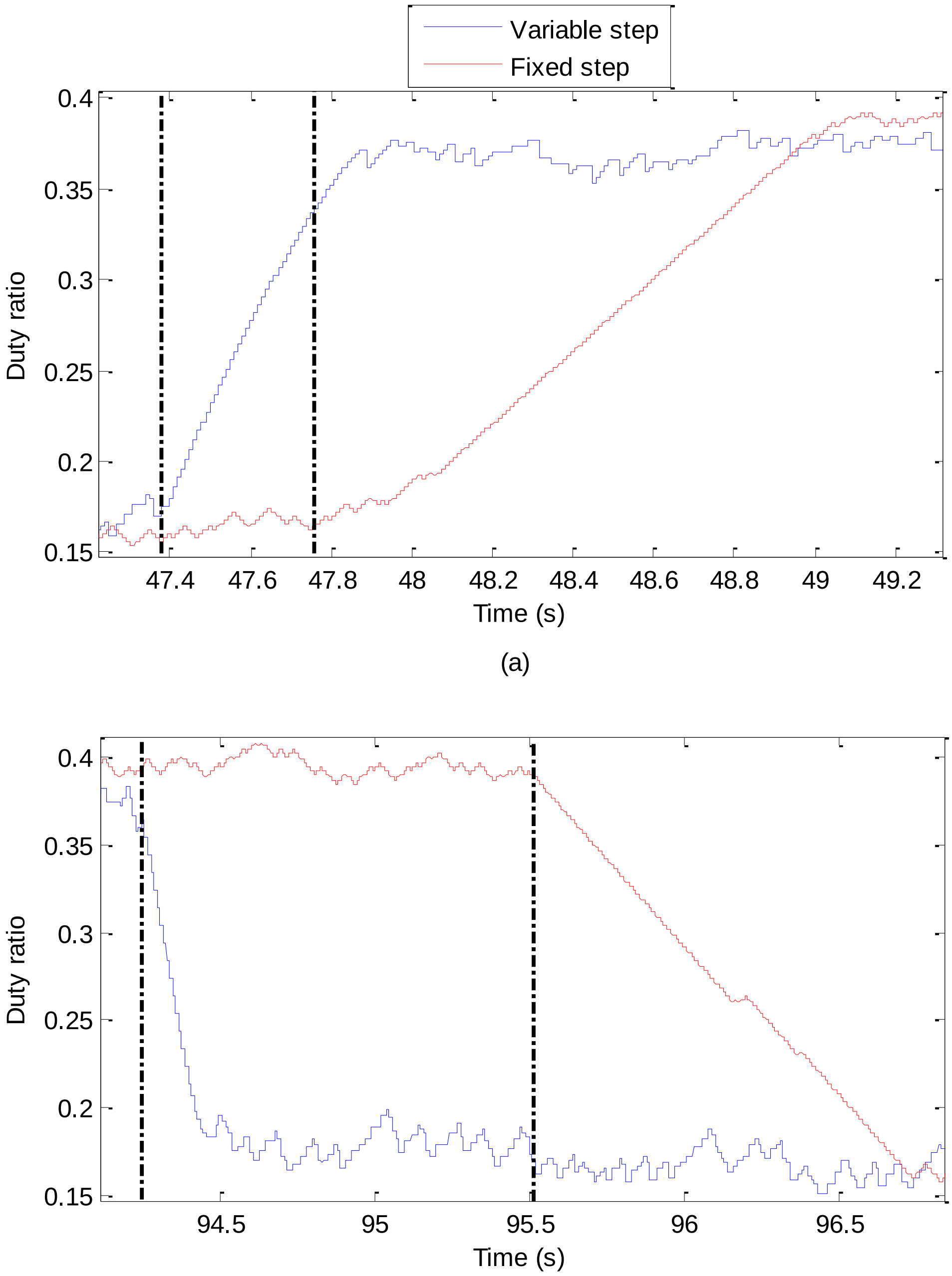

(a)

(b)

Figure (4.25) Proposed V.S.I.C control against fixed step I.C.

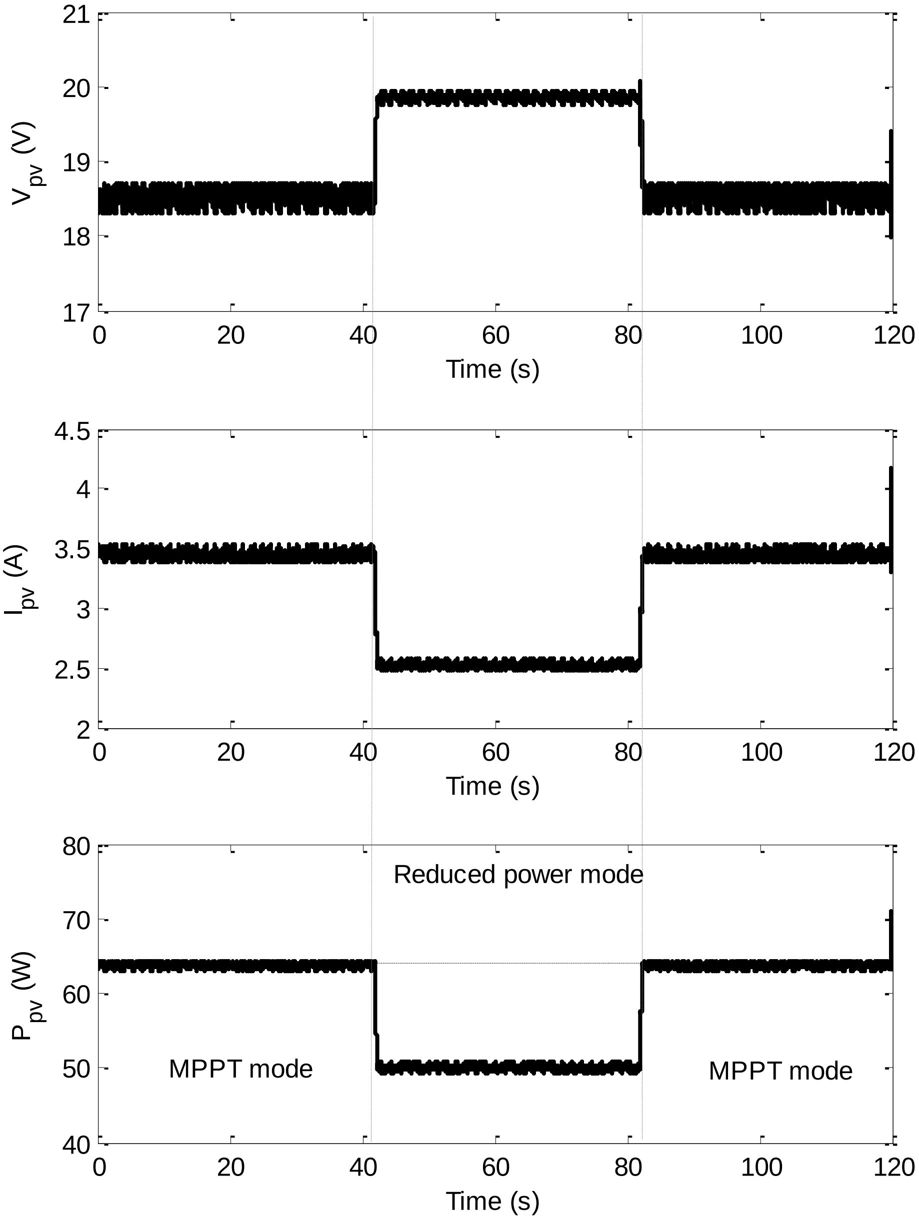

Figure (4.26) Experimental results for reduced power mode of operation as the solar radiation and the temperature *(1000* W/m^2 and *25* ^{o}C*)* respectively

CHAPTER (5)
INVERTER CONTROL

5.1. INTRODUCTION

As the market for small-scale renewable energy systems is rapidly increasing, the need for power electronic converters also increases. The inverter is necessary in the system to produce a sinusoidal wave to supply the ac load or connect to the grid. The dc/ac single phase inverters are used to interface the sources with the single-phase grid. The single-phase H-bridge inverter is a simple circuit topology with a small number of components. Furthermore, it is simple to control but has one disadvantage as manifested in the dc injection problem.

The proposed system in this study can be connected to the utility grid; therefore there are quality standards for such aspects as low THD, elimination of the dc component injected into the grid and active and reactive power control. The IEEE-*929* standard permits a limit of *5%* for the THD in the output current, with individual limits of *4%* for each odd harmonic from *3*rd to *9*th and *2%* from *11*th *to 15*th. However, the dc injection is limited to *0.5%* of the rated output current. The European IEC61727 suggests similar standards with dc injection limits less than *1%*. The dc current injection in England is limited to *20* mA, which is less than *.1%* for the proposed inverter. Other standards in the world have fewer restrictions and are easier to cope with. In this study, the work will focus on fulfilling these strictest standards. The proposed system is shown in Figure (5.1), where an H-bridge inverter interfaces a renewable energy source with the grid. The dc renewable energy source is modelled as a dc voltage source.

In this work, a small-scale H-bridge inverter is proposed to supply the power from the renewable sources on the dc side to the grid or to the ac load. In Section (5.2), a peak current controller (p.c.c.) is proposed first for PWM and output current control. Then, a grid connected control method is proposed in Section (5.3), based on the newly developed standalone mode control. This is also based on p.c.c., which is described in Section (5.2), to reduce the overall complexity of the system controller. The simulation at the end of this section demonstrates the method. At the end of this chapter, Section (5.4) suggests a method to remove the dc component of the inverter output current with simulation and experimental verifications.

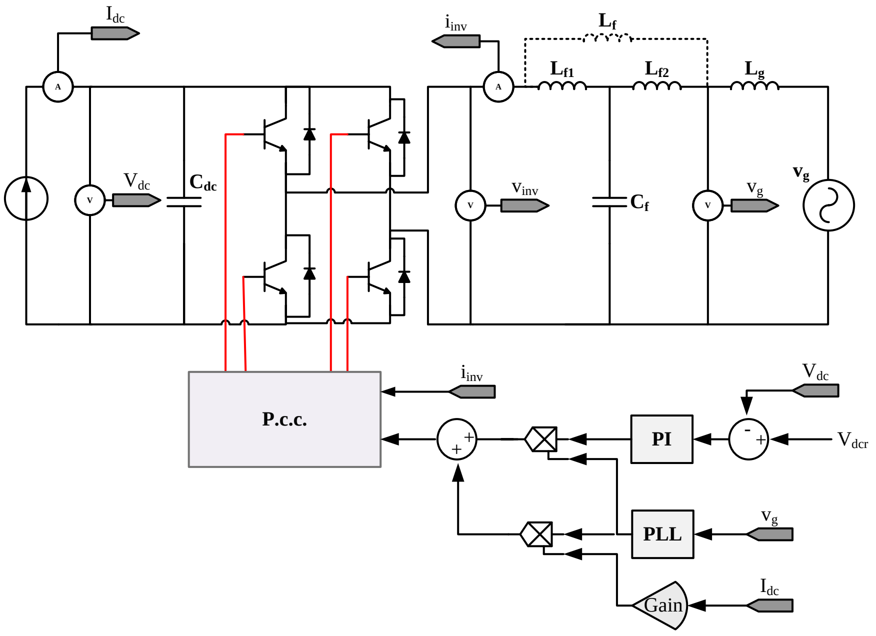

Figure (5.1) Grid-connected H-bridge inverter control and circuit

5.2. THE PEAK CURRENT CONTROL METHOD

As mentioned before in Chapter (2); applying PI controller is very common with small-scale inverters. However this kind of controller has relatively poor performance due to the steady state error with tracking the sinusoidal reference. Furthermore, this controller is unable to reject the noise in the current signal. With hysterias controllers, there would be high bandwidth of harmonic spectrum. The other solution is to use more complicated methods which need more analysis with faster DSPs.

A peak current control (p.c.c.) algorithm will be developed and modified to meet the international standards for the current wave quality. The following section develops a direct control method which is a new modification of the p.c.c method applied for single phase H-bridge inverters.

Peak current control was applied from the beginning to control power electronics, mainly with choppers [180]. It is normally implemented with dc/dc converters in analogue or digital forms [181]. The method in a simple form could be implemented by a clock to make the switching frequency constant. It could be described as follows: as the measured feedback current is less than the reference value the switch is on. The switch would be off when the current reaches the reference value. This method could produce instability to the system [182, 183]. Therefore, a compensating saw tooth signal is added or subtracted to the reference current control signal [184]. The slope of the saw tooth signal is selected to maintain stable operation and to provide as little oscillation as possible [185].

A simplified block diagram shows that a primary kind of controller is shown in Figure (5.2) [186, 187]. The method is as simple as the hysteresis current controller with constant frequency control. Furthermore, it has an automatic feed forward compensation and sample by sample current limiting capability.

Figures (5.3) and (5.4) show a part of the output current and voltage signals with and without slope compensator. It is clear that without slope compensator (Figure (5.3)); the inductor current is distorted due to the instability during some switching periods. Using the saw tooth slope compensator, the switching is well educated and the instability could be compensated. As a result, the current output would have less noise and lower THD.

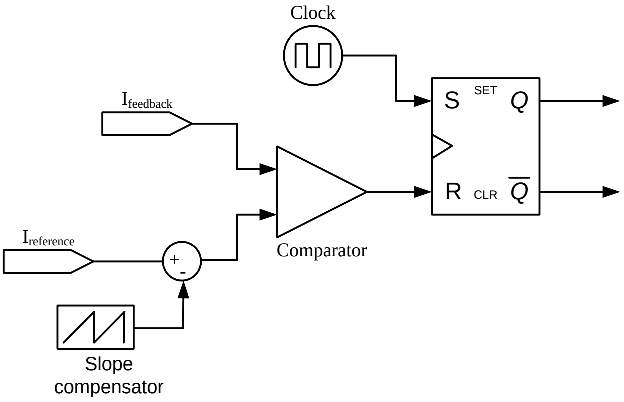

Figure (5.2) A simplified block diagram for p.c.c

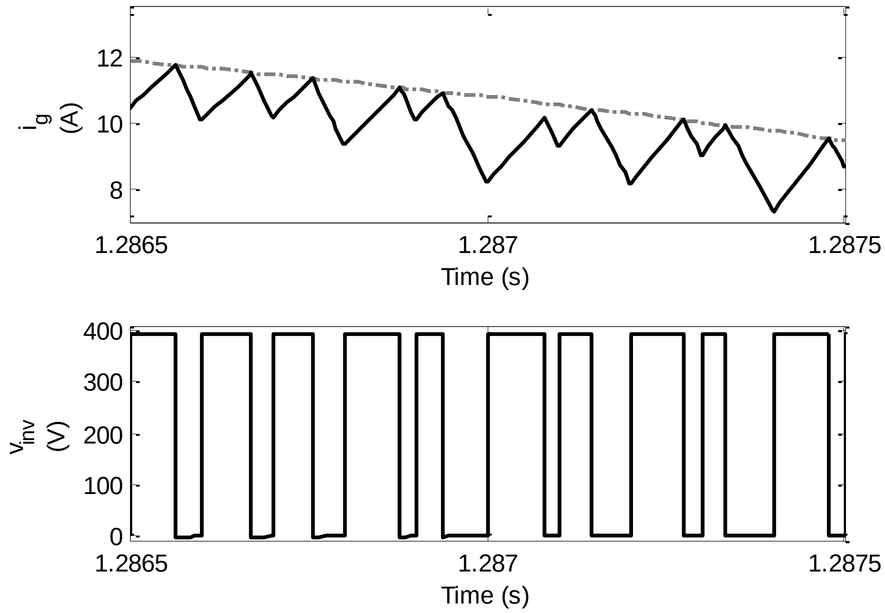

Figure (5.3) Inductor (L_f) current and output voltage waveforms without slope compensation

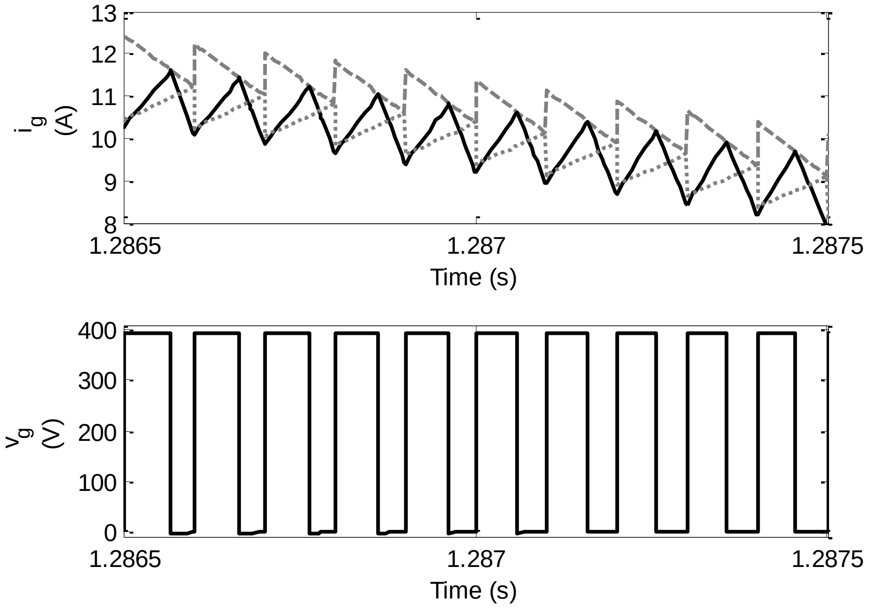

Figure (5.4) Inductor (L_f) current and output voltage waveforms with slope compensation

To design the slope value, which will compensate for the instability of the p.c.c., the circuit shown in Figure (5.4) can be analysed using simplified differential equations. All the elements in the circuit are considered ideal with L-filter (L_f). Furthermore, the dc voltage control is considered stable and fast, so the dc side is assumed to be a constant voltage source. For a unipolar switching pattern, there will be two modes of operation, the first mode with the dc voltage source connected and the other with the dc voltage disconnected, as shown in Figure (5.5).

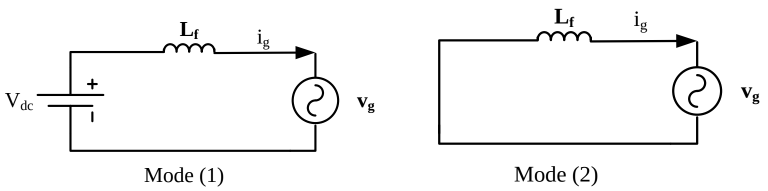

Figure (5.5) H-bridge inverter modes of operation with unipolar PWM

The inductor current, which is the inverter output current, is plotted for a single switching period T_s. The rising current edge during mode (1) has a slope value of m_1, and the falling current edge has a slope value of m_2. The compensating slope value will be assigned with the symbol m_c. These slopes are shown in Figure (5.6).

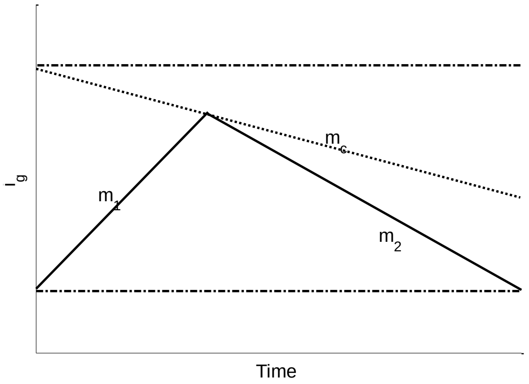

Figure (5.6) m1, m2 and mc in a one period of the inductor current

For mode (1):

$$L_f m_1 = L_f \frac{di_g}{dt} = V_{dc} - v_g \tag{5.1}$$

Fore mode (2):

$$L_f m_2 = -L_f \frac{di_g}{dt} = v_g \tag{5.2}$$

Equations (5.1) and (5.2) are only applicable for the first half of the sine wave, but the result is applicable for the whole sine. Using the results in references [188-191], the compensation ramp added for stable current loop can be found from the following equation:

$$m_c > \frac{1}{2}(m_2 - m_1) \tag{5.3}$$

Using Equations (5.1), (5.2) & (5.3), then:

$$m_c > \frac{1}{2Lf}\left(-V_{dc} + 2v_g\right) \tag{5.4}$$

Therefore, v_g in Equation (5.4) varies with time as it is a sine wave. Therefore, to assure stability of the p.c.c.:

$$m_c > \frac{1}{2L_f}(\text{maximum}\left(-V_{dc} + 2v_g\right)) \tag{5.5}$$

$$\xRightarrow{\text{Then}} m_c = \frac{1}{2L_f}\left(2V_{gmax} - V_{dc}\right) \tag{5.6}$$

From the last equation, it can be easy to design the compensating slope (m_c).

The proposed unipolar modified p.c.c strategy is shown in Figure (5.7). The method is the same as the one described before in Figure (5.2). Two S-R flip-flops are used to switch the four switches of the inverter. A slope compensator is added to the reference current ($I_{reference}$) and compared to the feedback signal ($I_{feedback}$) to switch on IGBTs (1, 3). To switch IGBTs (2, 4), the slope compensator is subtracted from the reference current and compared to the feedback current. The output voltage produced by this switching orientation is unipolar.

The system shown in Figure (5.1) was simulated using Matlab/Simulink with the PLECS software. At this stage, only the L-filter (L_f with the dash line) is used in the simulation process. The forward voltage and on-state resistances were taken into account with the H-bridge inverter IGBTs. The applied switching frequency is *10* kHz with a *2* kW inverter rating. The output voltage and current and their THD are shown in Figure (5.8). It shows that the inverter output voltage is unipolar and the THD is *8%*. The output current has a THD of less than *5.8* % which is higher than the required international standards. The harmonic spectrum shows some low harmonics with the switching harmonics in this case. Figure (5.9) shows how the output current tracks its reference accurately.

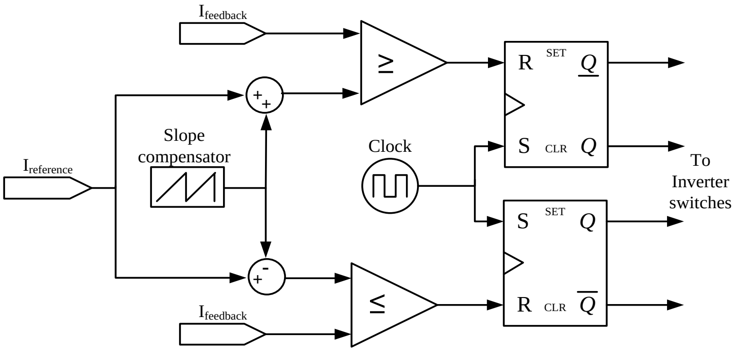

Figure (5.7) The proposed p.c.c. controller

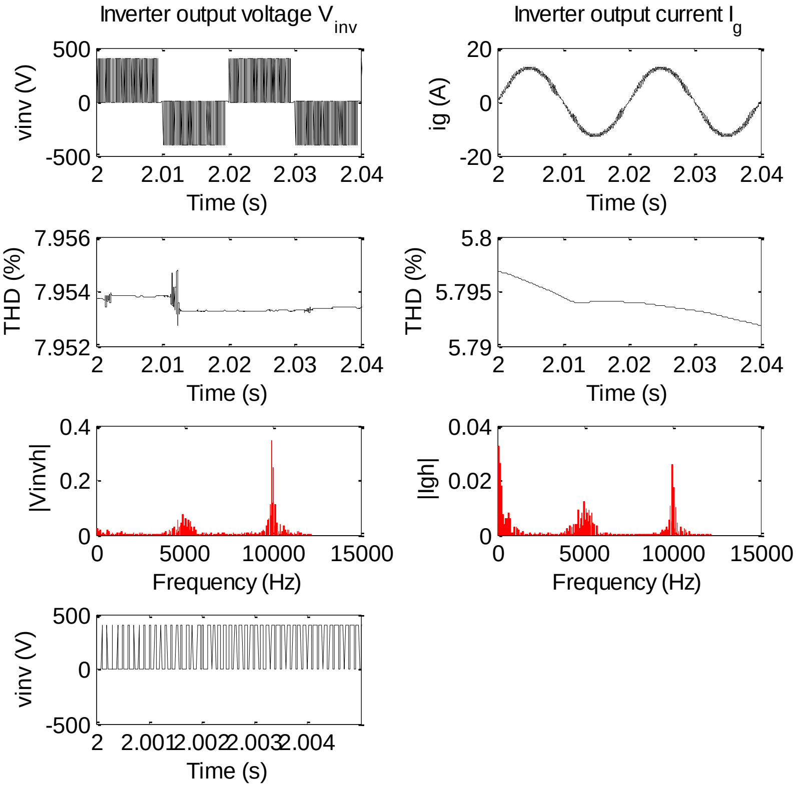

Figure (5.8) Inverter output current and voltage waveforms, THDs and harmonic spectrums (p.u. values)

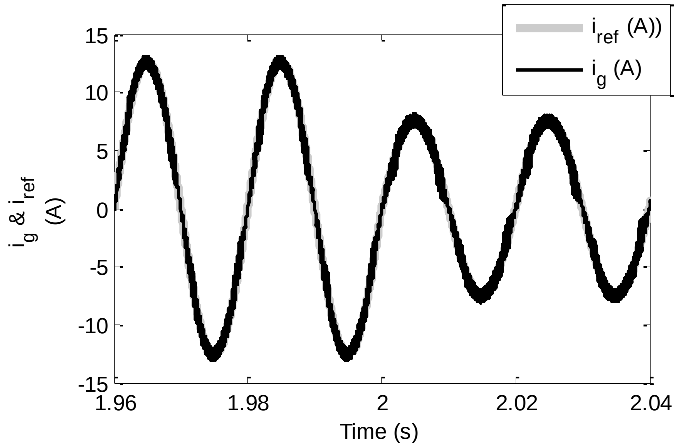

Figure (5.9) i_g versus i_{ref} with L-filter

5.2.1. LCL-FILTER

Due to the grid inverter’s switching operation, high frequency harmonics are produced, which could cause trouble to the power system. A line filter is needed in the inverter output in order to remove or reduce the harmonics to meet the standard values. Passive line filters are normally used as L or LCL filters. The LC filter is not desired with grid-connected inverters, as the resonance frequency of the filter would be largely affected with the grid inductance [192]. To choose between L and LCL filters, Figure (5.10) shows the frequency response of both filters. The figure was plotted using values of (5 mH) for the L filter and (3 mH, 3μF, 1.5 mH) for the LCL filter. The transfer functions used for L and LCL filters are as follows in Equations (5.7) and (5.8) respectively. The two filters were chosen to have nearly the same attenuation below the resonance frequency.

$$G_L = \frac{1}{sL_f} \tag{5.7}$$

$$G_{LCL} = \frac{1}{L_{f1}C_fL_{f2}s^3+(L_{f1}+L_{f2})s} \tag{5.8}$$

The figure shows that as the frequency is more than the resonance frequency, the LCL-filter has more attenuation compared to the L-filter. The following advantages can be concluded for the LCL filter [193-195]:

1. The voltage drop would be less as (L_{f1}+L_{f2} < L_f) for the same harmonic attenuation.

2. The power factor control range would be higher.
3. The total cost of the filter would be less.
4. The size of the filter would be less.

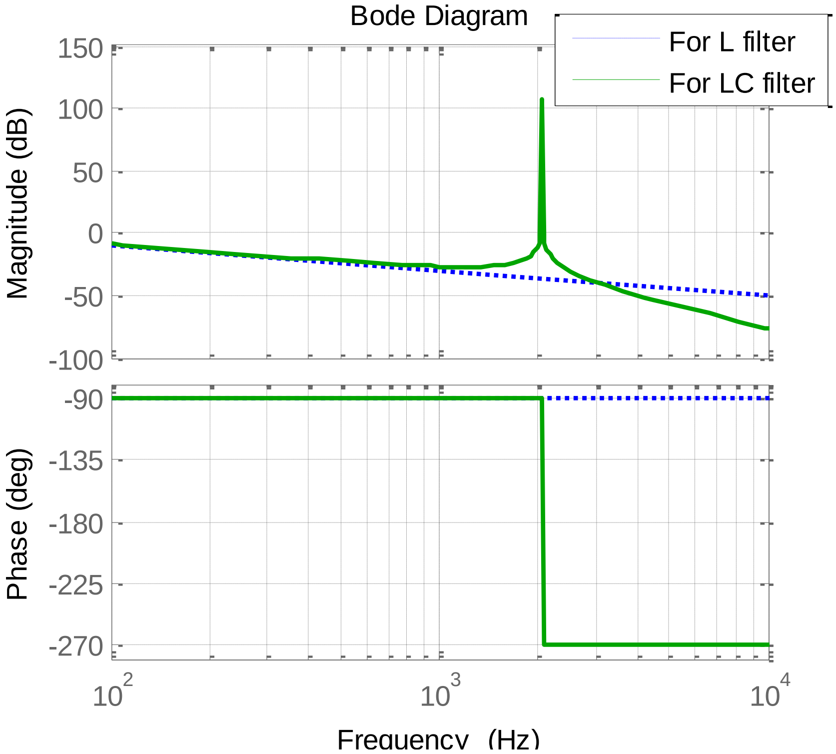

Figure (5.10) The L-filter versus the LCL-filter

The LCL-filter design is not an easy task as many research papers were heading towards this direction. Due to the notch around the resonance frequency, this filter may cause instability problem and it needs to be designed carefully. A detailed design procedure taking into account the system stability is not considered in this study. Following the results of these references [196], the values of the filter can be found through the following equations:

$$L_{f1} = 2L_{f2} \tag{5.9}$$

$$C_f = 0.05C_{base} \tag{5.10}$$

C_{base} is the base capacitor for the system. According to these equations, the values of 3 mH, 3 µF and 1.5 mH were considered to L_{f1}, C_f and L_{f2} respectively.

The system shown in Figure (5.1) was simulated in this stage with the LCL-filter only. The results of the simulation are shown in Figure (5.13) compared to the results that were proposed before in Figure (5.8); it is obvious that the current output of the LCL-filter has better THD. The measured THD is *3.4*% in case of the LCL-filter, while it is 5.8% in the case of the L-filter. The LCL-filter case complies with the limit imposed by the IEEE 929 standard, which is *5%*. Figure (5.12) also shows that the current smoothly tracks the reference values with different current values. In spite of this result, the 3rd harmonic is still relatively high, around *4%* of the fundamental component, which is on the edge of the international standards. Increasing the switching frequency, for example, to *12* kHz, would largely reduce the THD. This would keep the p.c.c. controller in the simple form. However, this would increase the switching losses. Another way is to implement a selective harmonic elimination technique for further THD reduction, keeping the switching frequency to *10* kHz. This kind of technique can be implemented because there is a limited number of harmonics with p.c.c., compared to other techniques such as hysteresis current control. In the following subsection, the selective harmonic elimination will be proposed.

5.2.2. SELECTIVE HARMONIC ELIMINATION

In a hysteresis controller, the ripple frequency bandwidth occupies a high range while the p.c.c. ripple bandwidth is limited to the low odd harmonics as the 3rd, 5th, and 7th. This would make selective harmonic elimination easily implemented in the p.c.c. case. Figure (5.13) shows the p.c.c with selective harmonic elimination. A PIS regulator was applied, as the one described In the letrature (Chapter 2), to eliminate the specified harmonics.

The results of the simulation with and without applying selective harmonic elimination are shown in Figure (5.14). The figure shows that before applying selective harmonic elimination there are high *3rd, 5th and 7th* harmonics, and the THD is *3.4%*. After the application of selective harmonics elimination, the *3rd, 5th* and *7th* are nearly eliminated while the THD is reduced to less than *1%*. These results apply for the rating current of the inverter. The selective harmonics elimination is very effective in this case.

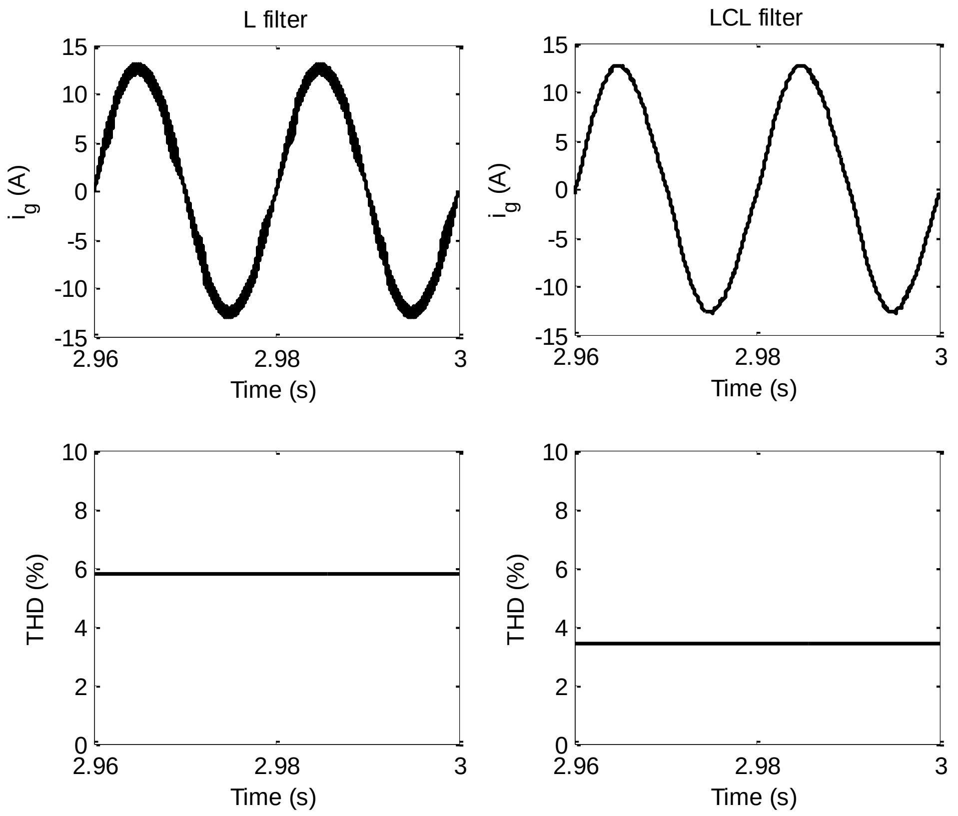

Figure (5.11) Current output and THD using LCL-filter compared to L-filter,

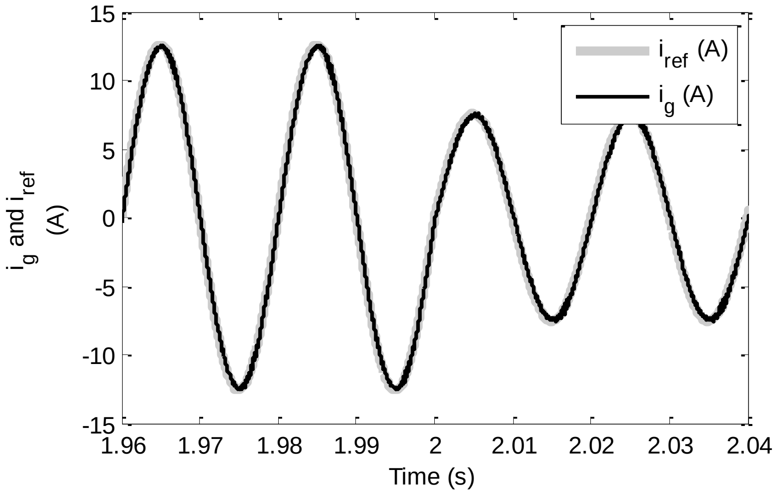

Figure (5.12) The proposed method tracking performance with LCL-filter.

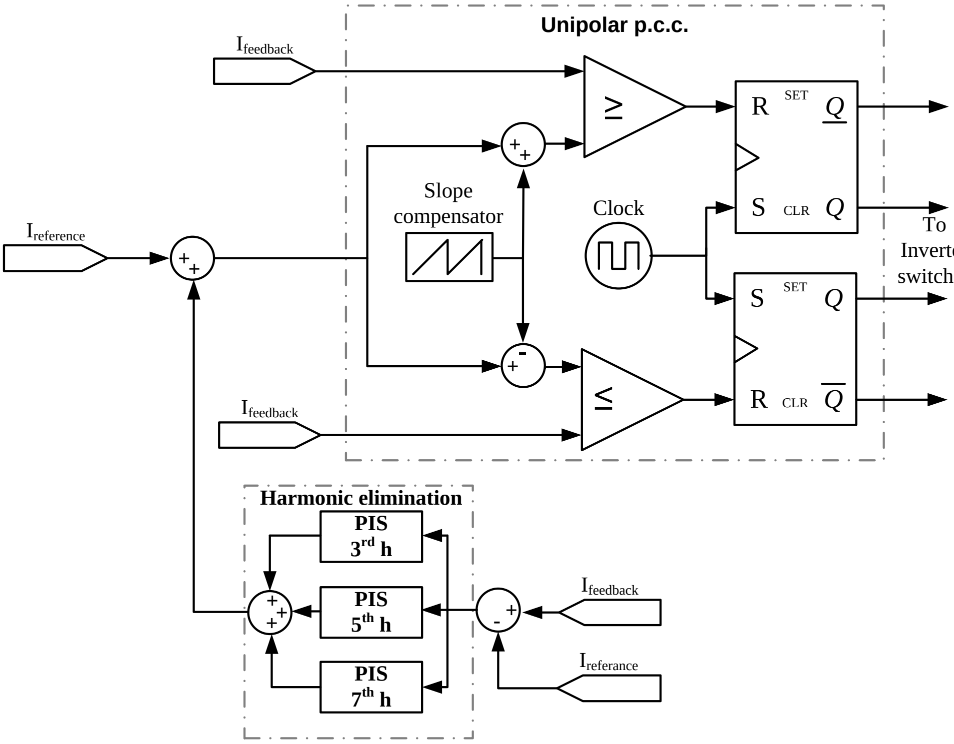

Figure (5.13) The proposed p.c.c. method with selective harmonic elimination

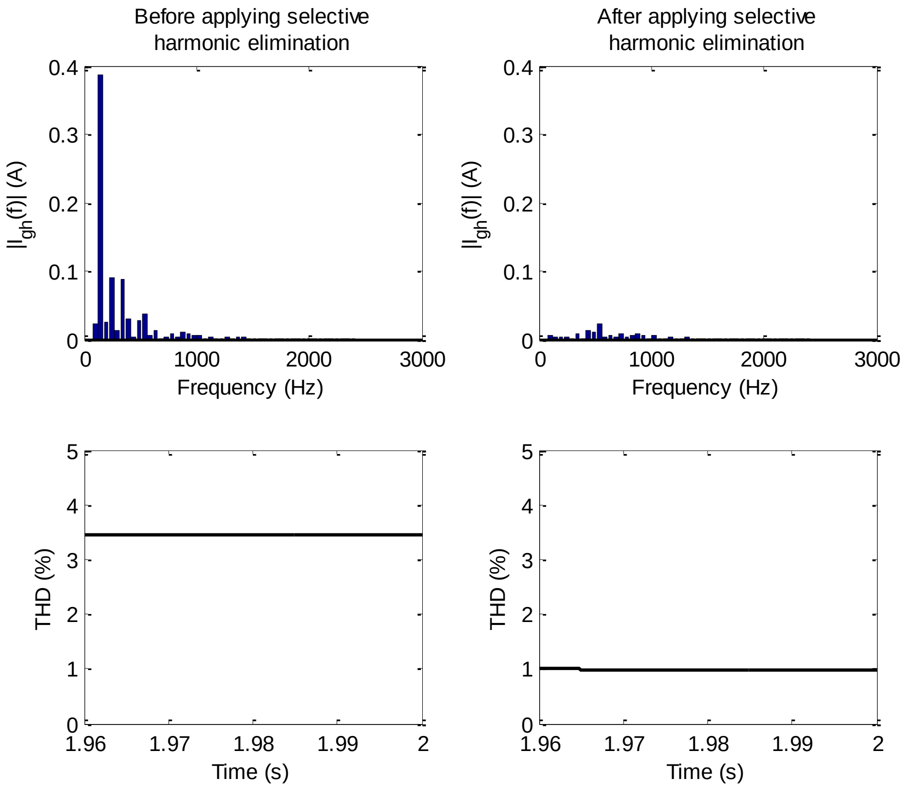

Figure (5.14) Harmonic spectrum and THD with and without selective harmonic elimination

A step change in the output current is shown in Figure (5.15) with the THD for the two different current values. The figure shows that as the current reduces to less than *50%*, the THD value is much less *2%* which is still less than the international standards.

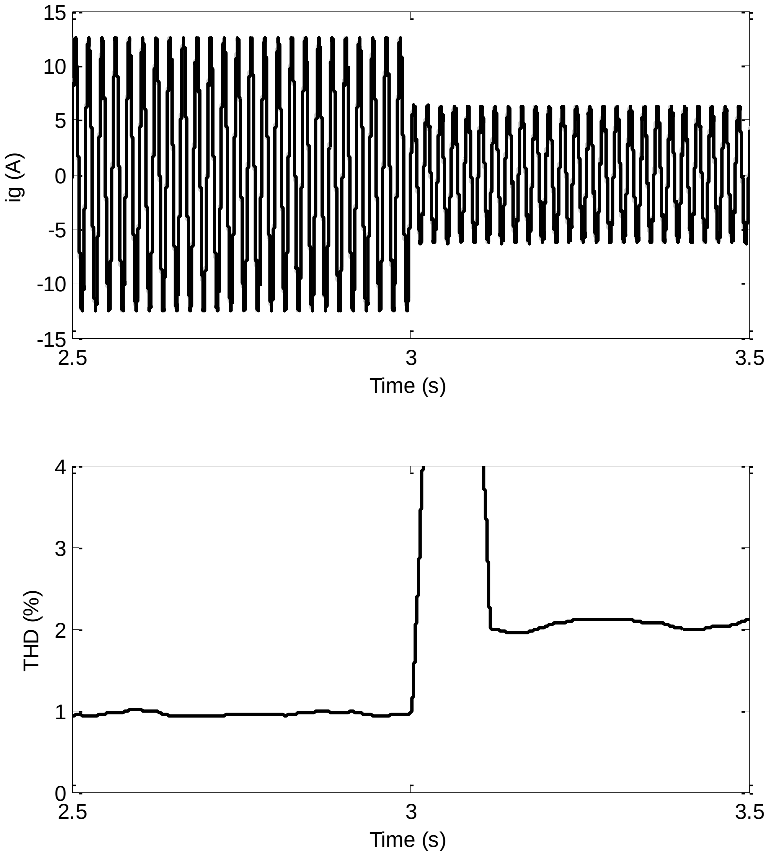

Figure (5.15) Effect of current reduction in the THD value

5.3. GRID-CONNECTED CONTROL

According to the grid demands, the selection of a proper power factor and active and reactive power control is another significant issue needed for grid-connected systems. Not only could the current injected into the grid be controlled effectively with the proposed method, but also the power factor within a certain range. The proposed method is described and simulation results will be proposed and explained in the following.

For multi-source inverters, the objective of control is to control the active and reactive power keeping the dc link voltage constant. Figure (5.16) shows a block diagram describing the proposed active and reactive power control method. The method is simple and easy to implement with small-scale renewable energy systems. The ac reference current is calculated from the dc power side. Equation (5.11) shows the equation used to calculate the ac reference current (I_{invr}). In this work, the power factor will be considered unity and the inverter efficiency (η_{inv}) is considered constant. A simplified method to calculate the root mean square (r.m.s) value (V_g) from the ac value (v_g) is shown in Figure (5.17).

$$I_{invr} = \frac{\eta_{inv} P_{dc}}{V_g \cos\phi} \tag{5.11}$$

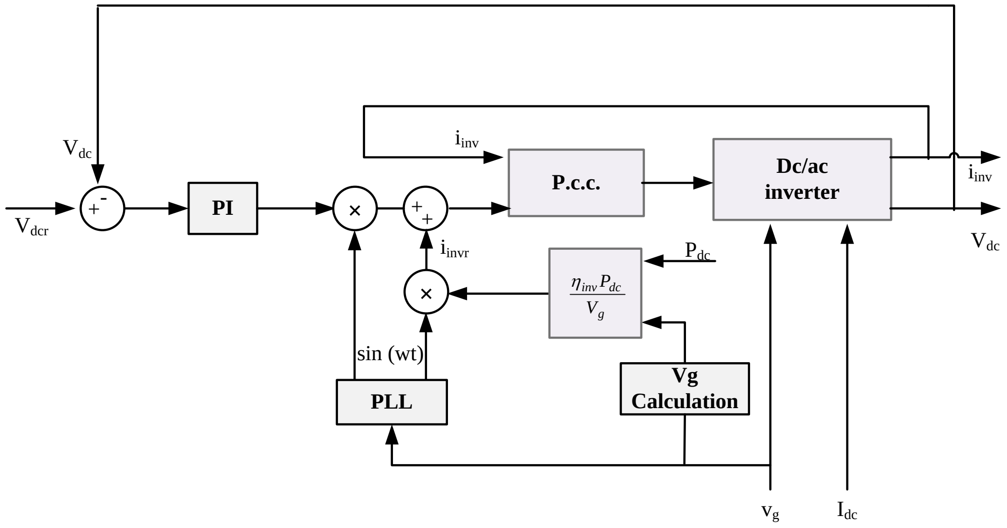

Figure (5.16) A simplified block diagram for the active-reactive power control method

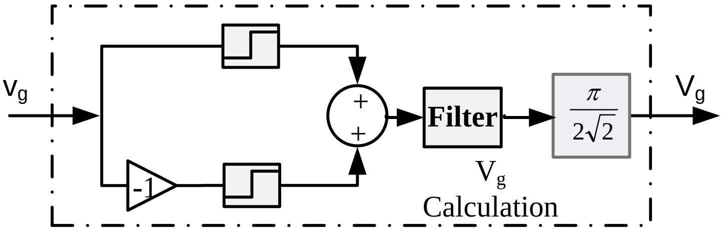

Figure (5.17) A simplified method for r.m.s value calculation

To design the PI dc-link voltage controller, the grid voltage magnitude is considered to be constant. Furthermore, the inverter works with a unity power factor and as a result, there is no phase shift between the voltage and current of the grid. According to Figure (5.1), the grid power (P_g), the dc side power (P_{dc}) and the dc link capacitor power (P_c) could be described by Equations (5.12), (5.13) and (5.14) respectively. The three equations are related by Equation (5.15)

$$P_g = V_g * I_g \tag{5.12}$$

$$P_{dc} = V_{dc} * I_{dc} \tag{5.13}$$

$$P_c = V_{dc} * C_{dc} \frac{dV_{dc}}{dt} \tag{5.14}$$

$$P_{dc} = P_g + P_c \tag{5.15}$$

From these equations, a simplified dc link control loop, shown in Figure (5.18), has been produced to design the PI controller. The Matlab/ control toolbox software has been used to design values for K_p and K_i. A typical value for K_p and K_i are *-0.2* and *0.1* respectively. These values were used to run the simulation of the system in Figure (5.1). The results of the simulation with changing the power values are shown in Figure (5.19). It shows that; the dc link voltage (V_{dc}) is controlled to track the constant reference values with acceptable starting response. As the output power (P_g) was changed by changing the input dc (I_{dc}) in Figure (5.1), V_{dc} was kept at the reference value V_{dcr}.

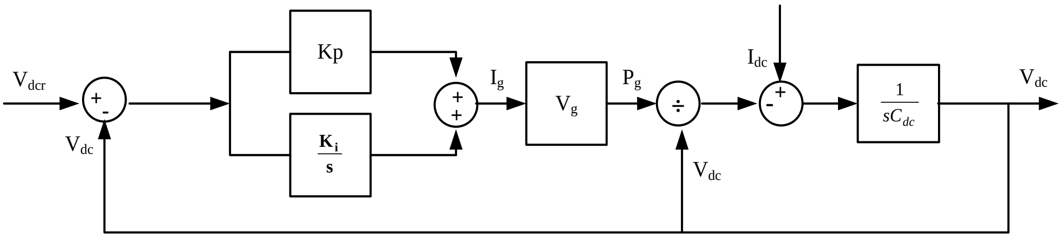

Figure (5.18) The simplified dc link loop controller for the inverter

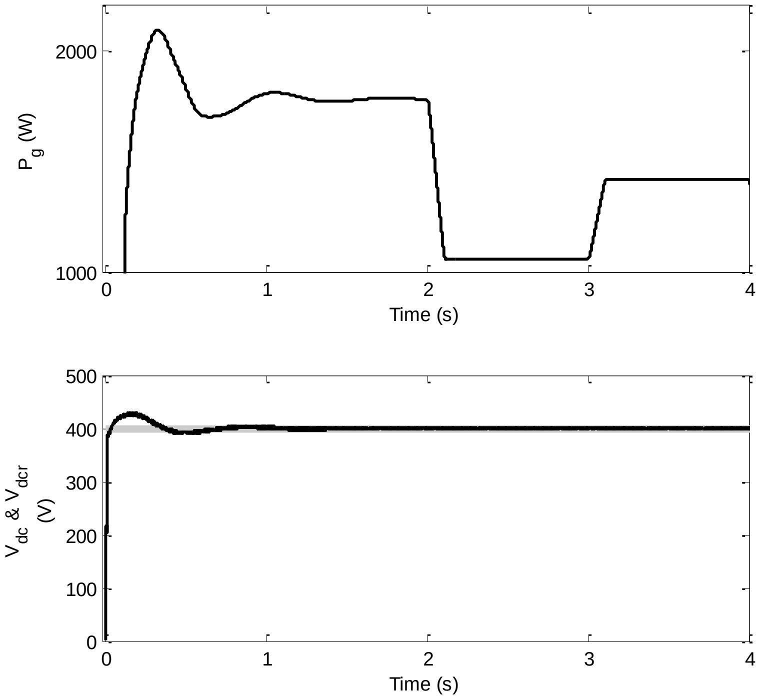

Figure (5.19) Dc link voltage controller with step change in active power

The dc voltage and power factor controllers were tested by simulation according to three conditions: active power change, two quadrant operations, and the variable power factor. The simulation tests were carried out on Simulink/Matlab with PLECS software. The system shown in Figure (5.1) was simulated as the reference value of the dc voltage (V_{dc}) was kept at *400* V. The simulation results are summarized as follows:

Active power change: Figure (5.20) shows I_{dc}, i_g, V_{dc}, P_g and Q_g with different active power values. The power factor is kept at unity in this test. The results show that; with step changes in the input dc (I_{dc}), the dc voltage is still constant at the reference value (*400* V). Furthermore, the VAR (Q_g) is still near to zero and the power factor is kept almost unity. This test clears the ability of the proposed controller to perform in different power levels.

Two quadrant operations: In Figure (5.21), the system tested in two quadrant operation as the grid power (P_g) reduced to be negative. This means the power was extracted from the grid to the dc side. This mode is very important when batteries in the dc side need to be charged. This is normally needed during the starting of the proposed system when the batteries were totally discharged before. This mode could also be used; if there is a dc load, which needs to be supplied, and the energy sources cannot provide this demand. The figure shows that even with the power extracted from the grid to the dc side, the dc voltage is still constant at its reference value. Furthermore, the power factor is nearly in its required unity value.

<u>Variable power factors:</u> The VAR (Q_g) reference was varied in this simulation with the results as shown in Figure (5.22). The power factor changed from lead to lag as shown in the figure and the active power was kept constant. The figure also shows that the dc voltage and the power factor controllers were working accurately.

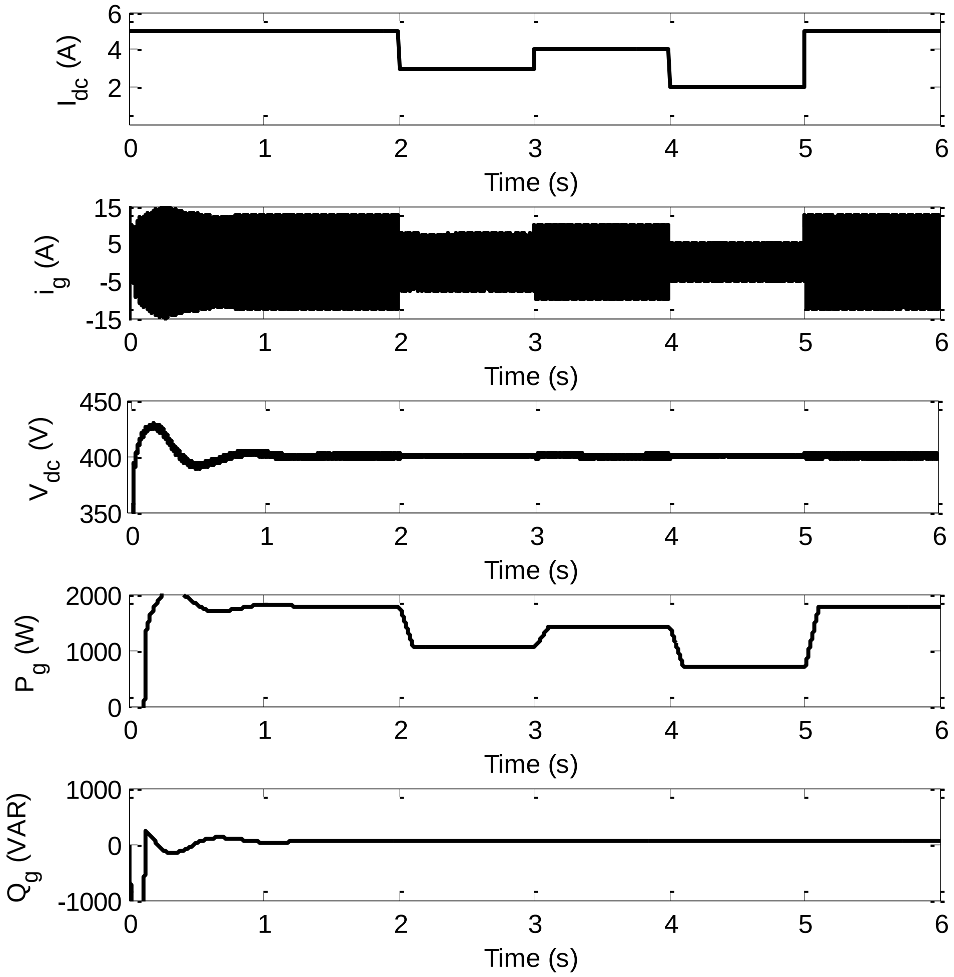

Figure (5.20) Grid-connected control with active power step change

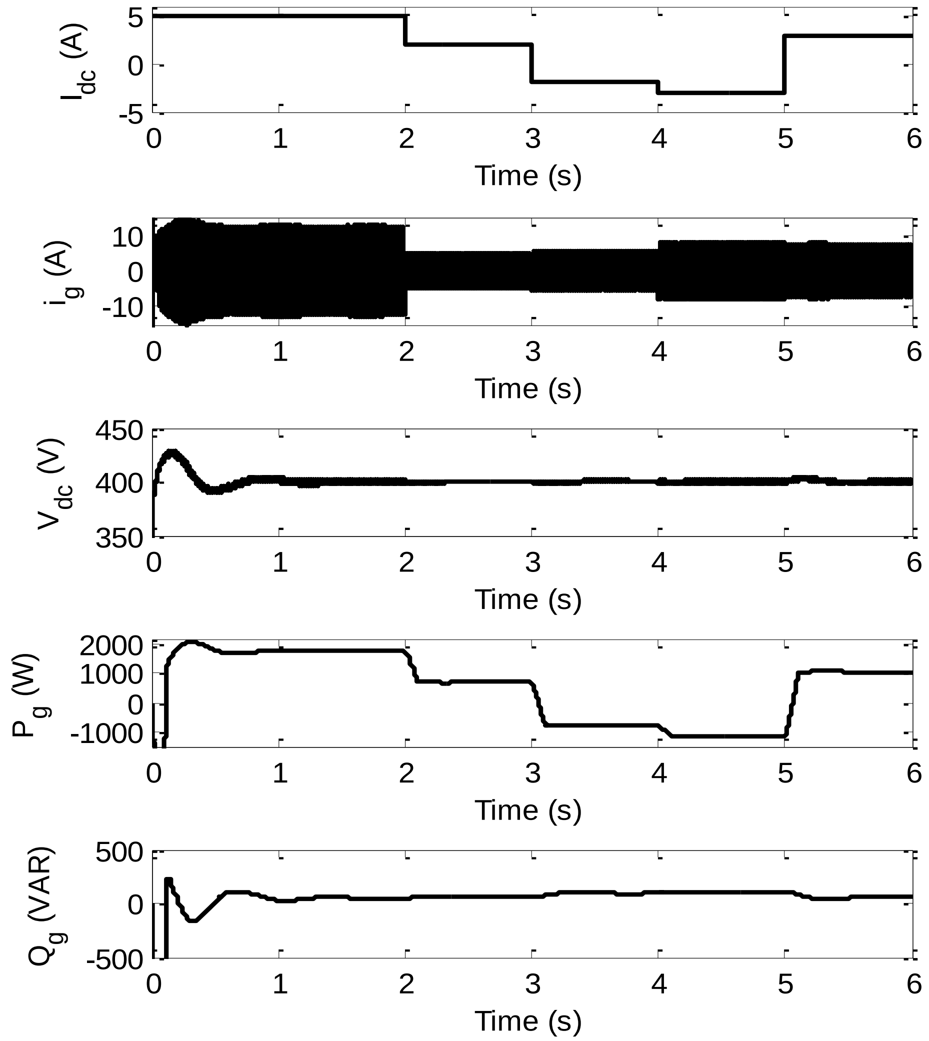

Figure (5.21) Grid-connected control with two quadrant operation

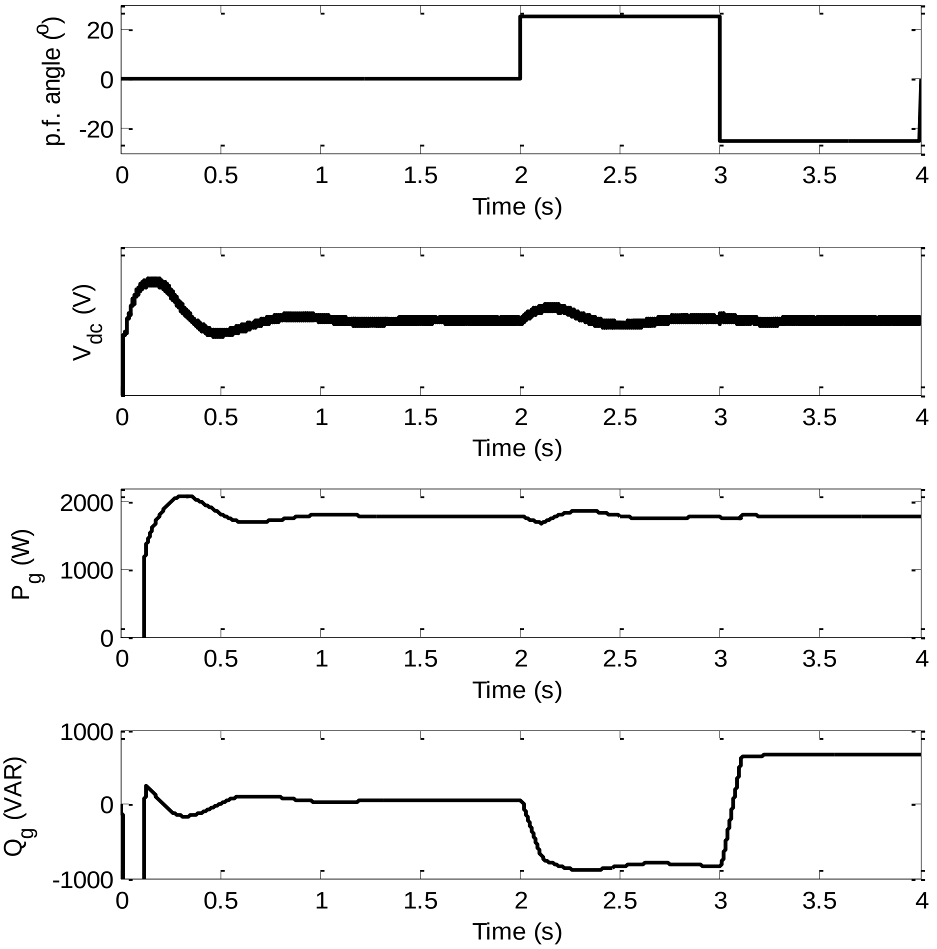

Figure (5.22) Grid-connected control with change in p.f.

5.4. STANDALONE MODE CONTROL

In this study, the proposed standalone control mode is based on the p.c.c. method, which is described early in this chapter. The inverter output current is controlled from the dereference current provided by the voltage control loop, as shown in Figure (5.23). An extra output filter (C_{fo}) is needed for better performance within this mode of operation. A value of 10 µF was found to give a good performance and lower THD. The ac voltage control loop is controlled using a PIS controller. The dc link voltage in this case is maintained constant by energy storage connected to the same dc link.

The load current is controlled using an instantaneous direct current control method (p.c.c.) that will guarantee fast transient response, reduced total harmonic distortion (THD), and higher disturbance rejection. Furthermore, the method is simple and easy to implement. There is no need for harmonic elimination to be used within this mode as it is observed that, with the simple form of the p.c.c method, satisfactory current and voltage waveforms are produced.

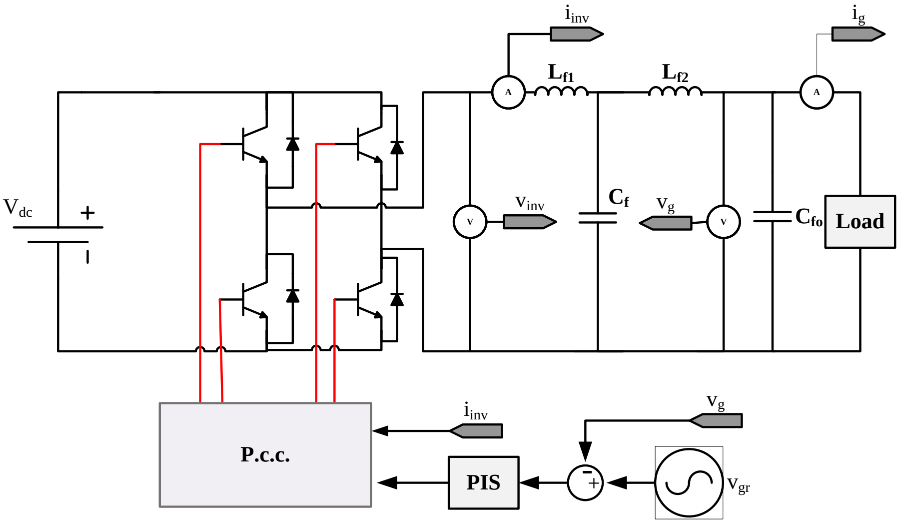

Figure (5.23) standalone mode control and circuit

The system shown in Figure (5.23) was simulated in Matlab/Simulink with PLECS software. The dc side was considered a dc voltage source as the dc link was controlled by the battery bank side controller. The output voltage (v_g) against the reference voltage (v_{gr}) is shown in Figure (5.24).The figure shows that the voltage output tracks the reference value in an efficient way. The output voltage and current waveforms with their THD values is shown in Figure (5.25), and the value shown is for rated load conditions. The THD for both wave forms according to the simulation is less than *2.8 %*, which is a very interesting value compared to the simplicity of the proposed control method.

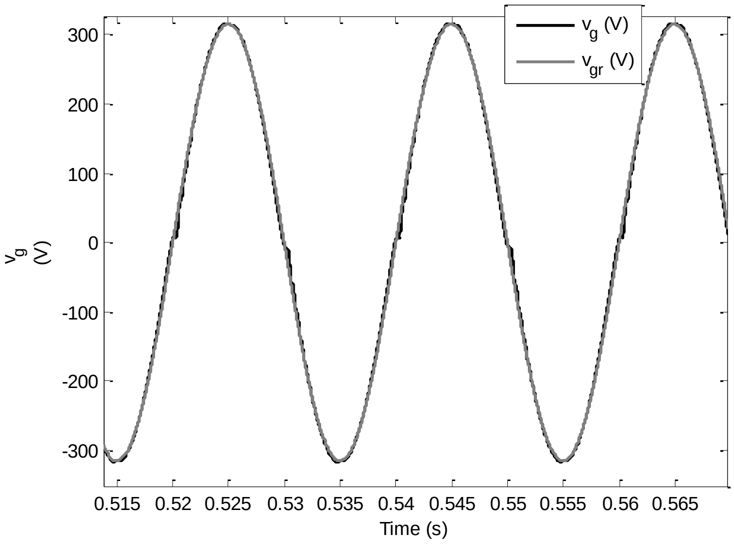

Figure (5.24) v_g versus v_{gr} on standalone mode

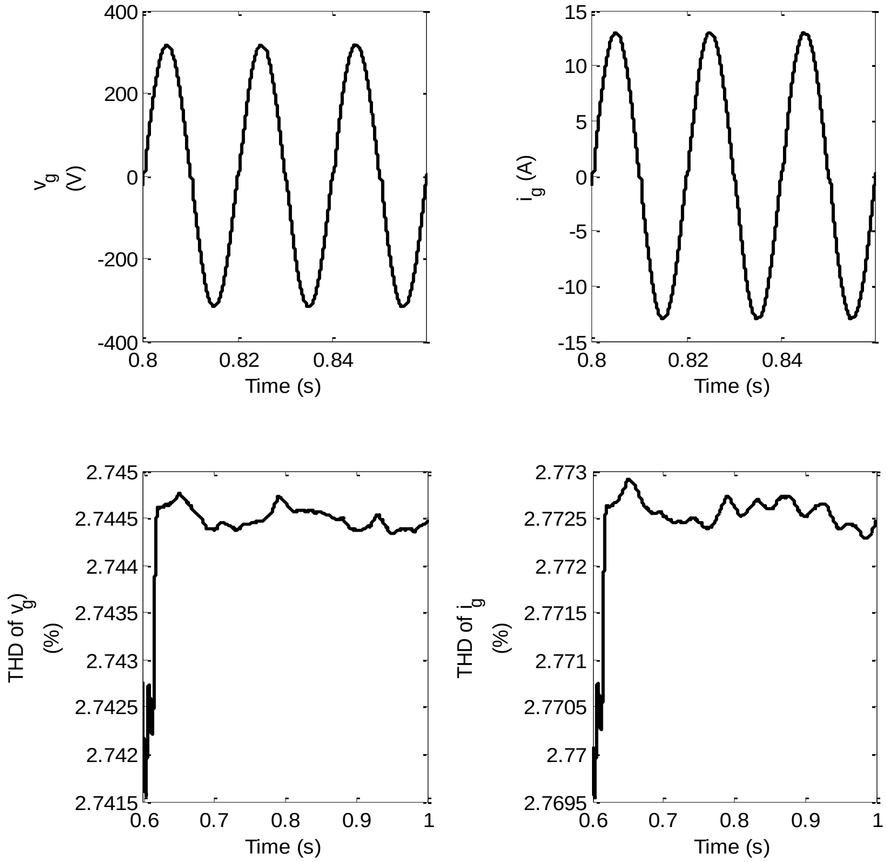

Figure (5.25) Output voltage and current waveforms with their THD on standalone mode control

To test the transient performance of the controller under load change, the load was simulated as a variable resistor in the output of the inverter. The reference value of the ac voltage (v_g) is a sine wave with r.m.s value of *220* V. The results of the simulation are exposed in Figure (5.26), which shows the output current (i_g), the output power (P_g), the output voltage (v_g) and the r.m.s. value of the output voltage. The figure shows that a step change was applied to the load from rated value 2kW to less than *.8* kW at t=1.08 in the time scale. In spite of the step change, the controller effectively keeps the voltage at the reference value with negligible transients. The proposed p.c.c controller is the same one used before with the grid connection control mode, and this will reduce the overall system control complexity.

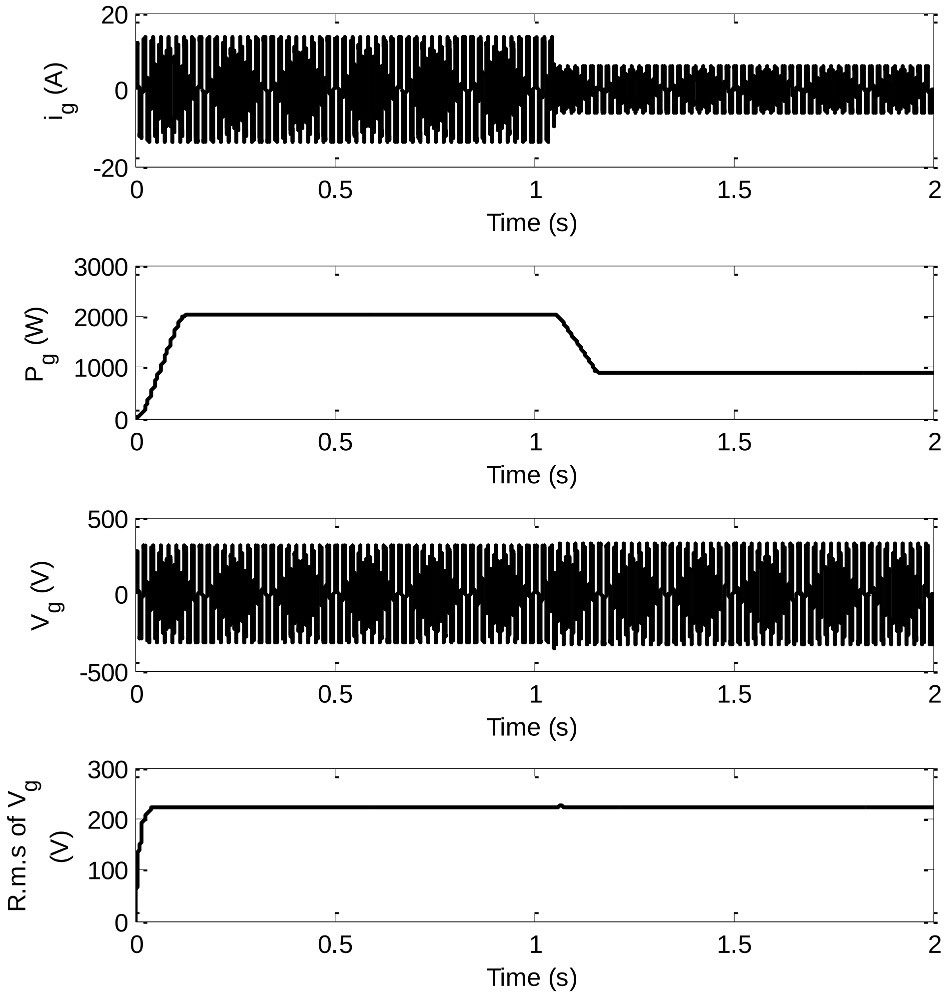

Figure (5.26) Standalone mode control simulation results

5.5. DC INJECTION ELIMINATION

The work described in this section is concerned with the risk of dc injection into the network from the small-scale single-phase inverters without output transformers. Due to an approximate short circuit characteristic of an ac network, a little dc voltage component, which can accidently be produced by the inverter, will produce large dc injection. This causes detrimental effects on the network components, particularly the network transformers which can saturate, resulting in irritant tripping. This may also increase the losses in and reduce the lifetime of the transformers, if not tripped. Moreover, the existence of the dc component can induce metering errors and malfunction of protection relays. There are thus stringent regulations in many countries to prevent the network from large dc injection. This thesis presents a new method of complying with such a requirement by an inverter that does not have a network side output transformer.

5.5.1. THE PROPOSED CONTROL STRATEGY

This study proposes a new method of measuring the dc component in the inverter output current. The output current is measured by a resistive shunt and the obtained voltage signal is processed by a specially designed and tuned analogue filter to increase the signal-noise ratio so that the dc level, as specified in standards, e.g. *.5%* of the rated inverter current, becomes measurable. The response is adequately fast even for renewable energy systems which are normally working under variable conditions. This work explains the design of the filter circuit and the use of it in a closed loop control system aiming to keep the dc injection low – below the standard limit. System performance is illustrated by simulation and experimental results. The study focuses on a full bridge voltage source inverter operating in a unipolar PWM mode. The block diagram of the transformerless inverter under study is depicted in Figure (5.27) showing the control for dc injection compensation.

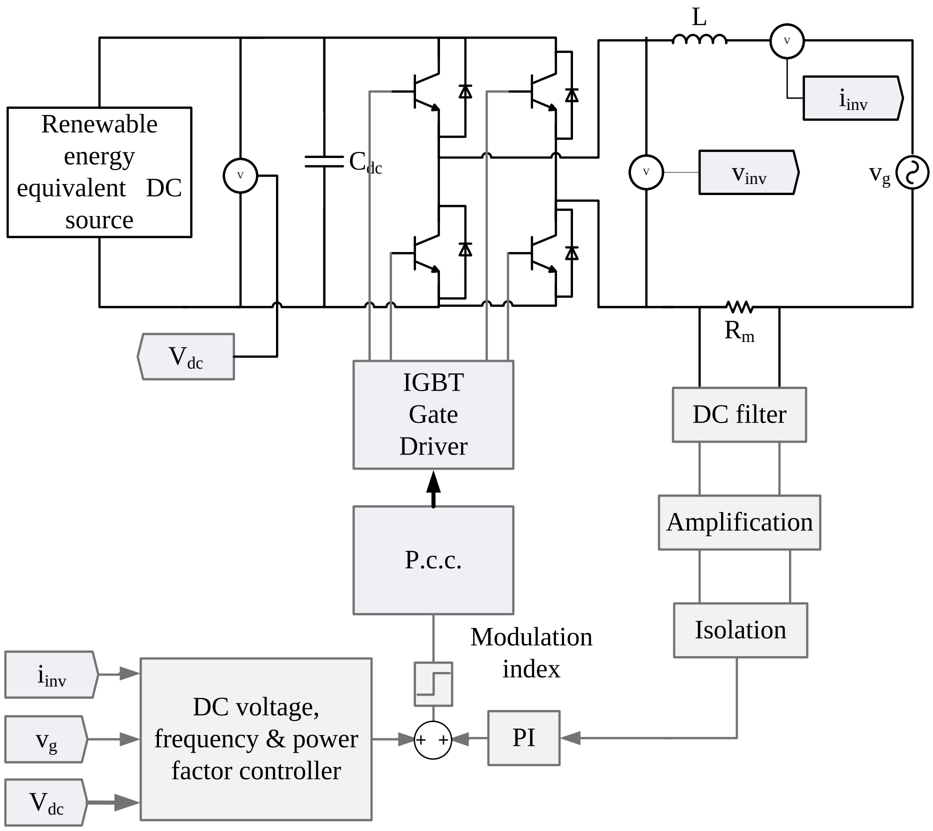

Figure (5.27) The grid-connected inverter circuit and control

5.5.2. CAUSES OF DC INJECTION

There are three main factors which can cause dc injection into the network from a single-phase H-bridge voltage source inverter. These are

-Unequal semiconductor device characteristics in the inverter, including on-state resistance and on-state forward saturation voltage, and the temperature coefficients of these parameters. The device characteristics are affected by inevitable variations during fabrication and packaging and can also drift in operation due to degradation mechanisms such as bond wire lift-off. The circuit in Figure (5.27) was built in Matlab/Simulink with PLECS software, and the simulation was performed assuming that the on-state voltage of the IGBT devices in the inverter is unbalanced by *0.05* V. Figure (5.28) shows the imbalance produced by the on-state voltages. A part of the positive cycle shows that the forward voltages in this leg of the inverter are the same. In the negative half-cycle, one of the IGBTs has less forward voltage by *.05* V. For a typical *230* V single-phase feeder, the series resistance in the Thévenin equivalent circuit representation would be *0.01* Ω to *0.04* Ω. For a modulation index of *0.8* in the inverter and *1* kW output power at unity power factor, the simulation showed that the dc injection was between *375* mA and *1500* mA. This shows how difficult it is to comply with the typical standard requirement of the dc injection being less than e.g. *20* mA, in this case of *1* kW inverter. The only way is probably to set the dc under close-loop control if a low frequency output transformer is to be avoided, which however depends on how accurately the weak signal of a small dc can be measured.

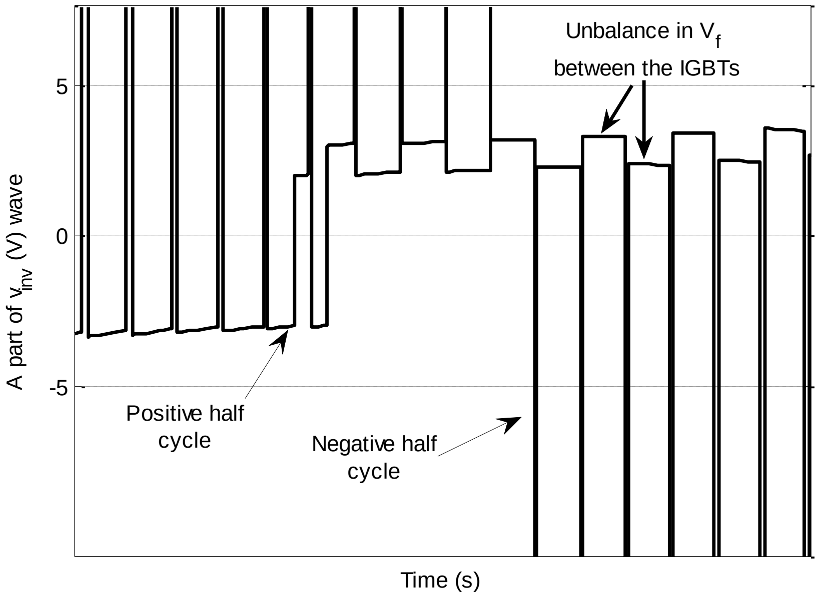

Figure (5.28) Effect of unbalance in forward IGBT voltages

- Dc bias that can be included in the inverter PWM switching process. This is particularly vulnerable to the blanking time between the upper and lower switches in the same leg of the bridge. Simulation shows that the dc injection in the range of hundreds of mA can be easily reached with unbalance of blanking time in a few microseconds between the positive and negative half cycles of the inverter output.

- Dc bias of the output current sensor, which also could provide dc bias to the PWM process. This will cause imbalance between the positive and negative half-cycles and causes dc component to be injected.

5.5.3. THE PROPOSED DC ELIMINATION TOPOLOGY

In the approach which is further pursued in this study, the dc component in the output current is sensed and used in the controller to eliminate the dc injection. One of the challenges to this approach is the accuracy, and this is due to the relatively small amount of dc component which needs to be accurately measured. As an illustration of this problem; the required specification in the UK and Australia is *20* mA, which is less than *0.1%* of the fundamental component. This is not easily measurable due to the offset and accuracy in the current measurement device. Another problem is the resolution as a very high DSP resolution is needed to measure the current directly from the line, and analyse it to find the dc component by filtering or FFT analysis. This will add cost to the inverter.

5.5.4. PROPOSED DC INJECTION MEASUREMENT CIRCUIT

A circuit based on the resonance approach is used for measuring the dc component in the current. The circuit is shown in Figure (5.29) as resistor R_a is the resistive current shunt in the path of the inverter output current. The series LC resonance circuit is used to bypass the majority of the fundamental ac component of the measured voltage across the shunt and block the dc component. As a result, the entire dc component of the shunt resistor voltage will be applied across the resistor R_m. V_m is measured as an indication of the dc component contained in the inverter output current. V_m also contains a residual of the *50* Hz (or *60* Hz) ac component that has not been filtered out. Nevertheless, for the reason to become clear later, this has little effect as long as much of the ac component has been bypassed and the signal-noise ratio regarding the targeted dc component in the measured current shunt voltage is significantly improved. A low offset differential amplifier is used to amplify the signal while another amplifier with isolated output is used to guarantee isolation between power and control circuits. The transfer function from the mains current to the filter output voltage can be derived as in Equation (5.16).

$$G_m = \frac{R_m R_a (sL_{res} + \frac{1}{sC_{res}})}{((R_a + sL_b)(R_m + s(L_m + L_{res}) + \frac{1}{sC_{res}}) + (sL_{res} + \frac{1}{sC_{res}})(R_m + sL_m))} \qquad (5.16)$$

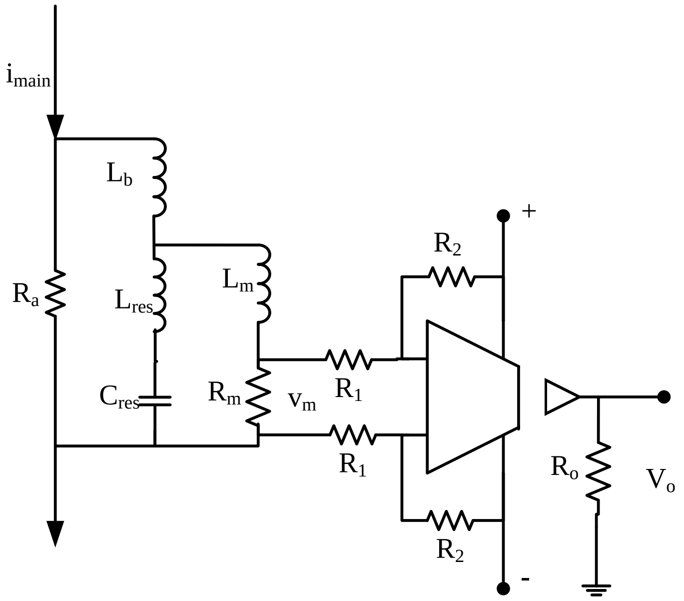

Figure (5.29) dc injection measurement circuit

5.5.5. CHOOSING MEASURING CIRCUIT COMPONENTS

In this section, design of the values of the filter component will be chosen. There are three components need to be chosen in the circuit, which is L_b, L_m, and R_m, and the resonance circuit filters. These components can be designed as follows:

-The value of the inductance L_b is chosen according to the filter rating where L_b blocks the mains ac current component and it is a short circuit to the dc component. L_b can be chosen according to

$$L_b = \frac{R_a}{\omega}\frac{I_{main}}{I_b} \tag{5.17}$$

where (ω) is the mains frequency (rad/s), I_b is the ac current through L_b and I_{main} is the inverter output rated current.

-The value of inductance L_m is chosen to give some tolerance in L_{res} and C_{res} in the series resonant branch.

-To choose ***<u>the precise value for the resistance R_m</u>***, consider the steady state transfer functions from the dc or fundamental ac component in the inverter output current to the corresponding components in V_m (Equation (5.16)). The ac and dc gains had been plotted against the resistance (R_m) as shown in Figure (5.30). The Figure shows that as R_m increases both the dc and ac gains of the filter increase. However, the increase of the dc gain saturates as R_m approaches 10 Ω. Furthermore, the ac gain attenuates the fundamental component of the main current by values from less than *0.5%* to *2%* while the dc gain attenuates the dc by values less than *20%* to more than *80%*. This shows how the proposed circuit makes the percentage of the dc component to the ac component increase from less than *.2%*, which is not measurable, to more than *15%*. Taking into account the maximum input value for the amplifier, the tolerance in the passive filter components (L_{res} and C_{res}), and the amplifier offset value, the value of R_m can be chosen. In our design case, a value of *3* Ω has been applied.

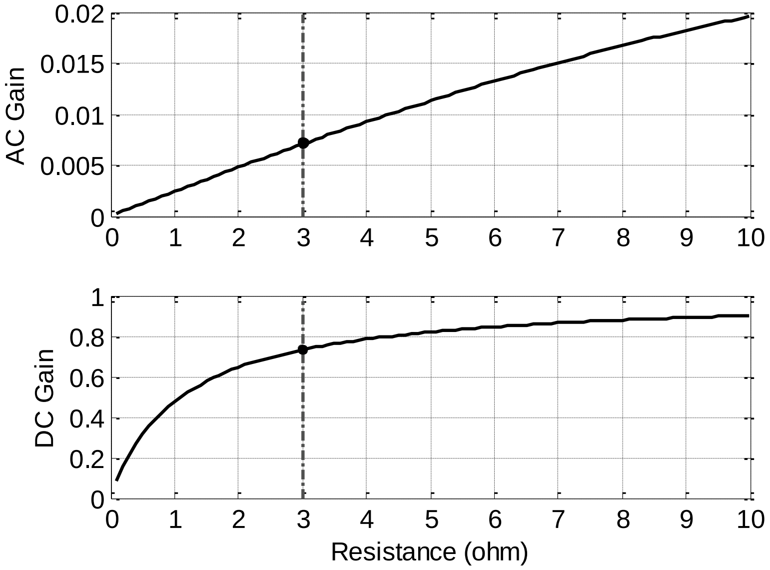

Figure (5.30) Choosing filter output resistance R_m

<u>-To show how to design the resonance components</u> values of L_{res} and C_{res}, a value of L_{res} was chosen with changing C_{res} in Equation (5.16). Figure (5.31) shows the ac gain against the capacitor values in farad with and without resonance circuit. It is obvious that the minimum ac gain occurs in the resonance case, but because of the tolerance in the capacitor and inductor values, the capacitors are designed to be *20%* more than the resonance values. The reason for this is to avoid the sharp increase in the ac gain less than the resonance value. The ac gain in the figure is attenuated to less than *25%* in the designed point while the dc gain is not affected.

5.5.6. CONTROLLER DESIGN

To simplify the system model, the causes of dc injection are collectively represented as a dc voltage source at the inverter output (V_s) as shown in Figure (5.32). Furthermore, the compensating voltage produced by off-setting the modulation index (M_{dc}) of the inverter is considered a controllable dc voltage source (V_c). The inverter control will also respond to the residual fundamental ac component in V_m. However, the response is small compared to the normal inverter output voltage. The grid exhibits series inductance (L_f) and resistance (R_f).

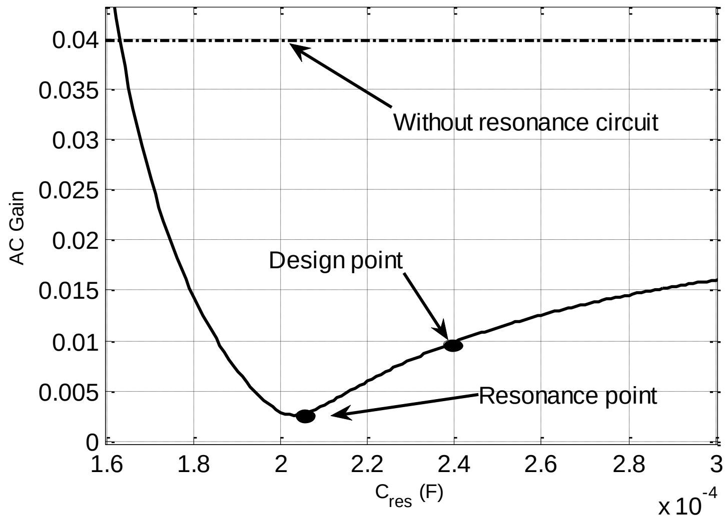

Figure (5.31) Choosing resonance filter components

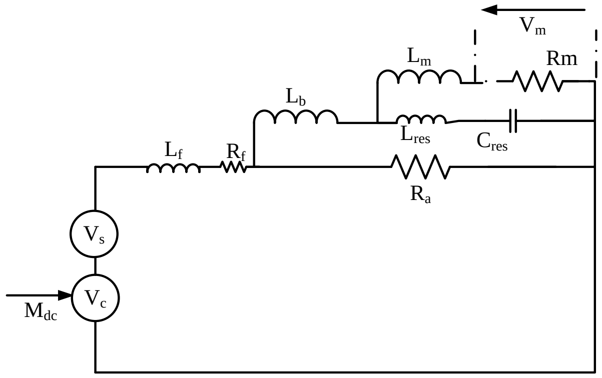

Figure (5.32) Circuit simplifications for analysis of the dc

The transfer function from the inverter output voltage to the current is:

$$G_s = \frac{K_s}{1 + sT_s} \tag{5.18}$$

where $K_s = 1/R_f$, $T_s = L_f / R_f$. The transfer function of the measurement circuit was proposed before in Equation (5.16). The block diagram of the closed-loop control system is shown in Figure (5.33) where a PI controller is used to control the dc component of the current by off-setting the modulation index of the inverter. In the design of the controller, disturbance rejection and noise suppression were taken into account. The Matlab control toolbox is used to design the system controller. The designed root locus and the open loop bode plot of the system are shown in Figure (5.34). The figure shows that the system is designed to show as faster response as possible without high peaks in the dc component.

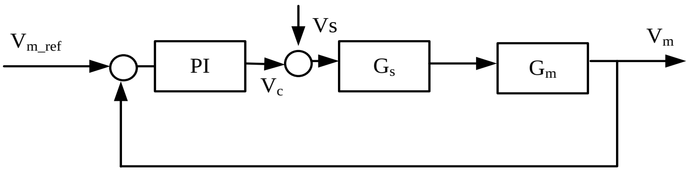

Figure (5.33) Controller block diagram for the dc component equivalent circuit

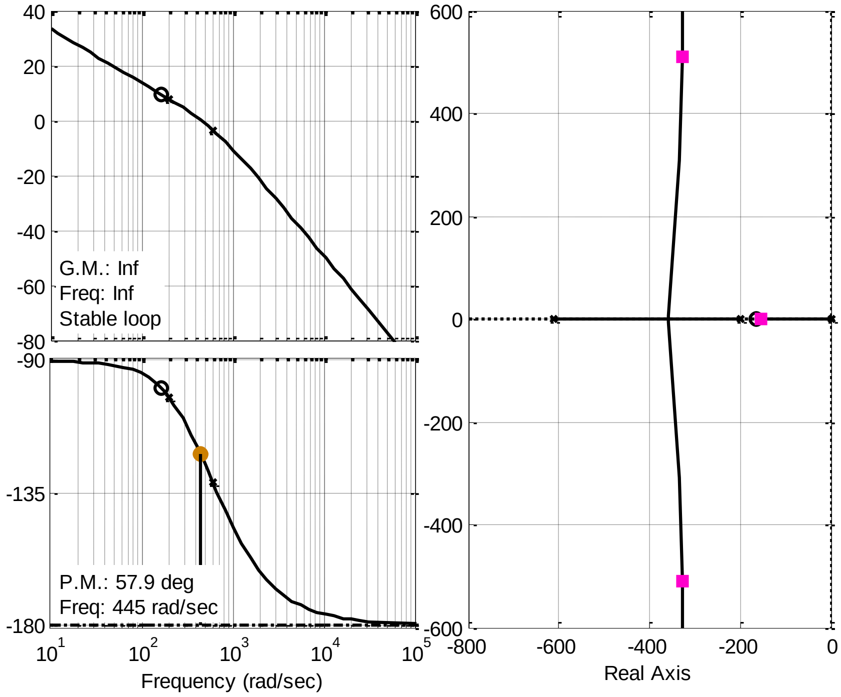

Figure (5.34) Bode and root locus diagrams of the inverter according to the dc component of the current

5.5.7. SIMULATION RESULTS

The time-domain simulation was carried out using Matlab/ Simulink for a simplified system configuration as shown in Figure (5.27). The dc link is a controlled voltage source emulating the renewable energy source supplying a single-phase grid-connected H-bridge inverter. The dc link voltage is maintained to be constant at *400* V and the inverter is controlled to supply the grid with *2* kW power with unity power factor. Unequal on-state state voltages between the inverter arms are adjusted to produce a dc of *20* mA injected into the grid while the dc elimination controller is applied at t=*1* s from the start of the simulation. The simulation results are shown in Figure (5.35), which illustrates the mains current (I_{main}), the mains dc component ($I_{main-DC}$), the filter output (V_m), and the dc component in the filter output voltage (V_{m-DC}). This simulation results demonstrate that the dc can be eliminated by the controller and this proves the controller design based on a simplified method. Furthermore, the filter increases the signal-noise ratio of the dc component in V_m with respect to the residual ac component which is regarded as noise. The dc component in V_m becomes measurable after amplification. To demonstrate this, the dc component in the mains current is less than *0.2%* while it is more than *5%* in the output of the filter, corresponding to a *25* times improvement of the signal-noise ratio.

5.5.8. EXPERIMENTAL VERIFICATION

A block diagram of the experimental test rig setup is shown in Figure (5.36)**Error! Reference source not found.** where a dc voltage source is connected to the H-bridge inverter, which supplies a passive load. To artificially cause a dc component in the inverter output current, a circuit of variable resistance connected to a diode is paralleled to the load resistance as shown in Figure (5.36). The controller for the dc injection elimination and the inner loop for the inverter PWM process are programmed in Matlab/Simulink and implemented using an embedded dSPACE real time control system [172]. The filter output is measured as shown in the figure and provided to the controller where the H-bridge inverter PWM control signals are generated. The dc injection elimination control is applied after *18* seconds from the start of the experiment.

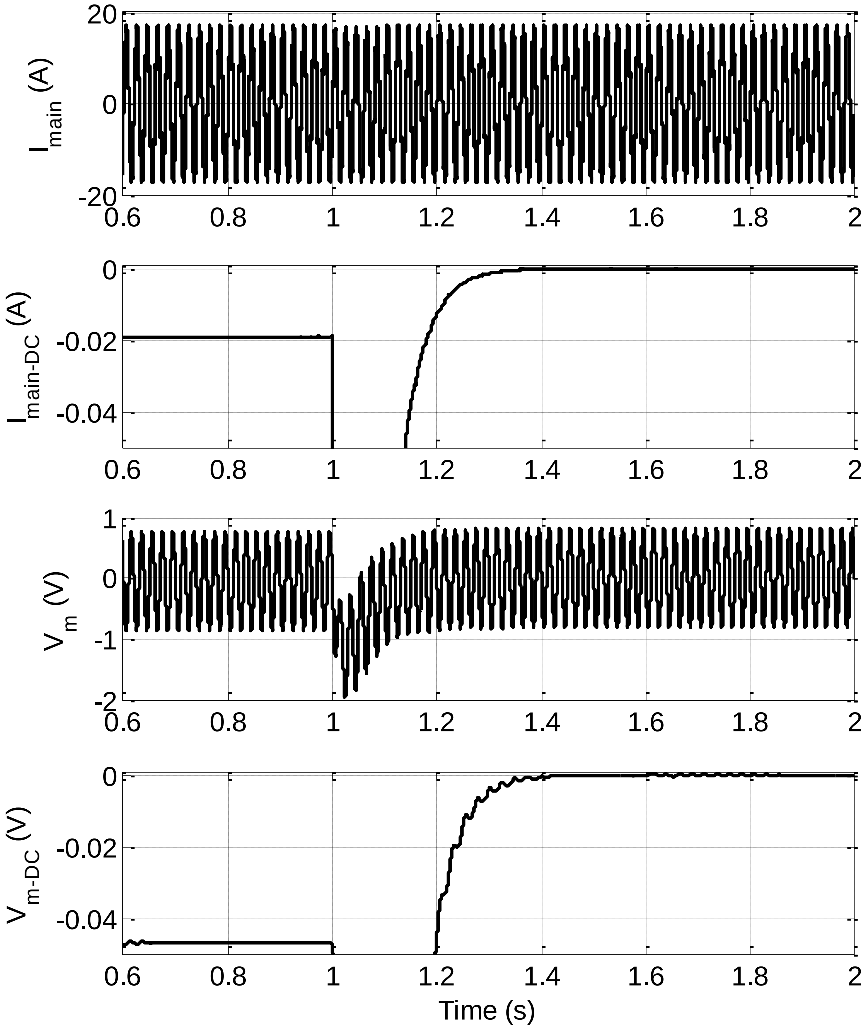

Figure (5.35) Time-domain simulation results

The experimental results are shown in Figure (5.37) and Figure (5.38) where the data were collected on a digital scope and dSPACE respectively. Figure (5.37) shows the inverter output current before dc component elimination, which contains a dc component. Figure (5.38) shows the output voltage of the measuring filter circuit V_m. The variable resistance was adjusted to produce almost *12.3* mA dc component in the inverter output current whose fundamental ac component is approximately *1.06* A, as shown in Figure (5.37). It is clearly shown in Figure (5.38) that the controller eliminates the dc component to a non-significant level. Furthermore, the test results show that as the inverter output current changes, the controller keeps the dc-injected current at the same level, which remains to be insignificant. This is particularly useful in renewable energy systems where the input power is always fluctuating. This experimental results show a slight divergence from the expected ideal characteristics and this is due to the tolerance of the passive filter component values. With this, the filter can still adequately sense the dc component in the inverter output current. As a demonstration, the dc component is only *0.8%* in the inverter output current, while it is almost *13%* in the filter output voltage signal. Consequently, the objective of the research has been achieved.

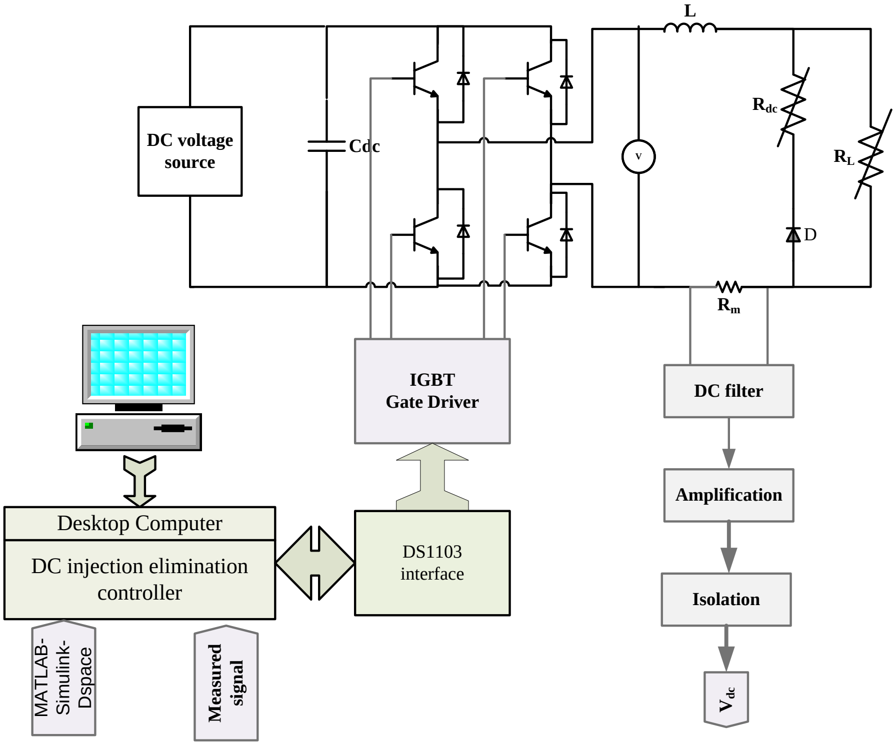

Figure (5.36) The experimental test rig Configuration

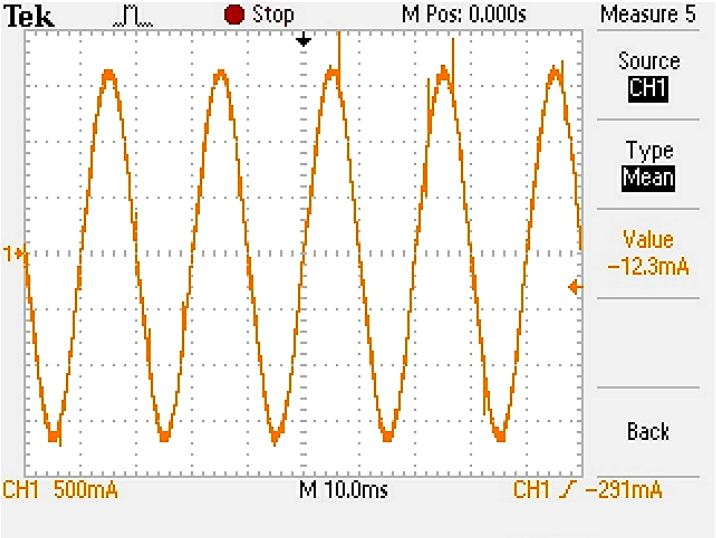

Figure (5.37) Measured inverter output current when the dc component was applied, its value is shown in the right side of the figure (-12.3 mA)

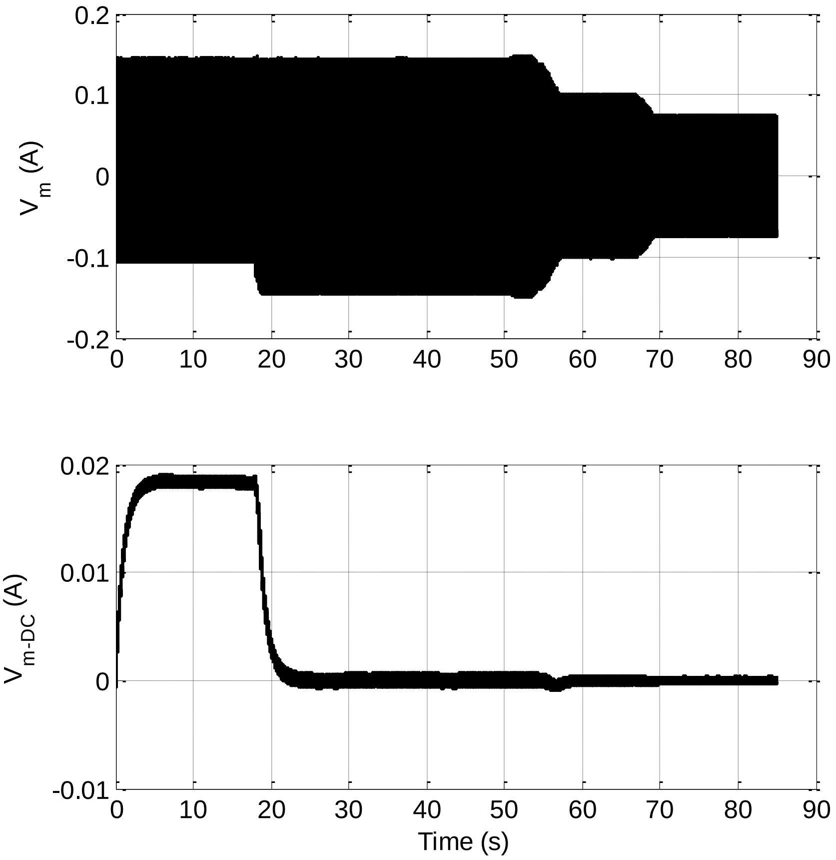

Figure (5.38**)** Experimental results showing the dc component eliminated at Time=18s, even with change in the fundamental component at Time=58s the controller kept the dc component limited

CHAPTER (6)

SUPERVISORY CONTROL

6.1. INTRODUCTION

Under different operating conditions, the power generating system can provide a desired quality of operation with power electronics and control processing units. Such a system is considered a hybrid power system, as it combines various electrical energy sources and energy storage, and contains both continuous and discrete signals. Renewable energy systems with batteries are an illustration of such hybrid energy systems. Supervisory control is essential to manage the power between the different components of a renewable energy system. Furthermore, it supervises and regulates the operations of the local controller for every component of the system in the various operating modes. Standalone systems with renewable energy resources are hard to control due to changing and unpredictable generator output.

Energy storage devices would smooth the power output and provide greater availability of the system. If the renewable energy system is connected to the utility grid, it increases the control difficulty. This happens because the system needs the capability to work in both modes, i.e. with and without grid connection. Furthermore, the number of operational modes will increase and the control problem will be complicated.

A supervisory controller, which manages the operation of the hybrid PV-Wind unit with a storage system in standalone and grid-connected modes, will be proposed in this chapter. The local controllers were designed and verified for the different system components in the previous chapters. The supervisory controller is then needed to provide a smooth operation through the different modes of the system. During the operational modes, this controller also has to be able to keep the system’s power quality within the specified constraints. The advantage of modularity, which adapts the controller to work with different system configurations with no or very little change, has to be considered with the supervisory controller. Therefore, the proposed control can supervise a PV-Wind hybrid or a single-sourced renewable energy generating system. Furthermore, it can work with standalone or grid-connected systems.

In this chapter, the system configuration and local controls will be summarized in Section (6.2). This is followed by explaining the proposed supervisory controller in Section (6.3). The simulation results will demonstrate the control strategy in the end of this chapter.

6.2. SYSTEM CONFIGURATION AND CONTROL

With reference to Figure (6.1), the PV and wind generators produce electrical power which is extracted from the solar and the wind energies respectively. The related symbols are shown in Table (6.1) below. The system configuration and control of all the involved system components will be described in the following subsections:

6.2.1. WIND GENERATOR SIDE CONTROL

The ac output power of the wind generator is rectified by a diode rectifier and controlled by a boost converter. The boost converter provides MPPT at low and moderate wind velocities while it limits the power and rotor speed by stalling the generator at high wind velocities. The details of the controller design, simulation results and experimental verification were explained above in Chapter (3). A braking resistor is used to switch off the wind generator according to a control signal from the supervisory controller.

6.2.2. PV GENERATOR SIDE CONTROL

The PV generator is a nonlinear dc source which is controlled by a dc/dc boost converter. This converter provides MPPT to the PV generator using the method described above in chapter (4). The reduced power operation (RPO) is also provided to limit the generated power from the system according to the following scenarios:

1. If the generated power is higher than the power electronics ratings. The reason is that the power generated from the PV generator can largely increase above the data sheet rating with temperature reduction. Furthermore, solar radiation can increase to high limits on certain summer days, which increases the power output over the ratings. This was fully discussed in Chapter (4).
2. If the system is on the standalone mode and the battery bank is fully charged, in order to reduce the renewable energy generator disconnection periods. A full discussion of this operational mode will be explained later in this chapter.

6.2.3. BATTERY BANK SIDE CONTROL

The battery storage devices can be used in a wide range of applications due to their fast response and silent operation. Recently, due to the increased application, the battery storage technologies have significantly improved. The batteries are used in many applications, such as power system frequency control, which helps to improve the stability and availability of power systems [196]. Using battery storage systems as a short-term home backup is also affordable [197]. Another very promising application is the integration with isolated or grid-connected renewable energy systems, which will be proposed in this system. The battery storage is very important to provide a smooth output power and to increase the overall availability of the system. In the following sub-sections, the battery bank model and the control strategy are proposed.

A. BATTERY BANK MODEL

A simplified battery bank model is proposed in this stage [198]. The electromotive force (E_{batt}) is modelled as a controlled voltage source, which is calculated as a function of the SOC (C_{soc}) (Equation (6.1)). The SOC is calculated according to the discharging / charging current Equations (6.2, 6.3) respectively.

$$E_{batt} = (E_{CC} - E_{CD})C_{SOC} + E_{CD} \tag{6.1}$$

$$C_{SOC\_disch} = \frac{\eta_{disch}}{3600 \times C_{cap}} \int I_{disch} dt + C_{soc0} \tag{6.2}$$

$$C_{SOC\_ch} = \frac{\eta_{ch}}{3600 \times C_{cap}} \int I_{ch} dt + C_{soc0} \tag{6.3}$$

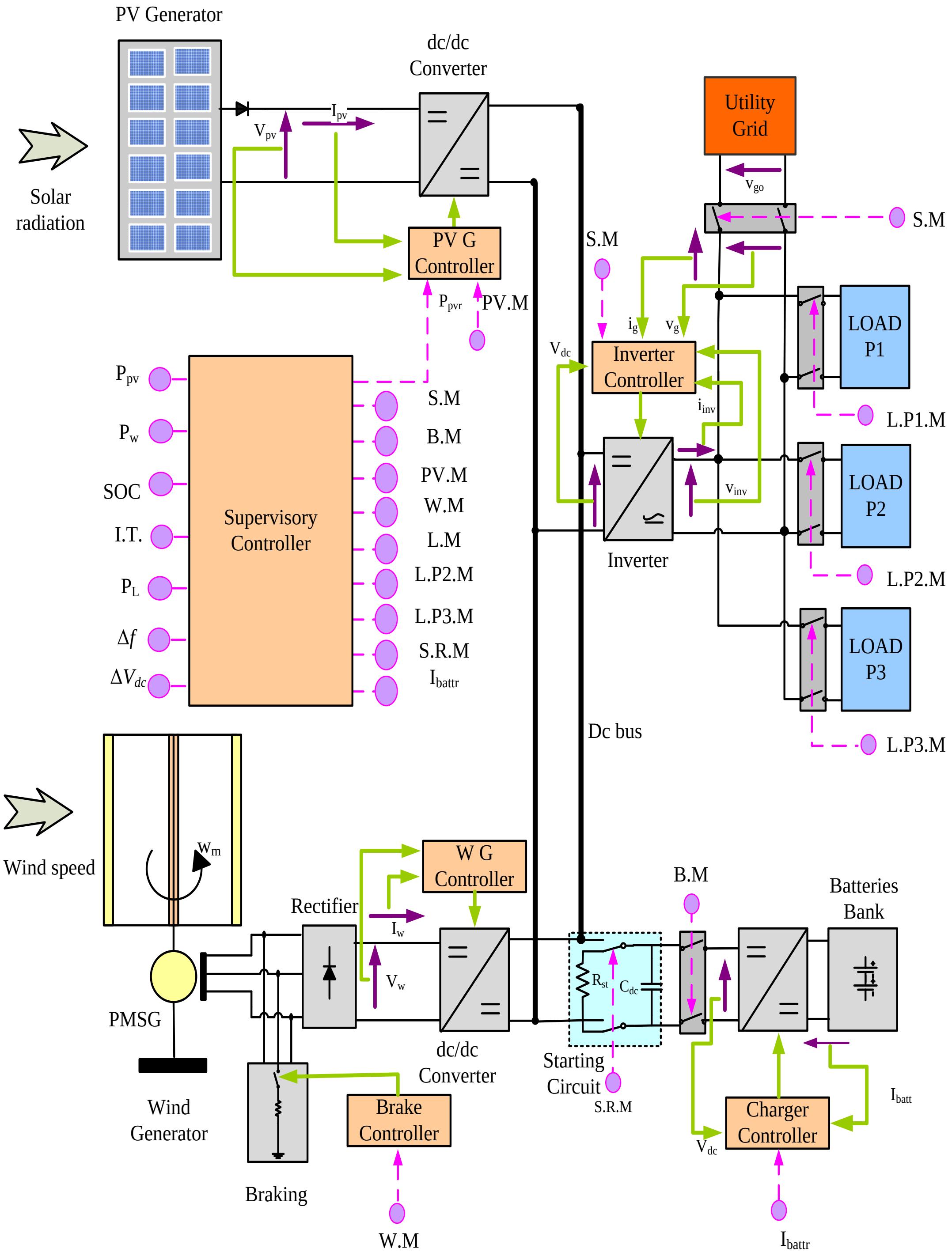

Figure (6.1) A block diagram for the proposed system

Table (6.1) Description of the symbols in Figure (6.2)

	Number	**Symbol**	**Description**
Inputs	1	P_{pv}	PV generated power (p.u.)
	2	P_w	Wind generated power (p.u.)
	3	SOC	State of charge of the batteries (p.u.)
	4	I.T.	Islanding test
	5	P_L	Load demand power (p.u.)
	6	Δf	The change in grid frequency
	7	ΔV_{dc}	The change in dc voltage (V_{dc})
Outputs	1	P_{pvr}	Reduced mode reference PV power (p.u.)
	2	S.M.	System mode
	3	B.M.	Batteries mode
	4	PV.M.	PV generator mode
	5	W.M.	Wind generator mode
	6	L.M.	Load priority 1 mode
	7	L.P2.M.	Load priority 2 mode
	8	L.P.M.	Load priority 3 mode
	9	S.R.M.	Starting resistance mode
	10	I_{battr}	Batteries reference current (p.u.)

The circuit is shown in Figure (6.2) as the battery output e.m.f (E_{batt}) is considered to increase linearly with the SOC (C_{SOC}). The minimum value of (E_{batt}) is the minimum discharge voltage (E_{CD}) and the maximum value (E_{CC}) is the maximum charging voltage. The steady state value of the SOC (C_{soc0}) is considered as input to the battery model in the simulation process. The dynamic instant value is calculated inside the model using Equations (6.2, 6.3) according to the charging and discharging currents. The charging current is considered positive at charging mode and negative at discharging mode. Practically, there are many methods to measure the SOC value, and many methods are described in references [199-201]. A detailed SOC measurement circuit is outside the scope of this work.

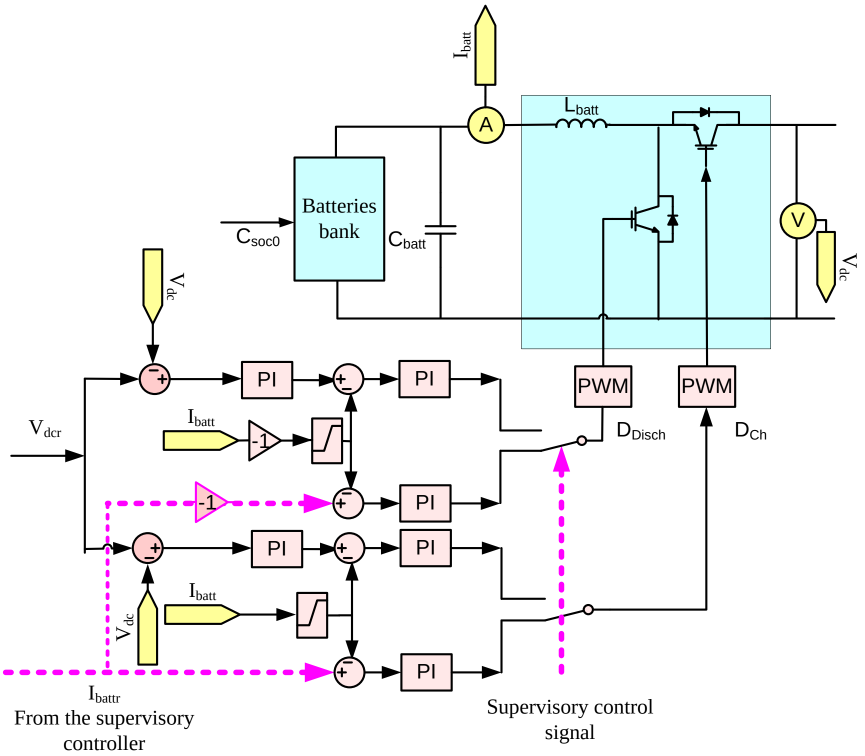

Figure (6.2) Diagram for battery side with charge/discharge circuit and control

B. BATTERY POWER ELECTRONICS AND CONTROL

A dc/dc converter is used to control the batteries as shown in Figure (6.2). A boost dc/dc converter works on the discharging mode while a buck dc/dc converter works on the charging mode [202]. The battery controller can be divided into the following modes of operation according to the supervisory control signal:

1. Standalone mode - the controller regulates the current to provide constant dc bus bar voltage (V_{dc}). The starting mode is controlled in the same way as this mode where the (C_{dc}) capacitor is charged using a starting resistor. The starting circuit will be discussed in Section (6.3).
2. Grid-connected mode - the dc/dc converter is controlled to provide the required reference dc current from the battery bank. The reference current is calculated by the supervisory controller.

The supervisory controller provides the batteries' current reference signal (I_{battr}) (see Figure (6.1)). If this signal is positive, the batteries will be charged by the buck converter dc/dc converter. The boost converter would then be switched off. However, if the (I_{battr}) signal is negative, the batteries will be discharged by the boost converter and the buck circuit would be OFF. The batteries would be switched off if the batteries' current is zero. In the grid-connected mode, the batteries would not be discharged to values less than (*50%)* of their capacity and would only be charged. This will increase the life time of the batteries [203]. In the standalone mode, discharging the batteries less than (*20%*) is acceptable under controlled circumstances; while at less than (*10%)* the batteries will be charged only [204] by the renewable energy generators. Therefore, the supervisory controller will manage the batteries' charging/discharging to provide a better performance. This will increase the battery life and increase the system availability. The battery charging/discharging currents are limited to the batteries and the charger circuit rating. More details on how to deal with this problem will be discussed in Section (6.3).

6.2.4. INVERTER SIDE

The H-bridge single-phase inverter control is controlled as discussed before in Chapter (5). The supervisory controller is used to switch between the grid-connected and the standalone modes of operation, as shown in Figure (6.3). This inverter is controlled to guarantee the following:

1. The dc bus voltage (V_{dc}) is constant.
2. The current and voltage waveforms are modulated to fulfil the international standards. This is performed using a control process was discussed before in Section (5) and summarized in Figure (6.3).
3. The load demand is fulfilled according to the supervisor control signals. Those signals are directed to the inverter reference currents.
4. The supplied power is controlled to be in the required power factor, which is unity in this case. This is performed by matching the reference current to the grid voltage using PLL controller.
5. The injected dc current component to the grid is eliminated by using the previously designed dc component measuring circuit.
6. The proposed system works properly during switching between different modes of operation.
7. The islanding condition is detected and the supervisory controller is driving the system accordingly [205].

The islanding case is detected and a zero signal would be seen by the supervisory controller, which will drive the system to the standalone operation. Once the grid was available again, another on signal would be provided to the supervisory controller to switch the grid on. The signal provided to the supervisory controller is called the islanding test signal (I.T.) and Figure (6.4) assembles how the test calculated. There are two signals compared by an (and) gate to provide the (I.T.) signal. The first signal is the grid side voltage (v_{go}), which is measured after the grid switch as shown in Figure (6.1). If v_{go} has a value (there is grid voltage), the switch output is (*1*), and if this value is zero the output is (*0*). The second value is the islanding measurement output signal which is (*0*) when the system is in standalone and (*1*) when the system is connected to the grid. The inverter output voltage is controlled on the standalone mode to provide constant output voltage. The dc voltage (V_{dc}) is controlled by the battery controller, as discussed before.

6.2.5. LOAD SIDE

Demand side load management is an essential subject in the recent years. One of its applications is to provide stability and security to the utility grid. Furthermore, it can be used by utility grid end users to reduce prices for the electricity market [204]. In this study, load management is performed to increase the total power captured by the load and to reduce the renewable energy generators disconnections. This will increase the overall availability of the system. The load management is needed when the system cannot provide the full demand on the standalone mode of operation. The local loads are given different priorities, according to the importance of every load. This can be switched ON and OFF by the supervisory controller.

In the research in the present study, every local load will be assigned with a priority. The loads will be switched ON and OFF according to the SOC of the batteries. A detailed description of the load management process will be discussed in the supervisory controller section. The loads are modelled in the simulation process as a controlled resistor. The resistor value is determined according to the load profile, the root mean square value of the load voltage and the power factor. The loads also have a capacitor and an inductor to model the reactive part of the load.

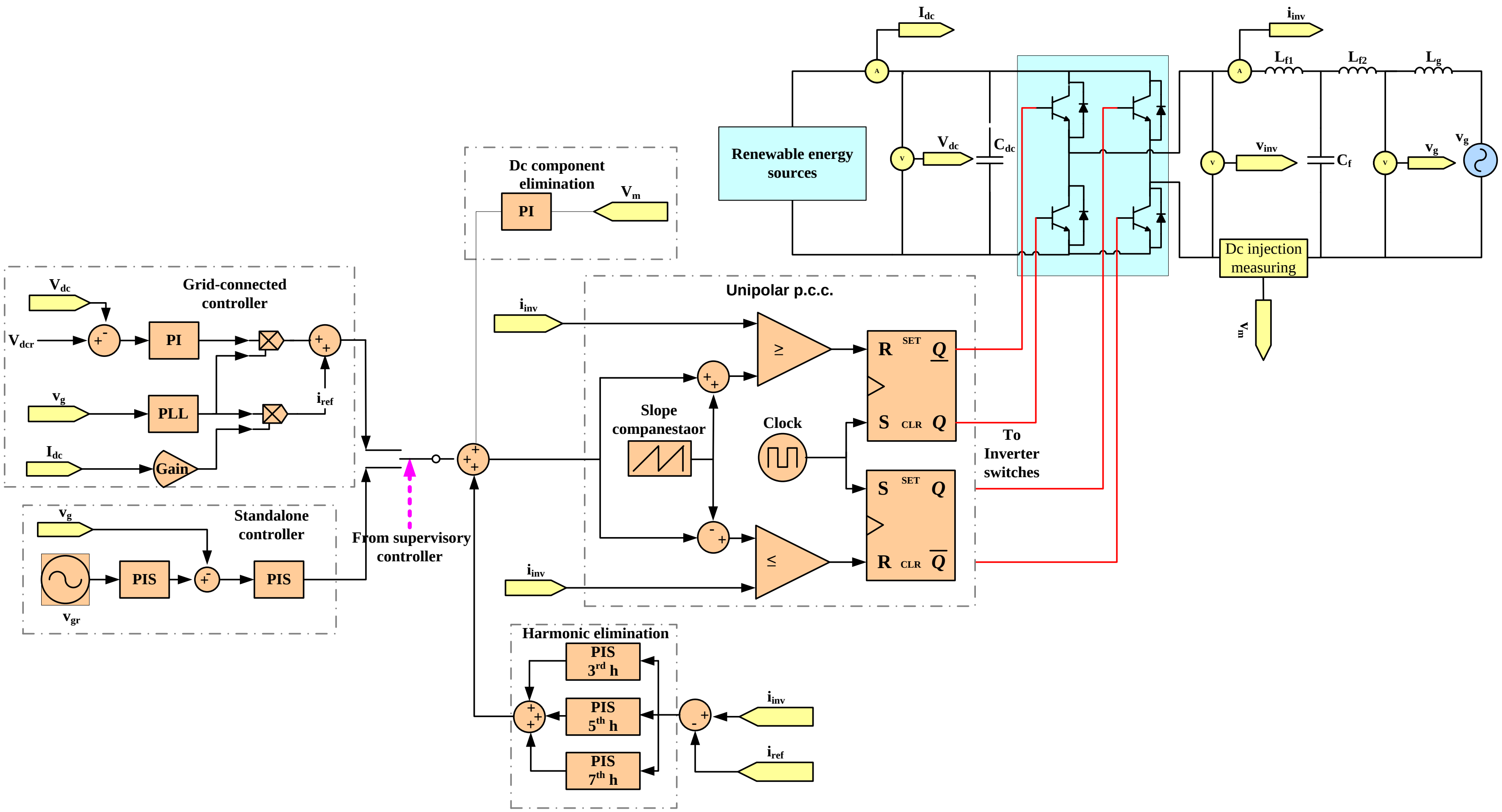

Figure (6.3) Control on the inverter side

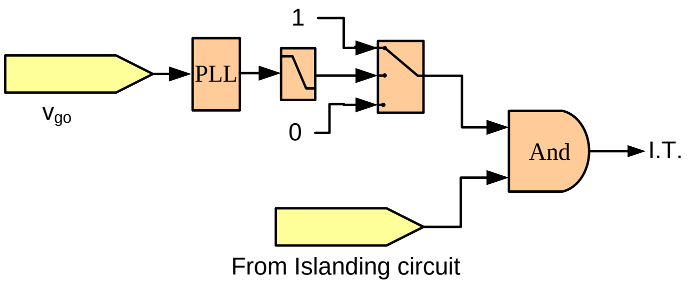

Figure (6.4) The islanding test (I.T.) signal calculation

6.3. THE SUPERVISORY CONTROLLER

The supervisory controller for hybrid power systems is a system wide controller which supervises the modes of operation and manages the power flow in the power system. One of the important controller rules is to guarantee smooth transition between the different modes of operation. Furthermore, the supervisory controller also sets the local controllers for the different components at the different modes of operation in order to ensure their optimum operation. The supervisory controller could be illustrated as shown in Figure (6.5).

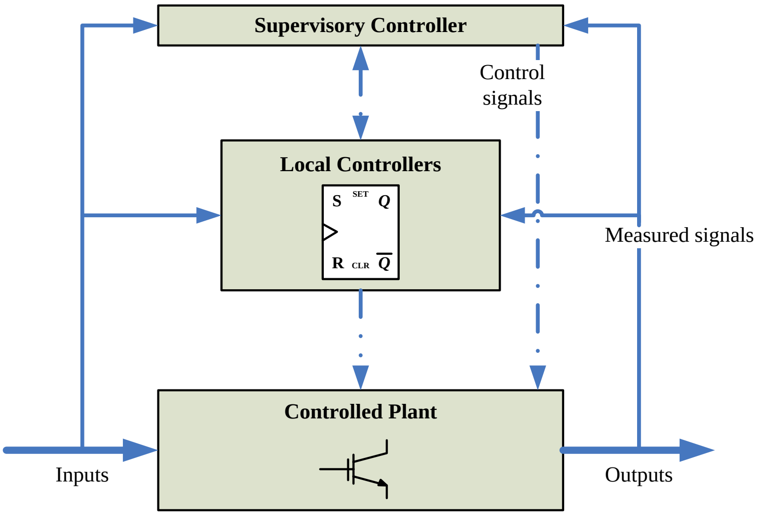

Figure (6.5) Supervisory controller for a hybrid system

The hybrid power system modes are designed to provide system equilibrium conditions. The system characteristics for these modes would be held in specific constraints. Furthermore, the energy flow would be balanced between the system components. The number and the assemblies of those operating modes are designed according to the system components and configurations. The proposed supervisory controller controls the hybrid PV-wind-generated system with batteries storage. The system can work in grid connection mode when the utility grid is available and in standalone mode when the utility grid is unavailable. The proposed power management strategy depends on the SOC of the battery storage and the utility grid availability. The main objective of the power management strategy, including load management, is to accomplish power balance between energy sources and loads on all modes of operation. The supervisory controller is based on the following:

1. The system will always be connected to the grid if the grid is available or if there is no fault.
2. The extra generated power to the load demands will be directly transferred to the grid when the batteries are fully charged or when the batteries do not exist in the system.
3. The load will draw power from the grid only if the power produced by the energy sources and the storage is not sufficient for the load. This could happen when the SOC of the batteries is lower than a specific value; then, the batteries would not be discharged.
4. In the standalone mode, the batteries are always connected to provide balance between the load and the renewable energy sources.
5. Load management will only be used in the standalone mode operation.
6. If the charge current is higher than the rating of the batteries or power electronics, the system will be regulated to the reduced power mode.
7. If the discharge current is higher than the rating of batteries or power electronics, the extra power would be supplied by the grid in the grid mode. In the standalone mode, the system would use load management to overcome this problem.

Therefore, the system has one starting mode and two main operating modes:

- Starting mode
- Standalone mode
- Grid-connected mode

The transitions between the modes of operations including the primary ones are shown in Figure (6.6). As shown in the figure, the operating modes of the system can be described in the following sub-sections.

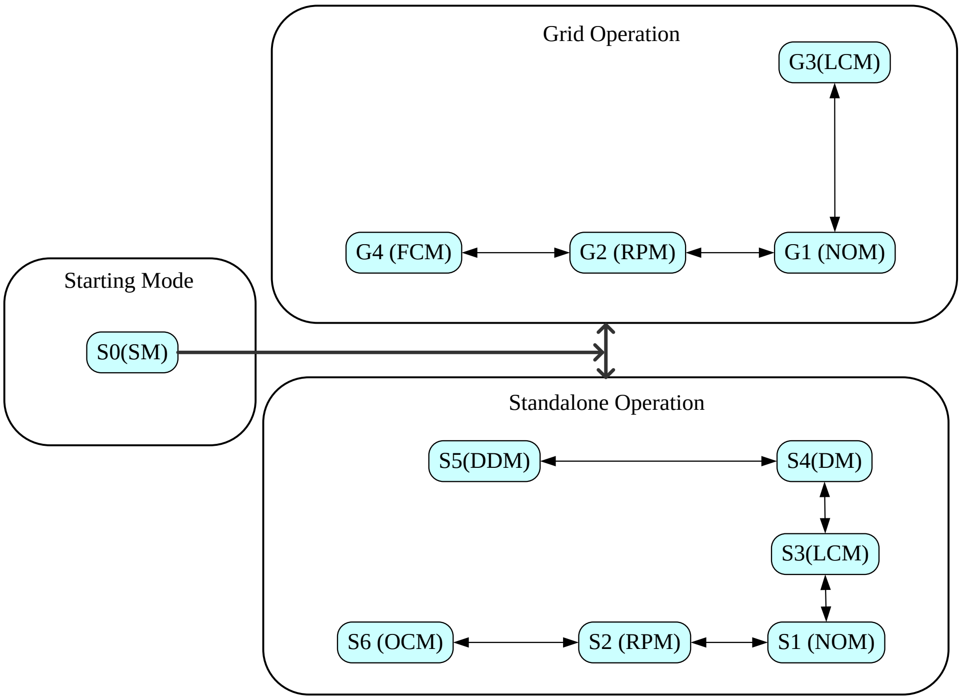

Figure (6.6) Different modes for the renewable energy system

6.3.1. STARTING MODE (S0(SM))

The starting, or standby operation, is the process deployed when the Hybrid PV-Wind generated system is switched on. It is the state S0(SM) on Figure (6.6) where all the generators, loads and grid are disconnected. In the circuit shown in Figure (6.1), where the supervisory controller tests the battery charge, and then switches on the starting resistance with batteries and dc capacitor (C_{dc}). The starting resistance is designed to reduce the high starting current when the storage element is connected to the fully discharged dc capacitor (C_{dc}). If the starting resistor is not there, the batteries will be shorted at the starting period and the battery charger circuit could not handle the starting current. The starting resistor is chosen to limit the starting current within the circuit rating. The starting resistor is applied for *1* s until the dc bus voltage reaches the required dc bus voltage (i.e. *400* V). In the next stage, the PV generator, wind generators, inverter and loads are switched on. In a very special case, the grid could be used to charge the batteries. That might be needed if the batteries were fully discharged and the renewable energy sources are not producing much power. Therefore, the batteries could be charged by the grid inverter. The capability of the proposed inverter control to work in such a mode was discussed in chapter (5).

6.3.2. STANDALONE MODE

This operational mode is activated when the utility grid is not available. The availability of the utility grid is detected according to the voltage and current sensors in the input of the utility grid. On this mode, the battery bank is always connected to the system. The dc link voltage (V_{dc}) is controlled directly by the battery bank side to be kept constant (i.e. *400* V). Furthermore, the different states are dependent on the battery state of operation. In the following, these operating states will be discussed.

A. NORMAL OPERATING MODE (S1(NOM))

This mode occurs when the SOC of the batteries, which, for the purpose of this study, is considered between *0.5* p.u. and *0.9* p.u., is in the normal working region. Furthermore, the PV and the wind generators are connected to the system normally and the power produced according to the weather conditions. All the loads also connected and the system is then capable to supply the full demand.

B. REDUCED-POWER MODE (S2(RPM))

The reduced power mode is needed when the power produced by the renewable energy sources increases to values higher than the rated ones due to the reasons discussed before in chapter (5). Furthermore, as the batteries are fully charged, i.e. SOC is above *0.9* p.u., it is necessary to reduce the power supplied by the renewable energy generators. This will keep the generators connected to the system, because the other solution is then to disconnect the generators. The reduced power mode was presented also in chapter (5).

C. LOW CHARGING MODE (S3(LCM))

The LCM will be considered as soon as the SOC of the batteries falls below *0.5* p.u.. To avoid the fast discharging of the batteries, the supervisory controller will then switch off the lowest priority load (Load P3).

D. DISCHARGE MODE (S4(DM))

If the SOC was decreased to a value below *0.3* p.u., the batteries would then be discharged. This means more loads have to be disconnected to keep the system working. The loads with the second priority (Load P2) added to Load P3 would be switched off on the system.

E. DEEP DISCHARGE MODE (S5 (DDM))

As the batteries continue to discharge (i.e. SOC< *0.1* p.u.) and the renewable energy generators is not able to supply the load, the supervisory controller will switch off all the loads. This will protect the batteries from deep discharge. In this stage, the renewable energy generators will only charge the batteries.

F. OVER -CHARGE MODE (S6 (OCM))

The OCM is the opposite of the DDM (i.e. SOC>= *0.95* p.u.), and then the renewable energy generators is disconnected to protect battery bank over-charging. Therefore, the batteries will only supply all the demands until the SOC is in the normal range again.

6.3.3. GRID-CONNECTED MODE OF OPERATION

The grid will be connected when it is available. The batteries work as the backup source on the normal operating mode while the grid will only be used in special cases, which will be discussed later. The dc link voltage (V_{dc}) is controlled from the inverter side. This means; the supervisory controller is working to reduce the power extracted from the utility grid. That will reduce the overall cost of the system. The operating states of the grid connected mode could be described in the following points.

A. NORMAL OPERATING MODE (G1(NOM))

As the utility grid is available and the batteries measure *0.9* p.u.>SOC >*0.5* p.u., the system would then work normally (G1(NOM)). In this mode, the renewable energy generators are both connected and their operation depends on the weather conditions. The battery bank would be charged if the generated power was more than the load demand, and it would be discharged if the generated power was insufficient to the load demands.

B. REDUCED POWER MODE (G2(RPM))

When the utility grid is available, the RPM is applied only if the power produced is more than the system rated value. The batteries work then is the same as the G1(NOM) discussed in the previous section.

C. LOW CHARGING MODE (G3 (LCM))

If the SOC of the batteries is less than *0.5* p.u., the system becomes on LCM and the batteries have to be disconnected. The utility grid works as a backup source for supplying the extra load demand if the generated power is less than the load demands. The generated extra-power will charge the batteries if it is more than load demand.

D. FULL CHARGE MODE (G4(FCM))

This mode is applied when the batteries are fully charged (i.e. SOC >*0.9* p.u.). This mode is the opposite of the G3(LMD) with respect to the battery operation. The batteries would be discharged when the generated power less than the load demands. In case of the generated power higher than the load demand, the extra-power will be supplied to the grid.

6.3.4. THE SUPERVISORY CONTROLLER ALGORITHM

A simplified proposed algorithm is shown in Figure (6.7), while the inputs and outputs of the algorithm are shown in Figure (6.1) and in Table (6.1). As the system starts the supervisory, controller tests the batteries and then drives the system to the starting mode (S0(SM)). The utility grid is tested and, if it is available, the controller switches on the grid, or the controller drives the system to the standalone mode. In the standalone mode, the secondary system modes are derived according to the SOC of the batteries as shown in the algorithm. The grid availability is tested all the time and, if it is available, the controller switches the system to the grid-connected mode. If the power generated at any time is higher than the rating, the system enters the reduced power mode. The batteries are always kept charged at least to *0.1* p.u. in any mode of operation; this protects them against deep discharging and keeps some charge for the next starting up. All the inputs and constraints in the supervisory controller are in per unit values. This will make the supervisory controller capable of supervising systems with different system ratings. Furthermore, the controller will be capable of supervising a single renewable energy source or multi-source systems. The modularity of the supervisory controller will provide a wide range of renewable energy systems which the controller can also supervise.

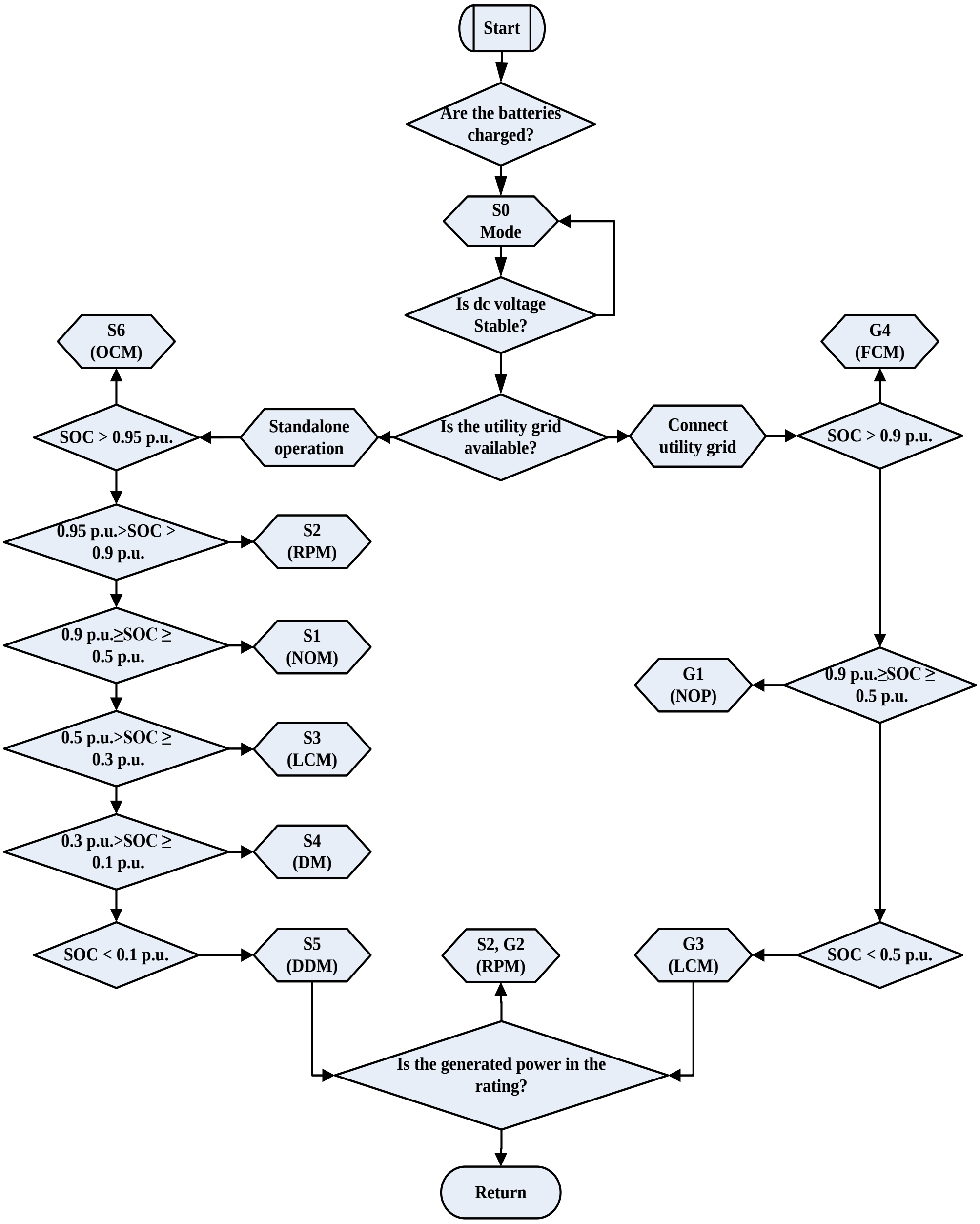

Figure (6.7) The algorithm of the supervisory controller

6.4. SIMULATION RESULTS

The system shown in Figure (6.1) was modelled and simulated by dynamic simulation using the Simulink/ Matlab with PLECS software. The supervisory controller was programmed by conventional programming using an embedded Matlab function. The system will run with dynamic measured input data of solar radiation and temperature. The SOC will be changed to simulate how the supervisory controller will supervise the system during the different modes of operation. This will demonstrate the ability of the controller to manage the system operation. The wind generator is considered in these results with very small inertia to speed up the starting operation and reduce the simulation time. The inputs of the system, in this section, were changed to actual measured solar radiation, wind velocity, and temperature data. The data was collected at Durham University, and it is shown in Figure (6.8). The load demand was divided as discussed before to three priorities

1- House load demand; it is considered at *.75* kW.
2- Pump Load demand which was assumed as constant power load of *.5* kW
3- Another constant load of *.5* kW, which was considered as a heating system.

Every load from the three loads was assigned a priority. The house load was assigned with the highest priority (P1 Load), the heating system with the second priority (P2 Load) and the Pump was assigned the lowest priority (P3 Load). According to the given data, the system has been simulated. The results are shown in Figures (6.9), (6.10), (6.11) and (6.12).

Figure (6.9) shows the supervisory controller output ON/OFF control signal. These control signals are described before as shown in Figure (6.1). The power flow and the SOC of the batteries are shown in Figure (6.10). The controlled power quality signals are shown in Figure (6.11).The system modes were controlled according to system mode signal (S.M.). This signal is 0 in the standalone mode at the first *85* s. However, it is 1 in the grid mode during the rest of the simulation time. The results can be discussed as follows:

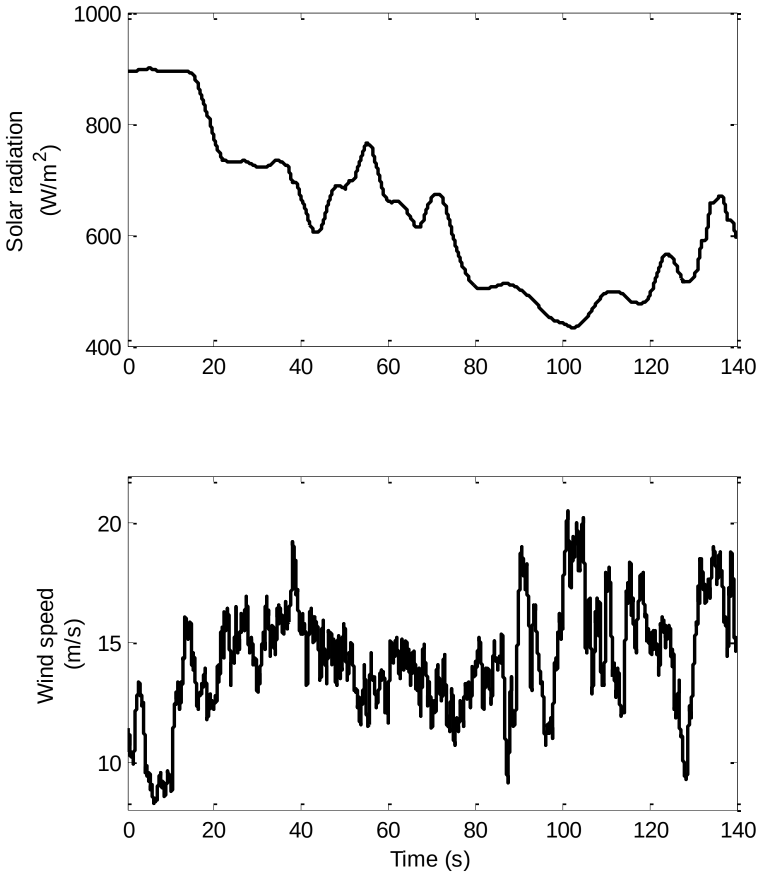

Figure (6.8) Simulation inputs: load demand profile (P1 Load), solar radiation, and wind velocity, respectively

__Starting Mode (S0(SM)) – (from 0 s to 1 s)__

On this mode, the system was started by the batteries – as discussed before – only to charge the dc link capacitors (C_{dc}). Figure (6.10) shows how the dc voltage (V_{dc}) is building up at this time. At the end of this mode, the supervisory controller provided signals to the PV and wind generators to start up. These are shown on the ON/OFF signals of Figure (6.9) (also see Figure (6.1) and table (6.1)). According to the SOC of the batteries, the load was also started by the load mode signal (L.M.).

__Standalone mode-(from 1 s to 85 s)__

The supervisory controller tested the availability of the grid after the starting up mode (S0(SM)). The utility grid was found unavailable, and for (*85* s) the system was simulated on the standalone mode. The different operating states of the standalone mode were controlled according to the SOC which is shown in Figure (6.10). During this time, the simulation output can be described as follows:

1. From *1* s to *20* s

The simulated SOC signal, between *1* s and *20* s, was *0.6* p.u. and 0*.8 p.u.*. Therefore, the system was on the (S1(NOM)) mode of operation. During this mode, the supervisory controller switched on all the loads and the generators while it switched off the grid as shown in Figure (6.9). According to the solar radiation, temperature and wind velocity, the PV and wind generators produced the power, as shown in Figure (6.10). The load demand is also shown in the same figure. As the load demand was higher than the generated power, the batteries current – as shown in Figure (6.10) – was positive, which means that the batteries were discharged during this time. In Figure (6.11), the dc voltage (V_{dc}) is kept at its designed value at *400* V. As the grid was off, all the power was supplied by the inverter and the grid power was zero. Furthermore, the reactive power was kept at zero value – as shown in the figure – to maintain a unity power factor.

2. From *20* s to *30* s

During this time the system was on the (S2(RPM)) mode of operation as the SOC measured *0.92* p.u., as shown in Figure (6.10). The total wind and PV generated power was lower than the load demand, so the supervisory controller discharged the batteries (the battery current was positive as in Figure (6.10)). Therefore, the system works the same as the S1(NOM). If the generated power had been more, the supervisory controller would have reduced the power generated to be equivalent to the demand load.

3. From *30* s to *40* s

As the SOC measured more than *0.95* p.u., as shown in Figure (6.10), the system was on the S6(OCM). On this mode of operation, the supervisory controller switches off the wind and PV generators as shown in Figures (6.9) & (6.10). As a result, the load was only supplied by the batteries.

4. From *40* s to *60* s time scale

When the SOC was reduced to *0.4* p.u. and then to *0.3* p.u. (Figure (6.10), the system was on the S3(LCM). In this mode, the supervisory controller again switched on the PV and wind generator as shown in Figures (6.9) and (6.10). The load with the lowest priority (P3 load) was switched off while the other load was kept on (Figure (6.9). By looking at Figure (6.10), it can be seen that the batteries were charging and the battery ban current was negative during this mode. This happened because the generated power from the PV and wind generator was higher than the load power. The dc voltage (V_{dc}) and the reactive power generated by the inverter were kept constant. This can be observed in Figure (6.11).

5. From *60* s to *70* s

If the SOC is reduced to more than *0.2* p.u., as shown in Figure (6.10), the system enters the S4DM. The supervisory controller switches off the load with the second priority (P2 load) over the load with the third priority (P3 load), as shown in Figure (6.9). As a result, more current would be directed to the batteries by the supervisory controller (Figure (6.10)).

6. From *70* s to *80* s

The SOC reduced to *0.1* p.u., which was the S5(DDM). Consequently, the supervisory controller switched off the whole demand (L.M.) as shown in Figure (6.9). The total power generated by the renewable energy sources would be instantly directed to the batteries. The dc voltage (V_{dc}) was also kept constant, which means that the capacitor was kept charged.

7. From *80* s to *85* s

The SOC was increased again to *0.2* p.u. as shown in Figure (6.10). Therefore, the whole demand was switched on again as shown in Figure (6.9) while the loads with priorities (P3 load, P2 load) were switched off. The battery bank current (Figure (6.10) was negative. This means it was charged during that time. Figure (6.9) shows that the batteries were always connected. The grid power was always zero, as shown in Figure (6.11); this means the grid was disconnected. The same figure shows that the dc voltage (V_{dc}) was kept constant during the whole standalone operation. Furthermore, the reactive power that was generated by the converter is also always zero. This means the power factor was kept constant during the entire stand-alone operation. This figure demonstrates that the inverter controller was successful during the standalone operation with different system modes and dynamic change of the input weather conditions. The supervisory controller was also successful in managing the power during the entire range of the standalone operation.

Grid mode (from 85 s to the end time scale)

At time (*85* s), the grid was available so the supervisory controller detected that and provided ON (S.M.) signal to switch on the grid. Therefore, the system is in the grid mode. The dc voltage control is transferred from the batteries side to the inverter side as explained before in Section (6.3). An over shoot happened in V_{dc}, during mode transfer, and that is shown in Figure (6.11). The secondary modes of the grid-connected mode during its operational time can be discussed as follows:

1. From *85* s to *100* s

The SOC was still measured as *0.2* p.u. and increased to *0.4* p.u., and hence the system was on the G3(LCM). Therefore, the supervisory controller would stop the batteries from discharging. The batteries were disconnected, as shown in Figure (6.9), as the batteries' mode signal (B.M.) was reassigned zero. This happened because the power generated from the renewable energy sources was lower than the load power as shown in Figure (6.10). As a result, the load drew power from the grid as shown in Figure (6.11).

2. From *100* s to *120* s

As the SOC signal was increased to *0.6* p.u. and *0.8* p.u., the system was in the G1(NOP). The batteries were switched on again (see Batteries mode signal in Figure (6.9)). As the power generated was higher than the load power (see Figure (6.10)), the batteries current was positive. The batteries were discharged during this time. All the power was provided by the inverter – as shown in Figure (6.11) – and the grid power was reduced again to zero.

3. From *120* s to *130* s

The SOC signal was simulated to a value of *0.9* p.u; hence, the system was switched to G4(FCM). As the power generated was less than the load demand (Figure (6.10)) the battery current was negative. The supervisory controller discharged the batteries, and the system acted the same as the G1(NOM). If the generated power had been higher than the load demand, the batteries would have been switched off and the extra power would have been converted to the grid.

4. From *130* s to *140* s

The system returned back again to the G1(NOM) as the SOC was *0.8* p.u.

Following on from the previous discussion, when the grid was available, the supervisory controller was always connected, as shown in Figure (6.9) (see S.M. Signal). The load also was always connected while the batteries were disconnected as the SOC was less than *0.5* p.u. The different controllers were working well with the different modes of operation, including battery ON/OFF modes and input weather condition dynamics (Figure (6.8)). The dc voltage (V_{dc}), as shown in Figure (6.11), was constant in the specified value with power changes. The reactive power in the output of the converter was always kept at zero, and hence the power factor was always unity.

The simulation results shown in Figure (6.12) are the ac currents of the inverter output, the load and the grid powers. In the standalone mode, the grid current was always zero, and the current of the demand supplied by the inverter. As the load was disconnected between times (i.e. *70* s, *80* s), the inverter was switched off (see mode S5(DDM)). The grid was switched on and the system was on the G3(LCM) (time scale *85* s to *100* s); hence, the batteries were switched off. A small current was provided by the grid to supply the extra demand as shown in the figure. On the rest of the time scale, the batteries were supplying the extra power, but a small current – shown in the figure – was supplied by the grid. The cause of this small current was that there was a small inductance in the load. Since the inverter was controlled to provide unity power factor (see Figure (6.11)), the reactive power was supplied by the grid.

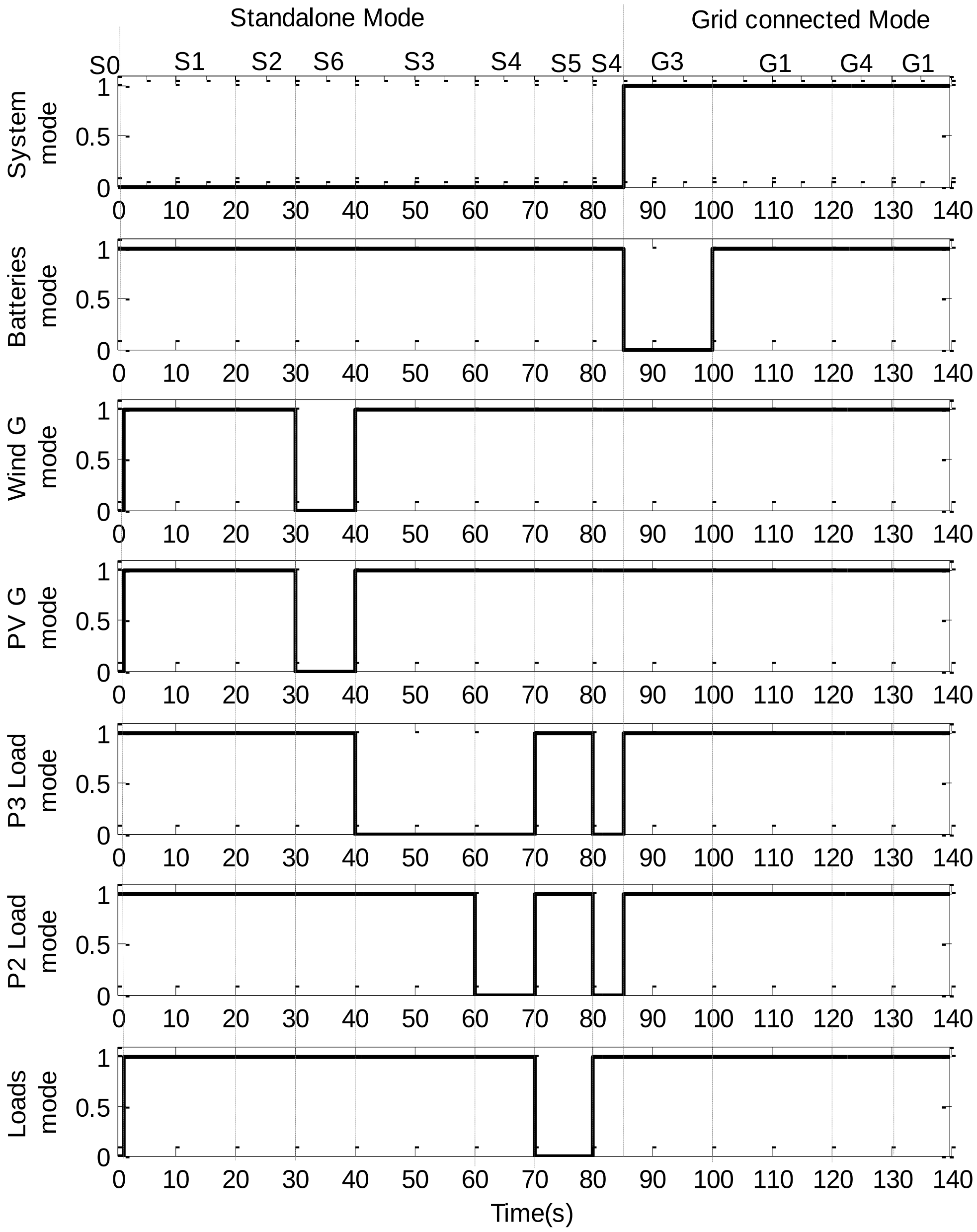

Figure (6.9) ON/OFF supervisory controller control signals

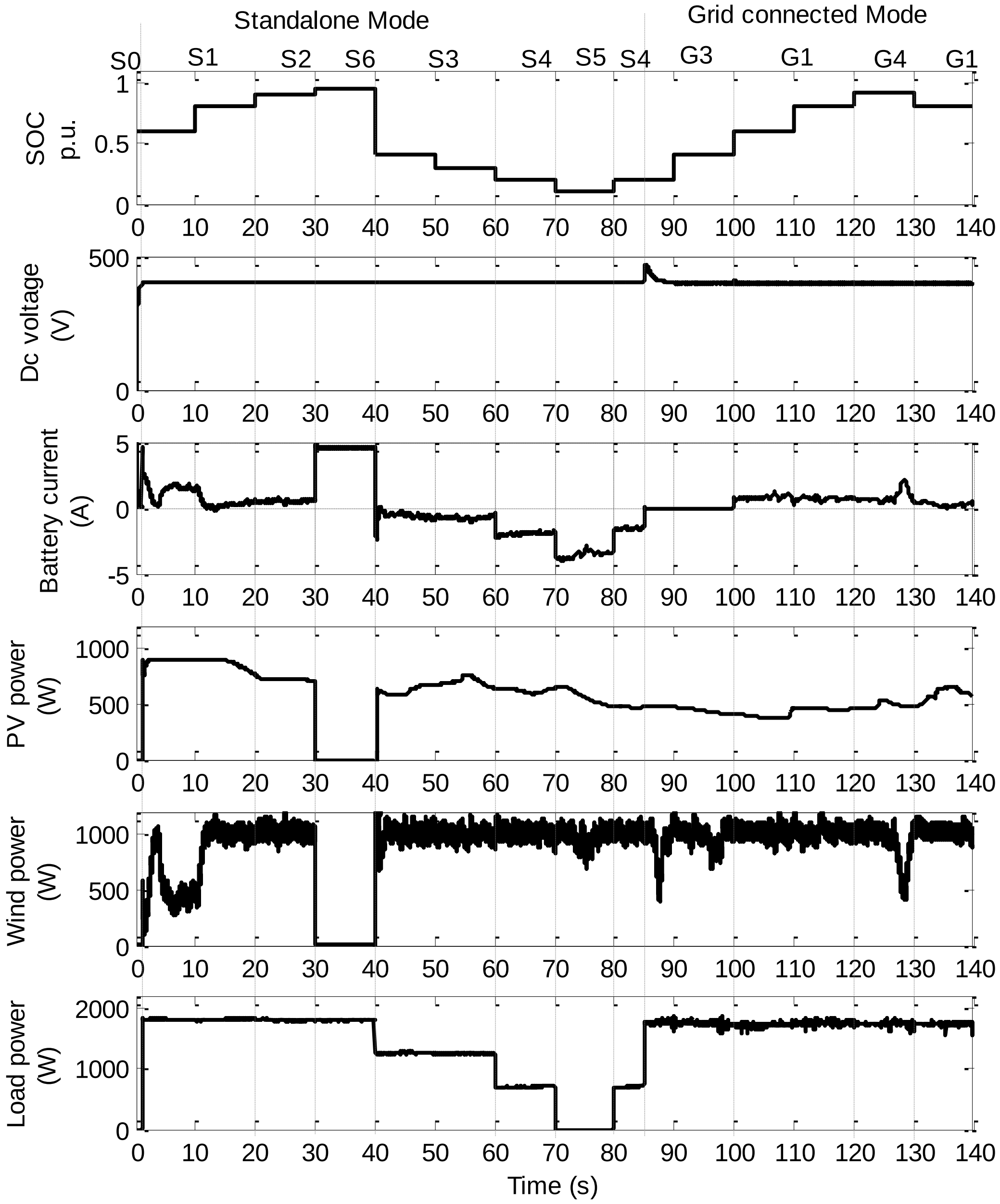

Figure (6.10) Batteries SOC, dc bus bar voltage, battery current, PV power, wind power, and load power

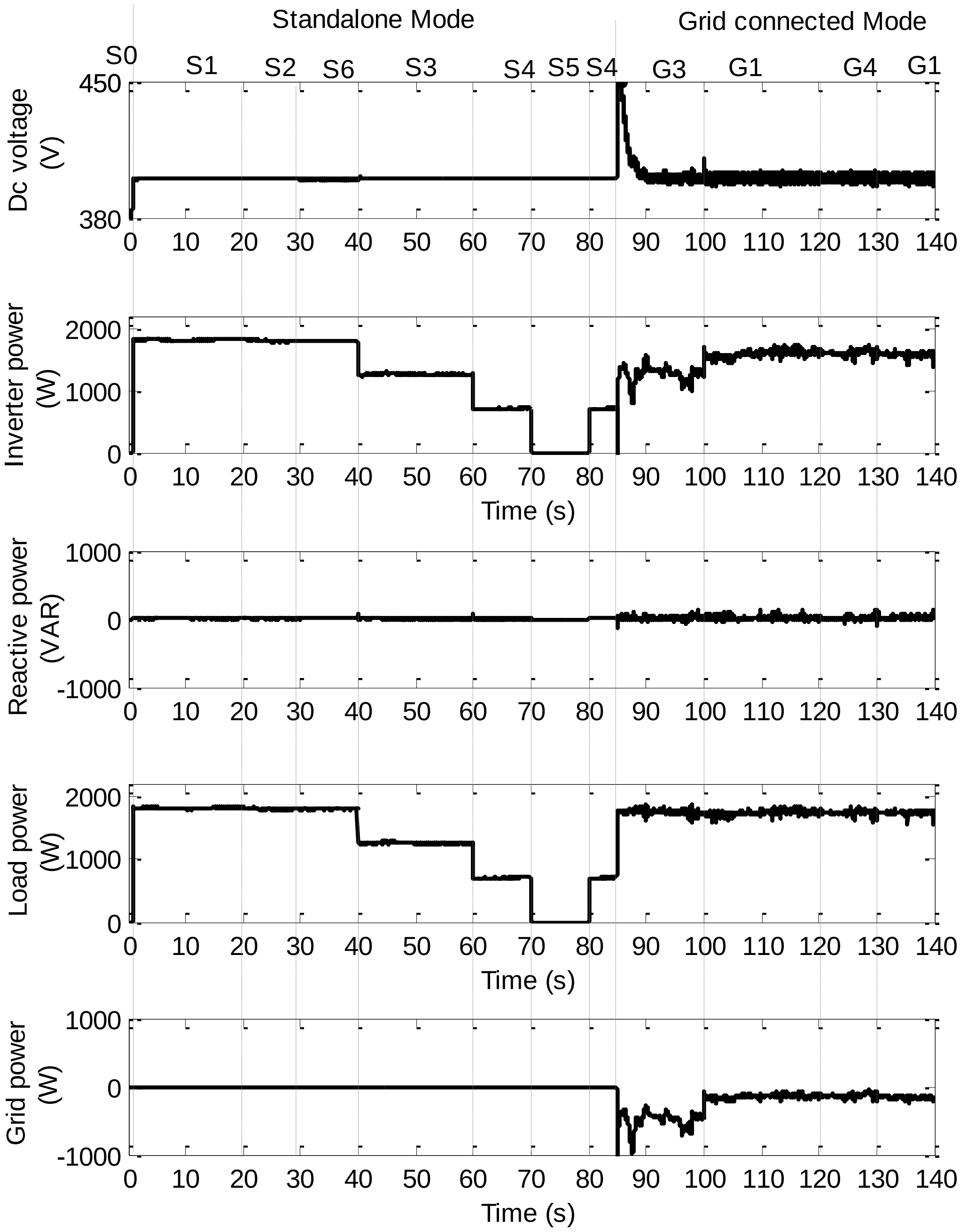

Figure (6.11) Demonstration of local inverter controllers

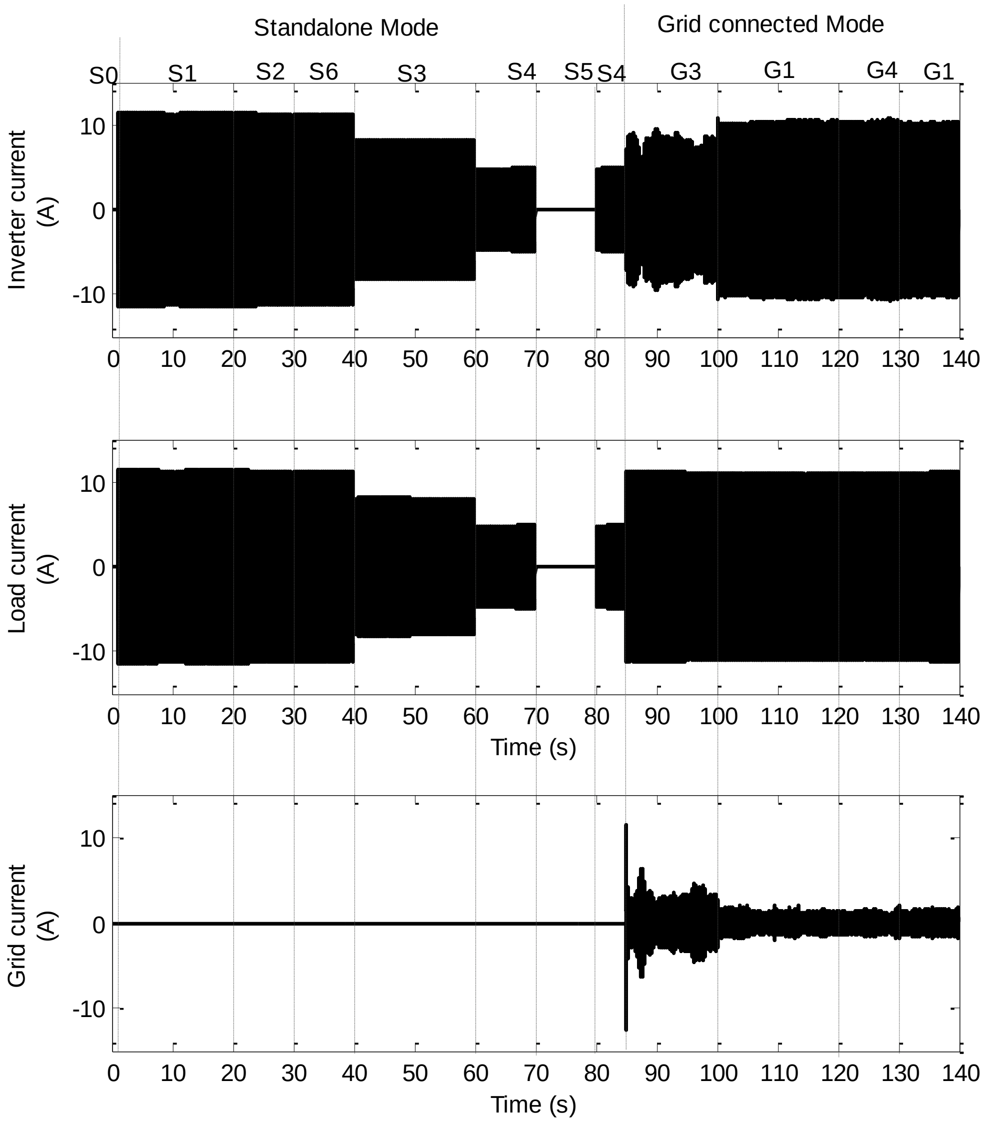

Figure (6.12) Ac side currents

CHAPTER (7)

CONCLUSION

This chapter concludes the thesis, as summarized in the following sections:

7.1. WIND GENERATOR SIDE

An electrical control scheme to deal with MPPT at low and moderate wind speeds and constant power soft stalling at excessive wind velocities has been proposed for small-scale vertical axis wind turbines. The MPPT is based on a simple lookup table for the characteristics of dc output voltage-current maximum power. The new constant electrical power stalling is based on the concept of, and aims at, keeping the electrical power and generator speed within limits. The method is the reverse of what is normally used for MPPT control and completely avoids the need for explicitly finding the target operating point, which changes with wind velocity. The system is modelled and a PI controller designed. As the wind velocity increases beyond the rated value, the system automatically enters the stall mode. A compensating 1st order lag is added in the control loop to stabilize the system. It has been found that the time constant needed increases, proportional to the turbine moment of inertia and the targeted maximum wind velocity. With different turbine characteristics and application scenarios, a customized design procedure was carried out to determine the PI control gains and the 1st order lag time constant. To prevent reduction in MPPT efficiency, the time constant was adapted online according to the current measured on the dc side of the generator rectifier. The proposed control method has been tested by simulation and laboratory experiment. Advantages of the proposed scheme include simplicity of controller design, ease of implementation, avoidance for an anemometer or shaft encoder, no need for aerodynamic control, and much reduced short-term over loading requirement on the generator and power semi-conductor devices. The scheme has the potential to reduce the cost and size of the wind turbine generator system.

7.2. PV GENERATOR SIDE

Direct duty ratio control of the PV generator, which is based on hill climbing algorithms, was described as a very advantageous method due to its simplicity and ease of implementation. Therefore, it was chosen as the base of the control algorithm for the PV generator side in this study. The design of the perturbation parameters for this proposed method was always found favorable. It was reported that it would guarantee better performance of the hill climbing MPPT controllers. It was also found that, as a result, the MPPT efficiency would be increased, the fluctuation in power reduced, and the output power quality of the system increased. Design guidelines for a hill climbing algorithm perturbation parameters have also been proposed. The effectiveness of the proposed guidelines was verified by simulation. The MPPT controller combined with reduced power mode algorithm was developed, and it was based on variable step size incremental conductance method. The proposed method was easy to implement in simple microcontrollers, and it was fast compared to normal fixed step incremental conductance, too. The reduced power mode was used to limit the output power of the PV generator if the power generated was over the system rating due to reduced ambient temperature values and high solar radiations. This mode was also used if there was excess power generated in the system as it operated on standalone mode. The algorithm was demonstrated by simulation and experimental results.

7.3. INVERTER SIDE

Based on peak current control, a novel current controller was developed to control a single-phase H-bridge inverter. The method was fast and easy to implement, and adding selective harmonic elimination made the method corresponding to international standards. This was demonstrated by simulation results. The method was applied to grid-connected control, as it was used to inject active power keeping the power factor and dc link voltage at specified values. To demonstrate the validity of the method, simulation was applied on different active power levels, power factor values and two quadrant operations. The simulation results were found adequate. The standalone mode was required in this study so that the same method might be applied to this operational mode. In this mode, the output ac voltage was required to be kept constant at different power levels. Simulation results were applied and they demonstrated the control method. The issue of dc current injection has generally been of growing concern due to the increasing usage of single-phase inverters as the demand for small scale renewable power generation increases. One of the challenges to eliminate the dc current injection is to accurately measure the small dc component contained in the inverter output current, because the fundamental ac component is very large. In this study, a method for eliminating the dc current injection of a single-phase H-bridge inverter was proposed. The proposed method was based on designing a passive filter to make the dc component more measurable in the filter output. A simplified method for designing the compensating control was proposed for the inverter PWM process. The method has been verified by both simulation and experimental test. The simulation and test results demonstrated that the proposed method improved the accuracy of measuring the very small dc current component. This improvement helped with removing the dc component to meet the obligatory local and international standards.

7.4. SUPERVISORY CONTROL

For the proposed small-scale hybrid PV-Wind generation systems, a supervisory controller, which manages the modes of operation and the power flow in the power system, was proposed. This controller was designed to operate in conjunction with the newly developed local controllers. The system modes and states were designed to provide system equilibrium conditions, and the characteristics of these modes were held in specific constraints. Furthermore, the energy flow was balanced between the system components. The number and the assemblies of those operating modes were designed according to the system components and configurations. One of the important controller rules was to guarantee smooth transition between the different modes of operation. The proposed power management strategy depended on the SOC of the battery storage and the utility grid availability. Furthermore, the supervisory controller also set the local controllers for the different components on different modes in order to ensure their optimum operation.

The system containing the entire power conditioning unit was modelled in Matlab/ Simulink with PLECS software. It included the supervisory controller and the local controllers for the different system components. The simulation ran took into account the different modes and states of the system. The results demonstrated that the power conditioning unit had a satisfactory performance and shifted between the different operational modes and states smoothly.

7.5. THE CONTRIBUTIONS

The contributions in this thesis could be summarized as follows:

1. A constant power soft stalling controller is proposed for VAWT generator. This is based on electrical control; therefore, it is simple, easy to design, and easy to implement. As a result, it will reduce the cost and size and increase the reliability of the VAWT generators.
2. Design guidelines for the perturbation parameters of the hill climbing algorithm are provided in the PV generator side. These guidelines are expected to increase the MPPT efficiency and improve the system performance.
3. A MPPT algorithm with reduced power mode based on variable step incremental conductance is proposed and verified.
4. Dc current injection elimination method is proposed for the single phase H-bridge inverter.
5. A new direct current control method for a single-phase H-bridge inverter is derived. This method is based on peak current control and single harmonic elimination.
6. Based on these proposed local controllers, a supervisory controller is also proposed to manage the power between the different system components. Furthermore, it supervises the local controller operations and system modes.

7.6. FUTURE WORK

The author believes that the power conditioning unit proposed in this study is the future for such small-scale hybrid PV-Wind generation systems. The following points would complete the work and make it available for the future market.

1. The proposed VAWT wind generator controller needs to be tested with different wind turbines of different Cp-λ(TSR) curve shapes. It also has to be applied in different power electronic configurations. Furthermore, this

controller needs to be tested with a real wind turbine and implemented in a microcontroller.

2. A microcontroller implementation is also required to the proposed PV generator controller.
3. The peak current controller, which has been applied to the H-bridge inverter, will experimentally be demonstrated.
4. The H-bride inverter and the proposed dc injection elimination circuit require more testing.
5. Experimental set-up is required for the verification of the proposed system with the power conditioning unit control.
6. A single layout integrating the converter power and control circuits will be designed and tested in the future.

References

[1] Organization Of The Petroleum Exporting Countries (OPEC). World oil outlook (2009). [Online]: http://www.opec.org/opec_web/en/.

[2] Exxonmobil. Outlook for energy - A view to 2030. [Online]: http://www.exxonmobil.com/.

[3] Energy Information Administration (EIA). International energy outlook (2009). [Online]: www.eia.doe.gov/oiaf/ieo/index.html.

[4] E Martinot and J Sawin, "Renewables global status report 2009 update," Renewable Energy World International Magazine, vol. 12, no. 4, 2009. [Online]: http://www.ren21.net/globalstatusreport/g2009.asp.

[5] M Liserre, T Sauter, and J Hung, "Integrating renewable energy sources into the smart power grid through industrial electronics," IEEE Industrial Electronics Magazine, vol. 4, no. 1, pp. 18-37, 2010.

[6] British Wind Energy Association (BWEA). UK market report: Small wind systems. [Online]: http://www.bwea.com/.

[7] Global Wind Energy Council (GWEC). Global Wind Report 2009. [Online]: http://www.gwec.net/index.php?id=8.

[8] J Guerrero, F Blaabjerg, and T Zhelev, "Distributed Generation: Toward a New Energy Paradigm," IEEE Industrial Electronics Magazine, vol. 4, no. 1, pp. 52 - 64 , 2010.

[9] International Energy Agency (IEA). Technology Roadmap: Solar Photovoltaic Energy. [Online]: http://www.iea.org/.

[10] C Wang, L Wang, L Shi, and Y Ni, "A survey on wind power technologies in power systems," in IEEE-Power-Engineering-Society General Meeting, Tampa, USA, pp. 2268-2273, 2007.

[11] A. Ahmed, L. Ran, and J. R. Bumby, “Sizing and Best Management of Stand Alone Hybrid PV-Wind System using logistical model” IFAC conference on control methodologies and technology for energy efficiency, Vilamoura, Portugal (CMTEE), 2010.

[12] S Kim, J Jeon, C Cho, J Ahn, and S Kwon, "Dynamic modeling and control of a grid-connected hybrid generation system with versatile power transfer," IEEE Transactions On Industrial Electronics, vol. 55, no. 4, pp. 1677-1688, 2008.

[13] A Mirecki, X Roboam, and F Richardeau, "Architecture complexity and energy efficiency of small wind turbines," IEEE Transactions On Industrial Electronics, vol. 54, no. 1, pp. 660-670, 2007.

[14] J Carrasco et al., "Power-electronic systems for the grid integration of renewable energy sources: A survey," IEEE Transactions on Industrial Electronics, vol. 53, no. 4, pp. 1002–1016, 2008.

[15] K Chau, C Chan, and C Liu, "Overview of permanent-magnet brushless drives for electric and hybrid electric vehicles," IEEE Transactions On Industrial Electronics, vol. 55, no. 6, pp. 2246–2257, 2008.

[16] J Baroudi, V Dinavahi, and A Knight, "A review of power converter topologies for wind generators," Renewable Energy, vol. 32, no. 14, pp. 2369–2385, 2007.

[17] D Hamill, "Power electronics: a field rich in nonlinear dynamics," in Specialists Workshop On Nonlinear Dynamics Of Electronic Systems, Dublin, 1995, pp. 164-179.

[18] S Kjaer, J Pedersen, and F Blaabjerg, "A review of single-phase grid-connected inverters for photovoltaic modules," IEEE Transactions On Industry Applications, vol. 41, no. 5, pp. 1292–1306, 2005.

[19] R Gonzalez, J Lopez, P Sanchis, and L Marroyo, "Transformerless inverter for single-phase photovoltaic systems," IEEE Transactions On Power Electronics, vol. 22, no. 2, pp. 693-697, 2007.

[20] T Kerekes, R Teodorescu, and E Aldabas, "A new high-efficiency single-phase transformerless PV inverter topology," accepted for publication in IEEE Transactions on Industrial Electronics, 2010.

[21] G Spagnuolo et al., "Renewable energy operation and conversion schemes a summary of discussions during the seminar on renewable energy systems," IEEE Industrial Electronics Magazine, vol. 4, no. 1, pp. 38-51, 2010.

[22] M Armstrong, D Atkinson, C Johnson, and T Abeyasekera, "Auto-calibrating DC link current sensing technique for transformerless grid connected h-bridge inverter systems," IEEE Transactions on Power Electronics, vol. 21, no. 5, pp. 1385-1393, 2006.

[23] T Ackermann, Wind power in power systems.: John Wiley & Sons, 2005.

[24] E Hau, Wind turbines : fundamentals, technologies, application, economics, 2006.

[25] T Burton, D Sharpe, N Jenkins, and E Bossanyi, Wind energy handbook.: John Wiley & Sons, 2001.

[26] M Prats et al., "A new fuzzy logic controller to improve the captured wind energy in a real 800 kW variable speed-variable pitch wind turbine," The 33rd Annual IEEE Power Electronics Specialists Conference (PESC 02), vol. 1-4, pp. 101 - 105, 2002.

[27] B Boukhezzar, L Lupua, H Siguerdidjane, and M Hand, "Multivariable control strategy for variable speed,variable pitch wind turbines," Renewable Energy, vol. 32, no. 8, pp. 1273-1287, 2007.

[28] E Muljadi and C Butterfield, "Pitch-controlled variable-speed wind turbine generation," in IEEE Annual Meeting of The Industry-Applications-Society, Phoenix, USA, 2001, pp. 240 - 246.

[29] W Chen and Y Hsu, "Controller design for an induction generator driven by a variable-speed wind turbine," IEEE Transactions On Energy Conversion, vol. 21, no. 3, pp. 625-635, 2006.

[30] W Chen and Y Hsu, "Unified voltage and pitch angle controller for wind-driven induction generator system," IEEE Transactions On Aerospace and Electronic Systems, vol. 44, no. 3, pp. 913-926, 2008.

[31] Z Chen, J Guerrero, and F Blaabjerg, "A review of the state of the art of power electronics for wind turbines," IEEE Transactions On Power Electronics, vol. 24, no. 8, pp. 1859 - 1875, 2009.

[32] S Hao, G Hunter, V Ramsden, and D Patters, "Control system design for a 20 kw wind turbine generator with a boost converter and battery bank load," IEEE 32nd Annual Power Electronics Specialists Conference (PESC), vol. 4, pp. 2203 - 2206, 2001.

[33] S Muyeen, R Takahashi, T Murata, and J Tamura, "A variable speed wind turbine control strategy to meet wind farm grid code requirements," IEEE Transactions On Power Systems, vol. 25, no. 1, pp. 331 - 340, 2010.

[34] W Qiao, L Qu, and R Harley, "Control of IPM synchronous generator for maximum wind power generation considering magnetic saturation," in 42nd Annual Meeting Of the IEEE -Industry-Applications-Society, vol. 45, New Orleans, USA, 2009, pp. 1095-1105.

[35] M Ali, M Park, I Yu, T Murata, and J Tamura, "Improvement of wind-generator stability by fuzzy-logic-controlled SMES," IEEE Transactions On Industry Applications, vol. 45, no. 3, pp. 1045-1051, 2009.

[36] N Nanayakkara, M Nakamura, and H Hatazaki, "Predictive control of wind turbines in small power systems at high turbulent wind speeds," Control Engineering Practice, vol. 5, no. 8, pp. 1063-1069, 1997.

[37] M El Mokadem, C Nichita, B Dakyo, and W Koczara, "Maximum wind power control using torque characteristic in a Wind diesel system with battery storage," The 6th International Conference on Electrical Machines (ICEM), Cracow, Poland pp. 385-396, 2006.

[38] C Pournaras, A Soldatos, S Papathanassio, and A Kladas, "Robust controller for Variable Speed Stall Regulated Wind Turbines," International Conference on Electrical Machines (ICEM'04), Cracow, 2004.

[39] S Kim and E Kim, "PSCAD/EMTDC-based modeling and analysis of a gearless variable speed wind turbine," IEEE Transactions On Energy Conversion, vol. 22, no. 2, pp. 421-430, 2007.

[40] M Malinowski, S Stynski, W Kolomyjski, and M Kazmierkowski, "Control of three-level PWM converter applied to variable-speed-type turbines," IEEE International Conference on Industrial Technology, Bombay, India, vol. 56, pp. 69-77, 2009.

[41] K Yuen et al., "Matching a permanent magnet synchronous generator to a fixed pitch vertical axis turbine for marine current energy conversion," IEEE Journal Of Oceanic Engineering, vol. 34, no. 1, pp. 24-31, 2009.

[42] M Simoes, B Bose, and R Spiegel, "Design and performance evaluation of a fuzzy-logic-based variable-speed wind generation system," in 32nd Annual Meeting Of The IEEE Industry-Applications-Society, New Orleans, USA, vol. 33, pp. 956 - 965, 1997.

[43] B Bose and M Simões, "Fuzzy logic based intelligent control of a variable speed cage machine wind generation system," IEEE Transactions on Power Electronics, vol. 33, no. 4, pp. 956-965, 1997.

[44] A Abo-Khalil, D Lee, and J Seok, "Variable speed wind power generation system based on fuzzy logic control for maximum output power tracking," IEEE 35th Annual Power Electronics Specialists Conference, Aachen, Germany, pp. 2039-2042, 2004.

[45] W Qiao, W Zhou, J Aller, and R Harley, "Wind speed estimation based sensorless output maximization control for a wind turbine driving a DFIG," IEEE Transactions On Power Electronics, vol. 23, no. 3, pp. 1156-1169, 2008.

[46] H Li, K Shi, and P McLaren, "Neural-network-based sensorless maximum wind energy capture with compensated power coefficient," IEEE Transactions On Industry Applications, vol. 41, no. 6, pp. 1548-1556, 2005.

[47] H Li, D Zhang, and S Foo, "A stochastic digital implementation of a neural network controller for small wind turbine systems," IEEE Transactions On Power Electronics, vol. 21, no. 5, pp. 1502-1507, 2006.

[48] M Chinchilla, S Arnaltes, and J Burgos, "Control of permanent-magnet generators applied to variable-speed wind-energy systems connected to the grid," IEEE Transactions On Energy Conversion, vol. 21, no. 1, pp. 130-135, 2006.

[49] A Ahmed, Li Ran, and J Bumby, "Simulation and control of a hybrid PV-wind system," IET 4th Conference on Power Electronics, Machines and Drives, pp. 421- 425, 2008.

[50] M Parker, P Tavner, L Ran, and A Wilson, "A low cost power-tracking controller for a small vertical axis wind turbine," The 40th International Universities Power Engineering Conference, Cork, Ireland, 2005.

[51] A Knight and G Peters, "Simple wind energy controller for an expanded operating range," IEEE Transactions On Energy Conversion, vol. 20, no. 2, pp. 459-466, 2005.

[52] S Dehghan, M Mohamadian, and A Yazdian, "A new variable-speed wind energy conversion system using permanent-magnet synchronous generator and Z-source inverter," IEEE Transactions On Energy Conversion, vol. 24, no. 3, pp. 714-724, 2009.

[53] T Senjyu et al., "Wind velocity and rotor position sensorless maximum power point tracking control for wind generation system," Renewable Energy, vol. 31, no. 11, pp. 1764-1775, 2006.

[54] S Morimoto, H Nakayama, M Sanada, and Y Takeda, "Sensorless output maximization control for variable-speed wind generation system using IPMSG," 38th IEEE Annual Meeting of the Industry-Applications-Society, Salt Lake, USA, vol. 41, pp. 60-67, 2005.

[55] T Senjyu et al., "Sensor-less maximum power point tracking control for wind generation system with squirrel cage induction generator," Renewable Energy, vol. 34, no. 4, pp. 994–999, 2009.

[56] B Shen, B Mwinyiwiwa, Y Zhang, and B Ooi, "Sensorless maximum power point tracking of wind by DFIG using rotor position phase lock loop (PLL)," IEEE Transactions On Power Electronics, vol. 24, no. 4, pp. 942-951, 2009.

[57] C Pan and Y Juan, "A novel sensorless MPPT controller for a high-efficiency microscale wind power generation system," IEEE Transactions On Energy Conversion, vol. 25, no. 1, pp. 207-216, 2010.

[58] N Mutoh and A Nagasawa, "A maximum power point tracking control method suitable for compact wind power generators," IEEE Power Electronics Specialists Conference, vol. 1-7, Cheju Isl, South Korea, pp. 1740-1746, 2006.

[59] A Raju, K Chatterjee, and B Fernandes, "A simple maximum power point tracker for grid connected variable speed wind energy conversion system with reduced switch count power converters," IEEE 34TH Annual Power Electronics Specialists Conference, vol. 2, Acapulco, Mexico, pp. 748-753, 2003.

[60] Q Wang and L Chang, "An intelligent maximum power extraction algorithm for inverter-based variable speed wind turbine systems," IEEE Transactions On Power Electronics, vol. 19, no. 5, pp. 1242-1249, 2004.

[61] T Tanaka, T Toumiya, and T Suzuki, "Output control by Hill-climbing method For a small scale wind power generating system," Renewable Energy, vol. 12, no. 4, pp. 387-400, 1997.

[62] R Datta and V Ranganathan, "A method of tracking the peak power points for a variable speed wind energy conversion system," IEEE Transactions On Energy Conversion, vol. 18, no. 1, pp. 163-167, 2003.

[63] C Liu, K Chau, and X Zhang, "An efficient wind–photovoltaic hybrid generation system using doubly excited permanent-magnet brushless machine," IEEE Transactions On Industrial Electronics, vol. 57, no. 3, pp. 831 - 839, 2010.

[64] E Koutroulis and K Kalaitzakis, "Design of a maximum power tracking system for wind-energy-conversion applications," IEEE Transactions On Industrial Electronics, vol. 53, no. 2, pp. 486-494, 2006.

[65] S Barakati, M Kazerani, and J Aplevich, "Maximum power tracking control for a wind turbine system including a matrix converter," IEEE Transactions On Energy Conversion, vol. 24, no. 3, pp. 705-715, 2009.

[66] R Hilloowala and A Sharaf, "A rule-based fuzzy logic controller for a PWM inverter in a stand alone wind energy conversion scheme," IEEE Transactions On Industry Applications, vol. 32, no. 1, pp. 57-65, 1996.

[67] F Bianchi, R Mantz, and C Christiansen, "Power regulation in pitch-controlled variable speed WECS above rated wind speed," Renewable Energy, vol. 29, no. 11, pp. 1911-1922, 2004.

[68] H Camblong, "Digital robust control of a variable speed pitch regulated wind turbine for above rated wind speeds," Control Engineering Practice, vol. 16, no. 8, pp. 946–958, 2008.

[69] L Pak and V Dinavahi, "Real-time simulation of a wind energy system based on the doubly-fed induction generator," IEEE Transactions On Power Systems, vol. 24, no. 3, pp. 1301-1309, 2009.

[70] T Barlas and G van-Kuik, "State of the art and prospectives of smart rotor control for wind turbines," Journal of Physics: Conference Series, vol. 75, no. 1, 2007.

[71] E Muljadi, K Pierce, and P Migliore, "Control strategy for variable-speed, stall-regulated wind turbines," American Control Conference, vol. 1-6, Philadelphia, USA, 1998, pp. 1710-1714.

[72] A Miller, E Muljadi, and D Zinger, "A variable speed wind turbine power control," IEEE Transactions On Energy Conversion, vol. 12, no. 2, pp. 181 - 186, 1997.

[73] A Haniotis, K Soutis, A Kladas, and J Tegopoulos, "Grid connected variable speed wind turbine modeling, dynamic performance and control," IEEE PES Power Systems and Exposition Conference, vol. 1- 3, New York, USA, pp. 759 - 764, 2004.

[74] E Muljadi, K Pierce, and P Migliore, "Soft-stall control for variable-speed stall-regulated wind turbines," Journal Of Wind Engineering And Industrial Aerodynamics, vol. 85, no. 3, pp. 277-291, 2000.

[75] J Bumby, N Stannard, J Dominy, and N McLeod, "A permanent magnet generator for small scale wind and water turbines," in International Conferece On Electrical Machines, vol. 1- 4, Vilamoura, Portugal, 2008, pp. 196-201.

[76] E Elshenawy and A Bahjet, “Development and implementation of maximum power point tracking controller for PV system using neural networks,” Cairo university, Giza, Egypt, PhD Thesis 2002.

[77] A Ahmed, O Mahgoub, and K Elmetwally, “Using neural networks photovoltaic system modeling in maximum power point tracking,” Cairo university, Giza, Egypt, M.Sc. Thesis 2005.

[78] A Özcan, y Mehmet, and E Feriha, “Application of genetic algorithms on a photovoltaic panel (PV)-pump motor matching to natural tracking of PV maximum power points,” in nternational XII. Turkish Symposium on Artificial Intelligence and Neural Networks (TAINN), vol. 1, Canakkale Turkiye, 2003.

[79] D Hohm and M Ropp, “Comparative study of maximum power point tracking algorithms using an experimental, programmable, maximum power point tracking test bed,” IEEE 28th Photovoltaic Specialists Conference, Anchorage, USA, pp. 1699-1702, 2000.

[80] M Saied, “Improved matching of photovoltaic solar arrays supplying DC motors through controlled motor saturation,” 11th International Conference On Microelectronics (ICM99), Kuwait, Kuwait, pp. 275-279, 1999.

[81] M Saied, “The available matching of solar arrays to dc motors having both constant and series-excited field components,” IEEE Transaction On Energy Conversion, vol. 17, no. 3, pp. 301-305, 2002.

[82] M Saied, “The advantages of using saturable DC series motors fed from solar photovoltaic arrays,” Electric Machines And Power Systems, vol. 28, no. 8, pp. 677-687, 2000.

[83] H Ibrahim, F Houssiny, H El-Din, and M El-Shibini, “Microcomputer controlled buck regulator for maximum power point tracker for DC pumping system operates from photovoltaic system,” IEEE International Conference Proceedings For Fuzzy Systems, vol. 1, Seoul, South Korea, pp. 406-411, 1999.

[84] W Swiegers and J Enslin, “An integrated maximum power point tracker for photovoltaic panels,” IEEE International Symposium On Industrial Electronics, vol. 1 and 2, pp. 40-44, 1998.

[85] M Masoum, “Optimal power point tracking of photovoltaic system under all operating conditions,” , Houston, Texas, 1998.

[86] S Alghwainem, “Matching of a dc motor to a photovoltaic generator using a step-up converter with a current-locked loop,” IEEE Transactions On Energy Conversion, vol. 9, no. 1, pp. 192-198, 1994.

[87] M Masoum, A Mohammad, S Dehbonei, and A Hooman, “Design construction and testing of a voltage-based maximum power point tracker (VMPPT) for small satellite power supply,” The 13th Annual AIAA/USU Conference on Small Satellites, pp. 1-12, 1999.

[88] S Togashi, T Noguchi, and R Nakamoto, “Short-Current pulse based maximum-power-point operation of photovoltaic generation system,” Conference in proceeding of IEEJ/IAS, vol. 3, pp. 221–224, 1999.

[89] T Noguchi, S Togashi, and R Nakamoto, “Short-current pulse-based maximum-power-point tracking method for multiple photovoltaic-and-converter module system,” IEEE Transactions On Inustrial Electronics, vol. 49, no. 1, pp. 217-223, 2002.

[90] C Hua, J Lin, and C Shen, “Implementation of a DSP_ controlled photovoltaic system with peak power tracking,” IEEE Transactions On Inustrial Electronics, vol. 45, no. 1, pp. 99-107, 1998.

[91] O Wasynczuk, “Dynamic behavior of a class of photovoltaic power systems,” IEEE Transactions On Power Application Systems, vol. 102, no. 9, pp. 3031–3037, 1983.

[92] N Kasa, T Iida, and L Chen, “Fyack inverter controlled by sensorless current MPPT for photovoltaic power system,” IEEE Transactions On Industrial Electronics, vol. 52, no. 4, pp. 1145–1152, 2005.

[93] Y Kim, H Jo, and D Kim, “A new peak power tracker for cost-effective photovoltaic power systems,” The 31st Intersociety Energy Conversion Engineering Conference (IECEC 96), pp. 1673–1678, 1996.

[94] Y Chen and K Smedley, “A cost-effective single-stage inverter with maximum power point tracking,” IEEE Transaction On Power Electronics, vol. 19, no. 5, pp. 1289-1294, 2004.

[95] E, Kalaitzakis, K Koutroulis and N Voulgaris, “Development of a microcontroller-based, photovoltaic maximum power point tracking control system,” IEEE Transactions On Power Electronics, vol. 16, no. 1, pp. 46-54, 2001.

[96] D Snyman and J Enslin, “Simplified maximum power point controller for PV installations,” The IEEE 23rd Photovoltaic Specialists Conference, Louisville, USA, pp. 1240-1245, 1993.

[97] H Koizumi and K Kurokawa, “A novel microcontroller for grid-connected photovoltaic systems,” IEEE Transactions On Industrial Electronics, vol. 53, no. 6, pp. 1889-1897, 2006.

[98] K Hussein, I Muta, T Hoshino, and M Osakada, “Maximum photovoltaic power tracking: An algorithm for rapidly changing atmospheric conditions,” IEE Proceedings-Generation Transmission And Distrbution, vol. 142, no. 1, pp. 59-64, 1995.

[99] W Wu et al., “DSP-based multiple peak power tracking for expandable power system,” in IEEE 18th Annual Applied Power Electronics Conference and Exposition, vol. 1 and 2, Miami, USA, pp. 525- 530, 2003.

[100] Y Kuo, T Liang, and J Chen, “Novel maximum-power-point-tracking controller for photovoltaic energy conversion system,” IEEE Transactions On Industrial Electronics, vol. 48, no. 3, pp. 594-601, 2001.

[101] A Nafeh, F Fahmy, O Mahgoub, and E Abouelzahab, “Developed algorithm of maximum power tracking for stand alone photovoltaic system,” Energy Sources, vol. 20, no. 1, pp. 45-53, 1998.

[102] A Bahgat, N Helwa, G Ahmad, and E El Shenawy, “Maximum power point traking controller for PV systems using neural networks,” Renewable Energy, vol. 30, no. 8, pp. 1257-1268, 2005.

[103] I Cha et al., “MPPT for temperature compensation of photovoltaic system with neural networks,” in IEEE 26th Photovoltaic Specialists Conference, Anaheim, USA, pp. 1321-1324, 1997.

[104] A Ahmed, K El-Metwally, and O Mahgoub, “A photovoltaic intelligent power conditioning unit for MPPT using neural networks,” in 5th International Engineering Conference, Sharm El-Shikh, Egypt, vol. 1, 2006.

[105] G Yu, M Jung, J Song, I Cha, and I Hwang, “Maximum power point tracking with temperature compensation of photovoltaic For air conditioning system with fuzzy controller,” in IEEE 25th Photovoltaic Specialists Conference, Washington, USA, pp. 1429-1432, 1996.

[106] W Tsai-Fu, C Chien-Hsuan, and C Yu-Hai, “A fuzzy-logic-controlled single-stage converter for PV-powered lighting system applications,” IEEE Transactions On Industrial Electronics, vol. 47, no. 2, pp. 287-296, 2000.

[107] V Salas, E Olías, A Barrado, and J Pleite, “Novel algorithm applied to maximum power point trackers (MPPT) measuring only one photovoltaic variable,” in 1ST SWH International Conference: Solar-Wind-Hydrogen/Fuel Cells-(Renewable Energies), Segovia, España., 2003.

[108] V Salas, E Olias, A Lazaro, and A Barrado, “Evaluation of a new maximum power point tracker (MPPT) applied to the photovoltaic stand-alone systems,” Solar Energy Materials And Solar Cells, vol. 87, no. 1-4, pp. 807-815, 2005.

[109] G Grandi, D Casadei, and C Rossi, “Direct coupling of power active filters with photovoltaic generation systems with improved MPPT capability,” in IEEE Bologna Power Tech Conference Proceedings, vol. 2, p. 6, 2003.

[110] K Irisawa, T Saito, I Takano, and Y Sawada, “Maximum power point tracking control of photovoltaic generation system under non-uniform insolation by means of monitoring cells,” in IEEE 28th Photovoltaic Specialists Conference, Anchorage, USA, pp. 1707-1710, 2000.

[111] M Ned, M Tore, and P William, Power electronics: converters, applications, and design.: John Wiley & Sons, 2003.

[112] [147]A Hava, R Kerkman, and T Lipo, “Carrier-based PWM-VSI overmodulation strategies: Analysis, comparison, and design,” IEEE Transactions On Power Electronics, vol. 13, no. 4, pp. 674-689, 1998.

[113] A Yazdian-Varjani, S Perera, and J Chicharo, “A centroid-based PWM switching technique for full-bridge inverter applications,” IEEE Transactions On Power Electronics, vol. 13, no. 1, pp. 115-124, 1998.

[114] R Lai and K Ngo, “A PWM method for reduction of switching loss in a full-bridge inverter,” IEEE Transactions On Power Electronics, vol. 10, no. 3, pp. 326–332, 1995.

[115] T Ai, J Chen, and T Liang, “A random switching method for HPWM full-bridge inverter,” IEEE Transactions On Industrial Electronics, vol. 49, no. 3, pp. 595-597, 2002.

[116] C Cecati, A Dell, M Liserre, and V Monopoli, “Design of hbridge multilevel active rectifier for traction systems,” IEEE Transactions On Industry Applications, vol. 39, no. 5, pp. 1541-1550, 2003.

[117] Fukuda S and Yoda T, “A novel current-tracking method for active filters based on a sinusoidal internal model,” IEEE Transactions On Industry Applications , vol. 37, no. 3, pp. 888-895, 2001.

[118] R Teodorescu, F Blaabjerg, and U Liserre, “A new control structure for grid-connected LCL PV inverters with zero steady-state error and selective harmonic compensation,” in 19th Annual IEEE Applied Power Electronics Conference (APEC), vol. 1, Aachen, Germany, pp. 580 – 586, 2004.

[119] B Bose, “An adaptive hysteresis–band current control technique of a voltage-fed PWM inverter for machine drive system,” IEEE Transactions On Industerial Electronics, vol. 37, no. 5, pp. 402–408, 1990.

[120] B Fernandes, S Pillai, and V Subbarao, “Performance of an adaptive hysteresis band current controlled induction motor drive,” in International Conference On Industrial Electronics Control Instrumentation And Automation (IECON 92), vol. 1, San Diego, USA, pp. 447 – 452, 1992.

[121] C Pan, Y Huang, and T Jong, “A constantly sampled current controller with switch status dependent inner bound,” IEEE Transactions On Industrial Electronics, vol. 50, no. 3, pp. 528-535, 2003.

[122] G Bode and D Holmes, “Implementation of three level hysteresis current control for a single phase voltage source inverter,” in IEEE 31st Annual Power Electronics Specialists Conferance, vol. 1-3, Galway, Ireland, pp. 33-38, 2000.

[123] M Bech, F Blaabjerg, and J Pedersen, “Random modulation techniques with fixed switching frequency for three-phase power converters,” IEEE Transactions On Power Electronics, vol. 15, no. 4, pp. 753-761, 2000.

[124] K Low, “A digital control technique for a single-phase PWM inverter,” IEEE Transactions On Industrial Electronics, vol. 45, no. 4, pp. 672-674, 1998.

[125] K Low, “A DSP-based single-phase AC power source,” IEEE Transactions On Industrial Electronics, vol. 46, no. 5, pp. 936-941, 1999.

[126] H Abu-Rub, J Guzin´ski, Z Krzeminski, and H Toliyat, “Predictive current control of voltage-source inverters,” IEEE Transactions On Industrial Electronics, vol. 51, no. 3, pp. 585-593, 2004.

[127] L Kay-Soon and C Runzi, “Model Predictive Control of Parallel-Connected Inverters for Uninterruptible Power Supplies,” IEEE Transactions On Industrial Electronics, vol. 55, no. 8, pp. 2884-2893, 2008.

[128] H Kojabadi, B Yu, I Gadoura, and M Ghribi, “A novel DSP-based current-controlled PWM strategy for single phase grid connected inverters,” IEEE Transactions On Power Electronics, vol. 21, no. 4, pp. 985-993, 2006.

[129] C Meza, J Negroni, D Biel, and F Guinjoan, "Energy-balance modeling and discrete control for single-phase grid-connected PV central inverters," IEEE Transactions On Industrial Electronics, vol. 55, no. 7, pp. 2734-2743, 2008.

[130] M Datta, T Senjyu, A Yona, T Funabashi, and C Kim, "A coordinated control method for leveling PV output power fluctuations of PV–Diesel hybrid systems connected to isolated power utility," IEEE Transaction On Energy Conversion, vol. 24, no. 1, pp. 153-162, 2009.

[131] L Hassaine, E Olias, and J Quintero, "Digital power factor control and reactive power regulation for grid-connected photovoltaic inverter," Renewable Energy, vol. 34, no. 1, pp. 315–321, 2009.

[132] J Liu, J Yang, and Z Wang, "A new approach for single-phase harmonic current detecting and its application in a hybrid active power filter," in The 25th Annual Conference of the IEEE Industrial Electronics Society (IECON '99), vol. 2, San Jose, USA, pp. 849 - 854, 1999.

[133] V Khadkikar, A Chandra, and B Singh, "Generalised single-phase p-q theory for active power filtering: simulation and DSP-based experimental investigation," IET Power Electronics, vol. 2, no. 1, pp. 67 - 78, 2009.

[134] J Correa, F Farret, and M Simoes, "Application of a modified single-phase P-Q theory in the control of shunt and series active filters in a 400 hz microgrid," in 6th Annual IEEE Power Electronic Specialists Conference, vol. 1-3, Recife, Brazil, pp. 2585 - 2591, 2005.

[135] T Wu, H Nien, C Shen, and T Chen, "A single-phase inverter system for PV power injection and active power filtering with nonlinear inductor consideration," IEEE Transactions On Industry Applications, vol. 41, no. 4, pp. 1075-1083, 2005.

[136] M Ryan, W Brumsickle, and R Lorenz, "Control topology options for single-phase UPS inverters," IEEE Transactions On Industry Applications, vol. 33, no. 2, pp. 493-500, 1997.

[137] W Stefanutti and P Mattavelli, "Fully digital hysteresis modulation with switching-time prediction," IEEE Transactions On Industry Applications, vol. 42, no. 3, pp. 763-769, 2006.

[138] A Kawamura and R Hoft, "Instantaneous feedback controlled PWM inverter with adaptive hysteresis," IEEE Transactions On Industry Applications, vol. 20, no. 4, pp. 769–775, 1984.

[139] O Kukrer, H Kmurcugil, and N BaYlndlr, "Control strategy for single-phase UPS inverters," IEE Proceedings-Electric Power Applications, vol. 150, no. 6, pp. 743-746, 2003.

[140] M Ryan and R Lorenz, "A high-performance sine wave inverter controller with capacitor current feedback and “Back-EMF” decoupling," in 26th Annual Power Electronics Specialists Conference (PESC 95), vol. 1-2, Atlanta, USA, pp. 507–513, 1995.

[141] T Kawabata, Y Shikano, and S Higashino, "Chargerless UPS using multi-functional BIMOS inverter—sinusoidal voltage waveform inverter with current minor loop," in IEEE IAS Annual Meeting Conferance, Denver, USA, pp. 513–520, 1986.

[142] V Salas, M Alonso, and F Chenlo, "Overview of the legislation of DC injection in the network for low voltage small grid-connected PV systems in Spain and other countries," Renewable and Sustainable Energy Reviews, pp. 575-583, 2008.

[143] R González, E Gubía, J López, and L Marroyo, “Transformerless single-phase multilevel-based photovoltaic inverter,” IEEE Transactions On Industrial Electronics, vol. 55, no. 7, pp. 2694-2702, 2008.

[144] H Haeberlin, "Evolution of inverters for grid connected PV-Systems from 1989 to 2000," in Proceedings Of The 17th European Photovoltaic Solar Energy Conference, Munich, Germany, pp. 426–430, 2001.

[145] V Salas, M Alonso, E Olias, F Chenlo, and A Barrado, "DC current injection into the network from PV inverters of less than 5 kW for low voltage small grid-connected PV systems ," Solar Energy Materials and Solar Cells, vol. 91, no. 9, pp. 801–806, 2007.

[146] V Salas, E Olias, M Alonso, F Chen, and A Barrado, "DC current injection into the network from PV grid inverters," in IEEE 4th World Conference On Photovoltaic Energy Conversion, vol. 2, Waikoloa, USA, pp. 2371 – 2374, 2006.

[147] M khan, "Supervisory hybrid control of a wind energy conversion and battery storage system," Graduate Department Of Electrical And Computer Engineering, University of Toronto, PHD thesis 2008.

[148] M Lemmon, K He, and I Markovesky, "Supervisory hybrid systems," IEEE Control Systems Magazine, vol. 19, no. 4, pp. 42-55, 1999.

[149] P Antsaklis and A Nerode, "Guest editorial hybrid control systems an introductory discussion to the special issue," IEEE Transactions On Automatic Control, vol. 43, no. 4, pp. 457-460, 1998.

[150] F Valenciaga and P Puleston, "Supervisor control for a stand-alone hybrid generation system using wind and photovoltaic energy," IEEE Transactions On Energy Conversion, vol. 20, no. 2, pp. 398-405, 2005.

[151] M Khan and M Iravani, "Hybrid control of a grid-interactive wind energy conversion system," IEEE Transactions On Energy Conversion, vol. 23, no. 3, pp. 895-902, 2008.

[152] C Wang and M Nehrir, "Power management of a stand-alone wind/photovoltaic/fuel cell energy system," IEEE Transactions On Energy Conversion, vol. 23, no. 3, pp. 957-967, 2008.

[153] D Ipsakisa, S Voutetakisa, P Seferlis, F Stergiopoulosa, and C Elmasides, "Power management strategies for a stand-alone power system using renewable energy sources and hydrogen storage," Internation Journal Of Hyderogen energy, vol. 34, no. 16, pp. 7081-7095, 2009.

[154] T Gebre, T Undeland, O Ulleberg, and P Vie, "Optimal load sharing strategy in a hybrid power system based on PV/Fuel Cell/ Battery/Supercapacitor," in International Conference On Clean Electrical Power, Capri, Itali, pp. 141-146, 2009.
[155] W Irena et al., "A power-quality management algorithm for low-voltage grids with distributed resources," IEEE Transactions On Power Delivery, vol. 23, no. 2, pp. 1055-1062, 2008.
[156] S Teleke, M Baran, A Huang, S Bhattachar, and L Anderson, "Control strategies for battery energy storage for wind farm dispatching," IEEE Transactions On Energy Conversion, vol. 24, no. 3, pp. 725-732, 2009.
[157] S Daniel and N Gounden, "A novel hybrid isolated generating system based on PV fed inverter-assisted wind-driven induction generators," IEEE Transactions On Energy Conversion, vol. 19, no. 2, pp. 416-422, 2004.
[158] L Krichen, A Ouali, and G Boukettaya, "Fuzzy logic supervisor for power control of an isolated hybrid energy production unit," International Journal of Electrical and Power Engineering, vol. 1, no. 3, pp. 279-285, 2007.
[159] E El Mokadem, V Courtecuisse, and C Saudemont, "Fuzzy logic supervisor-based primary frequency control experiments of a variable-speed wind generator," IEEE Transactions on Power Systems, vol. 24, no. 1, 2009.
[160] G Cimuca, C Saudemont, B Robyns, and M Radulescu, "Control and performance evaluation of a flywheel energy-storage system associated to a variable-speed wind generator," IEEE Transactions On Industrial Electronics, vol. 53, no. 4, pp. 1074-1085, 2006.
[161] C Abbey and G Joos, "Supercapacitor energy storage for wind energy applications," in 40th Annual Meeting Of The IEEE-Industry-Applications-Society, vol. 43, Hong Kong, China, pp. 769-776, 2007.
[162] M Datta, T Senjyu, A Yona, and T Funabash, "A fuzzy control based coordinated method for isolated power utility connected clustered photovoltaic systems to provide frequency control," in IEEE 15th International Conference On Intelligent System Applications To Power Systems, Curitiba, Brazil, pp. 1-6, 2009.
[163] L Krichen, B Francois, and A Ouali, "A fuzzy logic supervisor for active and reactive power control of a fixed speed wind energy conversion system," Electric Power Systems Research, vol. 78, no. 3, pp. 418–424, 2008.
[164] R Welch and G Venayagamoorthy, "Optimal control of a photovoltaic solar energy system with adaptive critics," in IEEE International Joint Conference On Neural Networks, vol. 1-6, Orlando, USA, pp. 985-990, 2007.
[165] J Hui and A Bakhshai, "A new adaptive control algorithm for maximum power point tracking for wind energy conversion systems," in IEEE Power Electronics Specialists Conferance (PESC 08), vol. 1-10, Rhodes, Greece, 2008, pp. 4003–4007.
[166] F Valenciaga and P Puleston, "High-order sliding control for wind energy conversion system based on a permanent magnet synchronous generator," IEEE Transactions On Energy Conversion, vol. 23, no. 3, pp. 860–867, 2008.
[167] B Beltran, T Ali, and M Benbouzid, "Sliding mode power control of variable-speed wind energy conversion systems," IEEE Transactions On Energy Conversion, vol. 23, no. 2, pp. 551–558, 2008.
[168] J Mauricio, A Leon, A Gomez-Exposito, and J Solsona, "An adaptive nonlinear controller for DFIM-based wind energy conversion systems," IEEE Transactions On Energy Conversion, vol. 23, no. 4, pp. 1025–1035, 2008.
[169] R Cardenas and R Pena, "Sensorless vector control of induction machines for variable-speed wind energy applications," IEEE Transactions On Energy Conversion, vol. 19, no. 1, pp. 196–205, 2004.
[170] B Kirke, "Evaluation of self-starting vertical axis wind turbines for stand-alone applications," Australia, 1998.
[171] J Bumby and R Martin, "An axial flux air-cored generator: The Savonius Generator," Durham, Uk, 2005.
[172] dSPACE,(2006, October). [Online]: http://www.dspace.ltd.uk/ww/en/ltd/home/products/hw/singbord/ppcconbo.cfm.
[173] T Esram and P Chapman, “Comparison of photovoltaic array maximum power point tracking techniques,” IEEE Transactions On Energy Conversion, vol. 22, no. 2, pp. 439-449, 2007.
[174] J Duffie and W Beckman, Solar engineering of thermal processes.: John Wiley & Sons, 2006.
[175] W Johnston, Solar voltaic cells. New York, , USA: Marcel Dekker, Inc, 1980.
[176] A Ahmed, O Mahgoub, and K El-Metwally, “Neural networks based photovoltaic model,” in Tenth Middle East Power Systems Conference , 2005.

[177] T Townsend, “A simplified method for estimating the long term performance of direct-coupled,” Mechanical Engineering,Universty of Wisconsin-Madison, M.S. Thesis 1989.

[178] W Levine, The control handbook.: CRC Press in cooperation with IEEE Press, 1996.

[179] F Giraud and Z Salameh, “Steady-state performance of a grid-connected rooftop hybrid wind–photovoltaic power system with battery storage,” IEEE Transactions On Energy Conversion, vol. 16, no. 1, pp. 1-7, 2001.

[180] T Suntio, “Analysis and modeling of peak-current-mode-controlled buck converter in DICM,” IEEE Transactions On Industrial Electronics, vol. 48, no. 1, pp. 127-135, 2001.

[181] R Sheehan. (2007) [Online]: http://powerelectronics.com/power_management/pwm_controllers/model-current-mode-control-0507/.

[182] F Tan and R Middlebrook, "A unified model for current-programmed converters," IEEE Transactions On Power Electronics, vol. 10, no. 4, pp. 397–408, 1995.

[183] G Andersen and F Blaabjerg, "Current programmed control of a single-phase two-switch buck–boost power factor correction circuit," IEEE Transactions On Industrial Electronics, vol. 53, no. 1, pp. 263-271, 2006.

[184] C Deisch, "Simple switching control method changes power converter into a current source," in IEEE Power Electronics Specialists Conference, Syracuse, USA, 1978, pp. 300–304.

[185] M Aimé, G Gateau, and T Meynard, "Implementation of a peak-current-control algorithm within a field-programmable gate array," IEEE Transactions On Industrial Electronics, vol. 54, no. 1, pp. 406-418, 2007.

[186] R Middlebrook, "Modeling current-programmed buck and boost regulators," IEEE Transactions On Power Electronics, vol. 4, no. 1, pp. 36-52, 1989.

[187] S Mazumder, A Nayfeh, and D Boroyevich, "Theoretical and experimental investigation of the fast- and slow-scale instabilities of a DC-DC converter," IEEE Transactions On Power Electronics, vol. 16, no. 2, pp. 201-216, 2001.

[188] I Zafrany and S Ben-yaakov, "A chaos model of subharmonic oscillations in current mode PWM boost converters," in IEEE 26th Annual Power Electronics Specialists Conference (PESC 95), vol. 1-2, Atlanta, USA, pp. 1111-1117, 1995.

[189] J Lu and X Wu, "A novel piecewise linear slope compensation circuit in peak current mode control," in IEEE International Conference On Electron Devices And Solid-State Circuits, Tainan, Taiwan, pp. 929-932, 2007.

[190] S Sammanta, P Patra, S Mukhopadhyay, and A Patra, "Optimal slope compensation for step load in peak current controlled dc-dc buck converter," in 13th International Power Electronics And Motion Control Conference, Poznan, Poland, pp. 485-489, 2008.

[191] T Grote et al., "Adaptive digital slope compensation for peak current mode control," in IEEE Energy Conversion Congress and Exposition (ECCE 2009), San Jose, USA, pp. 3523 - 3529, 2009.

[192] S Yang, Q Lei, F Peng, and Z Qian, "A robust control scheme for grid-connected voltage source inverters," in IEEE 25th Annual Applied Power Electronics Conference and Exposition, Palm Springs, USA, pp. 1002-1009, 2010.

[193] M Liserre, F Blaabjerg, and S Hansen, "Design and control of an LCL-filter-based three-phase active rectifier," IEEE Transactions On Industry Applications, vol. 41, no. 5, pp. 1281-1291, 2005.

[194] M Raou and M Lamchich, "Average current mode control of a voltage source inverter connected to the grid: Application to different filter cells," Journal Of Electrical Engineering, vol. 55, no. 3, pp. 77-82, 2004.

[195] H Karshenas and H Saghafi, "Performance investigation of LCL filters in grid connected converters," in IEEE/PES Transmission And Distribution Conference And Exposition Latin America, vol. 1-3, Caracas, Venezuela, pp. 565-570, 2006.

[196] P Mercier, R Cherkaoui, and A Oudalov, "Optimizing a battery energy storage system for frequency control application in an isolated power system," IEEE transactions On Power Systems, vol. 24, no. 3, pp. 1469 - 1477, 2009.

[197] Home Energy Solutions. (2008) [Online]: http://www.heshomeenergy.com/images/pdf/HES_article.pdf.

[198] G Stavrakakis and G Kariniotakis, "A general simulation algorithm for the accurate assessment of isolated diesel-wind turbines systems interaction," IEEE Transactions On Energy Conversion, vol. 10, no. 3, pp. 577-590, 1995.

[199] K Kutluay, Y Çadırcı, Y Özkazanç, and I Çadırcı, "A new online state-of-charge estimation and monitoring system for sealed lead–acid batteries in telecommunication power supplies," IEEE Transactions On Industrial Electronics, vol. 52, no. 5, pp. 1315-1327, 2005.
[200] M Coleman, C Lee, C Zhu, and W Hurley, "State-of-charge determination from EMF voltage estimation: Using impedance, terminal voltage, and Current for lead-acid and lithium-ion batteries," IEEE Transactions On Industrial Electronics, vol. 54, no. 5, pp. 2550-2557, 2007.
[201] A Anbuky and P Pascoe, "VRLA battery state-of-charge estimation in telecommunication power systems," IEEE Transactions On Industrial Electronics, vol. 47, no. 3, pp. 565-573, 2000.
[202] S Muyeen, R Takahashi, T Murata, and J Tamura, "Integration of an energy capacitor system with a variable-speed wind generator," IEEE Transactions On Energy Conversion, vol. 24, no. 3, pp. 740-749, 2009.
[203] M Torres-Hernandez and M Velez-Reyes, "Hierarchical control of hybrid power systems," in IEEE 11th International Conference On Power Electronics, Cuernavaca, Mexico, pp. 169 - 176, 2008.
[204] R Jazayeri et al., "A survey of load control programs for price and system stability," IEEE Transactions On Power Systems, vol. 20, no. 3, pp. 1504-1509, 2005.
[205] M Liserre, A Pigazo, A Dell'Aquila, V Moreno, "An Anti-Islanding Method for Single-Phase Inverters Based on a Grid Voltage Sensorless Control," IEEE Transactions On Industrial Electronics, vol. 53, no. 5, pp. 1418-1426, 2006